**The Effects of Small Changes in Alloy Chemistry on the Solidification Behaviour of the Cobalt-Base Superalloy FSX-414**

by

Kevin Paul Ronan

A thesis submitted to the Graduate Faculty of
Auburn University
in partial fulfillment of the
requirements for the Degree of
Master of Science

Auburn, Alabama
May 14, 2010

Keywords: cobalt superalloy, solidification,
alloy optimization, microporosity, hot tear, statistical analysis



Approved by

Ruel A. Overfelt, Chair, Professor of Materials Engineering
Jeffrey W. Fergus, Associate Professor of Materials Engineering
Barton C. Prorok, Associate Professor of Materials Engineering

Abstract

Controlled casting experiments have confirmed the industrial experience that small changes in alloy chemistry dramatically affect the frequency and severity of microporosity and hot tear defects in investment castings made from the cobalt-based alloy FSX-414. A statistical model has been constructed from the defect characterization data and the differential thermal analysis data gathered from experimental test castings. Elements both within and outside of specification control were found to interact and affect FSX-414 solidification behaviour and therefore influence the formation of casting defects. The statistical model was subsequently used to create both optimized and unbalanced composition ranges for FSX-414. The predicted effects of the statistically-generated alloy chemistries were successfully validated using additional test castings. Thermal analyses of samples extracted from the test castings revealed fundamental differences in the solidification behaviour of the different alloys. The results of this investigation explain how small variations in alloy chemistry can yield significant changes in alloy solidification behaviour and therefore create a range of FSX-414 investment casting quality. A powerful statistical analysis technique has been used to create statistically valid relationships between alloy chemistry and casting quality, leading to a proposal for a streamlined and cost-effective method for optimizing equiaxed alloy chemistry.

Acknowledgements

The author would like to acknowledge Paul Griffiths and Doug Orr of Precision Castparts Corp. for their support of the industrial casting trials which formed the basis for this investigation. Cannon-Muskegon Corporation and BodyCote Materials Testing Laboratory are acknowledged for their contributions and technical assistance with materials testing. The thermodynamic modeling portion of this research was completed by Dr. Victor Li of Portland State University and was generously funded by Jim Barrett of Precision Castparts Corp. via the Oregon Metals Initiative. Thanks to Jeff Marksthaler of BodyCote Materials Testing Laboratory in Portland, OR for facilitating my access to the BodyCote metallographic preparation and analysis facilities. Sean Doole's assistance with metallographic sample preparation was invaluable. Dr. Steven Cockcroft of the Department of Materials Engineering at The University of British Columbia and Dr. Ganjiang Feng of GE Power Systems in Greenville, SC are acknowledged for their support in providing access to their departments' scanning electron microscope laboratories and resources.

As chief advisor and mentor, Dr. Tony Overfelt has provided both technical guidance and encouragement for me to explore avenues and concepts which otherwise I may never have properly considered. Thank you for your invaluable counsel and patience along my journey.

Most importantly, I would like to acknowledge my wonderfully supportive and patient wife, Erin, who more than anyone, deserves credit and honourable mention. She has selflessly endured hundreds of hours alone while I have worked on this project, always the champion, always believing, always focused on eventual success and attainment of the goal. Thank you, Erin – I could not have completed this work nor achieved what we have without your support.

Table of Contents

Abstract ..... ii

Acknowledgements ..... iii

List of Tables ..... viii

List of Figures ..... ix

List of Symbols ..... xiv

List of Abbreviations ..... xvi

I. Introduction ..... 1

II. Literature Review ..... 6

A. FSX-414 ..... 6

B. Physical Metallurgy of Cobalt-Based Superalloys ..... 7

C. Microporosity in Castings ..... 12

1. Solidification shrinkage ..... 12

2. Types of feeding ..... 14

3. Metallostatic tension in liquids, pore nucleation and dissolved gases ..... 18

4. Interdendritic flow, permeability and interdendritic porosity ..... 20

5. Forms of porosity ..... 23

6. Effects of composition ..... 25

D. Hot Tearing ..... 28
1. Stress and strain concentration ..... 29
2. Grain boundary liquid films and wetting ..... 30
3. Critical temperature range ..... 32
4. Effects of solidification rate and strain rate ..... 34
5. Effect of microstructure ..... 37
6. Effect of alloying ..... 38
7. Role of feeding and eutectic solidification ..... 40
8. Nucleation of hot tears ..... 44
9. Control and elimination of hot tears ..... 46
E. DTA and DSC Testing and Interpretation ..... 47
III. Objectives ..... 54
IV. Experimental Methods ..... 55
A. Test Vehicle Casting ..... 55
B. Quantitative Analyses of HTTV Castings ..... 59
1. Hot tears ..... 59
2. Microporosity ..... 59
3. Carbide microstructure ..... 61
4. Secondary dendrite arm spacing ..... 62
5. Grain size ..... 63
6. Scanning electron microscopy ..... 64
C. Chemistry Determination ..... 65
D. HTTV Thermal Analyses ..... 66
E. Modeling ..... 68
1. Solidification and stress modeling ..... 68
2. Thermodynamic modeling ..... 70

F. Validation Test Bar Castings ..... 71
1. Chemistry determination ..... 72
2. Metallographic evaluation ..... 73
3. Differential scanning calorimetry ..... 73
V. Results ..... 74
A. Hot Tears ..... 74
B. Microporosity ..... 88
C. Microstructure ..... 91
1. Secondary dendrite arm spacing ..... 91
2. Carbide characterization ..... 91
3. Grain size and structure ..... 95
D. Chemical Composition ..... 102
E. Differential Thermal Analyses ..... 105
F. Thermodynamic Modeling ..... 108
VI. Statistical Analyses ..... 112
A. Basic Statistical Analyses ..... 112
B. Multiple Linear Regression Analyses – Fit Model ..... 116
1. Microstructure ..... 116
2. Hot tears ..... 120
3. Differential thermal analyses ..... 122
4. Microporosity ..... 125
5. Summary of statistical models ..... 127
C. Predictive Modeling ..... 128
VII. Validation Trials ..... 132
A. Validation Test Bar Microporosity ..... 134
B. Validation Test Bar Microstructure ..... 136

C. Validation Test Bar Grain Structure ..... 140

D. Stress Rupture Testing ..... 142

E. Differential Scanning Calorimetry ..... 144

VIII. Summary and Conclusions ..... 151

References ..... 153

Appendices ..... 158

List of Tables

Table 1 Nominal composition of FSX-414 and other Co-base superalloys .....6

Table 2 Alloying effects and carbide components in Co-based superalloys..... 8

Table 3 Analytical method used to establish HTTV chemical composition..... 65

Table 4 Carbide transition measurements for HTTV ..... 92

Table 5 Range of elemental concentration by element across all HTTV metal lots ..... 102

Table 6 Summary of event temperatures from DTA analyses of HTTV castings ..... 105

Table 7 Summary of chemistry versus DTA fit model analyses ..... 123

Table 8 Summary of chemistry versus SCMPR fit model analyses ..... 125

Table 9 Normalized comparison of actual chemistries of the VTB heats ..... 132

Table 10 Stress rupture results from the validation test bars ..... 142

List of Figures


Figure 1 Crow-AMSAA plot of the instantaneous FPI defect rate for hot tears for production FSX-414 IGT nozzle segments ..... 3

Figure 2 Typical carbide components and carbide morphology in as-cast FSX-414 ..... 9

Figure 3 Schematic illustration of the Co-Ni-Cr and Co-Cr-W ternary phase diagrams ..... 11

Figure 4 Schematic illustration of the volume change with decreasing temperature in liquid, during freezing, and in the solid state ..... 13

Figure 5 Schematic illustration of the progressive solidification of an unfed sphere ..... 14

Figure 6 Schematic illustration of the effects of eutectic liquid on the narrowest portions of the interdendritic passages ..... 16

Figure 7 Schematic illustration describing the dimensional effects of solid feeding ..... 17

Figure 8 Schematic illustration representing the five feeding mechanisms in castings ..... 17

Figure 9 Calculated metallostatic tensions in residual liquid for different feeding regimes ... 19

Figure 10 Schematic illustration of the various forms of shrinkage-related defects ..... 24

Figure 11 Schematic representation of the creation of layer porosity defects ..... 25

Figure 12 Λ curve for binary Al-Cu system, describing variation in measured porosity content with changes in alloy composition ..... 27

Figure 13 Schematic illustration of the distribution of liquid between hexagonal grains during the development of a hot tear ..... 29

Figure 14 Schematic illustration of the distribution of liquid on grain boundaries as a function of the dihedral angle ..... 31

Figure 15 Schematic illustration of hot the distribution of liquid on grain boundaries impacts castability ..... 32

Figure 16 Contraction rates of iron-, copper- and aluminum-based alloys cast into unrestrained test bars ..... 35

Figure 17 Fraction of remaining liquid as a function of temperature for two Ni-based superalloys with poor castability ..... 36

Figure 18 Fraction of remaining liquid as a function of temperature for two Ni-based superalloys with superior castability ..... 37

Figure 19 Schematic illustration of how grain size affects strain distribution at grain boundary liquid films given the same strain magnitude ..... 38

Figure 20 A backfilled hot tear in a grain-refined Al-10Cu alloy ..... 41

Figure 21 Alloy composition dependence on the shrinkage and mechanical pressure drop contributions at the roots of the dendrites for the Al-Cu system ..... 42

Figure 22 Comparison of the calculated hot tear susceptibility rating versus alloy composition for the Al-Cu system ..... 43

Figure 23 Schematic illustrations of classical and calorimetric DTA equipment ..... 48

Figure 24 Schematic illustration of power-compensated DSC equipment ..... 49

Figure 25 Melting temperature of gold heated at different rates, as determined by DTA ..... 52

Figure 26 Eutectic temperature of Co-18.5 at.% Al heated and cooled at different rates as determined by DTA ..... 53

Figure 27 Isometric views of the HTTV casting CAD model definition ..... 56

Figure 28 Annotated photograph of a set of HTTV castings prior to sectioning ..... 61

Figure 29 Typical SDAS evaluation micrograph, including an intercept line ..... 62

Figure 30 Typical macro grain size evaluation photo including the grain boundary intercept lines ..... 64

Figure 31 Illustration of the interpretations of DTA data employed ..... 67

Figure 32 ProCAST™ predicted cooling curves overlaid with HTTV experimental data ..... 69

Figure 33 Validation test bar geometry and mold configuration ..... 72

Figure 34 Hot tear severity rating versus metal lot for all Phase II and Phase III HTTV castings ..... 76

Figure 35 Photograph of longest bars and microstructure at hot tears from least severely torn HTTV casting ..... 77

Figure 36 Photograph of longest bars and microstructure at hot tears from most severely torn HTTV casting ..... 78

Figure 37 Results of ProCAST™ solidification simulation for the HTTV casting ..... 79

Figure 38 Results of ProCAST™ hot tear indicator for the HTTV casting ..... 80

Figure 39 SEM image of the facture surface of a hot tear ..... 81

Figure 40 Higher magnification SEM image of the hot tear surface shown in Figure 39 ..... 82

Figure 41 Higher magnification backscattered SEM image of a second area of the hot tear surface shown in Figure 39 ..... 83

Figure 42 Photomicrograph of the tip of a hot tear with little or no evidence of eutectic carbide on one side of the tear ..... 84

Figure 43 Photomicrograph of the tip of a hot tear with evidence of eutectic carbide on one side of the tear ..... 85

Figure 44 Hot tear decorated with large, rounded islands of $M_7C_3$ ..... 86

Figure 45 Hot tear decorated with large, elongated islands of $M_{23}C_6$ ..... 87

Figure 46 Examples of the range in microporosity developed between HTTV castings ..... 89

Figure 47 Semi-continuous microporosity rating versus metal lot for all HTTV castings ..... 90

Figure 48 Micrographs of the carbide microstructure on either side of a typical carbide transition ..... 93

Figure 49 Micrographs of the carbide microstructure on either side of a severe carbide transition ..... 94

Figure 50 Mean free path average grain size for the longest HTTV bar by metal lot ..... 96

Figure 51 Standard deviation of the mean free path average grain size across all HTTV bars by metal lot ..... 97

Figure 52 Micrographs illustrating the difference in cross-sectional grain size observed between metal lots at the center of the longest two HTTV bars ..... 98

Figure 53 Micrographs illustrating the difference in cross-sectional grain structure at the downsprue fillet radius in HTTV bars of identical length ..... 99

Figure 54 Micrographs illustrating the difference in cross-sectional grain size and structure at the downsprue fillet radius in the two longest HTTV bars ..... 100

Figure 55 Micrographs illustrating the differences in cross-sectional grain size and structure at the feeder fillet radius in HTTV bars of identical length ..... 101

Figure 56 Normalized representation of HTTV chemistries versus the FSX-414 material specification requirements ..... 103

Figure 57 Measured concentrations of other elements not controlled by the B50A489 specification, but detected in HTTV castings ..... 104

Figure 58 Selected DTA heating curves from the samples excised from seven different HTTV castings ..... 106

Figure 59 Selected DTA cooling curves from the samples excised from seven different HTTV castings ..... 107

Figure 60 Fraction solid versus temperature predictions provided by thermodynamic modeling of each of the HTTV chemistries using JMatPro™ and the Gulliver-Scheil equation ..... 109

Figure 61 Chart of the isothermal range in physical properties predicted by the thermodynamic modeling of each of the HTTV chemistries using JMatPro™ ..... 110

Figure 62 Chart of the change in the surface tension of the residual liquid predicted by modeling of each of the HTTV chemistries using JMatPro™ ..... 111

Figure 63 Plot of the total length of hot tears versus the SCMPR for all Phase II and Phase III HTTV castings ..... 113

Figure 64 Identical data to Figure 63 with the SCMPR data separated into two populations, which yields more statistically significant relationships ..... 114

Figure 65 Regression analysis of the total length of hot tears for all Phase II and Phase III HTTV castings versus boron concentration ..... 115

Figure 66 Fit Model analysis, parameter estimates and the summary of statistical fit for total hot tear length versus microstructural response variables; longest HTTV bar at the downsprue ..... 117

Figure 67 SEM backscatter image of the carbide structure at the tip of a hot tear including WDX element maps of Cr and W taken from the same field of view ..... 119

Figure 68 Fit Model analysis, parameter estimates and the summary of statistical fit for total hot tear length versus quantitative DTA data ..... 121

Figure 69 Fit Model analysis and the summary of statistical fit for the width of the mushy zone as determined by quantitative DTA analysis and HTTV actual chemistry ..... 124

Figure 70 Fit Model analysis and the summary of statistical fit for all SCMPR data and HTTV actual chemistry ..... 126

Figure 71 Map of the statistical connections discovered between small changes in FSX-414 alloy chemistry and the macro- and microscopic response variables ..... 127

Figure 72 View of the saddle-shaped second-order relationship between P and Fe within the Fit Model for microporosity ..... 129

Figure 73 Views of a portion of the JMP™ Fit Model Profiler describing the relationship between the SCMPR and chemistry ..... 130

Figure 74 Views of the JMP™ Fit Model Contour Profiler for two elements ..... 131

Figure 75 Comparison of the predicted SCMPR and HTSR for the target and actual chemistries of each of the VTB heats ..... 133

Figure 76 Micrograph of the most severe field of microporosity detected along the baseline alloy VTB centerline ..... 134

Figure 77 Micrograph of the most severe field of microporosity detected along the alloy VTB centerline ..... 135

Figure 78 Micrograph of the most severe field of microporosity detected along the unbalanced alloy VTB centerline ..... 135

Figure 79 Typical carbide microstructure at the centerline of a VTB cast from the alloy chemistry ..... 137

Figure 80 Typical carbide microstructure at the centerline of a VTB cast from the optimized alloy chemistry ..... 139

Figure 81 Typical carbide microstructure at the centerline of a VTB cast from the unbalanced alloy chemistry ..... 139

Figure 82 Typical grain structure at the center of a VTB cast from the baseline alloy ..... 140

Figure 83 Typical grain structure at the center of a VTB cast from the optimized alloy ..... 141

Figure 84 Typical grain structure at the center of a VTB cast from the unbalanced alloy ..... 141

Figure 85 Superimposed DSC curves from each of the three VTB trials ..... 145

Figure 86 Superimposed calculated fraction solid versus temperature curves from each the three sets of VTB trial DSC data illustrated in Figure 85 ..... 146

Figure 87 Superimposed average rate of change of calculated fraction solid versus temperature curves from each of the three sets of VTB trial DSC data ..... 147

Figure 88 Expanded view of the final 35% of solidification from Figure 87; average rate of change of calculated fraction solid versus temperature for the VTB trial alloys ..... 148

List of Symbols

| | | | |
|---|---|---|---|
| $a$ | grain diameter | $H_f$ | latent heat of fusion |
| $A_s$ | integral from DTA (DSC) response curve to the baseline | $\Delta H_s$ | enthalpy change of sample |
| atm | atmosphere | $k$ | Boltzmann's constant |
| $c_p$ | specific heat capacity | $k$ | distribution coefficient |
| $C_l$ | composition of the liquid | K | permeability |
| $C_o$ | initial alloy composition | $K_M$ | mold thermal conductivity |
| $d$ | dendrite arm spacing | $K_{DTA}$ | DTA (DSC) calibration factor |
| D | area of the mushy zone | $l$ | length of hot spot |
| $dx$ | thickness of metal solidified | L | casting length |
| $\frac{df_s}{dT}$ | solidification rate | $L_c$ | capillary length |
| $f_s$ | fraction solid | $L_{field}^{max}$ | maximum dimension of a discrete field of microporosity |
| $f_l$ | fraction liquid | mm | millimeter |
| $F_v(\theta)$ | algebraic expression relating the volume of a void to the angle, $\theta$ | mg | milligram |
| $g$ | gravitational constant | $m_s$ | mass of sample |
| G | thermal gradient | %MP | percent microporosity |
| G* | geometrical criterion to avoid shrinkage porosity | MPa | megapascal // $(10^6)$ Pa |
| GPa | gigapascal // $(10^9)$ Pa | MZ | mushy zone |
| H | enthalpy | $p$ | 1 - $k$ |

| | | | |
|---|---|---|---|
| $P_f$ | fracture pressure of the liquid | $\Delta T_{Decomp}^{Carbide}$ | Range of carbide decomposition |
| $\Delta P$ | pressure drop due to interdendritic viscous flow | μm | micrometers |
| $\Delta P^*$ | microporosity index | $v$ | flow velocity |
| $r_c$ | radius of a critically sized cavity | V | rate of solidification |
| R | cooling rate | | |
| $R_i$ | radius of interdendritic passages | α | coefficient of thermal expansion |
| $R^2$ | regression coefficient | α | statistical confidence interval |
| $R_{adj}^2$ | adjusted regression coefficient | β′ | liquid-solid contraction factor |
| $t$ | solidification time | γ | austenite |
| T | temperature | $\gamma_{LV}$ | surface tension of the liquid |
| $T_U$ | upper coherency temperature | $\gamma_{SS}$ | solid-solid interfacial energy |
| $T_E$ | eutectic temperature | $\gamma_{SL}$ | solid-liquid interfacial energy |
| $T_l$ | liquidus temperature | ε | strain |
| ΔT | width of mushy zone (°C) | $\varepsilon_b$ | strain accommodated by the grain boundary |
| $\Delta T_{CTR}$ | critical temperature range for hot tearing | η | interdendritic liquid viscosity |
| $T_{Liquidus}^{C}$ | Cooling curve liquidus temperature | θ | dihedral angle |
| $T_{Liquidus}^{C*}$ | Cooling curve liquidus temperature, alternate definition | $\theta_c$ | feeding angle |
| $T_{Eutectic}^{C}$ | Cooling curve eutectic solidification temperature | $\sigma_n$ | imposed stress intensity |
| $T_{Liquidus}^{H}$ | Heating curve liquidus temperature | $\rho_l$ | density of the liquid |
| $T_{Liquidus}^{H*}$ | Heating curve liquidus temperature, alternate definition | τ | interdendritic tortuosity factor |
| $T_{Carbide\_x}^{H}$ | Heating curve carbide decomposition temperature | ω | heat flow constant |

List of Abbreviations

| | | | |
|---|---|---|---|
| ANOVA | analysis of variance | ML | metal lot // master heat |
| AOD | argon oxygen decarburization | MZ | mushy zone |
| DS | directionally solidified | NDE | non-destructive evaluation |
| DSC | differential scanning calorimetry | OEM | original equipment manufacturer |
| DTA | differential thermal analysis | *p*-value | probabilistic measure of statistical insignificance |
| EDX | electron dispersive x-ray | PCC | Precision Castparts Corp. |
| *fcc* | face-centered cubic | PHACOMP | phase composition analysis |
| FPI | fluorescent penetrant inspection | SCMPR | semi-continuous microporosity rating |
| GDMS | glow discharge mass spectrometry | SDAS | secondary dendrite arm spacing |
| GEPS | General Electric Power Systems | SEM | scanning electron microscope |
| *hcp* | hexagonally close packed | SX | single crystal |
| HIP | hot isostatic pressing | *tcp* | topologically-close packed |
| HTSR | hot tear severity rating | TDM | thermodynamic modeling |
| HTTV | hot tear test vehicle | VIM | vacuum induction melted |
| IGT | industrial gas turbine | VTB | validation test bar |
| LCC | Lee, Chang, Chieu | WDX | wavelength dispersive x-ray |

# I. INTRODUCTION

Microporosity and hot tears are serious casting defects that continue to challenge superalloy foundry engineers. FSX-414 is a long-freezing range alloy which is prone to forming both microporosity and hot tears, especially in larger and more geometrically complicated castings and does not respond well to hot isostatic pressing (HIP) even at temperatures in excess of 1200°C. This lack of HIP response is primarily a result of effective solid solution strengthening and a high volume fraction of carbides. In addition, the effects of HIP on the FSX-414 primary carbide microstructure and the resultant mechanical properties have not been thoroughly explored. Therefore in contrast to most Ni-based and Fe-based superalloys, the use of HIP to heal microporosity in FSX-414 castings is not condoned by original equipment manufacturers (OEMs) or casting end users. For these reasons, microporosity defects in FSX-414 castings must be eliminated through the foundry engineer's development of robust and cost-effective production processes that produce sound castings which meet all end-use requirements. [1]

Although minor hot tear defects can be repaired by welding in many equiaxed superalloy casting alloys, the routine repair of inherent casting defects does not define an acceptable nor cost-effective long-term production process. Additionally, OEMs will not qualify production processes that generate castings with either hot tear defects or fields of microporosity in excess of specification allowances. Furthermore, foundry engineers are tasked with establishing and maintaining process stability which is a critical factor not only for business profitability, but also because the quality of production casting processes is monitored by their customers. Production casting processes which are permitted to drift from the quality established during baseline casting

qualification into ones that consistently produce casting defects can be subject to disqualification, even if the defects of concern are repairable. In circumstances of disqualification, the casting supplier must immediately stop producing hardware until a more stable process is developed and qualified. These situations often result in prolonged delays to casting deliveries which in turn may cause expensive stoppages to post-casting production lines, delays to engine delivery schedules and serious impacts to businesses.

Figure 1 provides production fluorescent penetrant inspection (FPI) data from the large (>40 kg) complex geometry FSX-414 IGT nozzle segment casting pictured on the left. Each of the castings was manufactured at PCC Deer Creek (PCC), an IGT nozzle foundry located near Portland, Oregon using a fixed process from wax molding through casting. The Crow-AMSAA chart illustrates significant dissimilarity in the number of hot tear defects developed in the castings as master heats of FSX-414 change. Han [2] has also documented similar experiences to these with FSX-414 castings made at another foundry. Radiographic inspection of the PCC castings revealed a similar degree of variation in microporosity development. An empirical analysis of the sets of FPI and radiographic defect data suggested an inverse relationship between the occurrences of microporosity and hot tears. This seemingly unpredictable and opposing performance of an investment casting foundry's two most critical response variables presents an engineering challenge that demands a robust solution in order to avoid the potential for significant business risk in scrap and/or rework costs.

Studies conducted at PCC prior to 2004 using various sets of production FSX-414 casting data were not successful in identifying any statistically significant links between individual elements and the tendency of FSX-414 to develop microporosity or hot tear defects. This suggests that these two casting response variables were being influenced by interactions between alloying elements and/or one or more lurking variables.

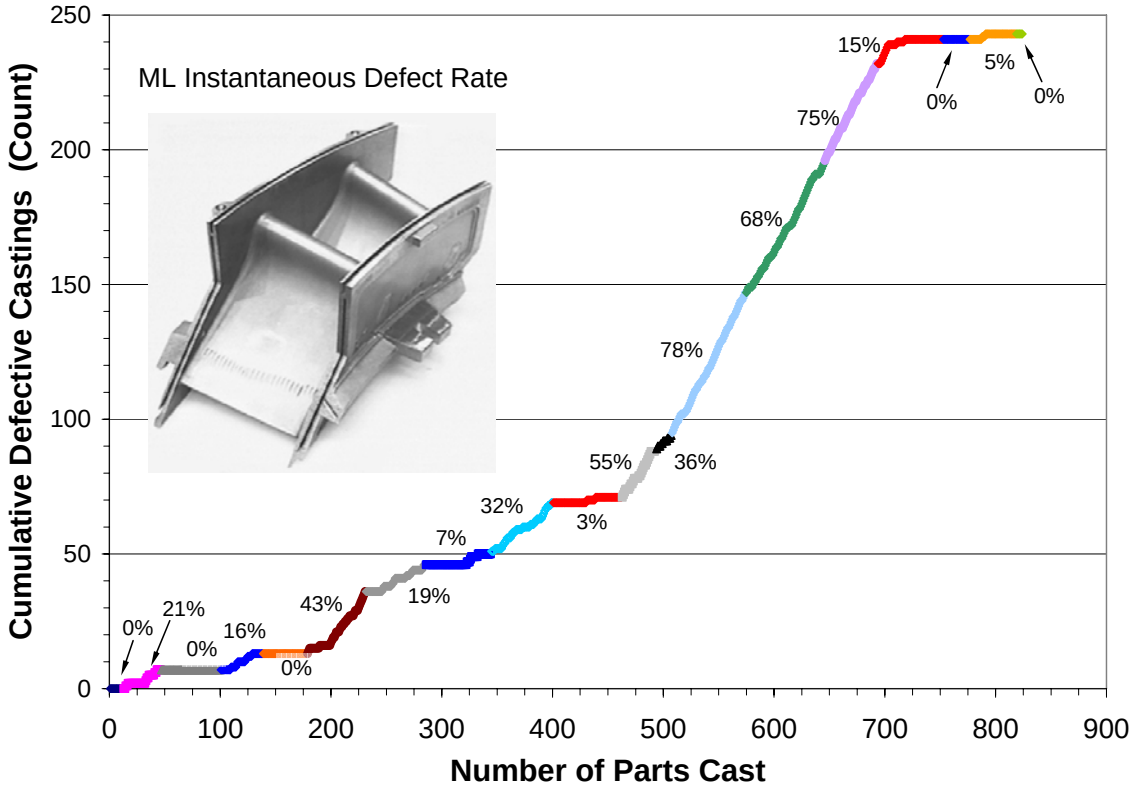


**Figure 1.** Crow-AMSAA plot of the instantaneous FPI defect rate for hot tears in a particular location for production FSX-414 IGT nozzle segments. Each colour series represents a change in metal lot and therefore a change in alloy chemistry. An increase in the slope of the line corresponds to an increase in the instantaneous defect rate. From Reference [1].

Relative to the nickel-based superalloys, there is little published literature available on investment cast cobalt-based alloys. There are two reasons for this: First, although cobalt-based alloys perform very well and have a stable position in the gas turbine superalloy applications base, the intermetallic phases formed upon solidification or heat treatment are not favourable for strengthening; $Ni_3(Ti, Al)$ gamma prime in cobalt alloys dissolves at lower temperatures and has greater matrix mismatch in comparison to the gamma prime phase in Ni-based alloys. Cobalt alloys reside very close to the phase boundaries for topologically close-paced (*tcp*) phases such as Laves, mu and sigma, making it very challenging to develop robust, intermetallic-strengthened alloys. As a result, cobalt alloy research has been largely displaced by much greater funding

aimed toward the rapid development and advancement of vacuum cast equiaxed, directionally solidified and single crystal gamma prime strengthened nickel-based alloys. [3,4] Secondly, much of the development work for cobalt alloys has been performed by companies such as Deloro Stellite (Stellite™, Tribaloy™, Ultimet™), Haynes (Haynes™ Alloys), General Electric (FSX-414™) and Martin-Marietta (MAR-M 509™, MAR-M 918™) for strategic industrial applications. The resultant detailed technical data have generally been left unpublished, safeguarded as trade secret information which can be critical to maintaining industrial competitive advantage. Consequently, the lack of available alloy characterization data presents a significant technical challenge for the supply chain and drives a perpetuating cycle of closed-door process development activities.

Most of the published literature regarding alloying additions made to cobalt-based and nickel-based alloys revolves around relatively large changes in alloy composition. [3-8] Although these studies are interesting, they do not address the effects of elemental interactions within a small and controlled alloy composition range. Consequently, these articles were not able to be directly leveraged toward a solution for the PCC challenge described above. The variability in production casting results and the lack of directly applicable technical data created the basis for a comprehensive study aimed at discovering the roots of the differences in production casting quality which appears to be driven by fluctuations in FSX-414 master heat chemistries.

This paper describes a detailed exploration of the effects of alloy chemistry on the solidification behaviour of FSX-414 based on statistical analyses of quantitative non-destructive evaluation (NDE), microstructural and thermal analysis data. These data sets were created from stringently controlled test castings which were deliberately constructed to rigorously limit process variation so as to isolate the influence of alloy chemistry on the solidification behaviour of FSX-414. By applying a powerful statistical analysis technique, a series of statistically-significant models have been created to link all of the critical predictor and response variables. The final phase of the investigation validates the statistical models with the ultimate

goal of identifying a robust chemistry for FSX-414 which could be used to both reduce and balance the occurrences of hot tear defects and microporosity. The success of the investigative and analysis techniques in identifying links between alloy chemistry and casting response variables that were not previously discovered leads to a proposal for a more timely and cost-effective method of equiaxed alloy predictive modeling and optimization.

# II. LITERATURE REVIEW

## A. FSX-414

FSX-414 is an equiaxed investment cast austenitic (γ) Co-Cr-Ni-W superalloy introduced in 1965 by the General Electric Company to provide comparable mechanical strength at service temperature to alloys X40 and X45 while simultaneously offering improved hot corrosion and sulfidation resistance. The nominal compositions of FSX-414 and other common cobalt-based superalloys are provided in Table 1. FSX-414 is most often used for static components in high temperature, oxidizing or corrosive aerospace and land-based industrial gas turbine (IGT) power generation applications. Even though it was developed in the 1960's, the annual consumption of FSX-414 remains significant; more than 120,000 kg is poured annually by the dominant supplier to the IGT nozzle market into first- and second-stage combustion nozzle (non-rotating) segments for legacy General Electric industrial gas turbines. [1]

| Alloy | C | Mn | Si | Cr | Ni | Fe | W | B | Ti | Ta | Zr |
|---|---|---|---|---|---|---|---|---|---|---|---|
| **FSX-414** | 0.25 | 0.70 | 0.75 | 29.5 | 10.5 | 1.0 | 7.0 | 0.01 | --- | --- | --- |
| **X40** | 0.50 | 0.50 | 0.50 | 22.0 | 10.0 | 1.5 | 7.5 | --- | --- | --- | --- |
| **MAR-M509** | 0.60 | --- | --- | 23.5 | 10.0 | --- | 7.0 | --- | 0.20 | 3.5 | 0.5 |

**Table 1.** Nominal compositions (wt. %) of FSX-414 and other well-known Co-base superalloys. [1,9]

## B. Physical Metallurgy of Cobalt-Based Superalloys

As a direct result of their higher melting temperatures, flatter stress rupture curves and superior hot corrosion resistance compared to Ni- and Fe-based superalloys, cobalt-based alloys like FSX-414, X45 and MAR-M509 are widely used in moderate-stress, non-rotating applications. [1,4] Cobalt alloys, like the austenitic stainless steels, are alloyed with chromium to provide superior hot (980°C – 1095°C) oxidation and corrosion resistance through their natural tendency to form resilient scales of $Cr_2O_3$. Nickel additions are made to both families of alloys to balance the effects of Cr by stabilizing the γ-*fcc* matrix and to suppress the allotropic *hcp* transition which in cobalt, takes place at 790°C. [3] Additions of iron, carbon and manganese also tend to stabilize *fcc* cobalt. [10] Chromium, tungsten and molybdenum participate in solid solution strengthening, *hcp* stabilization and in the formation of the primary and eutectic carbides. Although deliberate additions of elements such as tantalum, niobium and zirconium are not typically made to FSX-414, they can find their way into the alloy via revert streams. Each of these elements is a powerful carbide former that needs to be monitored. Table 2 outlines elemental alloying effects and which of the primary alloying elements tend to participate in the formation of particular carbides in heat-resistant cobalt-based alloys.

FSX-414 is moderately strengthened by solid solution elements, but similar to many cobalt-based alloys, the majority of its strength in service depends upon the generation and control of MC, $M_7C_3$ and $M_{23}C_6$ carbide particles located within grains, in the interdendritic spaces and on the grain boundaries. [3,4] Sullivan [3] discusses the importance of cobalt alloy matrix strength being sufficiently high to match the strength produced by grain boundary pinning; a significant strength mismatch will result in premature failure of the cast component when it is loaded in service.

| Element | Increase Solidification Range | Solid Solution Strengthener | HCP Stabilizer | FCC Stabilizer | MC | $M_6C$ | $M_7C_3$ | $M_{23}C_6$ | Rupture Strength Increase | Forms Intermetallics |
|---|---|---|---|---|---|---|---|---|---|---|
| C | | | | X | P | P | P | P | | |
| Co | | | | | | | S | S | | |
| Cr | | X | X | | | | P | P | | |
| Ni | | | | X | | | | | | $Ni_3Ti$ |
| Fe | | | | X | | | | | | |
| B | | | | | | | | | X | |
| Zr | | X | | | P | P | | | X | $Co_3Zr$ |
| Hf | | X | | | P | P | | | | $Co_3Hf$ |
| V | | X | | | P | P | | | | $Co_3V$ |
| Al | | | | | | | | | | CoAl |
| Ti | | | | | P | | | | | $(Co,Ni)_3Ti$ |
| Mn | | | | X | | | | | | |
| Si | X | | | | | | | | | Laves phase above solubility limit |
| Mo | X | X | X | | | P | S | S | | $Co_3Mo$ |
| W | | X | X | | | P | S | S | | $Co_3W$ |
| Ta | X | X | | | P | P | | | | $Co_3Ta$ |
| Nb | X | X | | | P | P | | | | $Co_3Nb$ |

**Table 2.** Alloying effects and carbide components in heat-resistant Co-based superalloys. 'P' identifies elements which are primary carbide formers while 'S' signifies elements which tend to participate as substitutional elements in carbide formation. Adapted from References [1, 4, 11].

In FSX-414, the aforementioned balance of matrix and carbide strength is achieved through a two-stage solution anneal and aging heat treatment where fine secondary $M_{23}C_6$ carbides are precipitated throughout the $\gamma$ matrix. Sullivan is careful to mention that both establishing proper casting parameters and tuning alloy chemistry are critical to producing an optimum balance between microstructure and mechanical properties. The specific caution regarding the casting process is most likely founded on his knowledge that the $M_{23}C_6$ primary carbides created during solidification cannot be resolutioned via heat treatment processes because melting begins before all of the carbides decompose. [11]

$M_{23}C_6$ is the most important carbide to the physical metallurgy and mechanical properties of FSX-414. It can precipitate as primary carbide during solidification, but is most commonly found in the interstices of the secondary dendrite arms and along grain boundaries, formed from last liquid to freeze. $M_{23}C_6$ is characterized by its blocky, semi-rounded pseudo-eutectic structure

of $M_{23}C_6$ lath alternating with γ matrix. During the solidification of thicker cast sections, $M_{23}C_6$ will also precipitate as fine secondary carbide particles immediately adjacent to the primary carbide islands. It is this fine dispersion of $M_{23}C_6$ secondary carbide particles which preferentially precipitate during aging heat treatment along stacking faults and twin boundaries in the matrix that provides substantial mechanical strength. [4] Figure 2 provides micrographs of typical $M_{23}C_6$ primary and secondary carbide particles in as-cast FSX-414.

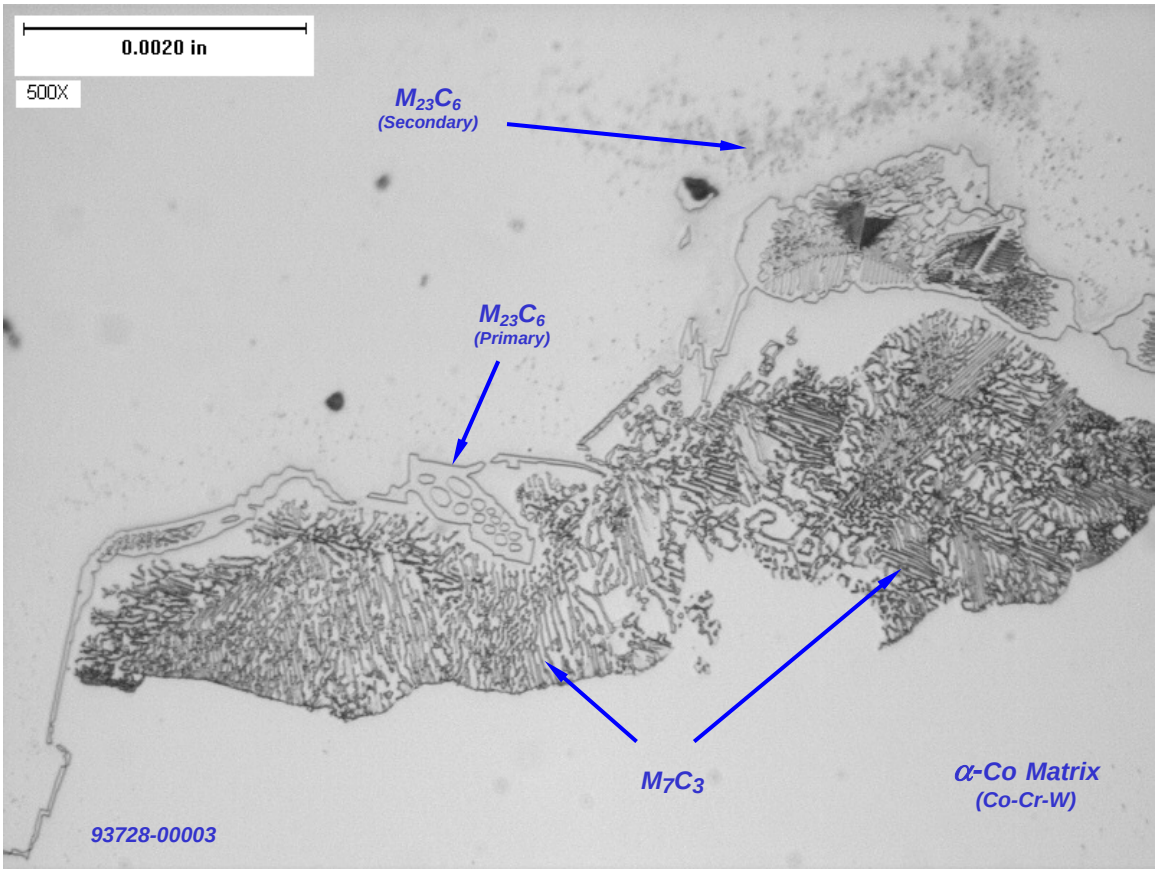


**Figure 2.** Typical carbide components and carbide morphology in as-cast FSX-414. Magnification: 500x. Etchant: Ammonium persulphate, electrolytic.

MC carbides in FSX-414 precipitate early in the solidification process, immediately after the initial dendrites form while the liquid is still at the hot end of the mushy zone. [7] Elements such as tantalum, niobium, titanium and zirconium are more effective in forming blocky MC carbides especially at higher (Nb, Zr, Ti)/C ratios, although additions of Nb, Zr and Ti have also been reported to refine the eutectic carbide structure of FSX-414. [8] The $M_7C_3$ and $M_{23}C_6$ eutectic carbides are predominantly chromium carbides with cobalt, tungsten and molybdenum substituting for chromium. The significant refractory element substitution that occurs in $M_{23}C_6$ was quantitatively described in a study recounted by Beltran who found the carbide has atom formula of $Cr_{17}Co_4W_2C_6$. $M_7C_3$ is a metastable pseudo-eutectic carbide that typically forms at lower carbon-chromium ratios and effectively transforms into secondary $M_{23}C_6$ upon heat treatment according to the following reactions: [4]

$$23Cr_7C_3 = 7Cr_{23}C_6 + 27C \quad (1)$$

$$6C + 23Cr = Cr_{23}C_6 \quad (2)$$

$M_2C_3$ can also precipitate in cast FSX-414, however without conducting either microprobe analyses of the individual particles or heat treatment investigations, it is not possible to distinguish between $M_7C_3$ and $M_2C_3$ as each takes the identical pseudo-eutectic form.

Chromium, tungsten and when present, molybdenum, are the primary solid solution strengthening elements for the *fcc* matrix of heat-resistant cobalt-based alloys like FSX-414. [4,8] Because the nominal alloy composition is located close to an intermetallic phase boundary, FSX-414 was developed with PHACOMP assistance to maintain phase stability away from the sigma-phase boundary. [4,11] Figure 3 provides schematic illustrations of the Co-Ni-Cr and Co-Cr-W ternary phase diagrams.

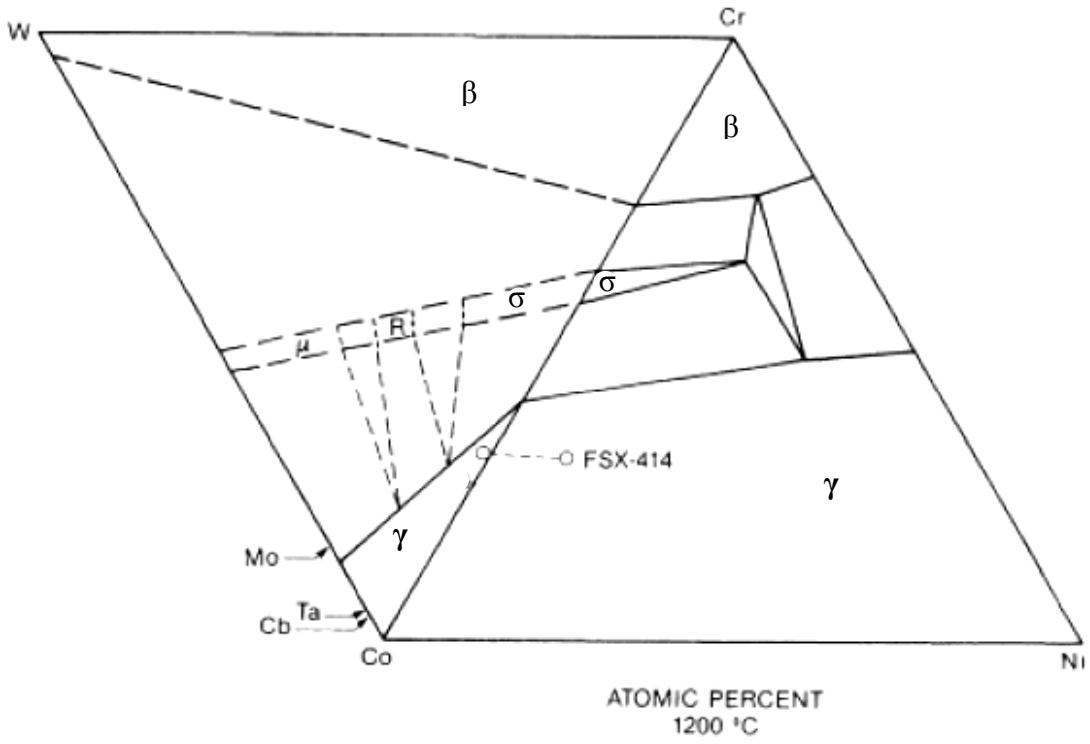


**Figure 3.** Schematic illustration of the Co-Ni-Cr and Co-Cr-W phase diagrams at 1200°C. The FSX-414 composition range is plotted for reference. The proximity to the σ phase field will increase as temperature decreases. From Reference [4].

## C. Microporosity in Castings

The great challenge foundry engineers face when making castings is to develop a robust process that is capable of producing both metallurgically sound and dimensionally compliant castings. Proper understanding and management of each alloy's solid to liquid phase transformation characteristics are critical to the success of the modern investment casting foundry where it is now a common requirement to measure and control solidification-related defects on the scale of tenths of a millimeter. A great many variables influence the solidification characteristics of any given alloy or casting, many of which continue to occupy the attention of academic and research communities.

### *1. Solidification shrinkage*

Although there are a handful of alloys that do expand upon solidification, the majority experience contraction as a function of the short range atomic order of the liquid changing into the densely packed lattice of solid metal. As Figure 4 illustrates, the reordering and densification process at the atomic level is accompanied by a significant, non-linear change in volume of the overall system. Due to their high atomic packing density, *hcp* and *fcc* alloys like the Ni- and Co-based superalloys experience the greatest change in volume upon solidification.

The metallurgical impact of solidification shrinkage is effectively illustrated by considering Campbell's unfed sphere experiments. [12] As solidification of a sphere progresses due to heat transfer through the outer shell, successive internal solid layers of thickness *dx* are formed as shown in the illustration provided in Figure 5. When a layer solidifies, the remaining volume of liquid is reduced disproportionately relative to the total volume remaining within the center of the sphere. This disparity in volume results from the contraction associated with the liquid to solid phase change discussed above and results in a pore forming, the liquid expanding due to the tensile forces and/or contraction of the solid sphere. Assuming for now that a pore is

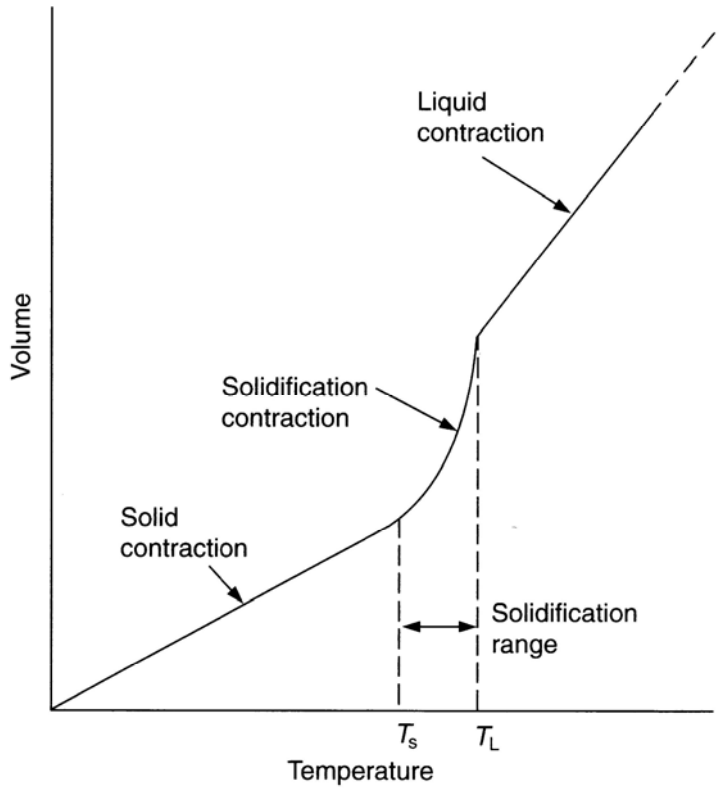


**Figure 4.** Schematic illustration of the volume change with decreasing temperature in liquid, during freezing and in the solid state. From Reference [13].

not nucleated, the successive formation of solid layers steadily increases the tensile forces placed upon the liquid. As these tensile forces increase, the liquid imposes an equivalent increase in negative metallostatic pressure, i.e. a tensile force, on the solid shell. This metallostatic tension will continue to increase until the solid shell deforms plastically inward, thus reducing the negative pressure within the liquid. If however a favourable nucleus for pore formation does exist, a pore forms of a size which is proportional to the properties of the phase change for that alloy. [13] For cobalt based alloys, the pore created due to a characteristic contraction rate of approximately 4% would be a 34 mm diameter hole remaining in the center of a 100 mm diameter unfed sphere. As a point of reference, the most widely used aerospace and IGT

investment casting specifications limit the maximum defect size to less than 2 mm for casting features that are similar in size of the example sphere.

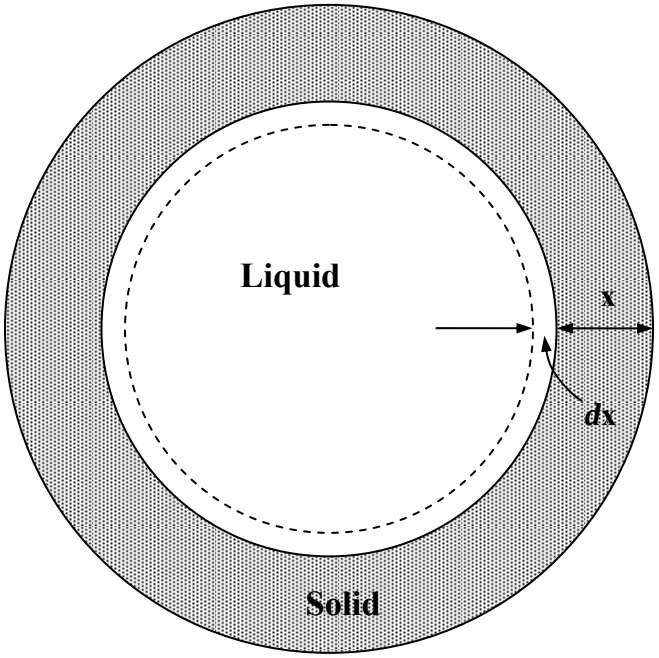


**Figure 5.** Schematic illustration of the progressive solidification of an unfed sphere. Adapted from Reference [13].

*2. Types of feeding*

The term "feeding" is used to describe the process of providing a cooling volume of liquid with a supply of additional, free flowing liquid which can adequately compensate for the volumetric contraction resulting from the liquid to solid phase change. Different modes of feeding occur based on the fraction liquid ($f_l$) that remains which is itself a function of the position (temperature) in the mushy zone (MZ). Most foundry engineers and papers published on the subject of casting feeding follow the nomenclature introduced by Campbell in 1969 [12] which he more thoroughly described in his more recent review of the subject. [13] From this point, it will

be assumed that for temperatures above the liquidus ($T_l$), no barriers to the feeding process exist and all demands for liquid metal (feeding) are satisfied without restriction.

Between $T_l$ and approximately 0.50 fraction solid ($f_s$), solidifying metals are relatively free flowing slurries of liquid and solidifying solids. While in this state, movement of the slurry to compensate for the pressure drop due to volumetric change ($\Delta P$) resulting from solidification generally proceeds unhindered. Campbell [13] reports that this mass feeding mechanism can continue up to ~0.68 $f_s$, when dendrite coherency has increased to the point that effective movement of the slurry can no longer take place. Casting section size can impact the efficiency of mass feeding due to the resistance that mold walls tend to exert on the movement of the first few adjacent solid particles. In thinner sections, ones that may only be 20 grains wide or less, mass feeding will be inhibited. However in thicker sections or in grain refined alloys, the central portion of the section will remain sufficiently open to permit free flow of the slurry. Choking of the feeding paths through restrictions in casting geometry and/or blockages by mechanical restriction of the solids in the slurry can render mass feeding ineffective earlier than expected. Should these blockages suddenly give way due to a build up in $\Delta P$, mass feeding efficiency is restored. Campbell refers to this and similar mechanisms of interrupted, explosive feeding as "burst feeding".

Once the dendritic structure has developed to the point where mass feeding is no longer effective, only the flow of the remaining residual liquid is available to satisfy the $\Delta P$ created by continuing solidification. While in this interdendritic feeding regime, the liquid must find its way through the capillaries within the dendritic network. Interdendritic feeding is a non-steady state and complicated process which will be addressed in more detail in subsequent sections. However it is important to note that as illustrated in Figure 6, the presence of eutectic liquid can act to reduce $\Delta P$ by increasing the size of the interdendritic passages.

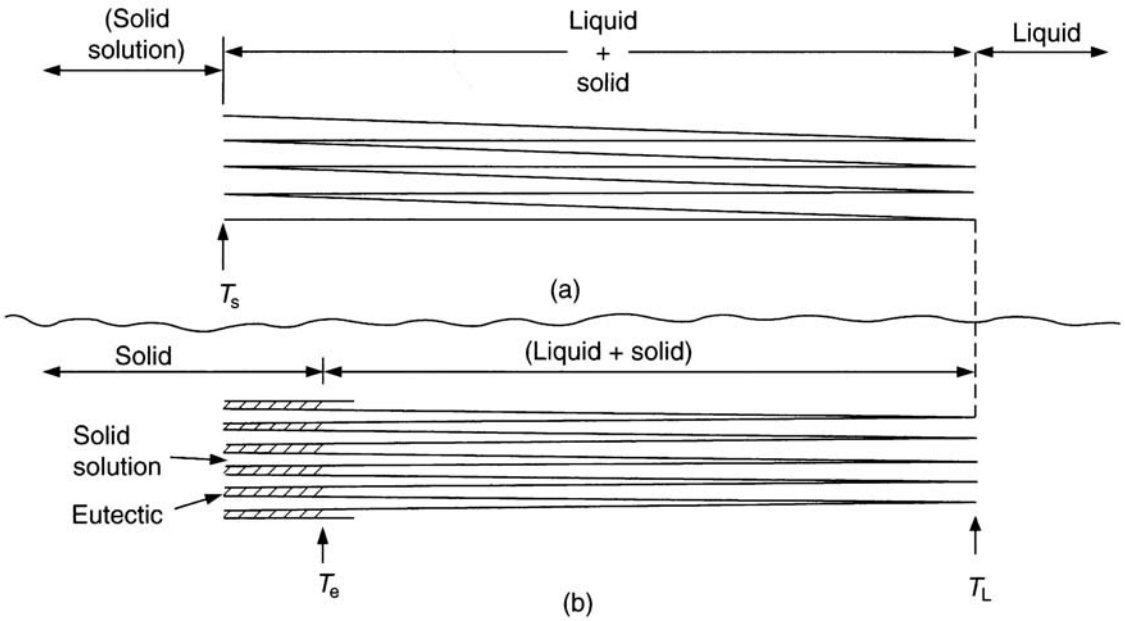


**Figure 6.** Schematic illustration describing how eutectic liquid can keep the narrowest portion of the interdendritic passages at the dendrite roots (a) more open and easier to feed as shown in (b). From Reference [13].

Solid feeding is analogous to the situation described in the example of the solidifying unfed sphere which in time plastically deforms its outer solidified shell. This feeding mechanism occurs late in the solidification process after the interdendritic passages have become isolated from liquid feed material. Solid feeding is often overlooked in industry as the common assumption is that once the feed source is depleted, the remaining isolated liquid will simply freeze and contract, with no regard given to the significant metallostatic tensions that result from unfed solidification. Campbell [13] contends that internal pressure can reach -1000 to -2000 atm (-101 to -202 MPa), a level which is certainly adequate to cause the skin of a casting to yield via creep in order to reduce internal tension. Figure 7 illustrates how this mechanism must certainly be responsible for some portion of casting dimensional variability and is especially relevant for equiaxed investment castings. As Campbell's experiments with unfed spheres illustrated, an increase in mold preheat will increase the distance over which solid feeding will influence the casting. [12] Figure 8 provides an illustration of how each feeding mechanism develops.

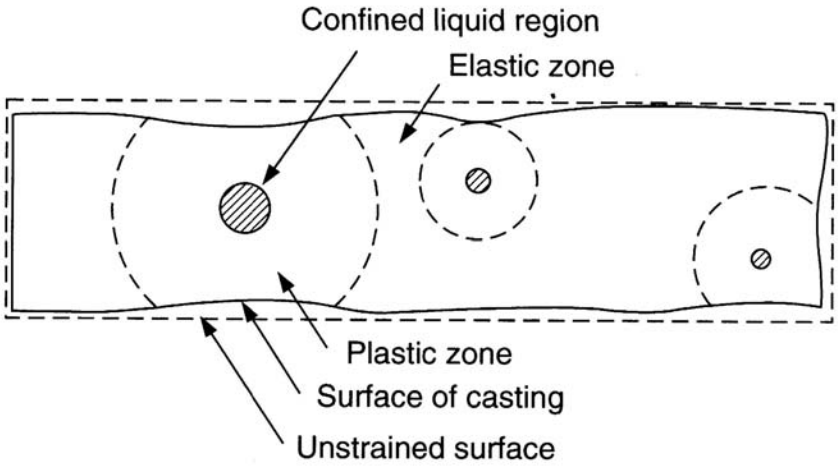


**Figure 7.** Schematic illustration describing the dimensional effects of solid feeding. The plastic deformation zones created by the solidification of isolated pockets of liquid result in localized distortion of the casting. From Reference [13].

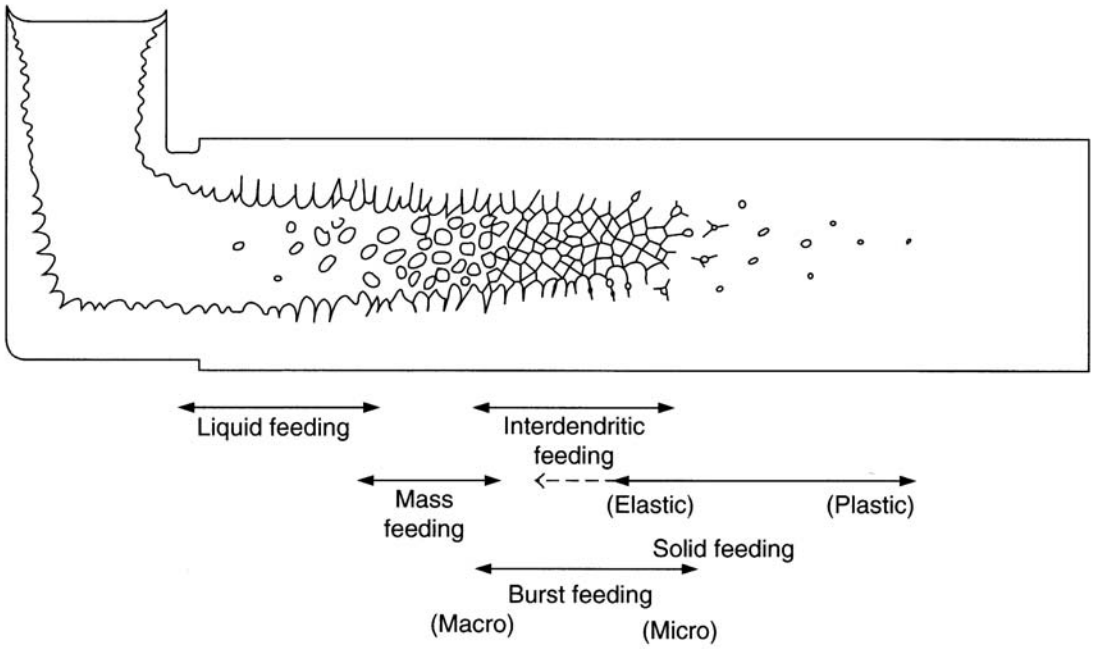


**Figure 8.** Schematic illustration representing the five feeding mechanisms in castings. From Reference [13].

It is useful to understand that both liquid and mass feeding mechanisms exist, however they generally occur independently of casting geometry or alloy and in temperature regimes that are largely unaffected by casting processes. In contrast, solid feeding is certainly a real and often disregarded mechanism that industry could benefit from addressing. For example, it is not an uncommon practice to locally add stock to an area of a casting which is affected by solid feeding in an attempt to meet the dimensional requirements of the drawing. The results of this action can of course go one of two ways; sometimes the dimensional issue is solved, but often the additional material acts to increase the demand for feed metal by increasing the size of the unfed internal region, in turn exacerbating the casting distortion due to solid feeding. From an engineering perspective, even if the casting is metallurgically sound, once solid feeding takes place damage to the geometrical integrity of the casting has occurred. Thus, it is more important that a solution for the lack of interdendritic feeding which initially caused the isolated pocket be identified.

*3. Metallostatic tension in liquids, pore nucleation and dissolved gases*

It is very difficult to homogeneously form pores in liquids due to their strong interatomic bonding forces and resultant high tensile strengths. According to Gupta *et al*., [14] fracture of liquid metals would require a pressure of -70,000 atm (-7.1 GPa) in order to exceed the critical stress state for fracture. Campbell validates this number in his theoretical analyses of aluminum; his results are provided in Figure 9 and are overlaid with each of the different feeding mechanisms. The magnitude of the critical liquid fracture stress values contrasts starkly with the previously mentioned prediction of -1,000 to -2,000 atm of internal pressure created by solidification contraction. Although some of the published work from the 1970's supports the concept of homogeneously nucleated pores in interdendritic areas, [14] most of the more recent studies align with the perspective that the pressure drop in the liquid flowing though the MZ is inadequate to generate pores. Therefore, some form of heterogeneous pore nucleation process must occur.

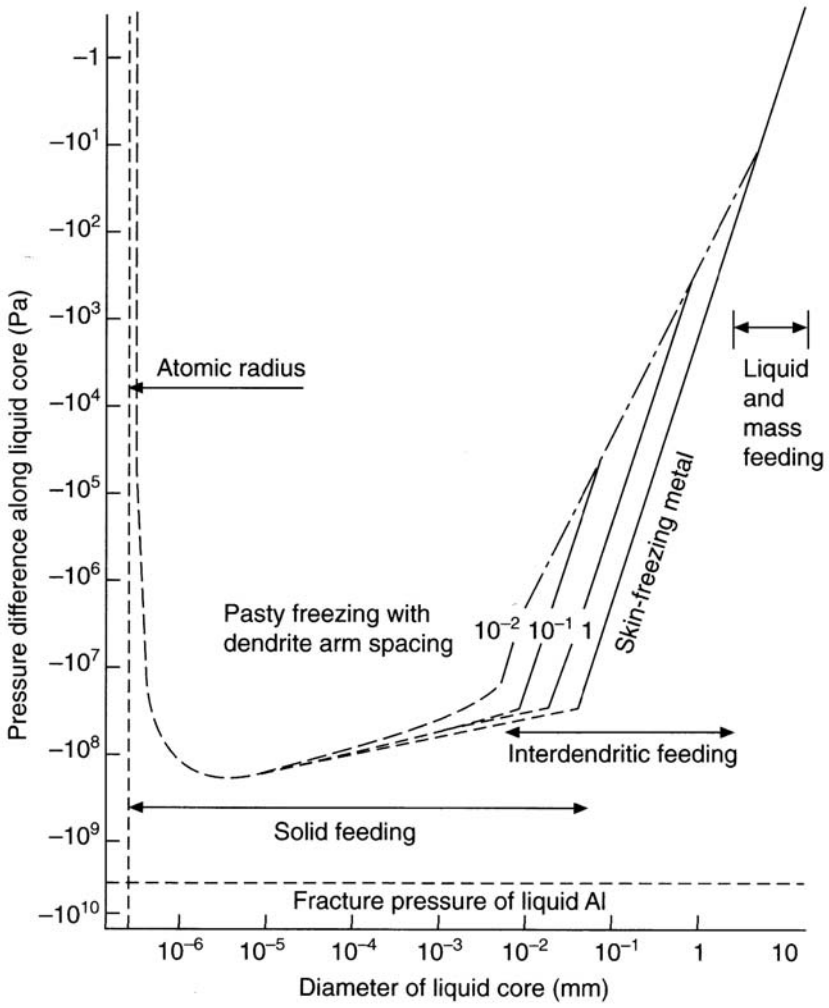


**Figure 9.** Calculated metallostatic tensions in residual liquid for different feeding regimes. Based on 20 mm diameter aluminum cylinder. From Reference [13], first published in Reference [12].

Pore formation becomes thermodynamically possible once a critical pore radius (r*) has been achieved. The r* is realized when the surface tension of the liquid which provides resistance to the formation of the pore is exceeded by the pressure difference between the interior and exterior of the pore. In their pioneering work, Piwonka and Flemings [15] show that even a small amount of gas dissolved in the liquid will increase the size of pores that would have otherwise been formed by shrinkage alone. Lecomte-Beckers [16] contends that in the modern superalloys, gas contents are generally kept sufficiently low to remain chemically bonded and in solution. Using Lecomte-Beckers' theory, the contribution of dissolved gases toward the

formation of pores would be minimal. This concept is supported by the conclusions of Piwonka and Flemings who determined there to be a critical initial gas content required to form gas-related porosity. One still must consider that for many industrial casting processes, the rates of solidification are sufficiently slow to allow gases and other solutes to concentrate at the solidification front. Such a local enrichment of gases may be adequate to achieve the critical volume for the formation of a pore proposed by Piwonka and Flemings. More recent publications combine the contributions of shrinkage and gas when describing pore formation. [13-15, 17-19]

The treatment of heterogeneous nucleation of pores has been inconsistently addressed in published research as not all authors have considered the wetting angle the liquid makes with an adjacent solid surface. Many phases precipitating from the melt including carbides, nitrides and much of the surface of the growing interface will be mostly or fully wetted by the liquid and will therefore be unsuitable as a pore nucleation site. [12,13] There has been evidence presented in the literature that suggests pores can nucleate at the base of sharp, narrow features in the solidifying structure. However oxides with low-angle or non-wetting surfaces provide the most effective opportunities for pore nucleation. [13,14]

*4. Interdendritic flow, permeability and interdendritic porosity*

Many of the expressions derived for interdendritic fluid flow have been created from work related to specific solidification systems such as directionally solidified (DS) castings or for specific alloy types rather than as a general definition of interdendritic solidification. Even though the flow of liquid during solidification is a non-linear time- and temperature-dependent process, it is most common to begin derivations describing the flow through interdendritic passages beginning with the use of Darcy's Law, [15,16,20-22] a form of which is provided in Equation 3. [22] Darcy's law provides a linear relationship between the pressure drop over a given distance ($\Delta P$), flow velocity ($v$), the permeability of the medium (K) and the viscosity of the fluid ($\eta$). Considering the preceding discussions on feeding and the development of porosity, it is

$$v = -\frac{K}{f_l \eta}\left(\Delta P + \rho_l g\right) \tag{3}$$

understandable how the treatment of these three variables can form a foundation for understanding interdendritic feeding.

Lecomte-Beckers [6,16] developed the microporosity index ΔP* for a DS Ni-based superalloy using Darcy's Law as a starting point. Her expression, which is provided in Equation 4, shows that in order to achieve sound castings, one must manage the critical pressure

$$\Delta P^* = \frac{24\eta\beta' n \tau^3}{\rho_l g}\left(\frac{\Delta T}{G}\right)^2\left(\frac{df_s}{dt}\right) \tag{4}$$

drop in the interdendritic fluid by decreasing the solidification range, the solidification rate, the number of dendrites and the tortuosity of the interdendritic passages. In addition, having larger volumes of high fluidity interdendritic fluid that are exposed to a large thermal gradient (G) also creates favourable pressure drop conditions. A shortcoming of this relationship is its assumption of the linearity of ΔP* across the MZ.

By expanding upon the work of Piwonka and Flemings [15] and employing the Hagen-Poiseulle equation for the specific permeability of the liquid flowing through a solid dendritic structure, Campbell [12,13] derived the expression shown in Equation 5 to describe the pressure drop in the residual liquid flowing through interdendritic pores. This equation is

$$\Delta P = 32\eta\left(\frac{\alpha}{1-\alpha}\right)\frac{\omega^2 {L_c}^2 d^2}{{R_i}^4 D^2} \tag{5}$$

implicitly related to solidification rate via the dendrite arm spacing ($d$) which itself is a function of the solidification rate. Upon further examination, Campbell's equation shares other similarities to Lecomte-Beckers' ΔP* criterion. In the case of Equation 5, tortuosity dependence is achieved through specific treatments of capillary length ($L_c$), area of mushy zone ($D$) and most importantly, the radius of the interdendritic passages ($R_i$). Lecomte-Beckers' criterion uses a solidification shrinkage term (β′) which is a linear ratio of the densities of the solid and liquid through the

mushy zone. β′ is also dependent on the coefficient of thermal expansion (α), which is explicitly applied in the work of Campbell.

Academia and industry alike have expended considerable effort to develop meaningful relationships to characterize feeding using the macroscopic variables of temperature gradient in the liquid (G), cooling rate (R) and rate of solidification (V). The well-known Niyama criterion $G/\sqrt{R}$, was originally developed for steel ring castings and was successfully applied by Minakawa *et al.* [21] to predict centerline porosity in steel plate castings. Based on their understanding of the thermal influence of casting geometry and risers (feeders) on feeding efficiency, Lee, Chang and Chieu [20] later introduced the LCC feeding efficiency parameter, $Gt^{2/3}/V$. Both of these semi-empirical criteria found favour within the foundry industry and with the solidification modeling community due to their relatively straightforward treatment of the feeding process. After careful adjustment of the boundary conditions of his model, Hermesmann [23] was able to demonstrate success using both the Niyama and LCC criteria to predict the occurrence of shrinkage porosity in small investment cast Stellite™ 3 ring castings.

Sigworth and Wang [17,18] and Lee dispute the validity of using Darcy's Law as a basis for developing an interdendritic feeding criterion. Their primary concern is that the solutions based on Darcy's Law provided by Lecomte-Beckers and Campbell do not account for feeding length nor do they account for the probability of creating isolated liquid pools during solidification. From his work, Sigworth arrives at the involved geometrical criterion in Equation 6 which is intended to set the critical thermal gradient necessary to avoid shrinkage porosity. Contrasting

$$G^* \geq \left(1 + \frac{2K_M \Delta T}{\rho_s H_f} \bullet \frac{t_c}{L^2}\right) \frac{K_M L}{t_c \rho_s H_f} \tan\theta_c \qquad (6)$$

the Darcy's Law-based solutions with Sigworth's and considering the latter's incorporation of the feeding angle ($\theta_c$), thermal conductivity of the mold ($K_M$) and latent heat of fusion of the bulk alloy ($H_f$) it becomes apparent Sigworth's expression may only be applicable to macro-feeding

problems similar in scale to those addressed by Chvorinov's Rule. Additional and more broadly-based investigations are required to validate whether Equation 6 is relevant for the prediction of microporosity at the scale of feeding addressed by the solutions of Lecomte-Beckers and Campbell. Evidently, creating an accurate mathematical characterization of the complex, non-linear mechanism of interdendritic feeding is not straightforward. However with that said, significant progress can be made toward improving as-cast quality by eliminating casting defects through understanding and influencing the variables that affect feeding during solidification.

*5. Forms of porosity*

Campbell has categorized the various types of shrinkage-related porosity defects and provided the useful visualization of each in Figure 10. However, the topic of this investigation concerns geometrically complex and highly scrutinized investment castings where 2% microporosity in a 100x field of view could be rejectable. Such low levels of microporosity demand a thorough understanding of interdendritic feeding and specifically, an understanding of the development of layer porosity defects.

Layer porosity defects are most commonly experienced by long freezing range alloys that are subjected to an inadequate thermal gradient which can be caused by high thermal conductivity alloys or an insufficient rate of heat extraction through the mold material. Using Campbell's [13] explanation illustrated in Figure 11 to explain the formation of layer porosity and referring to Equation 5 at the same time, we see that $\Delta P$ in the interdendritic fluid increases parabolically through the MZ. As solidification progresses from Stage 1, the local stress at some point along the parabolic stress curve will meet the fracture pressure ($P_f$) of the liquid at Stage 2. In Stage 3 a pore forms, assumedly by some form of heterogeneous nucleation event, and the metallostatic tension in the liquid is relieved to a large degree. The new layer-shaped pore will then act as a free surface to feed the build up of metallostatic tension in the remaining liquid as it solidifies, slightly delaying the formation of the next pore. The process of building up metallostatic tension,

pore nucleation and pore formation continues to repeat in the remaining liquid, creating a series of interconnected layers of microporosity that are spaced regularly throughout the affected area of the casting. When attempting to troubleshoot and eliminate these defects, it is instructive to note that the layers of porosity are typically oriented parallel to the isobaric and/or isothermal surfaces created during solidification.

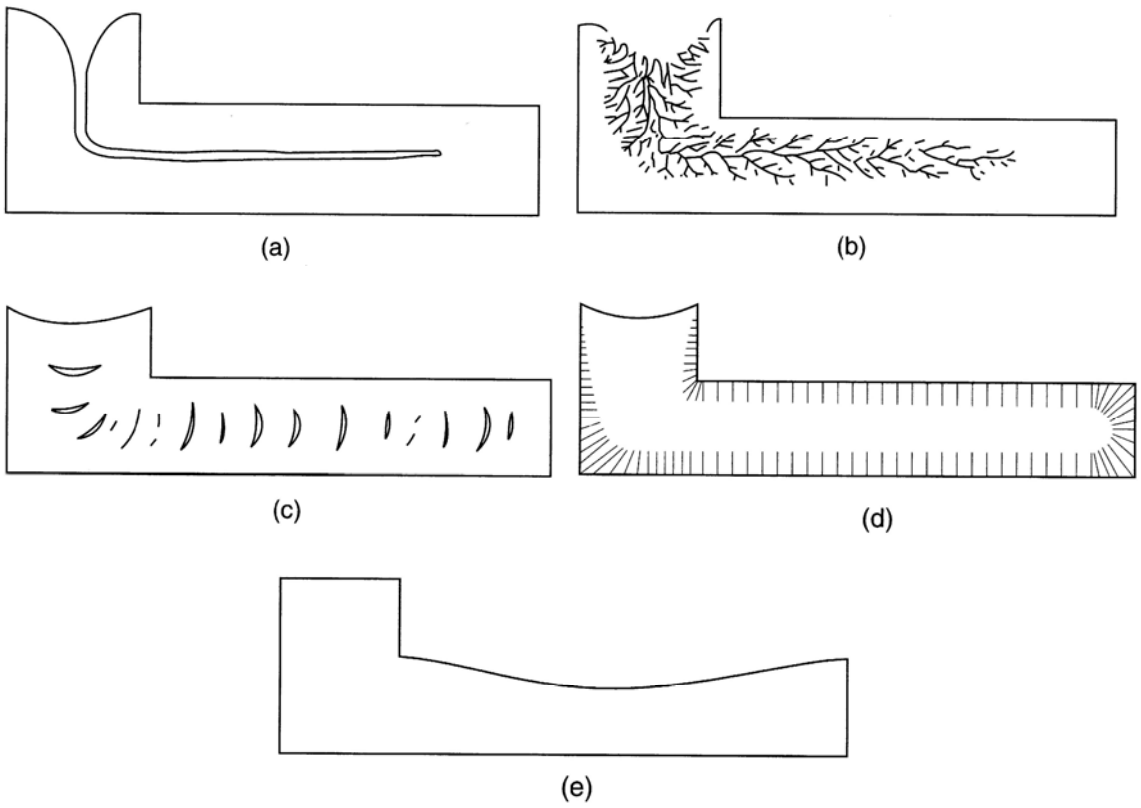


**Figure 10.** Schematic representations of the various forms of shrinkage-related defects. (a) *Centerline shrinkage:* Formed in alloys with small ΔT (skin freezing), solidifying with inadequate feed metal supply. (b) *Sponge porosity:* Formed in large ΔT alloys solidifying with inadequate G but sufficient feed metal supply. (c) *Layer porosity:* Formed in poorly fed system solidifying with inadequate G. (d) *Surface porosity:* Formed in large ΔT alloys with inadequate G but relatively few nucleation sites. (e) *Surface sink:* Formed in inadequate feeding situations with exceptional melt cleanliness and few nucleation sites. From Reference [13].

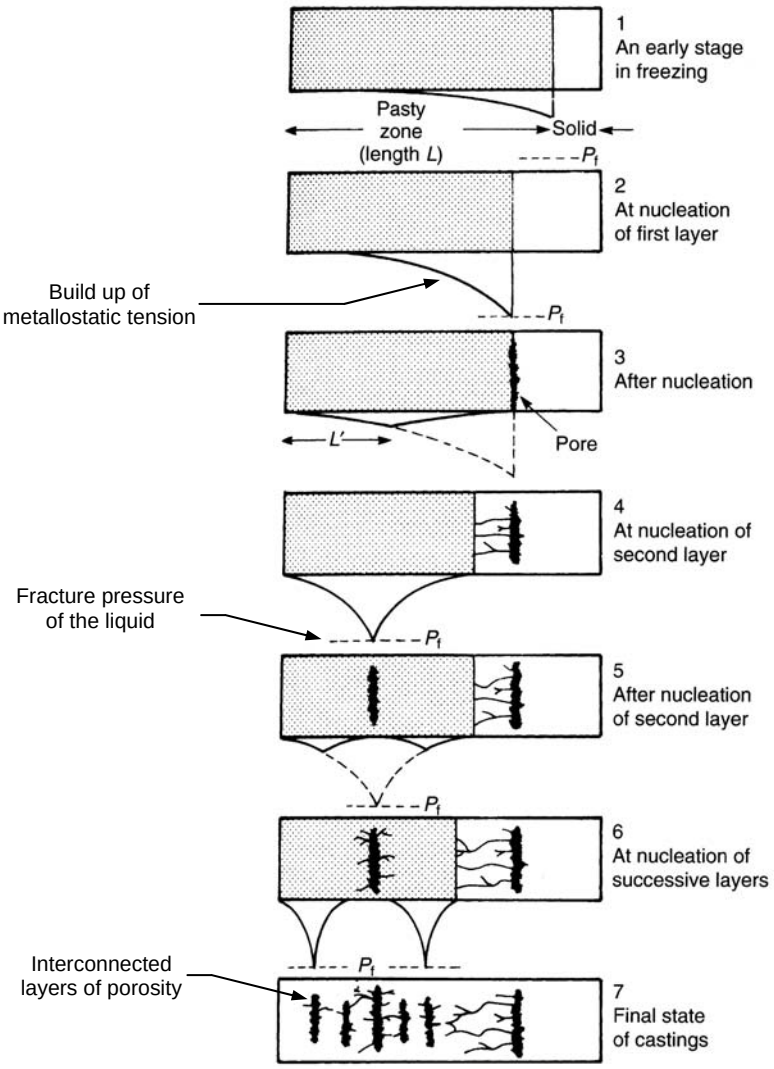


**Figure 11.** Schematic representation of the creation of layer porosity defects. From Reference [13].

*6. Effects of composition*

Countless researchers in academia and industry have run experiments to quantify the effects of different elements on alloy feeding characteristics and their tendency to develop microporosity. Lecomte-Beckers has detailed the effects of Al, Cr, Co, Mo, Ti and C on microporosity development in DS Ni-based alloys. [6,16] Cieslak *et al.* [24] have documented changes in $T_l$, $T_s$ and $\Delta T$ in Ni-based IN625 by adjusting Nb, C and Si. Burton [7] published her

findings regarding the differences in the solidification behaviours of IN100 and MAR-M200 by modifying the levels of boron and hafnium. Zhu *et al*. have detailed the effects of P, S, B and Si on the solidification characteristics of IN718 and a variety of other Ni-based alloys. [25,26] Dozens of articles have been published on Ni-based DS and single crystal (SX) alloys that describe a variety of elemental effects on second phases, porosity and casting defects. The negative effects of both S and P on the solidification behaviour of steels are common knowledge within the metallurgical community. Rappaz [27], Campbell [13] and other researchers have documented optimization curves or "Λ curves" of casting quality for binary Al-Cu alloys; Campbell's version is provided in Figure 12.

In summary, changing alloy chemistry will result in changes to any given alloy's liquidus and solidus temperatures, fluidity, density and its inherent kinetics and thermodynamics of solidification which in turn, will affect the shape, distribution, size and growth rates of dendrites, precipitated phases, residual eutectic and therefore, porosity. However, it is interesting to note that it is exceedingly difficult to find published investigations detailing the effects that small changes in elemental concentrations (1 wt. % or less) have on solidification behaviour. Surprisingly, this is even true of published articles that detail the process of developing the tightly controlled DS and SX families of alloys. [28] In addition, interactive effects between elements are not commonly addressed either, and only preliminarily so if the articles are specifically focused on primary alloy development. Even in the alloy development cases, the compositional ranges investigated are sufficiently broad that extrapolating elemental interactions found within the experiments into the chemistry range of one particular alloy would be ill advised.

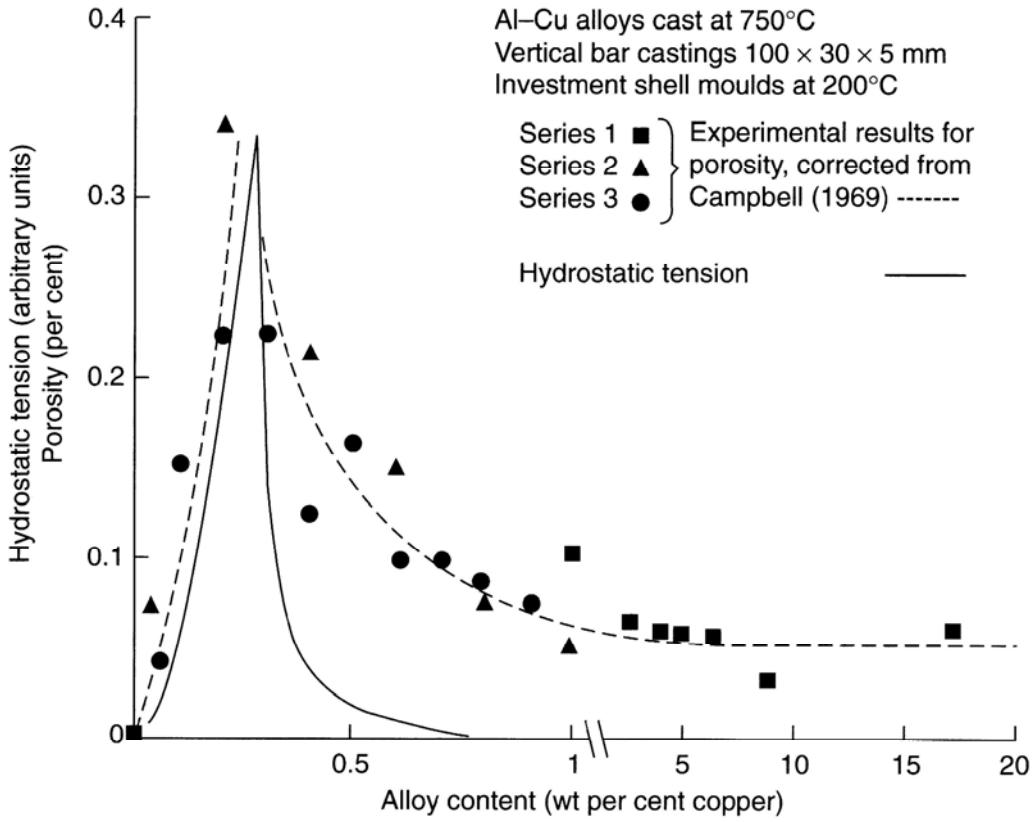


**Figure 12.** Λ curve for binary Al-Cu system, describing variation in measured porosity content with changes in alloy composition. From Reference [13].

## D. Hot Tearing

Hot tears are serious casting defects that present a constant challenge to the foundry industry. Hot tears are jagged, branched cracks that follow interdendritic paths through the microstructure. The surface of a hot tear defect is distinctly different from that of a crack that nucleates and propagates below the solidus temperature; cold cracks are crystalline in appearance whereas hot tears are interdendritic fractures that show evidence of residual liquid. Although this defect is not alloy specific, there is clear evidence in the literature that some alloys are more prone to developing hot tears than others. The fundamental mechanics of hot tear development has been the source of much debate in technical publications and still today, there is not a clear consensus on the exact mechanism of how these defects form or how many factors influence their formation and growth.

In his thorough review of hot tearing, Professor Campbell immediately points out that hot tears are the result of the failure of a weak material subjected to uniaxial tensile stress. [13] Although perhaps this is an intuitive notion, the concept does form the basis for understanding how hot tears form. Bishop, Ackerlind and Pellini [29] made a critical contribution to the understanding of hot tears when they published the results of their simultaneous radiographic and temperature profile investigation on solidifying steel and Al-4Cu alloys. Their work clearly showed that hot tears form along interdendritic paths late in the solidification process at temperatures above the solidus. Specifically, they determined that the susceptible period for hot tear formation occurs after approximately 0.90 fraction solid ($f_s$) when the remaining liquid has segregated to interdendritic and intergranular spaces, creating films of liquid along the grain boundaries. Should the hot spot of a casting in this partially-solidified state be subjected to uniaxial tensile stress, the grains will begin to slide along the interdendritic liquid films, extending proportionally to the amount of liquid present. As the schematic illustration in Figure 13 shows, continued strain will eventually lead to impingement of the grains and then rupture and

the development of a tear defect once the critical fracture stress is exceeded. [13] In uniaxial supersolidus compression tests of various cast IN718 samples, Lewandowski and Overfelt [30] confirmed the strong relationship between the deformation mechanism and the degree of dendritic alignment with the axis of compression. Directionally solidified dendritic microstructures tended to yield by plastic flow whereas equiaxed samples that did not display any alignment deformed by grain boundary sliding as described above.

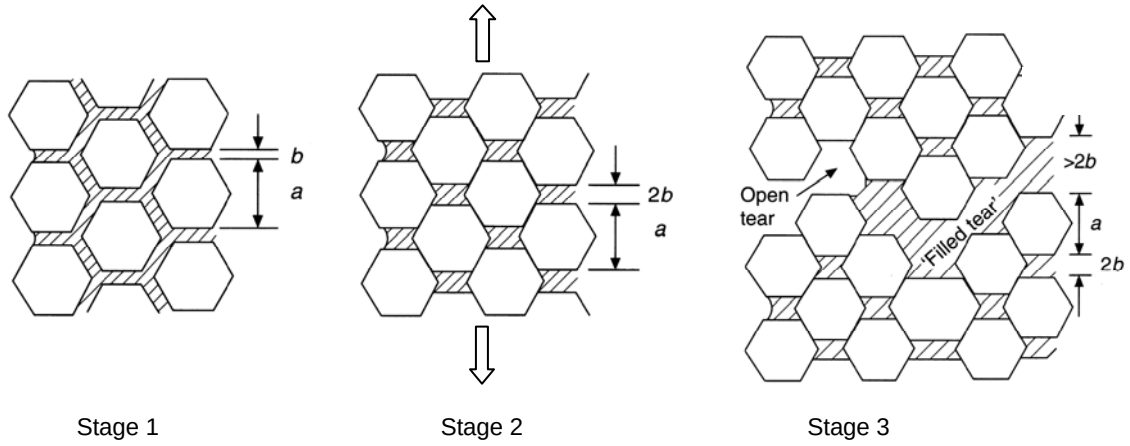


**Figure 13.** Schematic illustration of the distribution of liquid between hexagonal grains of size *a* during the development of a hot tear. Illustrations from Reference [13].
*Stage 1*: Liquid film of thickness *b* coating the grain boundaries; approximately 90% $f_s$.
*Stage 2*: Uniaxial stress applied, grains slide & impinge, liquid pools in intergranular spaces.
*Stage 3*: Continued strain. Extension exceeds the ability of the liquid to accommodate it which causes tears to form.

*1. Stress and Strain Concentration*

Campbell's simplified quantification of casting deformation shown in Equation 7 [13] is particularly useful to help with envisioning the magnifying impact of strain concentration. If all of the contraction from the liquidus in a casting of length *L* was to be concentrated in a hot spot of length *l*, the strain experienced by the hot spot would be:

$$\varepsilon = \frac{\alpha \Delta T L}{l} \tag{7}$$

Thus, a 250 mm long restrained casting would experience a 10x strain concentration within a 25 mm wide hot spot. At these levels of strain concentration, it is not difficult to exceed a solidifying material's elastic limit, especially considering the presence and impact of the grain boundary liquid films.

Castings unfortunately do not cool at uniform rates nor do they develop uniform constraint during solidification. Instead, they develop complex stresses and strains as a function of the contraction of solids that occurs during cooling, the non-uniform restraint of sections of the casting that develops from the casting geometry, the gating design, the mold design, and the non-uniform or non-sequential solidification sequence of isolated sections of the casting. The forces that develop during the cooling of castings are very large and dissipate by causing different types of deformation within the casting. Forest and Bercovici [31] found that deformation within an isolated hot zone of a casting which might be vulnerable to hot tearing is not met without resistance. They carefully measured resistive forces of 2 to 0.5 MPa between the solidus and 10% liquid in Al-4Cu; not until the liquid fraction reached 20% did the alloy reach nil ductility. Lin and Sekhar [32] measured nil ductility in René 108 at 0.32 $f_l$. Despite the inherent differences in hot tearing susceptibility between alloys, all can be made to tear with the application of sufficient tensile loads. [29]

*2. Grain boundary liquid films and wetting*

A number of different researchers have directly addressed the importance of grain boundary wetting as a mechanism of promoting hot tearing. Smith [33] related the shape taken by residual interdendritic fluid to the dihedral angle (θ), which provided there are no crystallographic influences, is defined by the balance of the interface energies of the solid-solid interface ($\gamma_{SS}$) and

$$\gamma_{SS} = 2\gamma_{SL}\cos\left(\frac{\theta}{2}\right) \tag{8}$$

the solid-liquid interface ($\gamma_{SL}$). The various distributions of liquid based on the dihedral angle of the liquid phase are illustrated in Figure 14.

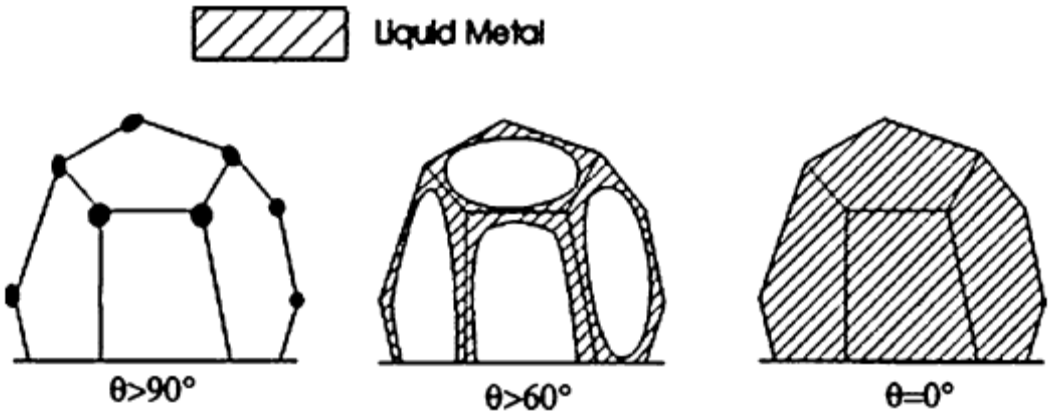


**Figure 14.** Schematic illustration of the distribution of liquid on grain boundaries as a function of the dihedral angle, θ. Illustration from Reference [34].

The distribution and amount of grain boundary liquid present at the time uniaxial tension is realized will affect the severity of hot tear defects. Zhang [35], Zhang and Singer [36,37] and Zhou, Volek and Singer [38] concluded from their experiments that avoiding continuous films of grain boundary liquid films significantly impacts the severity of hot tear defects in directionally solidified IN792. Similar results were found by Lin, Aliravci and Pekguleryuz [34] in their experiments on wrought aluminum alloys. Zhang, Singer, *et al.* also discovered that the cohesion of the grain boundaries in the final stages of solidification was affected by dendrite geometry as well as the fraction and distribution of remaining liquid. By eliminating continuous liquid films and allowing the secondary dendrite arms to bridge, the mostly solidified casting is able to build sufficient strength to withstand the tensile stresses generated by thermal contraction. [37] Figure 15 illustrates this concept.

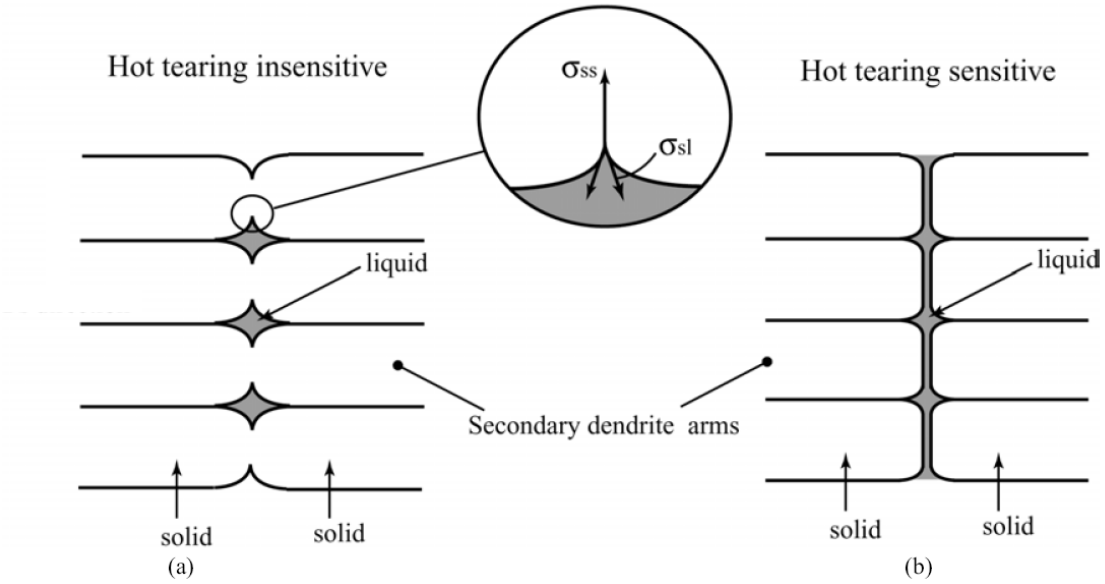


**Figure 15.** Schematic illustration of how the distribution of liquid on grain boundaries impacts castability. The alloy in (a) has improved castability versus the alloy in (b) due to the superior grain boundary cohesion and the isolation of the remaining liquid in pools rather than in continuous thin films along the grain boundary. Illustration from Reference [37].

In related work on single- and bi-crystals, Wang *et al.* [39] confirmed that hot tears appeared only at high-angle grain boundaries, where the increase in grain angle changes the grain boundary energy from an attractive to a repulsive force. This is analogous to the polycrystalline scenario of a large grain boundary film dihedral angle. In such situations, more undercooling of the residual liquid is required to overcome the repulsive force which in turn, prolongs the life of the liquid areas that have inherently lower shear strength, thus allowing continued localizing of strain due to contraction.

*3. Critical temperature range*

The critical temperature range for hot tearing ($\Delta T_{CTR}$) is defined as the range of temperature where the $f_s$ is sufficiently high to inhibit feeding and the structure is sufficiently developed to be able to transmit stresses. Fundamentally, this occurs after the transition from mass feeding to interdendritic feeding when the secondary dendrite arms have contacted each

other and formed bonds. Based on their work on a variety of alloys, Bishop, Ackerlind and Pellini [29] were perhaps the first to bound this region of hot tearing sensitivity to the last 10% of solidification and strongly challenged the previous general understanding that hot tear defects form below the solidus temperature. Monroe and Beckermann [40] measured the upper temperature limit of hot tear sensitivity, also known as the upper coherency temperature ($T_U$), to be 0.18 fraction liquid ($f_l$) in steel castings while Forest and Bercovici [31] and Lin and Sekhar [32] have measured $T_U$ to be as high as 0.30 and 0.32 $f_l$ in aluminum alloys and Ni-based René 108, respectively. In some of their later work conducted on a wider variety of alloys, Bishop and coworkers [41] refine the bounds of hot tearing sensitivity to the "film stage" of solidification. Wang [39] postulated that after liquid films become discontinuous at 0.94 $f_s$ hot tearing susceptibility is abated while Zhang and Singer [36] contend that hot tearing susceptibility can potentially continue below a $f_s$ of 0.99, depending on the rate of the liquid to solid phase transformation.

Bishop and coworkers also found that increasing the pouring temperature did not impact the severity of hot tear defects. [29] This again challenged the previously held notion that hot tear defects are driven by total temperature loss. Many researchers, including Lin *et al.* [34] and Cao and Kou, [42] have struggled to find clear proof of the belief that a larger freezing range equates to a greater susceptibility for hot tearing. Zhang and Singer address this concept directly in 2002 and continue the exploration in a series of papers focused on the complex multi-component Ni-based superalloy, IN792. [35-38,43] Their investigations begin with the observation that CM247 has a very similar freezing range to IN792 but displays very different hot tearing behaviour. Using Gleeble tests with very small tensile loads, Zhang and Singer were able to confirm IN792 $T_U$ at 10-12% fraction liquid. The lower boundary of $\Delta T_{CTR}$ was found to be very close to, but above the solidus temperature. Below this temperature, the solidified structure developed sufficient strength to withstand the forces of contraction. Interestingly, Zhang and Singer also

conclude that neither the overall width of the mushy zone nor the size of $\Delta T_{CTR}$ correlate with an alloy's propensity to form hot tears.

*4. Effects of solidification rate and strain rate*

The tendency of solidifying polycrystalline metals to form interdendritic liquid films is generally accepted as a fundamental aspect of solidification. In fact, these films can be used to determine the equilibrium phase diagram solidus temperature. [41] However in order to create a hot tear defect, the residual interdendritic liquid must also interact with a mechanically imposed strain while the metal is within the low to nil ductility region of the $\Delta T_{CTR}$. In experiments aimed at understanding the differences in hot tearing behaviour between different alloys, Bishop, Ackerlind and Pellini [41] characterized the free contraction rates of many different alloys. Their results shown in Figure 16, illustrate clearly that the amount of strain developed by different alloys is markedly different. This inherent time-rate extension property of metal through $\Delta T_{CTR}$ helps to establish hot tear susceptibility; if an alloy has a short film stage but a high contraction rate, its propensity to form hot tear defects may be identical to an alloy that has a long film stage but experiences a small degree of inherent contraction. Thus, both the contraction and the solidification characteristics of an alloy must be considered simultaneously when troubleshooting hot tear defects.

Forest and Bercovici [31] arrived at similar conclusions as a result of their tensile strength measurements conducted on a variety of aluminum alloys in controlled solidification experiments. These researchers contend that the shape of the cooling curve throughout the entire mushy zone defines the morphology of the solidified metal in regard to grain size and the extent of dendrite branching. A greater cooling rate equates to greater branching of the dendrite arms, greater levels of mechanical cohesion of dendrites, lesser extents of grain boundary films within $\Delta T_{CTR}$ and hence, a greater ultimate tensile strength for a given fraction liquid remaining within the critical temperature range.

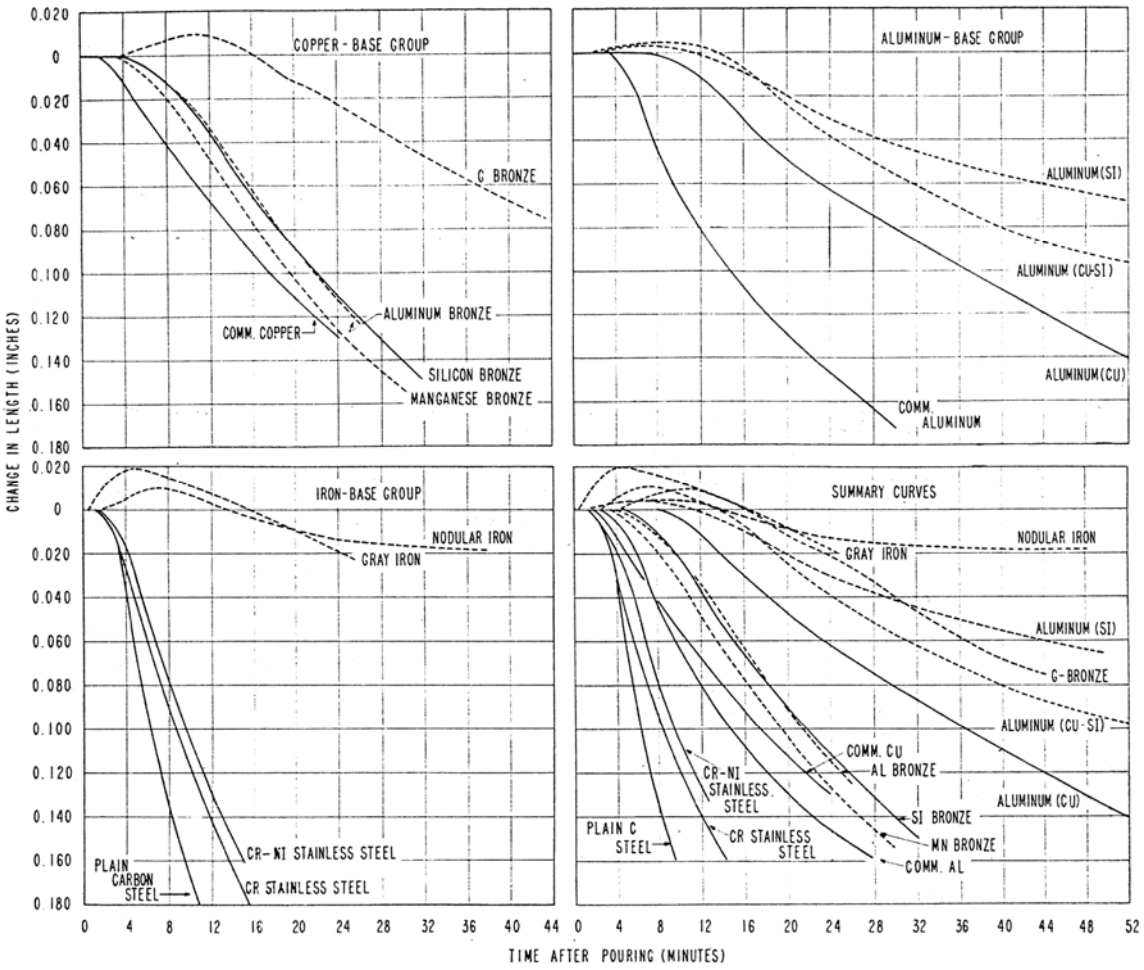


**Figure 16.** Contraction rates of iron-, copper- and aluminum-based alloys cast into unrestrained test bars. Alloys plotted with solid lines developed hot tears when cast into restrained test bars. Results from Reference [41].

Lin and Sekhar report a decrease in $T_U$ with an increase in cooling rate although it was not clear whether this was associated with an increase in $f_s$ at the new upper coherency temperature. Zhang and Singer [36] show that the rate of solidification with respect to temperature ($\frac{df_s}{dT}$) through $\Delta T_{CTR}$ differs between alloys and more importantly, will help to determine hot tear susceptibility. This relationship can be seen in their data provided in Figures 17 and 18. This finding, substantiated by the work of Forest and Bercovici, suggests that in order to eliminate hot tear defects, alloy compositional modifications should be focused on optimizing $\frac{df_s}{dT}$.

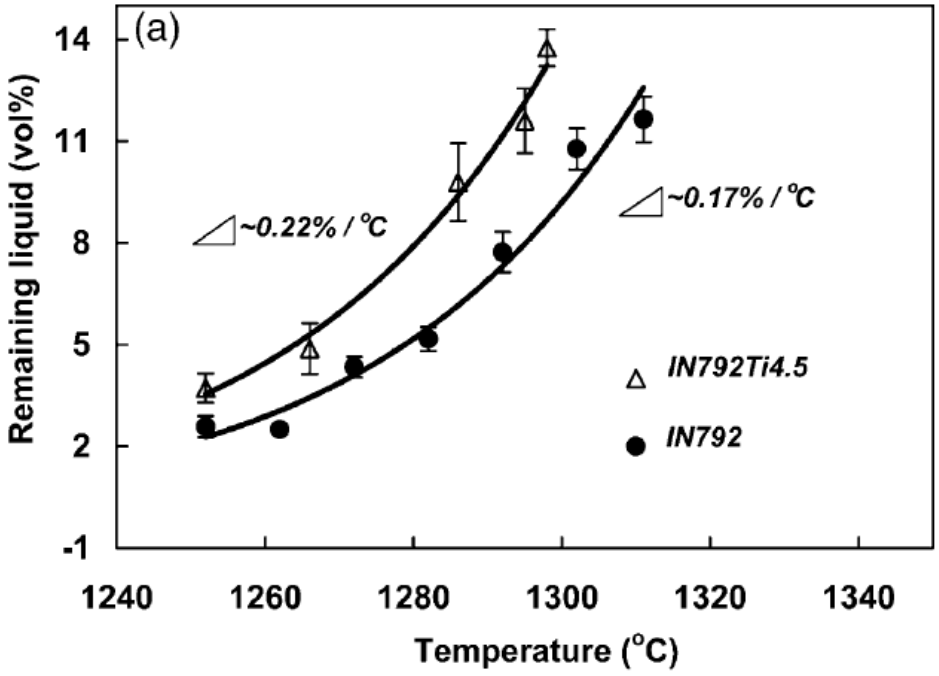


**Figure 17.** Fraction of remaining liquid as a function of temperature for two Ni-based superalloys. Alloys with poor castability - a high propensity for forming hot tears - are shown here. The slope of the curves represent the change in fraction solid versus temperature and clearly differ from those in Figure 18 which represents alloys with little or no hot tearing. Results from Zhang and Singer, Reference [36].

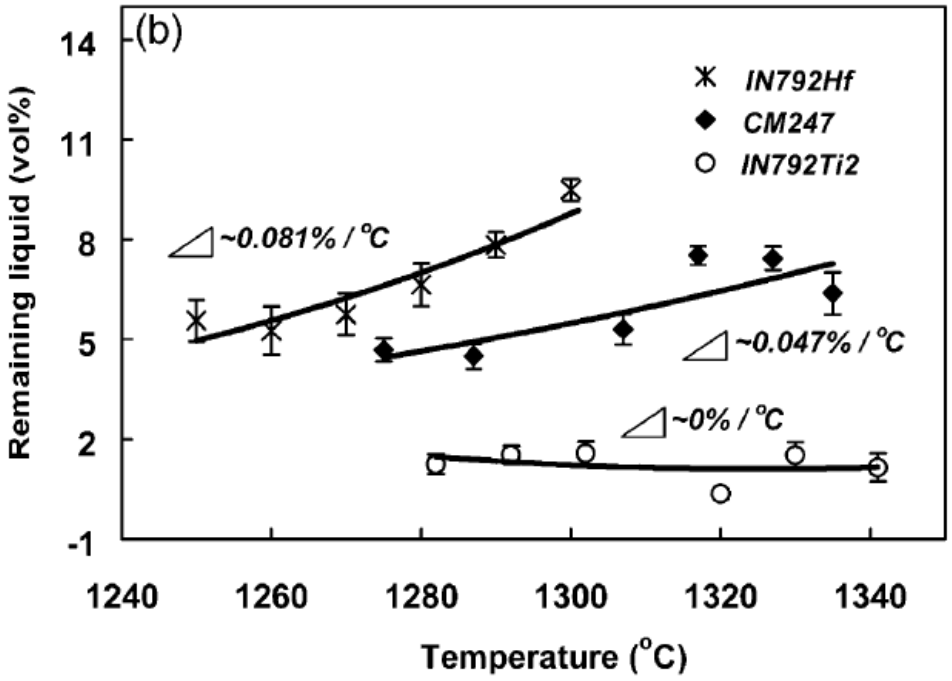


**Figure 18.** Fraction of remaining liquid as a function of temperature for two Ni-based superalloys. Alloys with superior castability – low or no propensity for forming hot tears - are shown here. The slope of the curves represent the change in fraction solid versus temperature and clearly differ from those in Figure 17 which represents alloys with a high occurrence of hot tearing. Results from Zhang and Singer, Reference [36].

*5. Effect of microstructure*

In high rate directional solidification experiments on IN792, Zhou, Volek and Singer [38] confirm many of the findings of Forest and Bercovici as do Lin and Sekhar in their René 108 testing. All three groups agree that the grain size refinement, smaller secondary dendrite arm spacing achieved through higher cooling rates result in a more discontinuous distribution of the remaining liquid and a greater degree of grain boundary cohesion, as illustrated in Figure 15. By expanding upon his previous mathematical relationship for strain concentration, Campbell illustrates the impact of grain size refinement on the amount of strain accommodated per boundary. For grains of diameter $a$, within the hot spot of length $l$, the strain accommodated per boundary, $\varepsilon_b$ is:

$$\varepsilon_b = \frac{\alpha \Delta T a L}{l^2} \tag{9}$$

Thus, grain size refinement equates to less strain to be accommodated by each grain boundary, a greater fracture stress throughout the $\Delta T_{CTR}$ and thus, a reduction in hot tear susceptibility. A pictorial representation of this concept is provided in Figure 19. Unfortunately for most equiaxed casting designs, alloys and methods, achieving any significant refinement of microstructure is extremely challenging, especially in the areas that are most prone to developing hot tear defects. However, these concepts have been expanded into full scale industrial practice within the last few years as the world's first liquid metal cooling directional solidification furnaces are now commissioned and producing production castings.

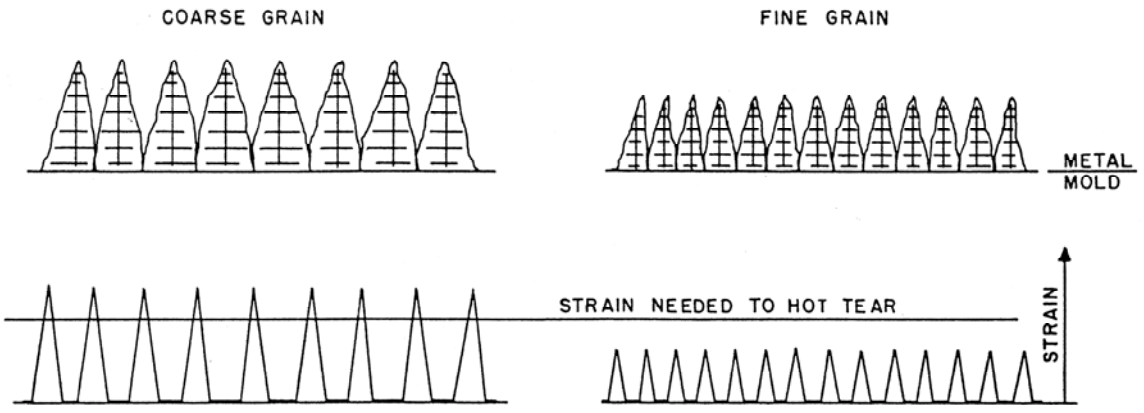


**Figure 19.** Schematic illustration of how grain size affects strain distribution at grain boundary liquid films given the same strain magnitude. Illustration from Reference [41].

*6. Effect of alloying*

As dendrites grow during solidification, solute and trace element atoms are rejected to the liquid phase. Continued solidification results in only grain boundary films of liquid remaining and the liquid phase enriched with solute which in effect, creates a grain boundary alloy that may have very different solidification kinetics from the solidified matrix. In extreme cases, the solidus

temperature of the enriched segregate may be hundreds of degrees below the matrix solidus temperature. The enrichment of the grain boundary solute provides an opportunity to prolong the life of interdendritic films which can then be subjected to a greater accumulation of strain and a greater risk of failure or separation. This condition can be further exacerbated by alloys which have inherently high free contraction rates. [41] The films which build up at the grain boundaries due to elemental segregation act to prevent the secondary dendrite arms from bridging and hinder the development of adequate strength in the solid to help it withstand tensile forces.

Sulphur and phosphorous rich segregates in steels are very familiar examples of elements that partition to the liquid upon solidification and act to depress the solute solidus temperature. By adding S and P to the melt, Bishop and his coworkers produced hot tears in previously sound steel castings, 28°C below the equilibrium phase diagram solidus temperature. [29] Chojecki found that increasing C levels interacted with S to further exacerbate the effect. [44] In similar experiments with IN792, Zhang and Singer [37,45] adjusted boron and zirconium, two elements well known to negatively impact hot tearing susceptibility in most Ni- and Fe-based superalloys. They found that by increasing the B level, the IN792 solidus temperature could be significantly depressed and the γ/γ′ eutectic was coarsened considerably. Although neither B nor Zr alone affected the liquidus temperature, when both were added to the melt the liquidus temperature was marginally decreased. Alloys containing Zr additions were found to be particularly prone to hot tear defects, especially when B was also present.

Hafnium has been used as an addition to Ni-based superalloys for decades as a method of making alloys less prone to hot tearing. It does unfortunately, create other less desirable side effects such as a substantial lowering of the alloy incipient melting point which makes full solutioning of γ' impossible. [36] Zhang found some success in improving IN792 castability by adjusting the Ti/Ta ratio of to raise the melting point of the interdendritic liquid and reducing its volume. [35]

*7. Role of feeding and eutectic solidification*

In his text, Campbell clearly describes how the creation of hot tear defects via the failure of weak, partially solidified material subjected to uniaxial tensile stress is an entirely different condition than a lack of feeding. The case of insufficient feeding creates a three dimensional stress state that expands the remaining liquid triaxially through metallostatic tension, but does not affect the dendrites. This is in contrast with the development of a hot tear which requires the dendrites to first be moved apart by the tensile strains, providing an opportunity for the residual liquid to coat the surfaces of the tear. [13] It should be noted that the exception to this would be grossly underfed regions which cause the surface of the casting to collapse, thus creating tensile forces on the partially solidified skin at the mold surface which results in the creation of a defect that looks like a hot tear. It is this case, coupled with very strong restraint as a function of the test vehicle design that appears to be at play in the work of Monroe and Beckermann. [40] Bishop [29] found that underfed castings formed hot tear defects at temperatures 10°C to 23°C higher than castings that were properly fed. This phenomenon was primarily attributed to the greater width of the interdendritic liquid films in the under fed castings.

The explanation above defines two basic parameters for the development of hot tear defects. First, metallostatic tension due a lack of feeding alone does not have the ability to create hot tear defects; a tensile force of some sort must also be available to separate the dendritic structure. Second, in order for tensile stresses to pull dendrites apart, there must be a minimum level of coherency at the location of the hot spot such that tensile stresses can be transmitted and therefore can be effective in exerting enough force to pull the two sides of the eventual defect apart. This necessarily requires the tear to take place in the lower portion of the mushy zone, within the $\Delta T_{CTR}$ for the alloy.

These two criteria may still be satisfied yet the casting may not to the naked eye, present evidence of a hot tear defect. Several researchers make reference to, or directly recount instances of hot tear defects having been "healed" by eutectic liquid. In Campbell's example shown in

Figure 20, the hot tear has formed but has since been backfilled by eutectic liquid which has drained from the surrounding interdendritic spaces, in effect "healing" the separation defect. In this instance, one would assume there is sufficient variability in all casting processes to expect with confidence that it will be a matter of time before a casting is produced with an open defect.

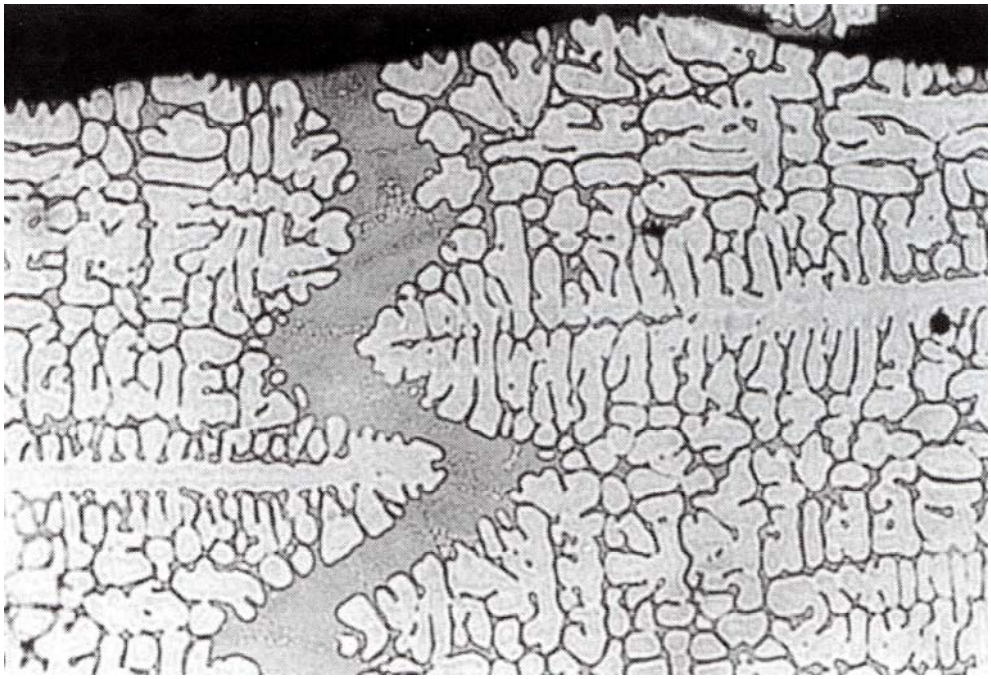

**Figure 20.** A backfilled hot tear in a grain-refined Al-10Cu alloy. From Reference [13].

Many authors, including Rosenberg *et al.* [46], Bishop *et al.* [29], Lin *et al.*, [34] Cao and Kou [42], Rappaz *et al.* [27] and Campbell [13] make reference to the importance of having long feeding range alloys and adequate amount of eutectic liquid available in order to minimize hot tear susceptibility. Cao and Rosenberg focus more on the need for eutectic being present for the incipient filling of hot tears. However both Rappaz and Campbell relate this requirement to the need for the remaining liquid to have adequate feeding characteristics in the mushy zone so it can satisfy the pressure drop resulting from solidification. They also provide strong evidence of the

need to balance feeding and hot tear resistance with alloy content; examples of these peaked relationships are provided in Figures 21 and 22. As Campbell explains, the further the alloy is away from the eutectic composition, the less eutectic is formed and the more prone it will be to forming continuous liquid films, the presence of which exacerbate hot tearing tendencies.

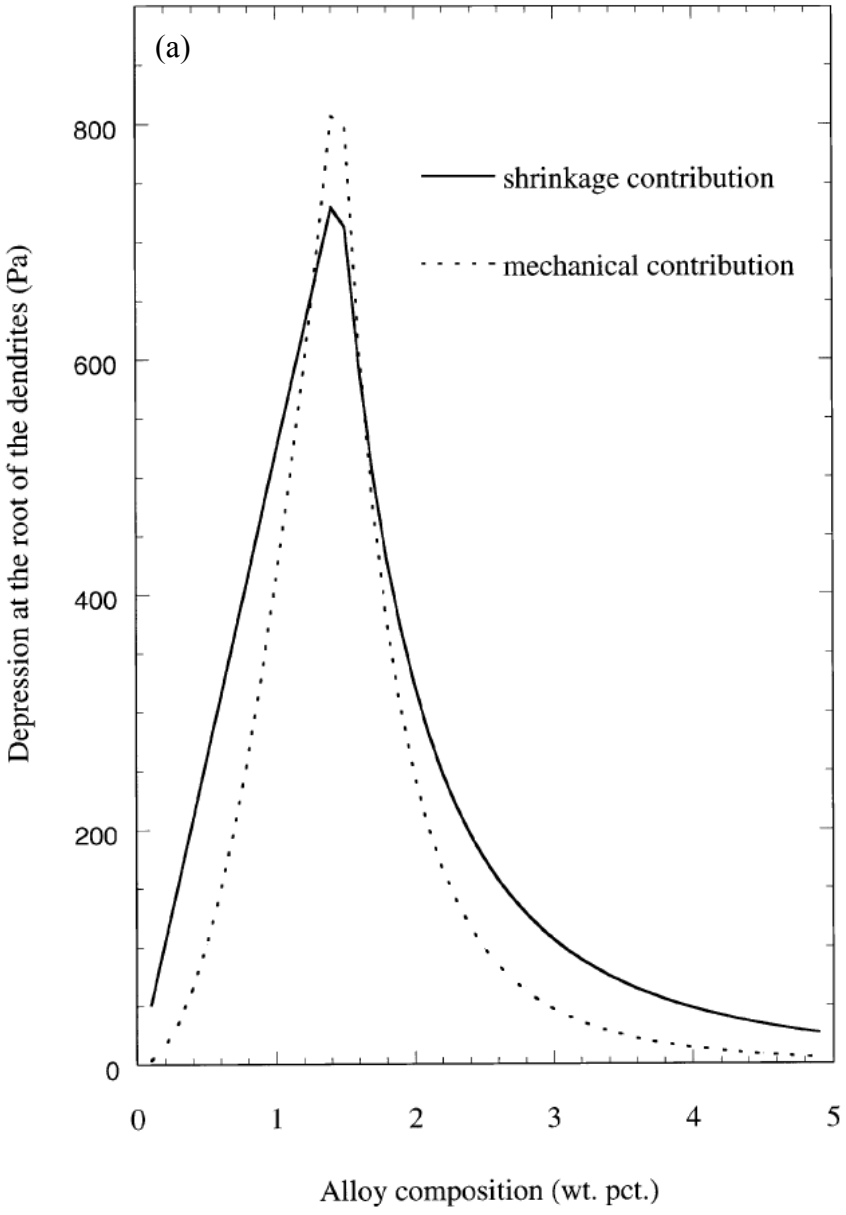


**Figure 21.** Alloy composition dependence on the shrinkage and mechanical pressure drop contributions at the roots of the dendrites for the Al-Cu system. From Reference [27].

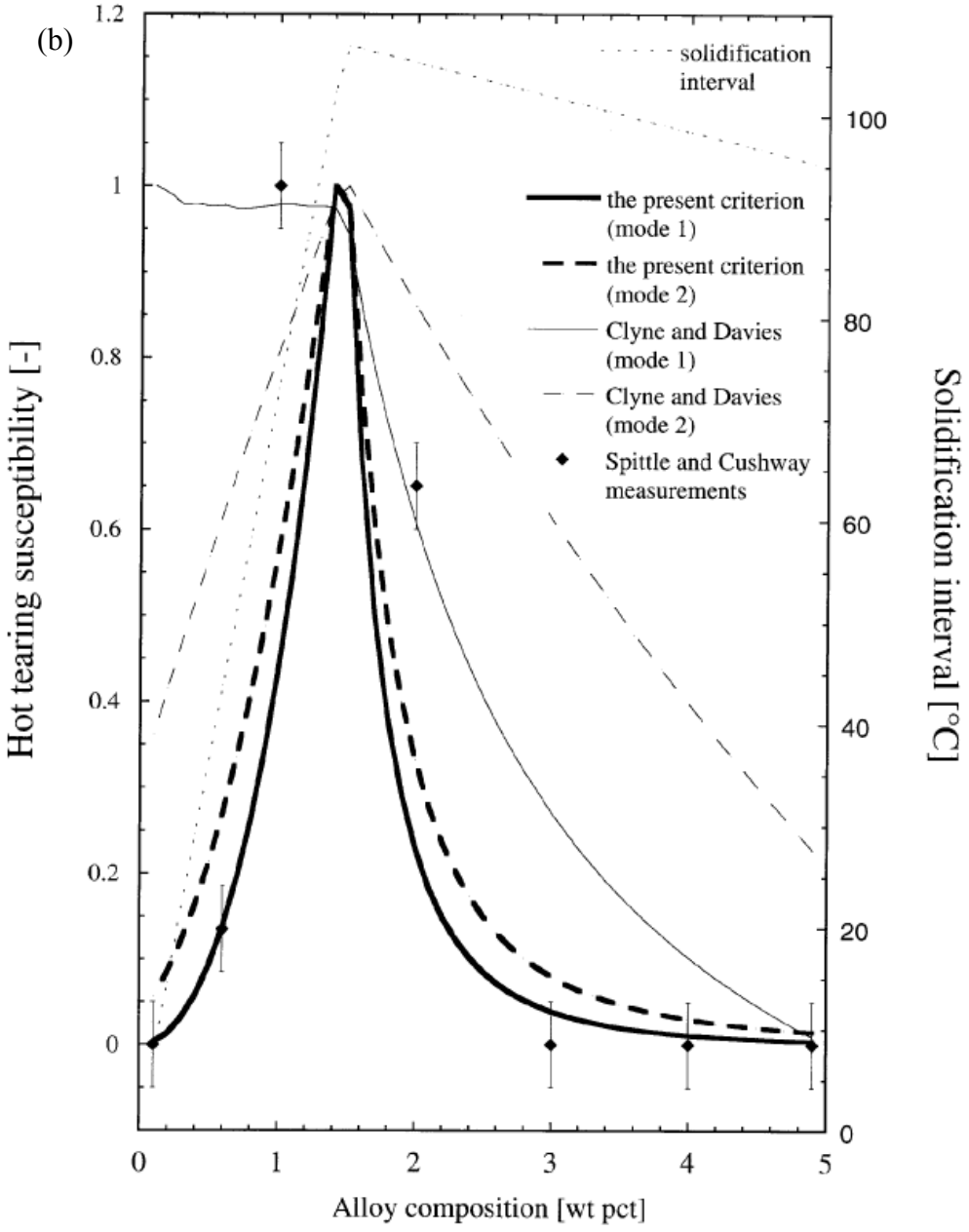


**Figure 22.** Comparison of the calculated hot tear susceptibility rating versus alloy composition from several authors' work for the Al-Cu system. From Reference [27].

*8. Nucleation of hot tears*

Although hot tear nucleation is not yet adequately investigated nor understood, it is certainly a concept that should be considered when troubleshooting these defects. Professor Campbell focuses a great deal on the concept of hot tear nucleation and especially on the occurrence of bifilms – atomically thin folded oxides that are formed and entrapped between grains during pouring. [13] In Campbell's assessment, bifilms act as nucleation sites for hot tears based on the lack of bonding between the two mating sides of the folded film and the alloy's inability to resolution the oxide film. Due to their scale, bifilms are inherently difficult to quantifiably detect. However, Campbell's success in eliminating hot tears by degassing the metal prior to pouring, changing the running system to fill the mold in a less turbulent fashion and/or implementing a molten metal filter is difficult to dispute. In addition, both he and Lin [34] recount the experiments of Hunt and Durrans who were able to indefinitely stretch clean, solidifying material without creating a hot tear. Their results show that only if an impurity was present in the area of tension would a hot tear nucleate. Hirth and Pound's calculations reveal that the actual fracture stress of liquids is on the order of $1/20^{th}$ of the theoretical value which gives strong support to the concept of heterogeneous nucleation of voids in real liquids. [47]

In their work to develop a hot tear predictor, Beckerman and Monroe [40] adopted the assumption that hot tears nucleate heterogeneously at microporosity voids developed from insufficient feeding or porosity that is nucleated as a function of tensile deformation. Rappaz and coworkers [27] began down the same path several years prior when they developed a strain rate dependent pressure drop cavitation model to explain the nucleation of pores which could then lead to hot tear defects. Campbell also mentions shrinkage porosity, gas holes, grain boundaries and molten metal inclusions as potential hot tear nucleation sites.

As part of their work on mushy zone deformation of IN718, Overfelt, Lewandowski and Wilcox [48] revisit first principles of void nucleation. From their relationship describing the critical Gibbs free energy for the nucleation of a void in liquid metal which is shown in

Equation 10, it is clear that the radius of the critically-sized cavity ($r_c$) required to form a void depends strongly on the surface tension of the liquid ($\gamma_{LV}$) and an imposed stress intensity ($\sigma_n$) which is applied normal to the interface. Yoo and Trinkaus [49] show that solute segregation to

$$\Delta G_C = \frac{r_c^3 F_v(\theta)\sigma_n}{2} = \frac{4F_v(\theta)\gamma_{LV}^3}{\sigma_n^2} \tag{10}$$

interdendritic regions and interfaces reduces the size of the critical cluster required to form a void and affects the grain boundary diffusion kinetics, both of which can result in an increase in the cavity nucleation rate.

Overfelt and team continued to refine Equation 10 by compensating for the maximum number of potential nucleation sites and the number of critically sized nuclei per unit area. The final modification employs the Zeldovich factor, an adjustment for back and forth oscillations between subcritical and supercritical cavity states which is affected by those vacancies that have sufficient energy to jump across the liquid/cavity interface. The final result is the steady state nucleation rate relationship in Equation 11 which remains highly dependent on both surface

$$I = 3.3\left(10^{-16}\right)\frac{\sigma_n^4}{\gamma_{LV}^3 F_v(\theta)}\exp\left(-\frac{4F_v(\theta)\gamma_{LV}^3}{\sigma_n^2 kT}\right) \tag{11}$$

tension and the imposed stress intensity. The experimental results of Lewandowski [50] as well as Overfelt and coworkers supports these concepts and the previously published work suggesting that a stress- and time-based model of cavity nucleation is more appropriate than a strain-based model, although both suggested more analyses were required to better understand the effects of strain rate dependence.

*9. Control and elimination of hot tears*

It is clear from the preceding discussion that the conditions for hot tear development are multi-dimensional and complex. Tendencies for different alloys to respond differently to the same conditions for hot tearing adds another level of challenge for the foundry engineer and casting designer. Nonetheless, based on both theoretical investigations and practical trial results, there are a number of variables which are known to reduce hot tearing susceptibility:

- Metal cleanliness
  - Elimination of oxide inclusions, excessive soluble gases
  - Improve mold filling systems to minimize gas entrapment and oxide films

- Reduce linear contraction and restraint
  - Modify casting design
  - Modify mold properties
  - Modify post-cast cooling parameters
  - Modify gating and feeding system design

- Eliminate isolated hot spots
  - Reduce constraint developed during solidification and cooling
  - Modify casting design
  - Modify mold properties
  - Modify post-cast cooling parameters
  - Improve feeding of isolated hot spots

- Grain refinement
  - Pour temperature modification
  - Modify pre- and post-cast thermal parameters
  - Modify mold properties

- Alloy modification
  - Optimize amount of eutectic formed
  - Reduce low melting point segregates
  - Increase amount of secondary dendrite arm cohesion
  - Improve feeding characteristics throughout mushy zone

- Reduce strain rate and strain concentration
  - Modify mold design
  - Modify mold properties
  - Modify post-cast thermal parameters

- Manage development of fraction solid through $\Delta T_{CTR}$
  - Modify post cast thermal parameters
  - Alloy modification
  - Eliminate isolated hot spots
  - Improve feeding of isolated hot spots

## E. DTA and DSC Testing and Interpretation

Classical and calorimetric differential thermal analyses (DTA) have been the most widely used methods of determining phase transformation temperatures of the superalloys. The more recent introduction of high temperature differential scanning calorimetry (DSC) equipment capable of accurate heat capacity ($c_p$) measurements up to ~1400°C and DTA-style measurements up to ~2000°C has expanded the available tool kit to alloy developers. Figure 23 provides an illustration of the differences between the two DTA tests and Figure 24 provides a schematic of power-compensated DSC equipment. Despite the difference in output signal, transformation events recorded by DTA and DSC thermograms can be interpreted using similar techniques.

In order to maintain as close to a zero temperature gradient within the sample as possible to encourage phase transitions throughout the sample to take place simultaneously, DTA and DSC sample sizes are kept small; typically on the order of 50 – 150 mg. In superalloys, such small sample sizes require multiple specimens to be analyzed to minimize the effects of segregation. [1,7,51-54] The use of machining chips for testing rather than an excised sample can also help to provide consistent results that are more representative of the bulk specimen. Bouse notes in his experiments with Inconel 718, that given the same sample and therefore identical chemistry between DTA tests, a change in microstructure will markedly affect the solidus temperature of the alloy. [55]

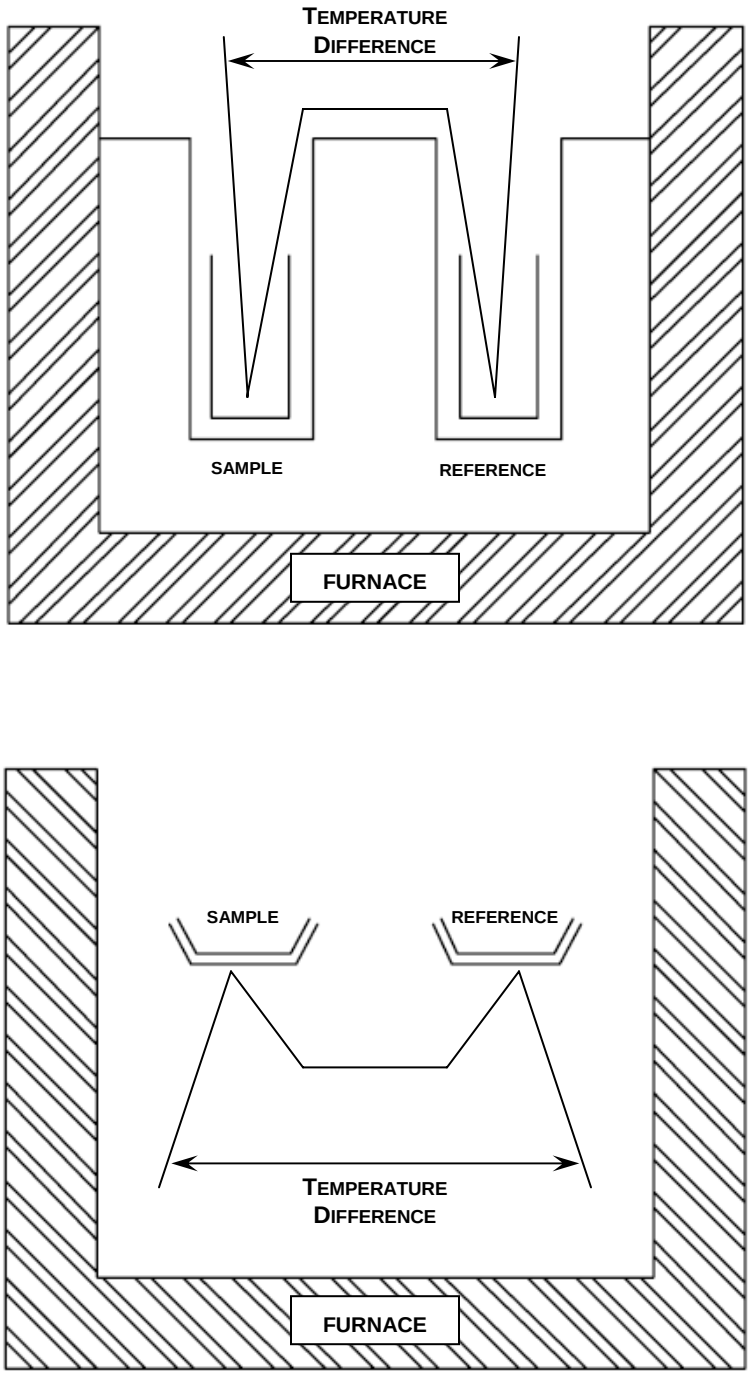


**Figure 23.** Schematic illustrations of classical (top) and calorimetric (bottom) DTA equipment. DTA equipment monitors the difference in temperature between the sample and the reference materials. Calorimetric DTA sample holders are typically flat pans attached to thermally conducting bases. Although the signal response is slower, this system provides the advantage of reduced output signal dependence on the thermal properties of the sample. Adapted from Reference [56].

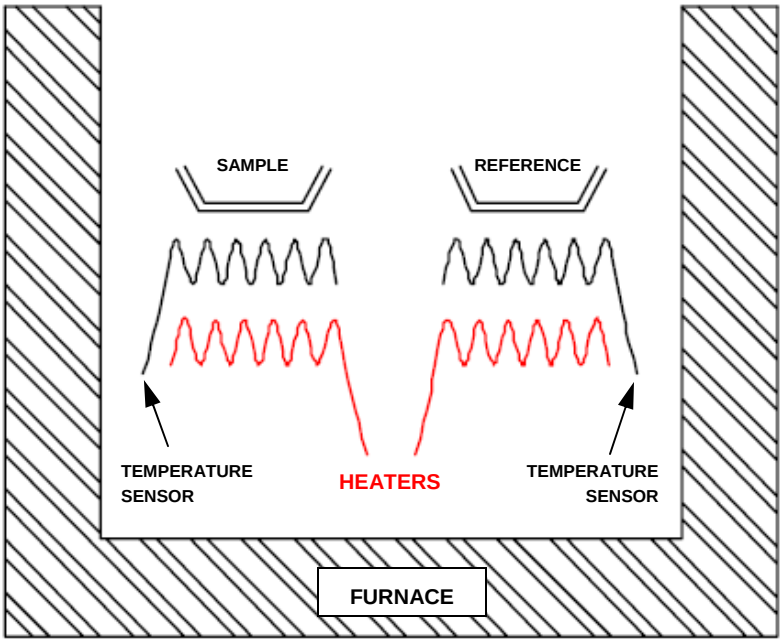


**Figure 24.** Schematic illustrations of power-compensated DSC equipment. DSC tests aim to maintain a 0°K temperature difference between the sample and the reference material. Rather than measure the difference in temperature (DTA), DSC monitors the difference in heat flow between the reference and sample materials. Adapted from Reference [56].

Although Austen-Roberts developed the calorimetric DTA technique more than 100 years ago in 1899, [56] it is sill difficult to find agreement within published literature on the proper interpretation of phase transition temperatures from DTA and DSC response thermograms. This is especially true for the solidus temperature where the heat capacity of the material changes as a function of temperature. In this case, there is broad acceptance for the use of the intersection point of the extrapolated tangent to the baseline to define the solidus temperature. However as Burton [7] explains, this approach is only valid if the thermogram recovers the baseline within 30°F (16.6°C), the temperature difference attributed to DTA instrument lag, sample size and heating rate. If baseline recovery requires more than 30°F, Burton contends that the reaction is continuing to proceed and event completion occurs once the response again meets the baseline.

Although not as clearly stated, Brown's explanation of the integral of the thermogram being proportional to the enthalpy of the event would also support this convention. [56] D'Souza *et al.* [54] and Lecomte-Beckers [52] have adopted this approach and attempt to impose a more controlled interpretation technique for broadened transformation peaks by using modified extrapolation approaches. It is unfortunate that this nuance of irregular peak interpretation of DTA and DSC thermograms is often missed, as solidus temperatures are often reported in published articles at much higher temperatures than the reported thermogram data would suggest is the case.

Transformation onset temperatures are handled more consistently between published studies, but some variation in interpretation does exist. Although Kearsey [53] and Cao [57] use the peak of the cooling curve to define the liquidus temperature, there is greater consensus and more theoretical support from Burton [7], Bouse [55], Brown [56], Lecomte-Beckers [52] and D'Souza [54] for the use of the departure point of the thermogram response curve from the baseline.

As both D-Souza and Brown describe, the area between the DTA or DSC response curve and the baseline is proportional to the enthalpy of the reaction. The calculation of the enthalpy change for the phase transformation can be determined from:

$$\Delta H_s = \frac{\left(K_{DTA} \times A_s\right)}{m_s} \tag{12}$$

where $m_s$ is the mass of the sample, $A_s$ is the area between the response curve and the baseline and $K_{DTA}$ is a calibration factor for the reference material. $K_{DTA}$ is essentially independent of temperature for power-compensated DSC measurements, but is significantly temperature dependent for DTA tests. [56] In addition to evaluating the area beneath (above for heating) the thermogram and the baseline, it is also informative to evaluate the peak intensity which is proportional to the rate of the transformation. [6]

D'Souza makes use of a numerical program written by Dong [58] which accounts for calibration of heat flow through all parts of the DTA system to prevent smearing of the measured signal over a range of temperature. D'Souza also relates the observations of Dong and others in that the differential signal measured by DTA is proportional to the effective heat capacity temperature difference only when latent heat is not evolved as a function of the reaction.

It is well documented that the heating and/or cooling rate employed in DTA and DSC tests affect phase transformation peak temperatures and the area between the response curve and the baseline. [7,51,56,59] Figure 25 and Figure 26 show some published results describing the effect of cooling rate on transition temperature. Figure 26 also illustrates the difference in transformation temperature between heating and cooling curves as a function of heat transfer rate. Although one would prefer the analytical system to be as close to equilibrium as possible in order to get a true reading of the transition temperature, the rate of heat transfer must be rapid enough so that the peaks for the transitions can be resolved. Lecomte-Beckers [52] devised a clever method of negotiating the heat transfer challenge for DTA by running multiple samples of the same material at three different cooling and heating rates. This technique provides the opportunity to create a linear extrapolation of the transition temperature data back to the equilibrium cooling rate. Although an apparently sound method of establishing actual transition temperatures at equilibrium heat transfer rates, the procedure does require a great many samples. Upon further consideration, the method could be considered of more academic interest as most industrial melting and solidification processes do not proceed at equilibrium. Heating and cooling rates of 5-20$^{\circ C}/_{minute}$ are typical for superalloy DTA and DSC experiments intended to span the mushy zone, with $10^{\circ C}/_{minute}$ being the most common. [6,7,51,52,55,57,58] Wu and Perepezko [51] and Cao, Kennedy and Willis [57] have reported measuring more accurate phase transition temperatures with DTA by using an interrupted heating process.

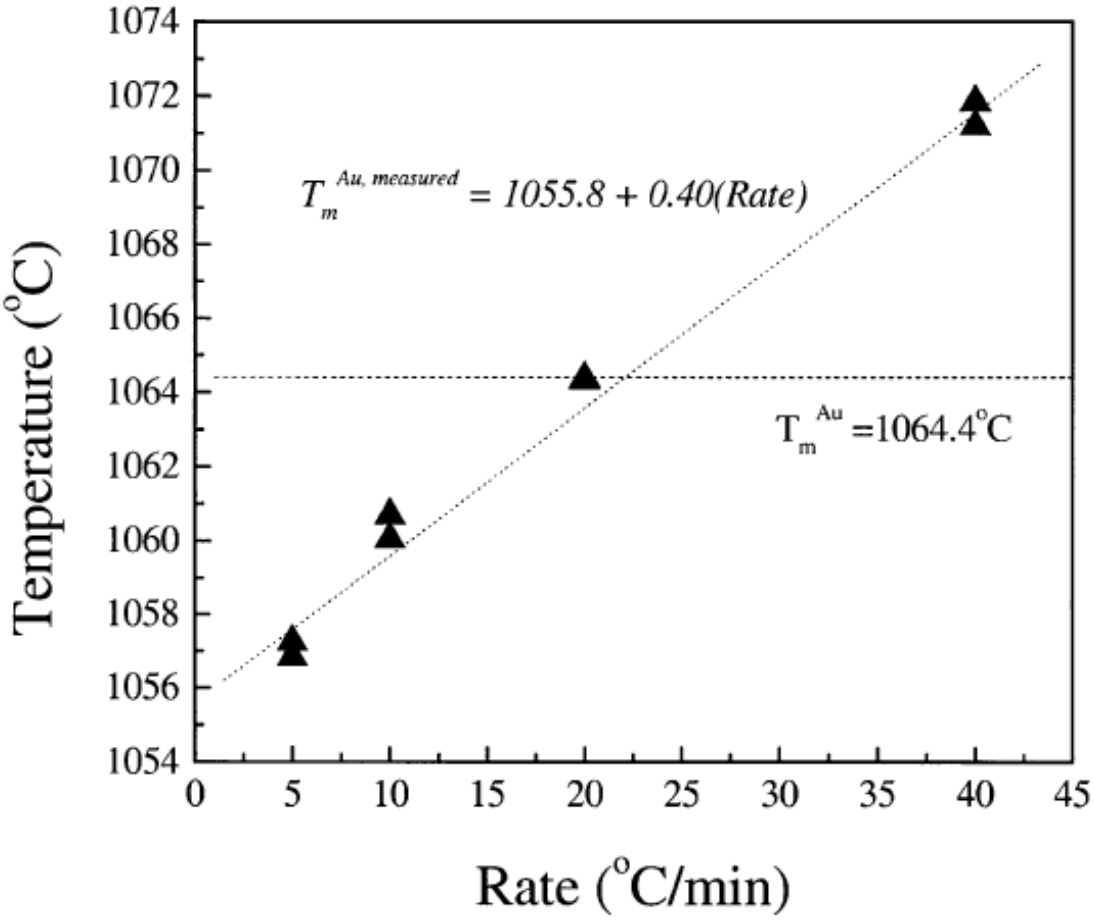


**Figure 25.** Melting temperature ($T_m$) of gold heated at different rates, as determined by DTA. From Wu & Perepezko [51].

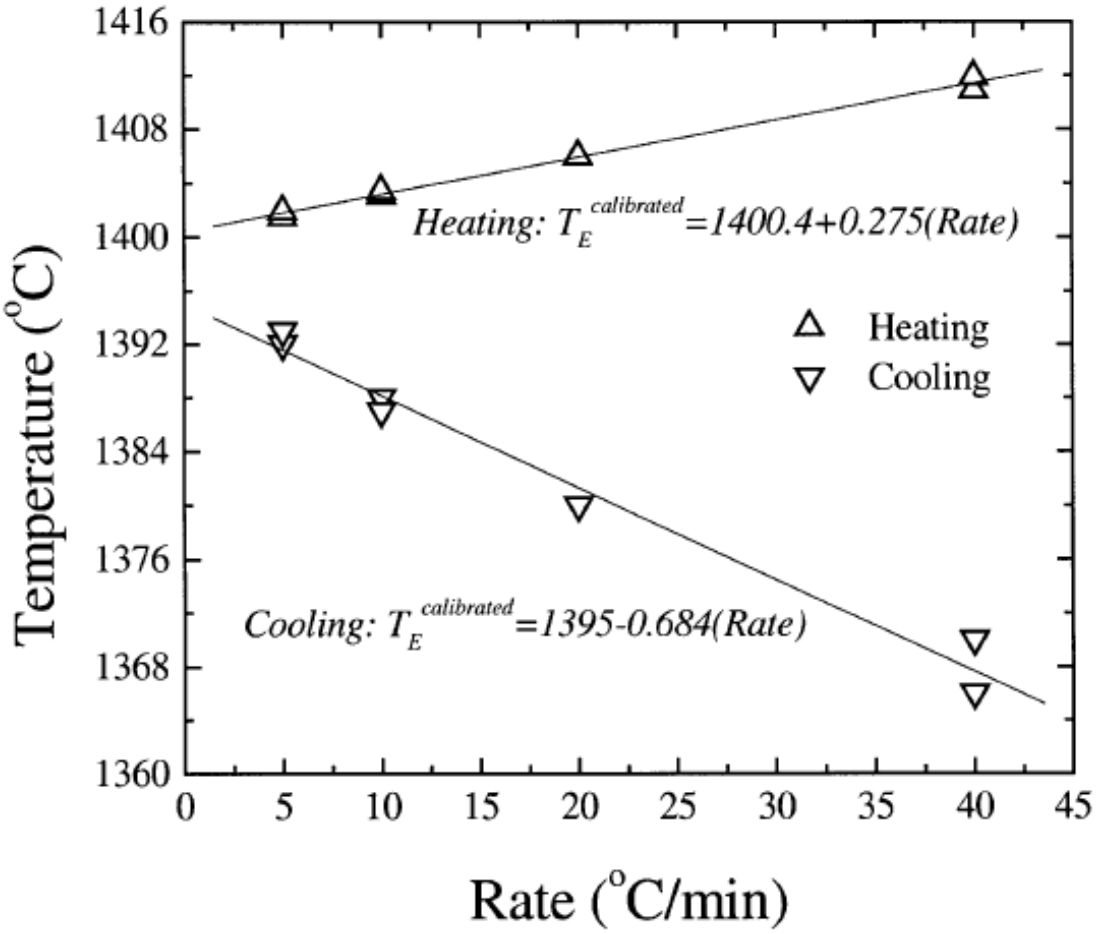


**Figure 26.** Eutectic temperature ($T_E$) of Co-18.5 at.% Al heated and cooled at different rates as determined by DTA. From Wu & Perepezko [51].

# III. OBJECTIVES

There are three objectives for this investigation. First, the PCC FSX-414 production casting results continue to be variable despite the well controlled production environment in place for making IGT castings and notwithstanding all of the master alloy is within the engineering control limits which are themselves, set inside the alloy specification limits. There is a strong body of evidence that shows the variations in casting quality are aligned with changes in master alloy and not with inconsistency in the casting process. Therefore the first and primary objective of this investigation is to arrive at a robust chemical composition for FSX-414 that will consistently yield defect-free production castings.

The second objective of this investigation will be to gain an understanding of how small variations in alloy chemistry within even the engineering control limits, can dramatically affect the quality of FSX-414 castings. The work presented in this investigation on alloy composition differs from much of the published literature on this same topic due to the small scale in the changes of composition that are considered.

The final objective is to create and validate an improved method for developing a quantitative understanding of the effects of alloy chemistry on casting quality. Traditional approaches to chemistry issues in the foundry have been centered on straightforward, single variable statistical analyses or designed experiments based on relatively arbitrary adjustments in the concentration of a few elements which experientially, are known to influence casting quality. This investigation will detail a more comprehensive, statistically based method of evaluating and predicting the influence of multiple elements on solidification behaviour. Although the method may not be new, its application in the foundry industry is unique, powerful and can be leveraged.

# IV. EXPERIMENTAL METHODS

Over a period of approximately one year, 40 kg to 100 kg ingots from twenty one 5,000 kg production vacuum induction melted (VIM) master heats of FSX-414 were selected at random and set aside. The ingots were sampled from metal lots (ML, master heats) produced over a long period of time as products of the controlled production alloy making process. At the time, PCC Deer Creek was producing FSX-414 castings at a rate sufficient to consume 50 to 60 master heats annually. Based on a review of historical production data, the author ensured that chemistries of the master heats selected spanned the typical range of foundry control chemistry. Effort was also applied to ensure the heats selected represented the widest variety of production casting NDE results possible. The focus on selecting FSX-414 ML samples that represented the total variation of the production casting process form the foundation for this investigation and abate concern for the samples not representing the natural production environment.

## A. Test Vehicle Casting

To avoid confounding interactions between the casting geometry and any production casting part-specific process variables, a simple test vehicle casting was used as the basis for this investigation. The test casting geometry is designed to deliberately create hot tear defects and for this reason, is referred to as the Hot Tear Test Vehicle (HTTV) throughout this investigation. An illustration of the HTTV is provided in Figure 27 and a detailed drawing is provided in Appendix A. By creating a single casting with restrained bars of varying lengths, ranges of mold and solidification temperature gradients, contraction strains and requirements for a variety of feeding distances are all established simultaneously and within the environment of constant alloy

chemistry. Similar versions of the HTTV have been used to evaluate alloy hot tear susceptibility at PCC and other foundries.

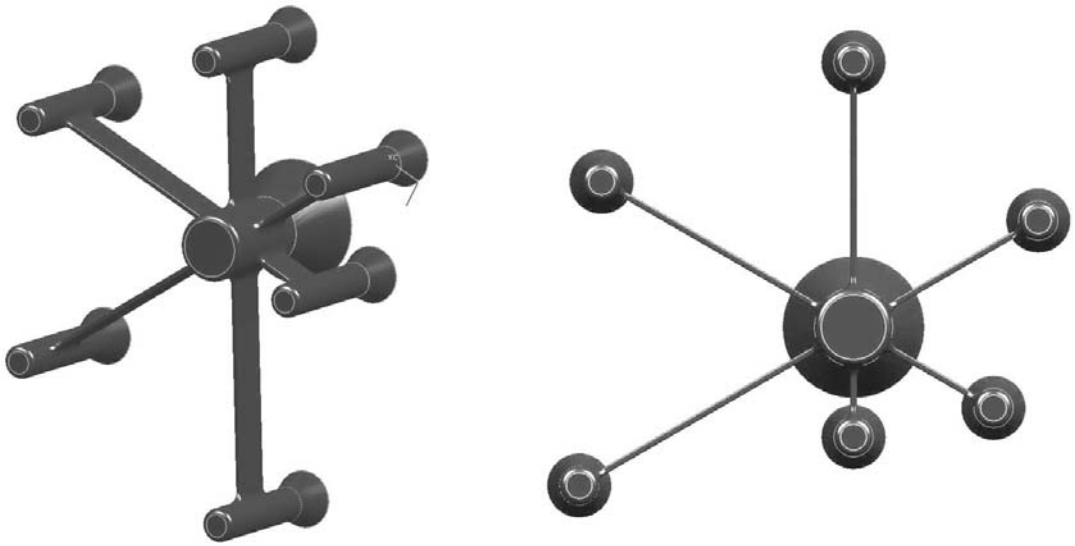


**Figure 27.** Isometric views of the HTTV casting CAD model definition. Appendix A provides a detailed explanation of the assembly detail.

The HTTV casting consists of six bars 50 mm wide by 6.3 mm thick in lengths varying from 50 mm to 250 mm long. Each bar was attached directly to a central downsprue at the inner ends and a feeder at the outer ends. The sheet wax used to create the bars was cut from a slab injected from a wax pattern tool, so the thickness of each bar was known to be constant. All fillet radii at bar-feeder connections were held constant at 12.5 mm and 2 mm edge radii were applied to all bars. The assembly of the wax patterns was carried out at PCC Deer Creek by a small group of the most highly skilled Engineering Assemblers using industry standard wax assembly techniques and detailed work instructions. A serialization pad containing the production lot traceability number as well as the bar length was attached to the radially outboard surface of the feeder of each bar. Standard 38 mm x 13 mm chill samples for chemistry analysis were serialized

and applied to the downsprue of each mold. A detailed inspection of each assembly was carried out by the author to ensure that the molds were constructed consistently in all respects.

The HTTV assemblies were invested using the automated robotic investment shell production equipment at PCC Deer Creek. All raw material, slurry composition, dip and drain parameters and drying conditions were identical to those used for production castings. The PCC Deer Creek shell system consists of a cobalt-aluminate inoculated face coat followed by successive layers of a fused silica backup shell. The face coat along with the wax pattern, primarily governs the surface quality of the casting while the backup shell provides the mechanical strength required for the mold to hold metal.

The first phase of this investigation consisted of a two mold HTTV screen trial to validate the sensitivity of the test vehicle casting to the PCC Deer Creek process. Metal lots which were known to represent the typical and worst-case production results for hot tearing were selected for this trial. Based on the results of the screen trial experiments, it was determined that the designed variety of solidification conditions generated by the HTTV provided adequate sensitivity to discern differences in microporosity development and hot tear susceptibility between FSX-414 ML that were within both the specification limits and foundry control limits. [60]

In the second phase of the investigation, an expanded seven ML HTTV casting trial was conducted. The metal lots from the original screen trial were replicated in the second phase of the investigation to ensure there were no time-related or process-related confounding effects. The hot tear severity from the Phase II HTTV castings was compared against the frequency of hot tears detected for each of the same ML in Deer Creek production castings. The results of the Phase II HTTV investigation aligned very closely with production casting data. These results provided sufficient proof of both the sensitivity of the HTTV to detect differences in ML behaviour and proof that the difference in casting quality between metal lots was in fact as significant as the production data had suggested. These conclusions warranted the release of the third phase of the investigation, which was to cast and analyze HTTV castings poured from an additional 14 metal

lots. The primary intention of the expanded trial was to generate an adequate data set to allow for a meaningful statistical analysis to be conducted. [61]

As outlined above, the HTTV molds for this investigation were assembled and invested in two batches, one for each phase, with each batch completed over approximately a one week period to reduce the opportunity for confounding the experimental results with natural shifts in the production investing process. Similarly, the HTTV castings for each phase of the investigation were poured back-to-back over the course of a single day using melting and casting techniques established and proven on Deer Creek FSX-414 production IGT castings. The batched casting campaign helped to ensure as much consistency in post-cast cooling conditions as possible, with the goal of providing uniform cooling rates based on consistent ambient conditions in the foundry. The author witnessed the entire melting and pouring process for each mold to ensure that all mold preheat temperatures, melting techniques, casting parameters, mold transfer times and cooling conditions remained consistent for each mold and between each phase of the investigation.

After the castings had cooled to ambient temperature, removal of the investing mold materials was performed using a combination of production standard mechanical knock off for the bulk shell followed by steel shot blasting to remove residual shell materials. The bars were separated by sectioning the downsprue axially into six equal sections by air-arc torch cutting. Final surface preparation included deburring of the torch-cut surfaces and aluminum oxide sandblasting of the exterior surfaces of each bar to facilitate fluorescent penetrant inspection. Throughout the shell removal and surface cleaning processes, care was taken to avoid mutilation of hot tear surfaces and to ensure that bars which had completely dissociated by hot tearing were kept paired with their respective feeders or downsprue sections.

## B. Quantitative Analyses of HTTV Castings

From the outset of this investigation, the intention was to generate enough data to be able to use some form of statistical analysis to achieve the objectives of the investigation. Although it is typical of the foundry industry to generate and collect combinations of both discrete and continuous data to evaluate the quality of castings, the variety of statistical analysis tools available for the analysis of continuous data is far more extensive. Therefore in order for the statistical analyses from this investigation to be most meaningful, the quality of the HTTV castings needed to be distilled into objective, quantitative terms against which statistical analysis tools for continuous data could be applied.

### *1. Hot tears*

Each HTTV bar was subjected to fluorescent penetrant inspection (FPI) to assist in the visual identification of hot tears. FPI data was compiled for each bar on the basis of total hot tear length by radial location from the end of the fillet radius at the downsprue end. Hot tears were mapped on both sides of each bar. The maximum width of each tear was also measured to the nearest 0.005" (0.127 mm).

### *2. Microporosity*

Based on hot tear defects only being observed in the longest four HTTV bars across all metal lots, these same bars were selected for metallographic evaluation of microporosity. Prior to sectioning with a liquid cooled bandsaw, each bar was marked with radial position locating marks with the origin located at the radially outboard end of the downsprue fillet radius. Figure 28 contains a photo of a fully marked set of HTTV bars prior to sectioning. All longitudinal sections were taken at a nominal axial position of 12.5 mm down from the top edge of the bar in the casting orientation. This position was chosen after considering several factors. First, assuming that there would be some gravitational influence on feeding across the axial section of the bar, the

upper third of the bars in the casting orientation should be more prone to developing microporosity than the lower third. [13] Second, knowing that the axial centerline of the bar should be most prone to developing microporosity, quantitative evaluation of microporosity defects at that position may not provide sufficient resolution; too much metallographic work was at stake to take this risk. Next, radiographic interrogation of each bar showed that microporosity would be available for metallographic evaluation at the section chosen. Finally, by sectioning above the centerline of the bar, a significant portion of material remained available for additional evaluations, if required.

The 12.5 mm wide sections were marked for axial sectioning, the section lines were mapped and the samples subsequently cut such that the samples would fit within a 65 mm metallographic mount. Following mounting, the samples were polished for metallographic evaluation using standard metallographic preparation techniques. Optical measurements of microporosity were taken along the entire length of each sample in the as-polished condition in fields viewed at a magnification of 10x, using a Nikon Epiphot inverted metallographic microscope and a Beuhler Omnimet Image Analyzer. Care was taken to ensure that focusing techniques, microscope light settings and Image Analyzer settings were held constant for each measurement. Each microporosity field over 1% (surface area) encountered along the length of each sectioned bar was evaluated for the maximum porosity in a single field of view, the maximum size of the continuous porosity field and the longitudinal position of each field relative to the origin adjacent the downsprue. It is believed that longitudinal locating measurements for each field of microporosity were accurate within ±1.5 mm.

Regardless of the ML, no hot tears or appreciable amounts of microporosity were observed in either of the two shorter bars. For this reason, no further microstructural evaluations of these castings were conducted.

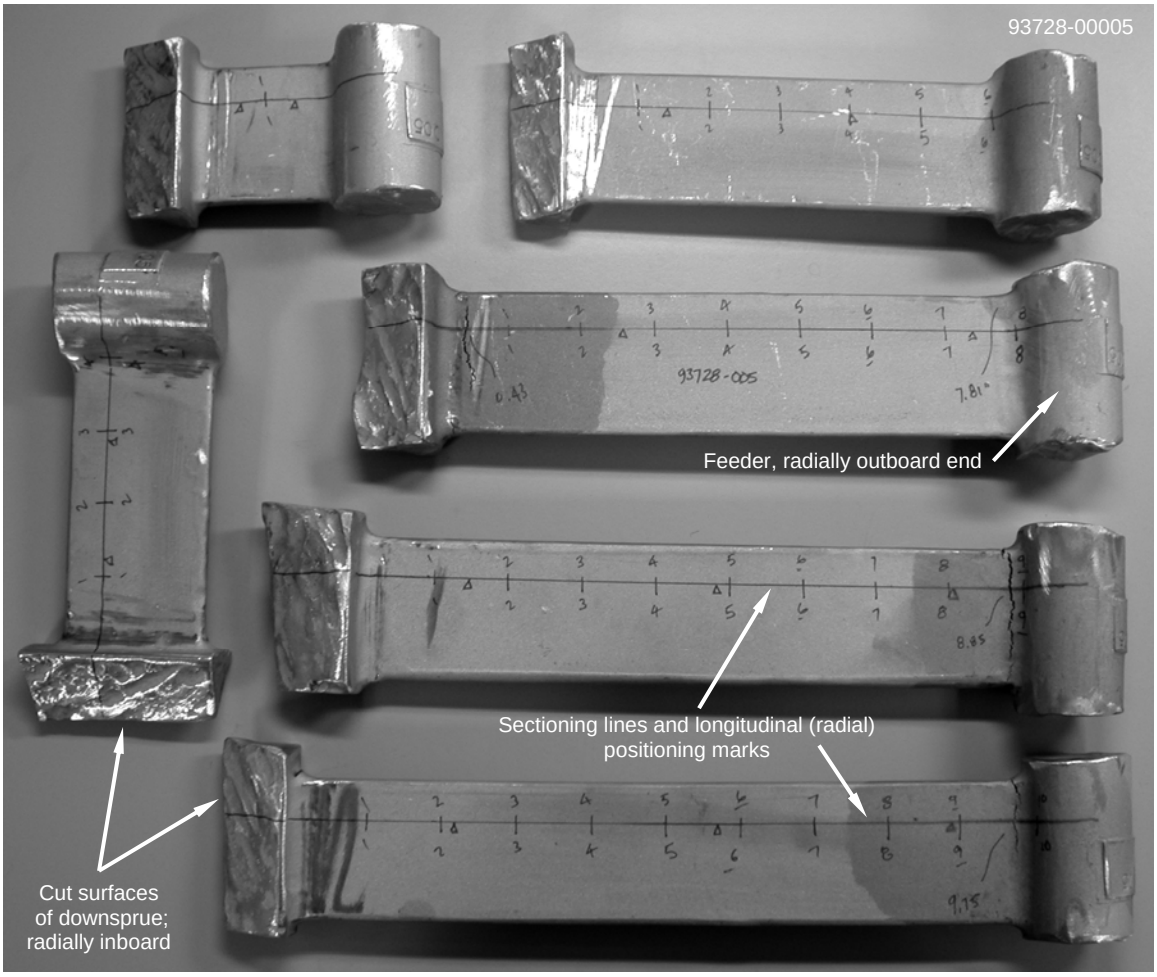


**Figure 28.** Annotated photograph of a set of HTTV castings prior to sectioning. Hot tear locations are marked. FPI bleed out from hot tears is evident on the longer three bars.

*3. Carbide microstructure*

Following the quantitative microporosity measurements, all samples were electrolytically etched with 10% ammonium persulfate to reveal the microstructure. Quantitative measurements of $M_{23}C_6$, $M_7C_3$, and MC carbide typical and maximum dimensions were taken at 500x magnification at the downsprue fillet, bar center, feeder fillet and feeder centerline as detailed in Appendix B. Measurements of the total carbide area fraction were taken across the entire width of each bar in each of the same four pre-determined locations. Microstructural analyses were conducted using the same Nikon Epiphot optical microscope, and quantitative carbide assessments were made using the commercially available digital image analysis software,

PaxIT™. It was found to be critically important that microscope light settings, focal techniques and PaxIT™ settings be kept consistent to ensure the accuracy of the carbide measurements. Quantitative assessments of carbide microstructures were also made along the edges of hot tears and traversing each of the hot tears which happened to be sectioned, as described in Appendix B. Appendix C contains example micrographs from the microstructure interpretation guide developed to ensure consistent visual identification of each phase encountered. [4,11,62]

*4. Secondary dendrite arm spacing*

The typical secondary dendrite arm spacing (SDAS) was determined in similar locations to the areas interrogated for carbide characterization. Using digital micrographs taken at a magnification of 25x with the Epiphot microscope, PaxIT™ was used to draw straight lines of known length normal to the dendrite arm growth direction as shown in Figure 29. The SDAS was determined by counting the number of dendrite arms that intercepted each line. By employing the equation detailed in Appendix B, an average SDAS value was calculated at each location.

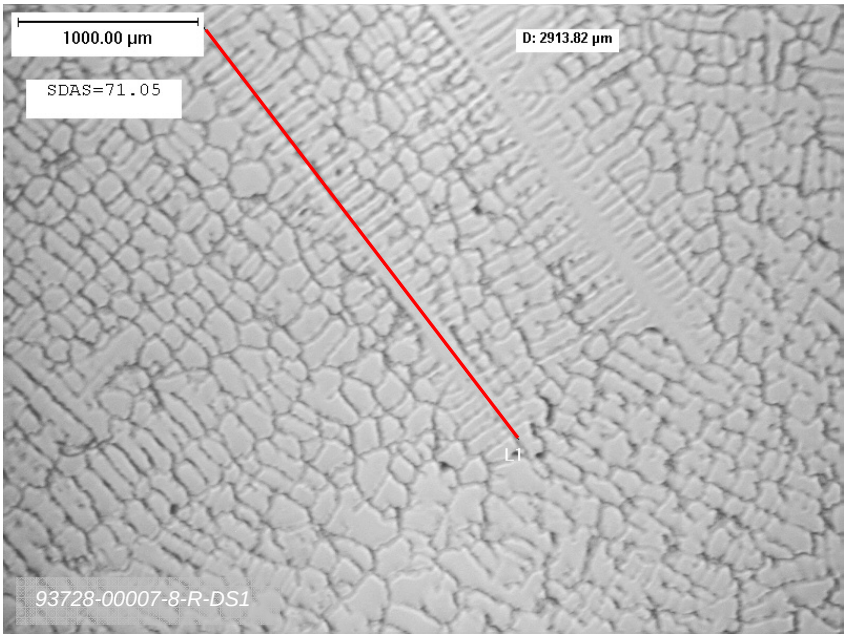


**Figure 29.** Typical SDAS evaluation micrograph, including an intercept line.

*5. Grain size*

The evaluation of the surface grain structure is a standard requirement for the qualification of most IGT and aerospace castings. When cast into surface-inoculated investment shells as was the case in this investigation, FSX-414 is known for having a very small and consistent surface grain structure that does not vary appreciably with changes in the casting process. However, because of the known stability of the FSX-414 heterogeneously nucleated surface grain size and structure, the cross-sectional grain structure of the HTTV castings was evaluated in an attempt to provide a better understanding of any potential changes in solidification behaviour after the initial fine grained (chill) layer forms.

Following the completion of all of the microporosity and microstructural evaluations, each of the metallographic mounts were swab etched to reveal the macro grain structure with a solution of HCl + $H_2O_2$ which was mixed at a ratio of 9:1. Digital photos of the grain structure were taken at approximately 7x magnification at the center and fillet radii of each bar using a Wild M400 stereomicroscope and PaxIT ™. The Heyn Lineal Intercept Procedure from ASTM E112 – 96 (2004) detailed in Appendix B was used to determine the average grain size in each location. An identical array of five lines was used to count the grain boundary intercepts in each field of view. When the initial array was constructed, care was taken to avoid placing a line in the narrow chill zones at the edges of the section so as not to artificially distort the cross-sectional grain size evaluation results. Figure 30 provides an example of a grain size evaluation photo including the intercept array.

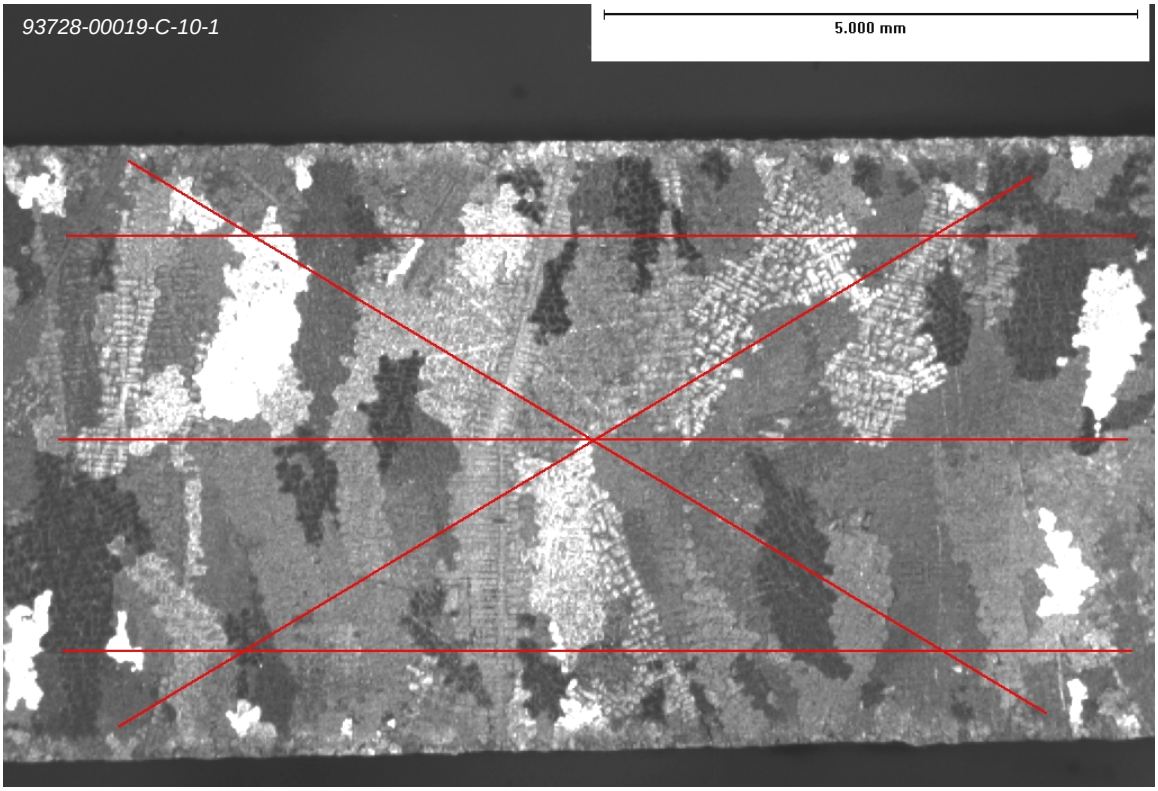


**Figure 30.** Typical macro grain size evaluation photo including the grain boundary intercept lines. Note the chill sections on either side of the bar, located top and bottom in the photo.

*6. Scanning electron microscopy*

Scanning electron microscopy of the fracture surface of a hot tear excised from a HTTV casting was conducted at GE Power Systems (GEPS) in Greenville, SC. The sample was examined in a LEO SEM in the unmounted and graphite vacuum coated condition.

Backscatter scanning electron microscopy and wavelength dispersive x-ray (WDX) element mapping of transverse sections of hot tears from Phase II samples was conducted at The Department of Metals and Materials Engineering at The University of British Columbia using a Hitachi S-3000N SEM equipped with a Quartz XOne EDX. These samples were the same metallographic mounts used for the previously described optical microscopy investigations. Each of the samples examined was in the as-polished condition.

## C. Chemistry Determination

The cylindrical chill samples from each mold were analyzed at both BodyCote Materials Testing Laboratory in Portland, OR (now Exova) and at Cannon-Muskegon Corporation in Muskegon, MI. Both of these sites have considerable experience testing FSX-414 and it was of interest to baseline the two sets of analytical results. Glow Discharge Mass Spectrometry (GDMS) analysis was conducted on chill samples from the seven Phase II HTTV castings at Northern Analytical Laboratory, Inc. (NAL) located in Merrimack, NH. Due to the lack of variation in the single digit, part per million concentrations of the trace elements that only GDMS could detect reliably, it was determined that there was little risk in not completing the full campaign of GDMS testing. The analytical methods used to determine the final HTTV chemical compositions are listed in Table 3.

| | | | | | | | |
|---|---|---|---|---|---|---|---|
| **C** | LECO | | **Co** | XRF | | **K** | GDMS |
| **Mn** | XRF | | **Al** | XRF | | **Zn** | GDMS |
| **Si** | XRF | | **Ti** | XRF | | **Ga** | GDMS |
| **Cr** | XRF | | **Cu** | XRF | | **As** | GDMS |
| **Ni** | XRF | | **V** | XRF | | **Sn** | GDMS |
| **Fe** | XRF | | **Nb** | XRF | | **Sb** | GDMS |
| **W** | XRF | | **Ta** | XRF | | **Re** | GDMS |
| **P** | XRF | | **Mo** | XRF | | **Pb** | GDMS |
| **S** | LECO | | **Ca** | GDMS | | **Bi** | GDMS |
| **B** | OE | | **Na** | GDMS | | **La** | GDMS |
| **N** | LECO | | **Mg** | GDMS | | **Ag** | GDMS |
| **O** | LECO | | **Cl** | GDMS | | **Au** | GDMS |

| | |
|---|---|
| **Xx** | Primary, B50A489 specification controlled element. |
| **Xx** | Foundry control element, used in statistical analyses. |
| **Xx** | GDMS only, not used in statistical analyses. |

**Table 3.** Analytical methods used to establish chemical composition of FSX-414 HTTV castings.

## D. HTTV Thermal Analyses

Samples were excised from the center of the 6" (152 mm) long bar from each Phase I and Phase II HTTV casting and prepared into ~90 mg samples for differential thermal analysis. Each sample was tested against a Pt reference thermocouple at heating and cooling rates of 10 $^{\circ C}/_{min}$ in an alumina crucible under an argon gas cover set at a flow rate of 100 $^{ml}/_{min}$. Tests were conducted in a TA Instruments Universal 2960 SDT V3.0F thermogravimetric-DTA (TGA-DTA) at BodyCote Materials Testing Laboratory in Portland, OR and at The M&P Lab in Schenectady, NY. To mitigate the effects of alloy segregation and the relatively coarse microstructure of FSX-414 from affecting the quality of the DTA results, two samples were excised, prepared and tested for each HTTV casting. Based on the work of a number of researchers, [7,51-54] duplicate samples have been suggested to be the minimum requirement for superalloy DTA testing.

Detailed analyses of the thermal events recorded during DTA testing were carried out on the raw numerical data, rather than using a charting method or using the values selected by the OEM analytical software. Interpretation of the recorded DTA events was consistent with the works of Burton [7], Bouse [55], Brown [56], Lecomte-Beckers [52] and D'Souza [54]. Figure 31 provides definitions of the interpretations of the thermal events used to develop the quantitative DTA analysis matrix used for the statistical analyses.

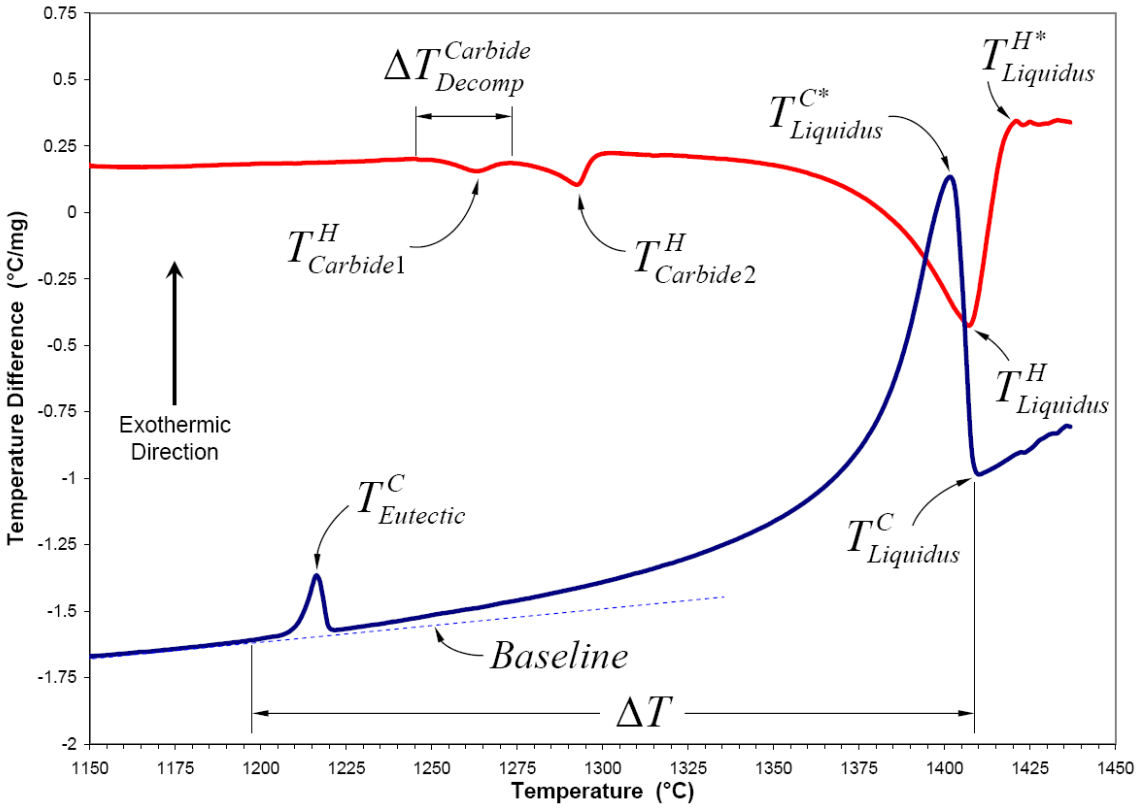


**Figure 31.** Illustration of the interpretations of DTA data employed during this investigation.

| | |
|---|---|
| $T^{C}_{Liquidus}$ | Cooling curve liquidus temperature |
| $T^{C*}_{Liquidus}$ | Cooling curve liquidus temperature, alternate definition<br>Not employed in this investigation |
| $T^{H}_{Liquidus}$ | Heating curve liquidus temperature |
| $T^{H*}_{Liquidus}$ | Heating curve liquidus temperature, alternate definition<br>Not employed in this investigation |
| $T^{C}_{Eutectic}$ | Cooling curve eutectic solidification temperature |
| $T^{H}_{Carbide\_x}$ | Heating curve carbide decomposition temperature |
| $\Delta T^{Carbide}_{Decomp}$ | Range of carbide decomposition |

## E. Modeling

*1. Solidification and stress modeling*

A predictive solidification model of the HTTV casting was run by the PCC Structurals Inc. Materials and Technology department. The model was created in ProCAST™ using boundary conditions which replicate the shell system and cooling conditions used in the manufacturing of the HTTV castings. The boundary conditions of the model were validated against actual thermocouple data gathered during pouring and cooling of the HTTV castings. To carry out the validation, virtual thermocouples were placed on the electronic model in the same locations as the thermocouples in the actual castings. The virtual traces generated in the ProCAST™ model were overlaid with the experimental thermocouple data from a HTTV casting. The results provided in Figure 32 demonstrate reasonable correlation between the predictive model and the experimental data. It was determined that the level of correlation obtained was sufficient for the purpose of gaining a general understanding of what directions and sequence the bars of the HTTV casting would solidify.

Based on the thermal profiles generated by the ProCAST™ solidification model, the ProCAST™ stress prediction module was used to generate colour contour plots of the stress distribution developed in the HTTV bars during solidification and to baseline the newly implemented ProCAST™ Hot Tear Indicator module against actual HTTV results.

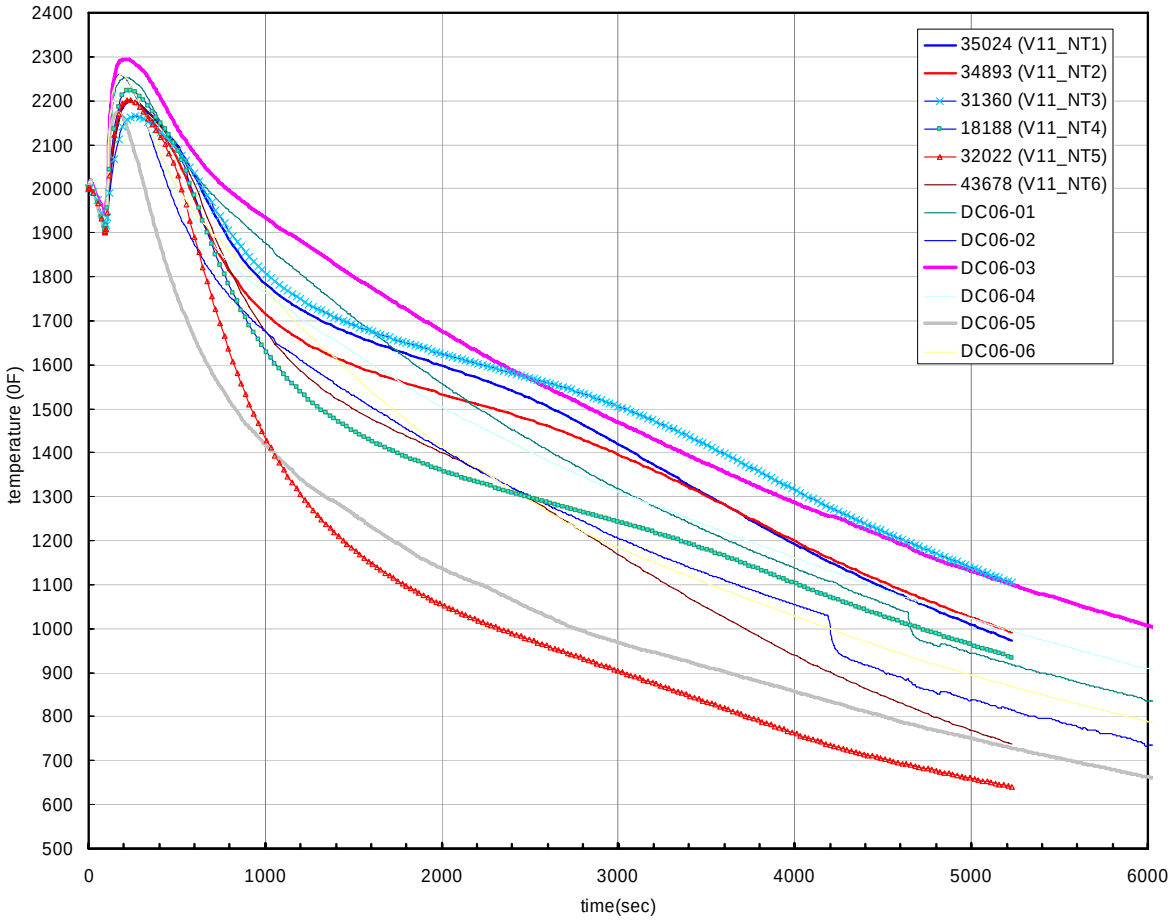


**Figure 32.** ProCAST™ predicted cooling curves overlaid with HTTV experimental data. Reasonable correlation between the predictive model and actual results are observed. From Reference [63].

*2. Thermodynamic Modeling*

Thermodynamic modeling of each of the chemistries determined from the Phase II and Phase III HTTV castings was conducted using JMatPro™ at the Institute of Materials and Manufacturing at Portland State University (PSU) in Portland, OR. The JMatPro™ database in use at PSU did not contain data specific to the evolution of phases specific to Co-based alloys, therefore the Ni-based alloy database was used as the foundation for the predictive work. There were several other caveats to the modeling work which are listed below:

- The effects of S and P were not considered by the database and were therefore excluded from the model. S and P contents were set to zero.
- O and N tended to cause model divergence problems and were therefore omitted from the analyses. O and N contents were set to zero.
- For each HTTV chemistry, the actual contents of S, P, O and N were summed and the Co content adjusted upward by this amount. By taking this approach it was ensured that the Ni content of each alloy remained correct.
- Fraction solid calculations were made with the assumption that back-diffusion does not occur in the solid, thus the Gulliver-Scheil equation applies. The consistent presence of interdendritic eutectic carbide in FSX-414 shows this to be a reasonable reflection of FSX-414 solidification behaviour. [64]

$$\frac{C_l}{C_o} = \frac{1}{(1-f_s)^p} = \frac{1}{f_l^{\,p}} \tag{13}$$

## F. Validation Test Bar Castings

Many foundries struggle to cast net-shape test bars in Ni- and Co-based superalloys that are free from centerline shrinkage and interdendritic porosity. It was of particular concern to the success of this investigation that the validation test bars (VTB) be sound so that elevated temperature and mushy-zone tensile testing would be representative of the alloy and not the alloy plus any latent shrinkage porosity. Therefore, knowing that PCC had not yet identified a suitable geometry for shrinkage-free test bar castings, a new test bar design was developed. Several criteria were imposed during the conception of the new geometry:

(a) The overall test bar length and diameter needed to be sufficient to satisfy room temperature, elevated temperature, stress rupture and mushy zone (Gleeble™) test samples.

(b) Adding a gate to the gauge section (center gating) was not an acceptable solution as the grain size would become enlarged in the test area.

(c) The gauge length needed to be sound in the as-cast condition; relying upon HIP to heal shrinkage porosity was not an acceptable solution.

(d) The mold needed to be configured such that all of the bars cast experienced the same thermal conditions.

(e) The test bar geometry needed to be independent of the alloy; a successful geometry should be able to be leveraged to other superalloy systems.

Figure 33 provides an illustration of the final VTB geometry and mold configuration.

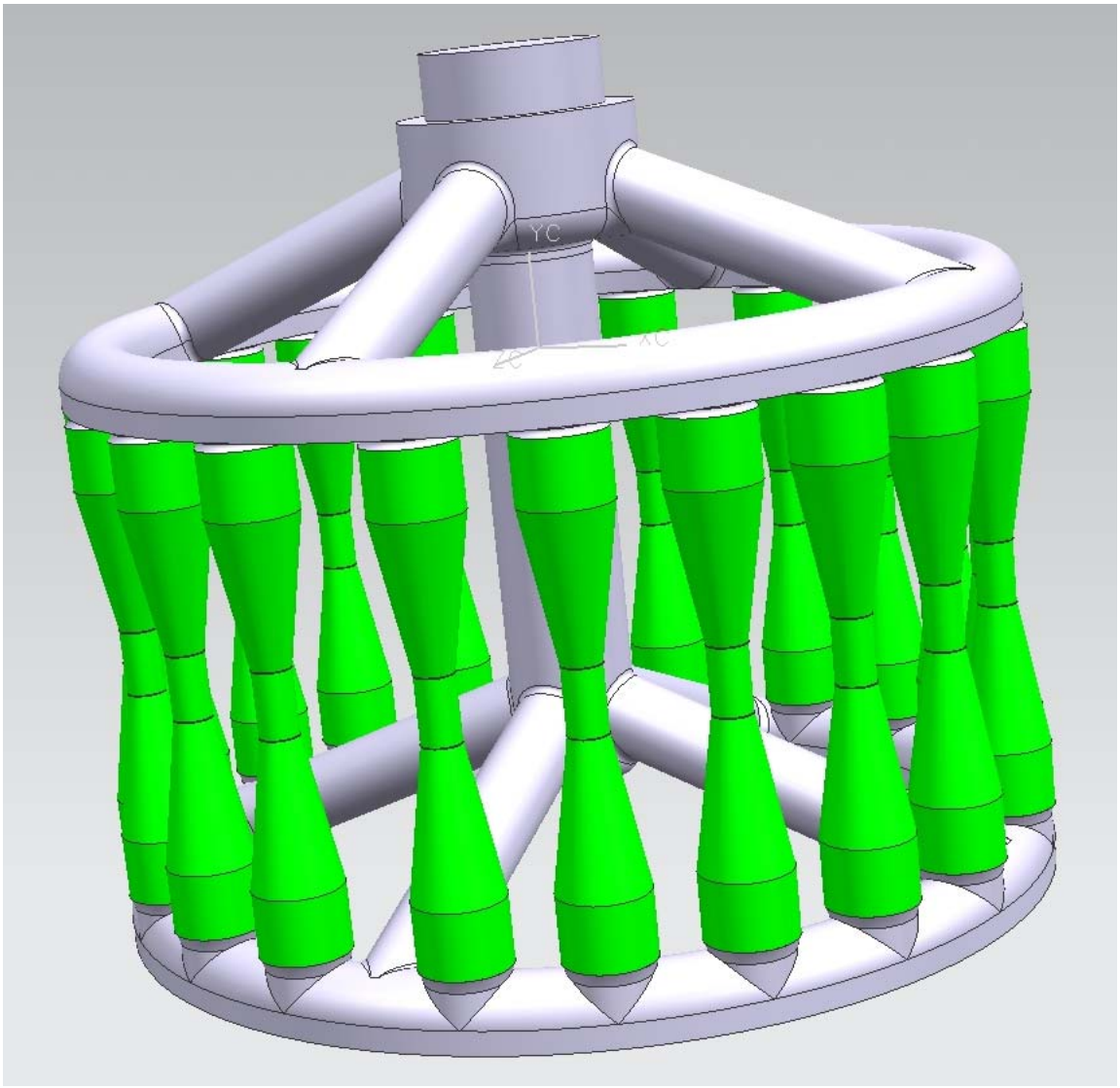

**Figure 33.** Validation test bar geometry and mold configuration.

*1. Chemistry determination*

The same standard 38 mm x 13 mm chill samples for chemistry analysis that were used for the HTTV castings were attached to each of the VTB molds. Analyses of the chemical composition were again carried out at Exova (formerly BodyCote) in Portland, OR and at Cannon-Muskegon Corporation. Table 3 outlines the analytical methods used to determine the concentration of each element. No GDMS testing was conducted on any of the VTB samples.

*2. Metallographic evaluation*

The gauge length was excised out of one bar from each mold and machined (milled) up to the longitudinal centerline. The remaining section was then mounted in a 65 mm diameter metallographic mount and polished using standard metallographic preparation techniques. The axial centerline of the casting gauge length was used as the primary location plane for these investigations. Because the VTB castings were designed specifically to be resistant to developing microporosity, the as-polished samples were evaluated for all discernable areas of microporosity greater than 0.25% in order to gain some sensitivity of measurement.

Each of the three samples was electrolytically etched to reveal the carbide microstructure using a 10% ammonium persulphate solution. Following the microstructural assessment, the macro grain structure was revealed with the 9:1 mixture of HCl and $H_2O_2$. The metallographic equipment used in these investigations was the same as that which was described in Section IV-B.

*3. Differential Scanning Calorimetry*

Using a dry drilling operation, shavings from the chemistry chill samples were created for differential scanning calorimetry (DSC) testing. Metal shavings were used instead of excised solid samples in an effort to minimize any effects that segregation and coarse microstructure may have on the test results. Each sample was tested against a Ni reference at heating and cooling rates of 10 $^{\circ C}/_{min}$ in an alumina crucible under an argon gas cover set at a flow rate of 80 $^{ml}/_{min}$. Tests were conducted by the analytical lab at Cannon-Muskegon Corporation using a Netzsch 404 DSC/DTA. For the reasons previously discussed, each chill sample was tested in duplicate, using a mass of shavings weighing between 70 and 100 mg.

Interpretation of the thermal events recorded via DSC testing was carried out on the raw numerical data. Interpretation of the thermal events was consistent with the previous DTA investigations and the thermogram interpretation key provided in Figure 31.

# V. RESULTS

This section presents the results discovered from the HTTV casting trials. The data described in this section was compiled and statistically analyzed; those results are detailed in Section VI. The results of the VTB castings will be provided and discussed in Section VII.

## A. Hot Tears

The HTTV castings showed significant differences between metal lots in the severity of the separation defects generated for bars of identical length. Some HTTV bars tore so severely that bars became completely dissociated from either the downsprue or the outer feeder. In other cases, only relatively minor tears developed in even the longest bars, despite the fact that the HTTV casting was designed to deliberately create tearing defects. The production casting results for hot tearing were confirmed with the HTTV castings; very different propensities for hot tearing were realized from ML compositions that conform to both the specification and the established engineering control limits.

To facilitate statistical analyses and objective comparison of hot tearing performance between metal lots, an initial hot tear severity rating (HTSR) system was developed and is described in Equation 14. For fully separated tears, an arbitrary value that was larger that that of

$$\underset{ML}{HTSR}' = \sum_{Bar1}^{Bar6}\left[\sum_{i}^{No.tears}\left(length_{tear}\right)_i * \left(width_{tear}^{\max}\right)_i\right] \tag{14}$$

the widest connected tear was needed to properly complete the equation. Although this rating system is very similar to the one used by Cao and Kou, [42] finding a reasonable width value to assign to fully separated bars without overpowering the results and still providing adequate

sensitivity for the investigation proved to be impossible with only 18 data points. Assigning arbitrary values as Cao did for the location factor in his semi-continuous rating system may have been successful for a large sample size, multiple alloy investigation, but in this case the approach proved to overpower the sensitivity of the HTSR assessment. Lin and coworkers [34] adopted a similar approach and assigned a subjective multiplier for hot tear severity, however without quantified hot tear severity data, the fidelity of any subsequent statistical analyses would be highly suspect.

Zhang and Singer [36] developed a different version of Equation 14 and divided the product of the length and width of each tear by the length and circumference of their test casting, effectively normalizing each tear against the geometrical influence the casting has over the tendency to create a hot tear defect. In the case of the HTTV however, the small sample size and the need to assign a width value to fully separated tears continued to be points of contention. The relatively simple HTSR rating system described in Equation 15 proved to be the most viable and

$$\underset{ML}{HTSR} = \sum_{Bar1}^{Bar6}\left[\sum_{i}^{No.tears}\left(length_{tear}\right)_i\right] \tag{15}$$

sensitive solution. Hot tear defects on both sides of each bar were assessed, thus ensuring the more severe through-wall and separated tears automatically received an equitable increase in influence over the rating. The results of the HTSR for the Phase II and Phase III HTTV castings are provided in Figure 34.

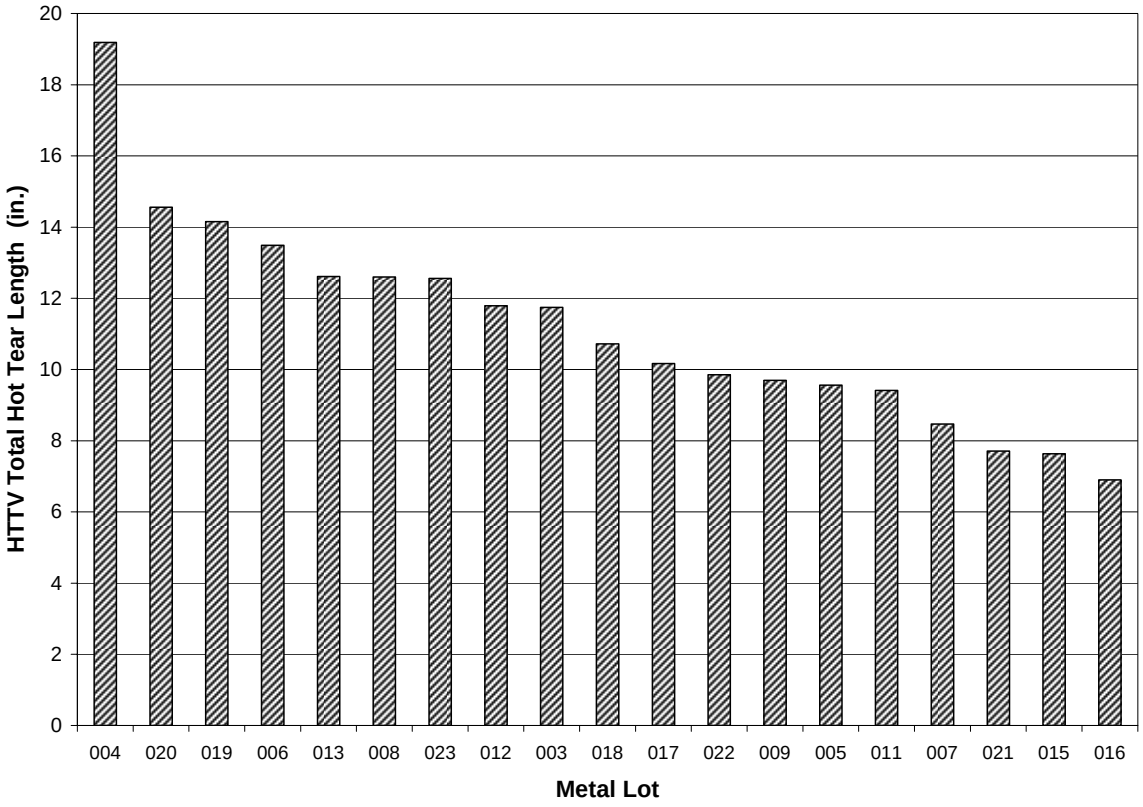


**Figure 34.** HTSR (total hot tear length) versus metal lot for all Phase II and Phase III HTTV castings.

All HTTV metal separation defects occurred adjacent to one or both of the inner downsprue or outer feeder fillet radii. Although metal separation defects did not occur at every hub or riser fillet, the general location of the defects aligned with the last areas to solidify as predicted by the ProCAST™ solidification simulation and also agreed with the ProCAST™ stress model predictions. Figures 35 and 36 illustrate the typical locations and the range of hot tear severity observed in this investigation. Selected views of the ProCAST™ simulations are shown in Figure 37 and in Figure 38.

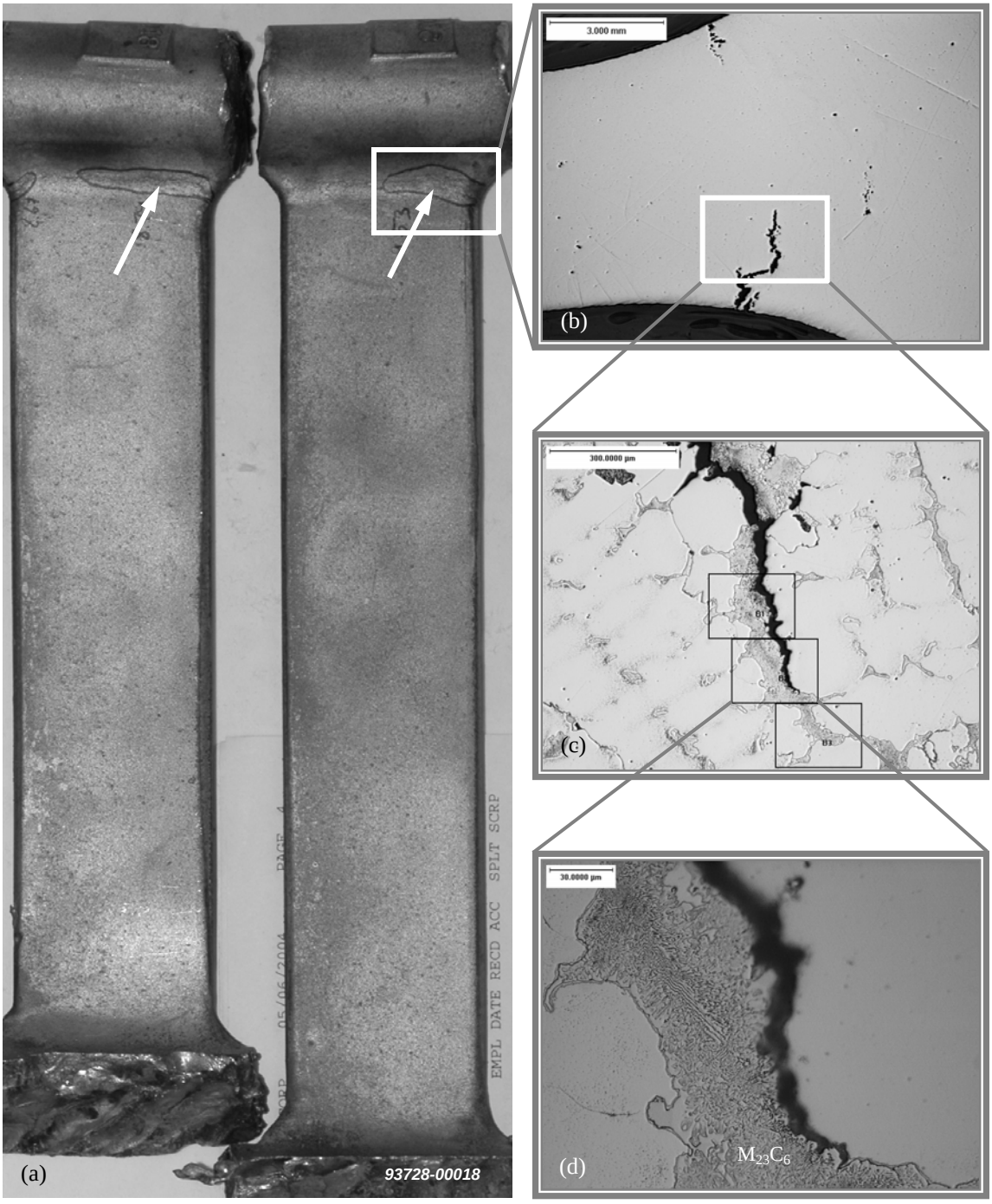


**Figure 35.** (a) Photograph of the two longest HTTV bars from a ML that tore the least. (b) Section through hot tear, as-cast and as-polished condition, approximately 0.52x magnification. (c) View of tip of hot tear clearly showing separation taking place between the grain boundary and the eutectic liquid. 100x magnification (d) View of the $M_{23}C_6$ eutectic carbide at the tip of the hot tear taken at 500x magnification.

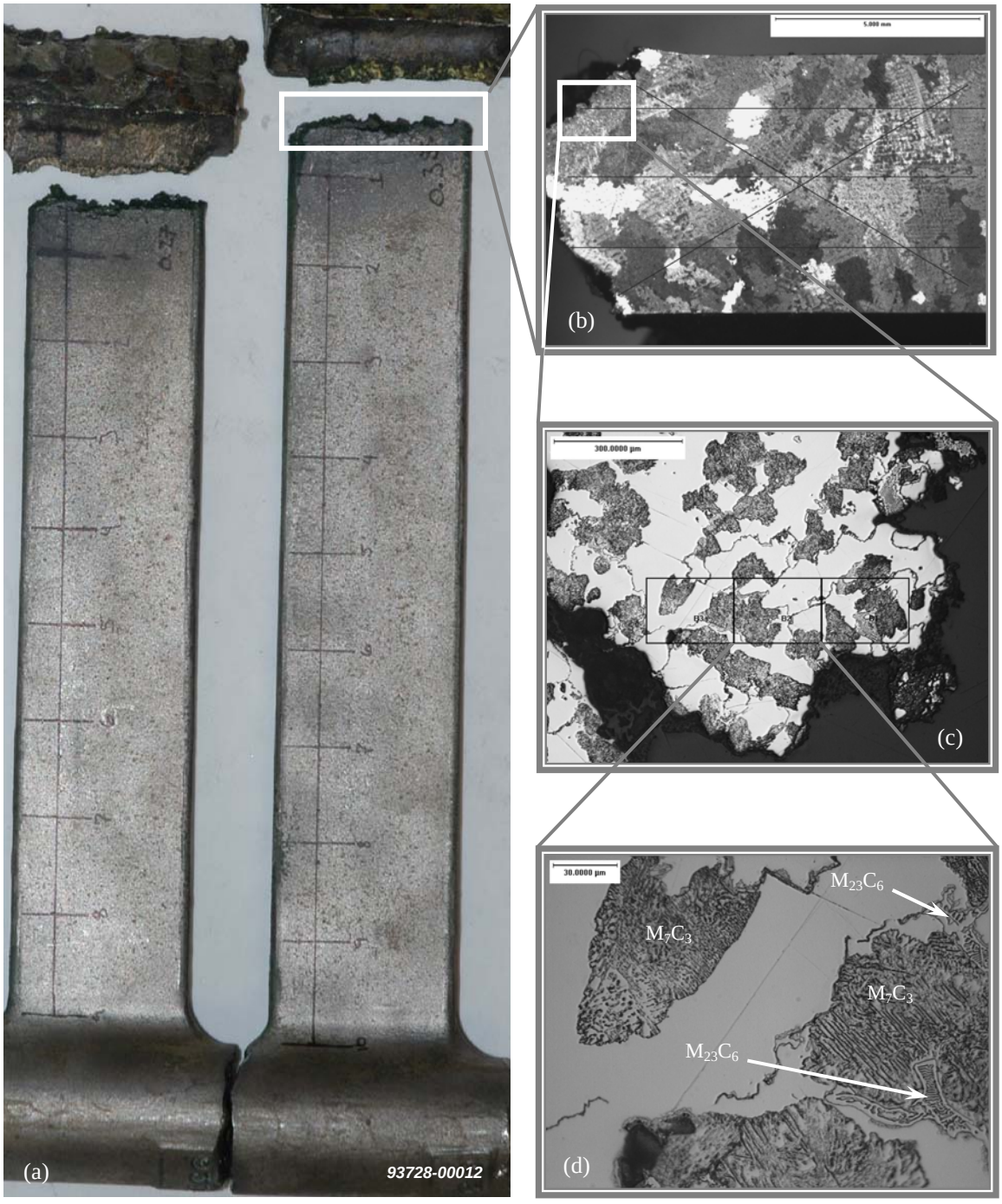


**Figure 36.** (a) Photograph of the two longest HTTV bars from a ML that tore most severely. (b) Section through hot tear, as-cast and grain etched condition, approximately 0.52x magnification. (c) View of area adjacent to the hot tear clearly showing separation taking place along grain boundaries. 100x magnification (d) View of the $M_7C_3$ and $M_{23}C_6$ eutectic carbides adjacent the hot tear taken at 500x magnification.

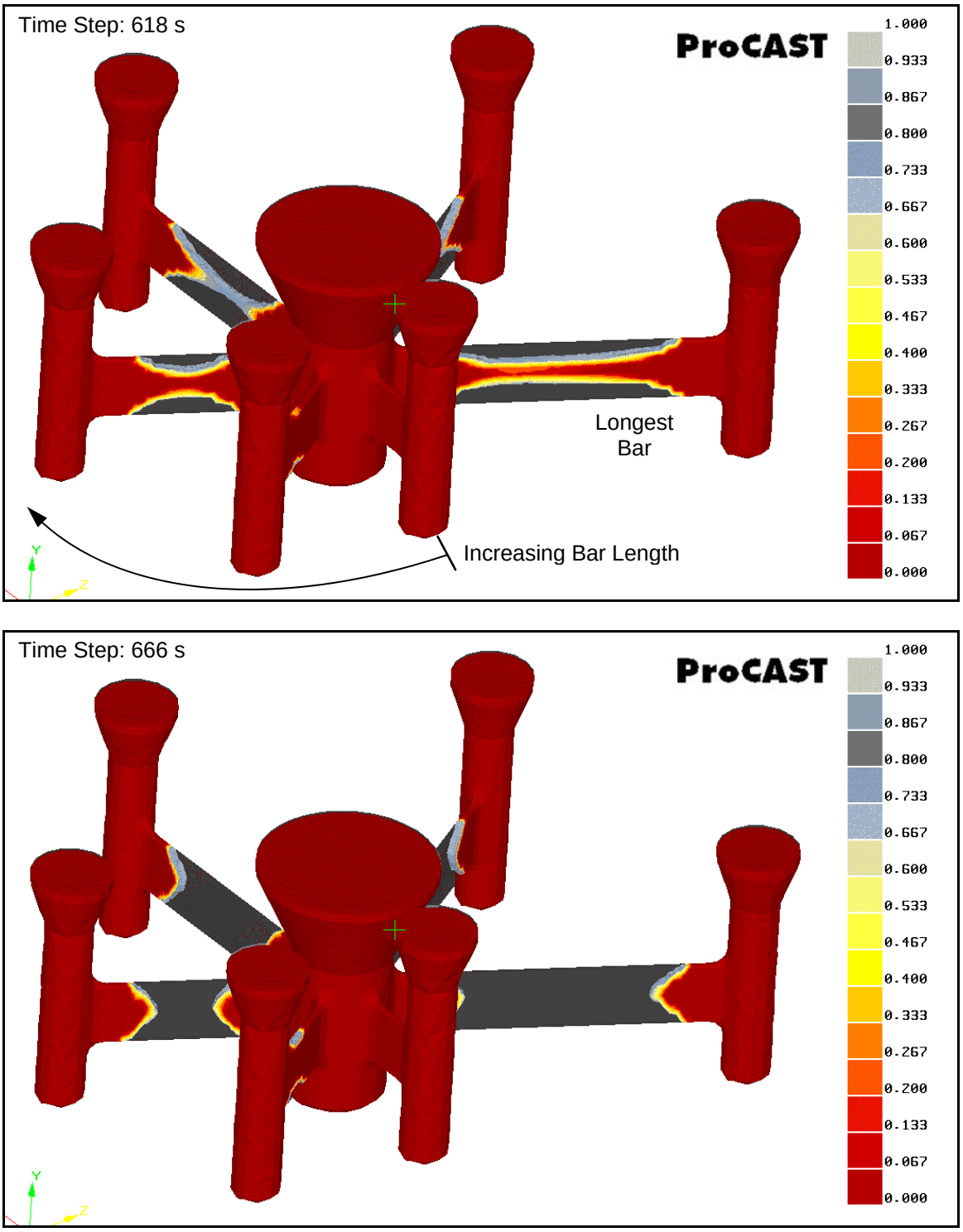


**Figure 37.** Results of ProCAST™ solidification simulation for the HTTV. The numbers adjacent to the colour scale on the right hand side represent fraction solid. The simulation shows the bars solidify from top and bottom at the center of the bar, then toward the feeder and downsprue with a much steeper solidification rate and gradient.

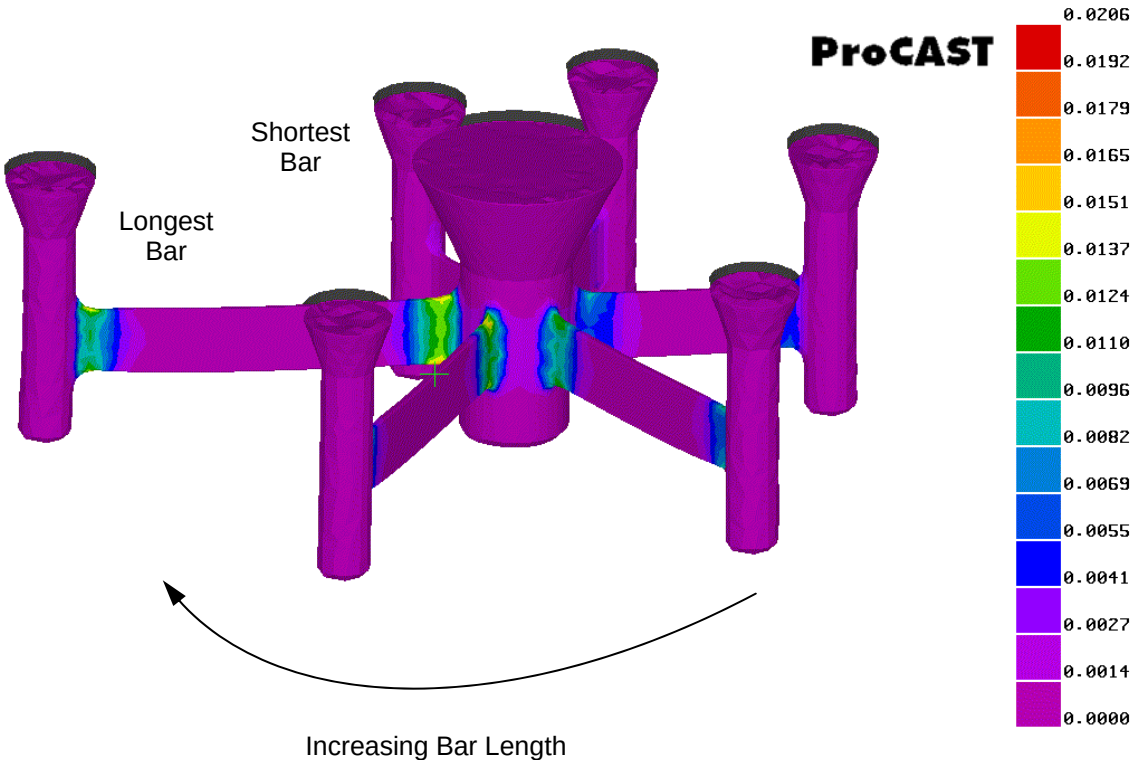


**Figure 38.** Results of ProCAST™ hot tear indicator for the HTTV. The numbers adjacent to the colour scale on the right hand side represent a relative probability of hot tear occurrence. The two shortest bars both show less than 0.005 probability in all areas. From Reference [63].

The scanning electron microscopy (SEM) analysis of the fracture surface of a more severely torn HTTV casting confirmed the absence of crystallographic features and the presence of liquid at the time of metal separation. These observations confirm the HTTV metal separation defects are indeed hot tears, as defined by the results of many different researchers previously discussed. Figure 39 illustrates the lack of crystallographic features on the fractured surface while Figures 40 and 41 show clear evidence of the presence of liquid at the time of separation.

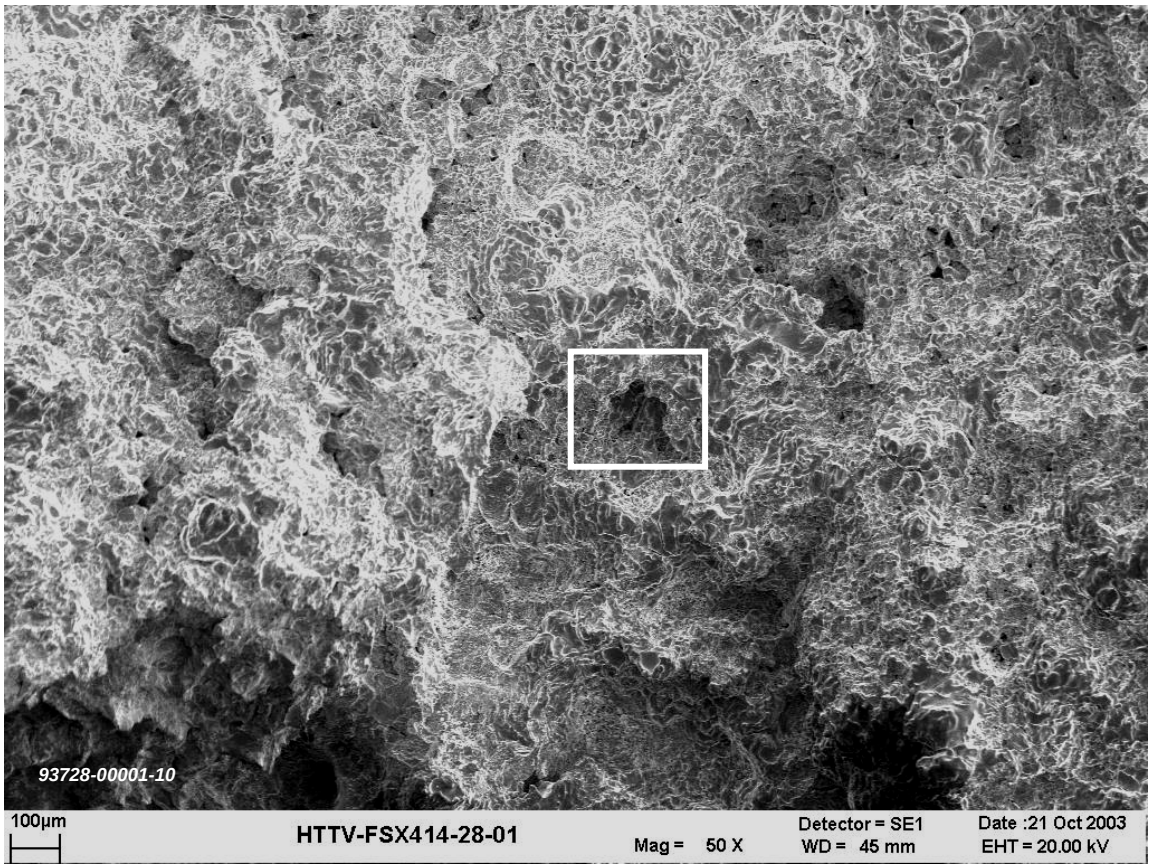


**Figure 39.** SEM image of the fracture surface of a hot tear. No crystallographic features are present. Outlined area viewed at higher magnification in Figures 40 & 41.

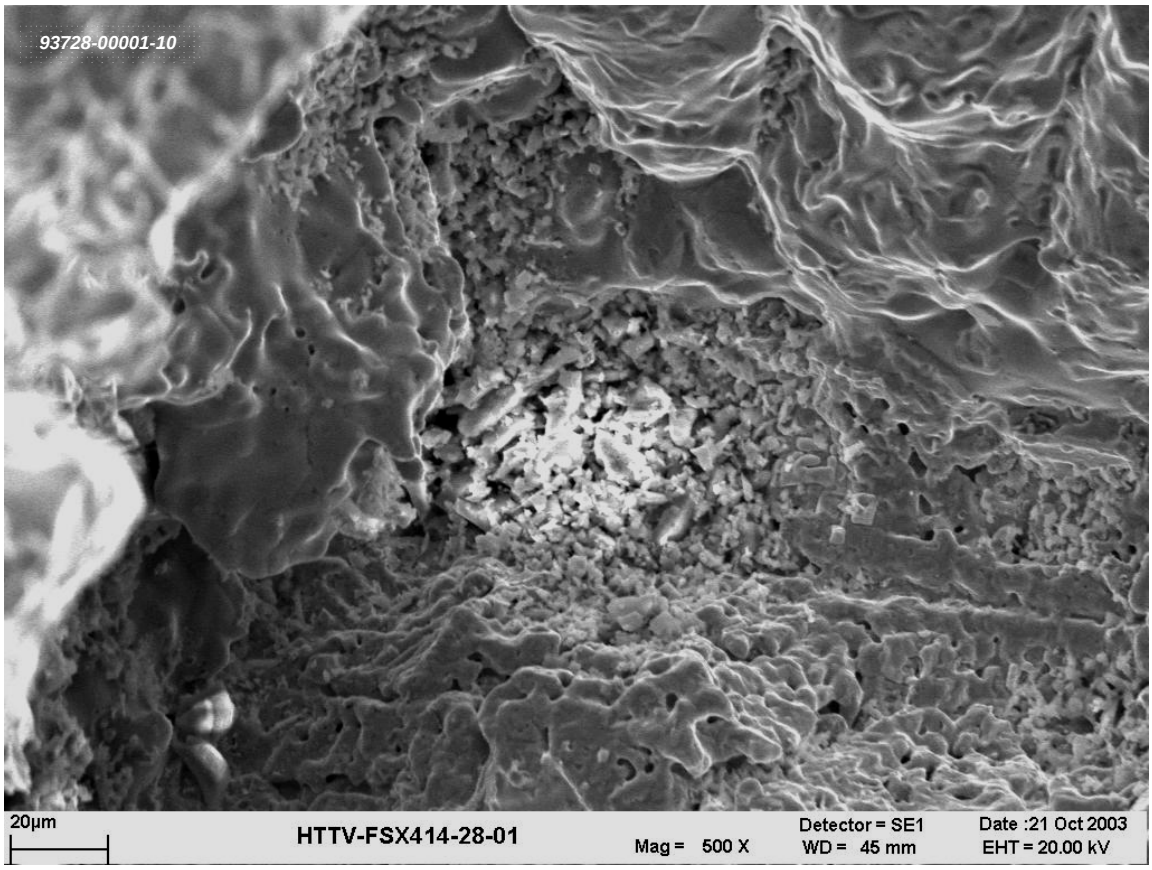


**Figure 40.** Higher magnification SEM image of the outlined portion of the hot tear surface shown in Figure 39. Smooth surfaces clearly show presence of liquid at the time of separation.

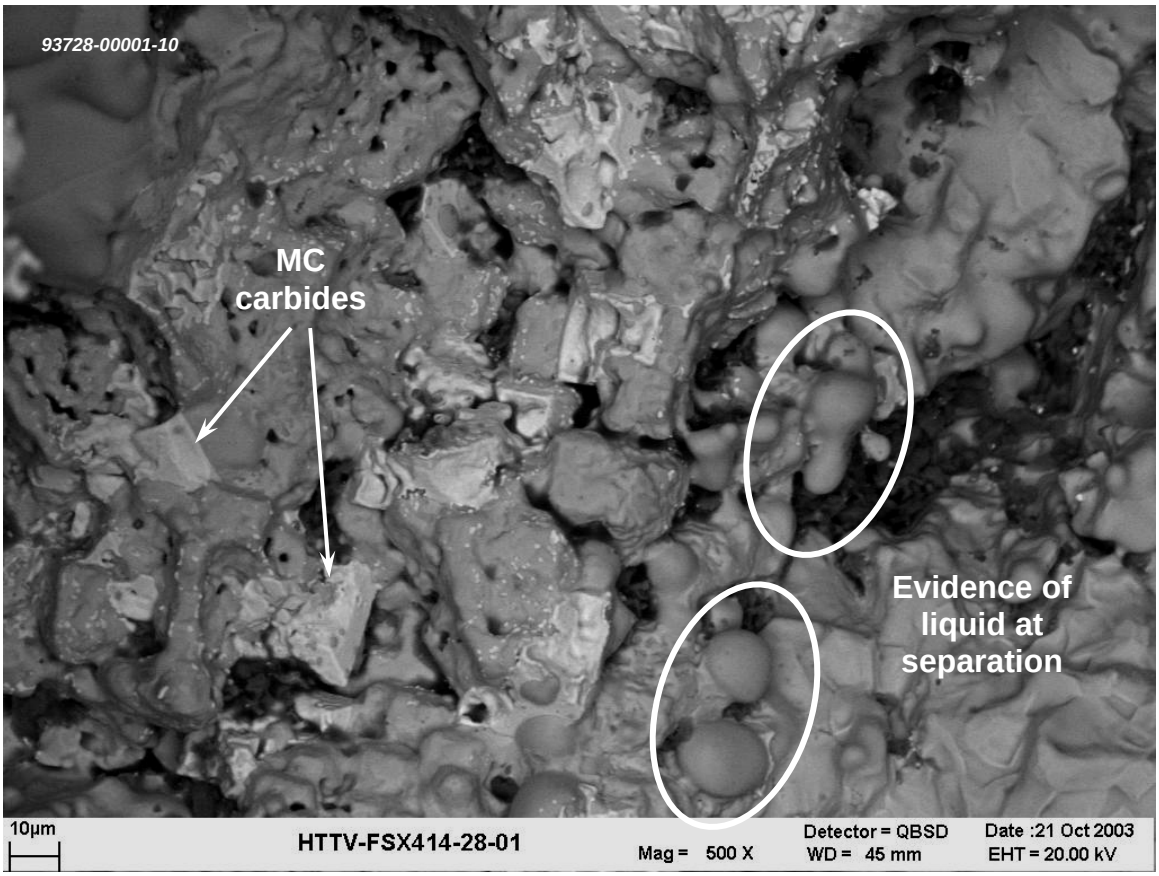


**Figure 41.** Higher magnification backscattered SEM image of another area of the surface shown in Figure 39. Evidence of both liquid and primary MC / $M_6C$ carbides precipitated early in the solidification sequence are observed.

Each metal separation defect examined from the HTTV castings progressed along interdendritic paths. As one would expect from previous discussions on hot tear formation and growth, one or both sides of every tear was decorated with eutectic carbide. However for some hot tears, the carbides remaining within tear appeared well bonded to one side, leaving no evidence of eutectic liquid on the opposite side. Although in Campbell's explanation [13] this may simply be a case of the remaining eutectic liquid having drained from the separated area, the presence of the large island of well-formed and adherent carbide on the opposite side does not agree with this theory. It would instead suggest that the tear formed at an extremely high fraction solid ratio, perhaps above 0.99 $f_s$ as Zhang and Singer [36] indicate. This assumedly, would be the

result of having extremely thin films of residual liquid remaining which would not be visible with transverse optical microscopy, perhaps of a composition different to that of the interdendritic eutectic carbides and formed via the rejection of solute during the solidification of the eutectic. Lin and Sekhar's [32] experiences with incipient melting in cobalt-based alloys and René 108 support this possibility. Considering the solidification and stress models in Figures 37 and 38, one could conceive sufficient strain accumulating in the hot tear prone areas due to solid contraction through the middle of the bar to provide enough activation energy for a tear to form very late in the solidification sequence. Figures 42 and 43 provide examples of hot tears with single- and double-sided evidence of eutectic carbide.

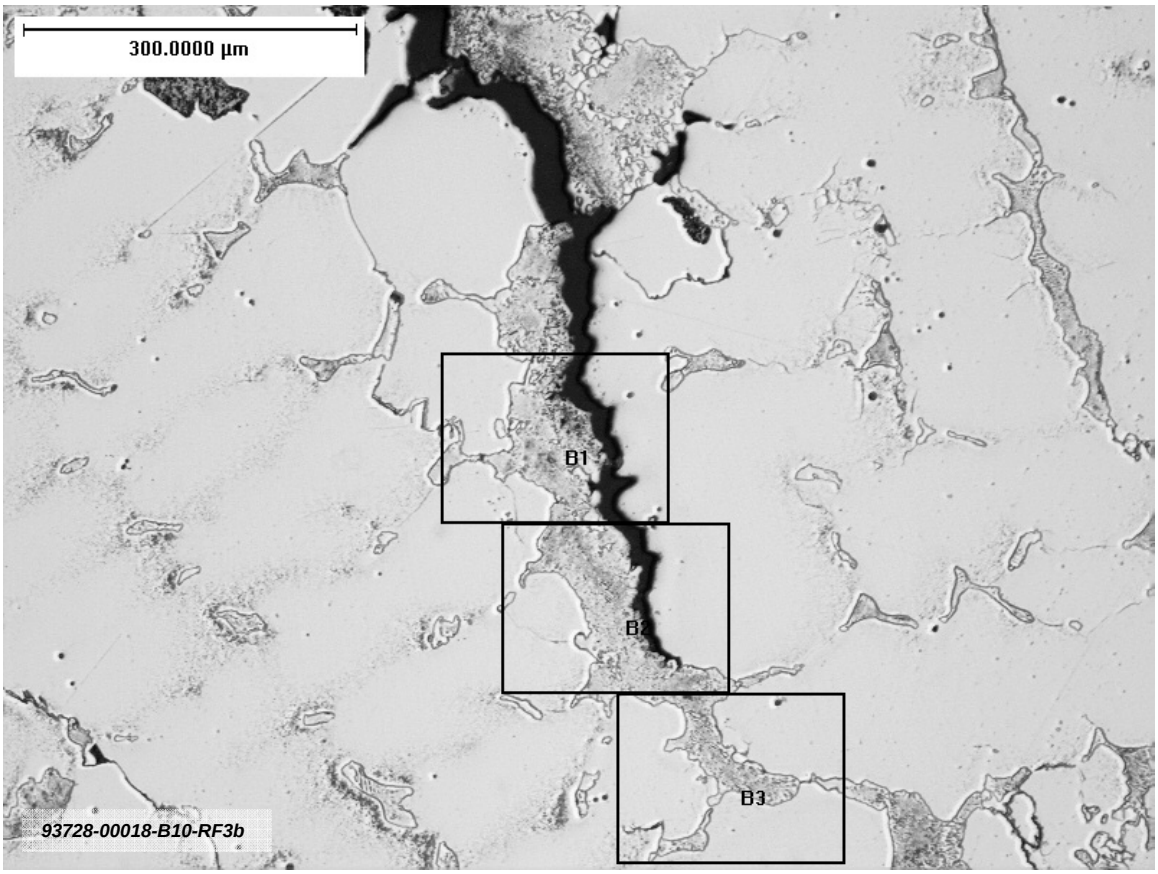


**Figure 42.** Hot tear tip with little or no evidence of eutectic carbide on one side of the tear. Also note that in some areas, the two sides of the tear fit together well, suggesting a very high $f_s$ at separation.

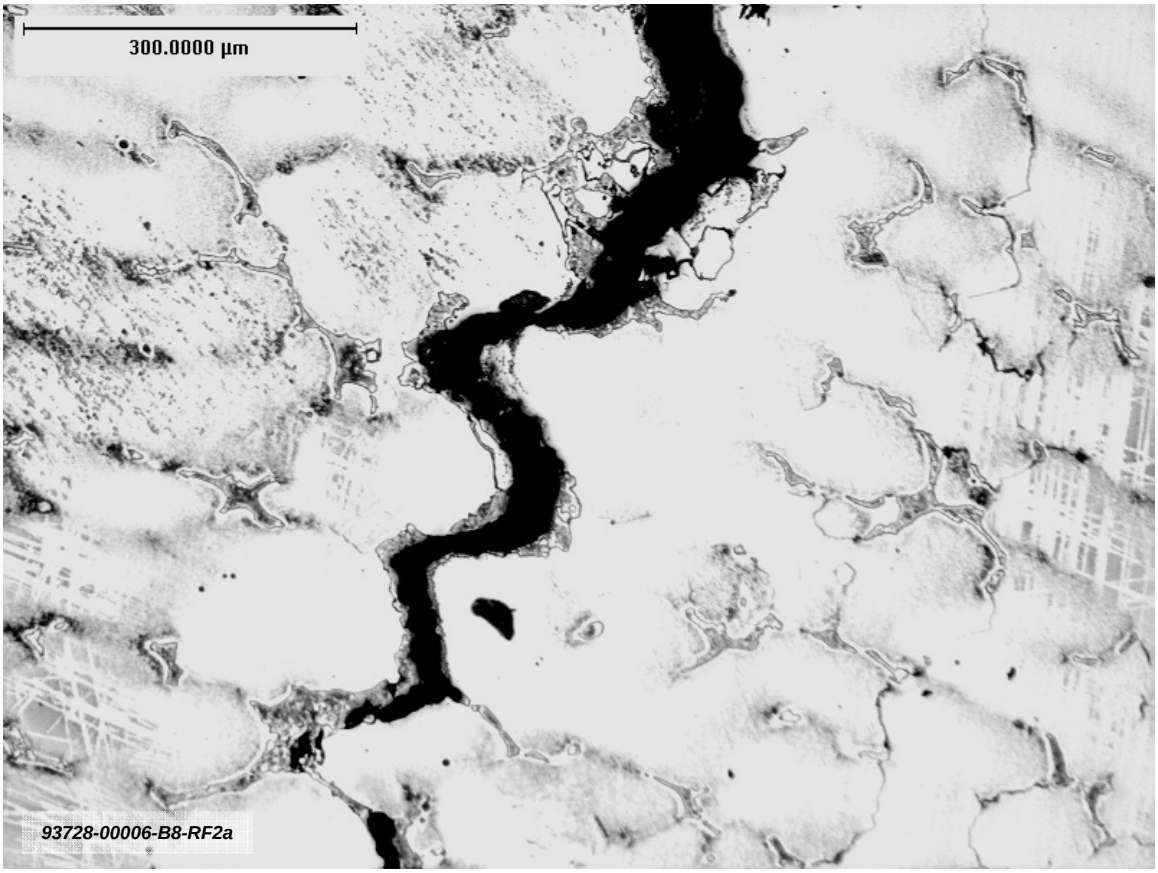


**Figure 43.** Hot tear tip with significant evidence of eutectic carbide on both sides of the tear. This tear has significantly less opportunity to cleanly fit the two sides of the tear back together.

There were also marked microstructural differences observed in the areas surrounding hot tears. Specifically, there were differences in the volume and/or morphology of the eutectic carbides. The volume difference can be seen clearly when comparing the tear shown in Figure 44 with that shown in Figure 45. The interdendritic carbides adjacent to both of these tears are elongated in shape with length to width ratios in excess of 10:1. However Figure 44 shows carbides along the surfaces of the hot tear and within the microstructure adjacent to the tears that are massive, almost spherical islands of $M_7C_3$ rather than the more commonly occurring $M_{23}C_6$ shown in Figure 45.

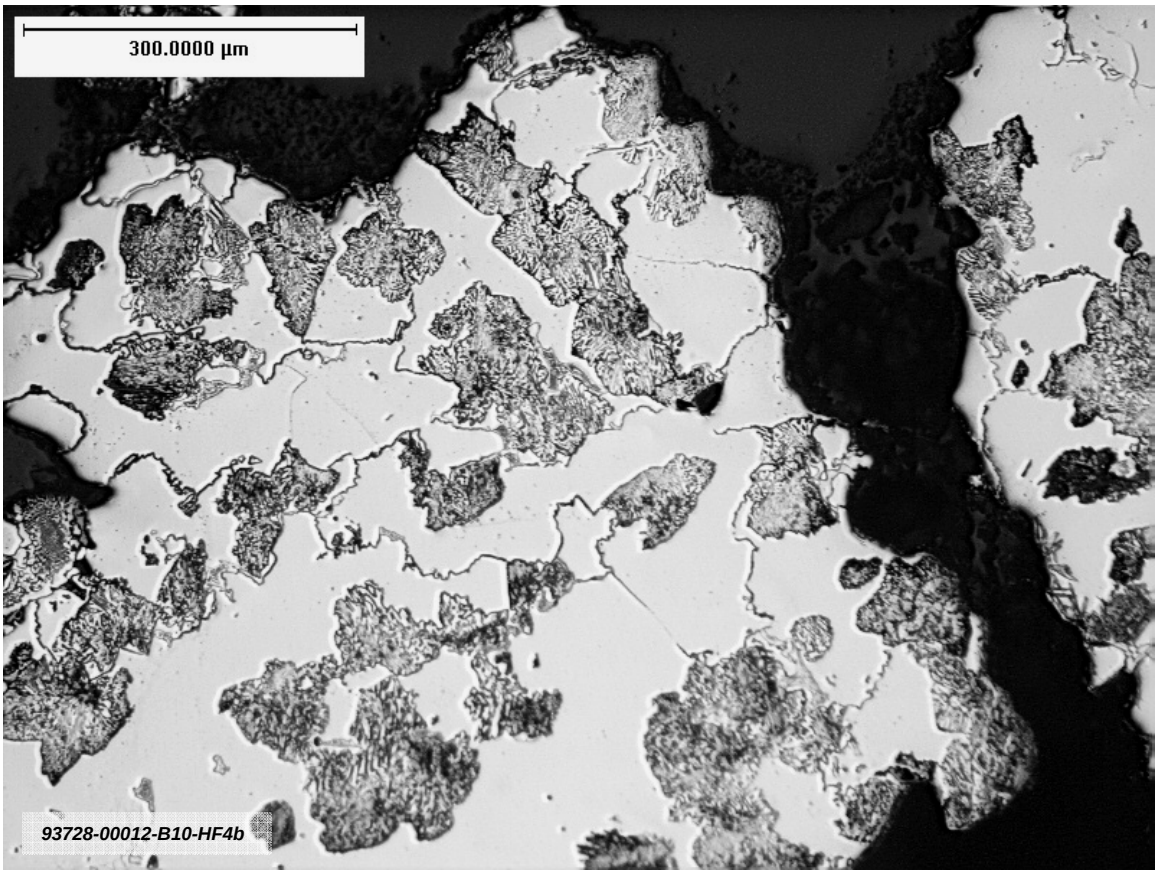


**Figure 44.** Hot tear decorated with large, rounded islands of $M_7C_3$. The adjacent microstructure contains carbides of identical morphology.

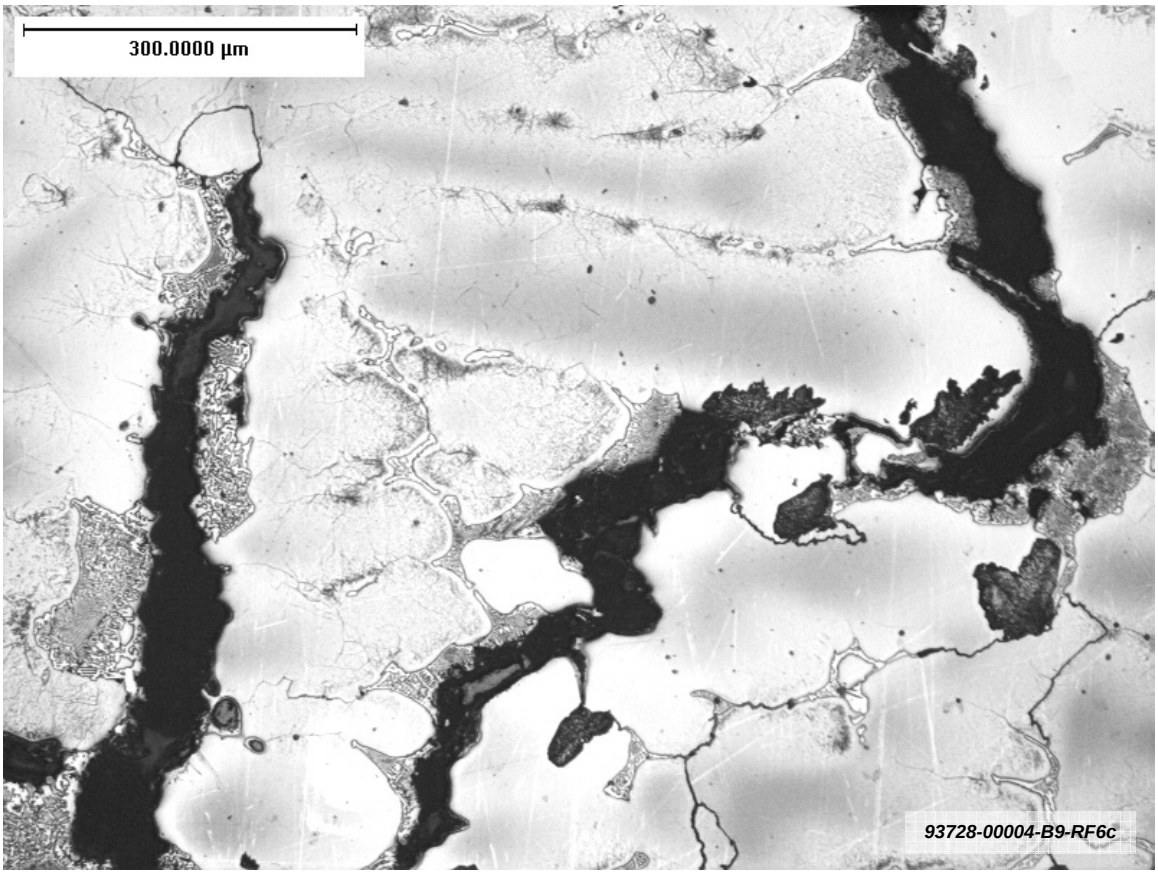


**Figure 45.** Hot tear decorated with large, elongated islands of $M_{23}C_6$. The adjacent microstructure contains carbides of identical morphology. The overall volume fraction of carbide is considerably less than what is present in the sample shown in Figure 44.

## B. Microporosity

The severity of microporosity developed between metal lots was as widely varied as the hot tear results. The HTTV porosity defects typically appeared as layer porosity rather than as evenly dispersed interdendritic sponge, which correlates with the results typically seen in affected production castings. The micrographs in Figure 46 provide examples of the range in microporosity developed between master heats.

A quantitative porosity rating system was used to objectively evaluate and statistically analyze the microporosity performance of the individual metal lots. The semi-continuous microporosity rating (SCMPR) for each metal lot was generated using Equation 16 where *%MP* is the maximum percentage of microporosity detected for each continuous microporosity indication and $L_{field}^{\max}$ is the maximum size of the same discrete field of porosity.

$$SCMPR_{ML} = \sum_{Bar\,3}^{Bar\,6}\left[\sum_{i}^{No.\,fields}\left(\%MP\right)_i \times \left(L_{field}^{\max}\right)_i\right] \tag{16}$$

The SCMPR was developed from the quantitative metallographic analyses for the entire length of the four longest HTTV bars. Figure 47 provides an illustrative summary of the SCMPR results obtained for all Phase II and Phase III HTTV castings.

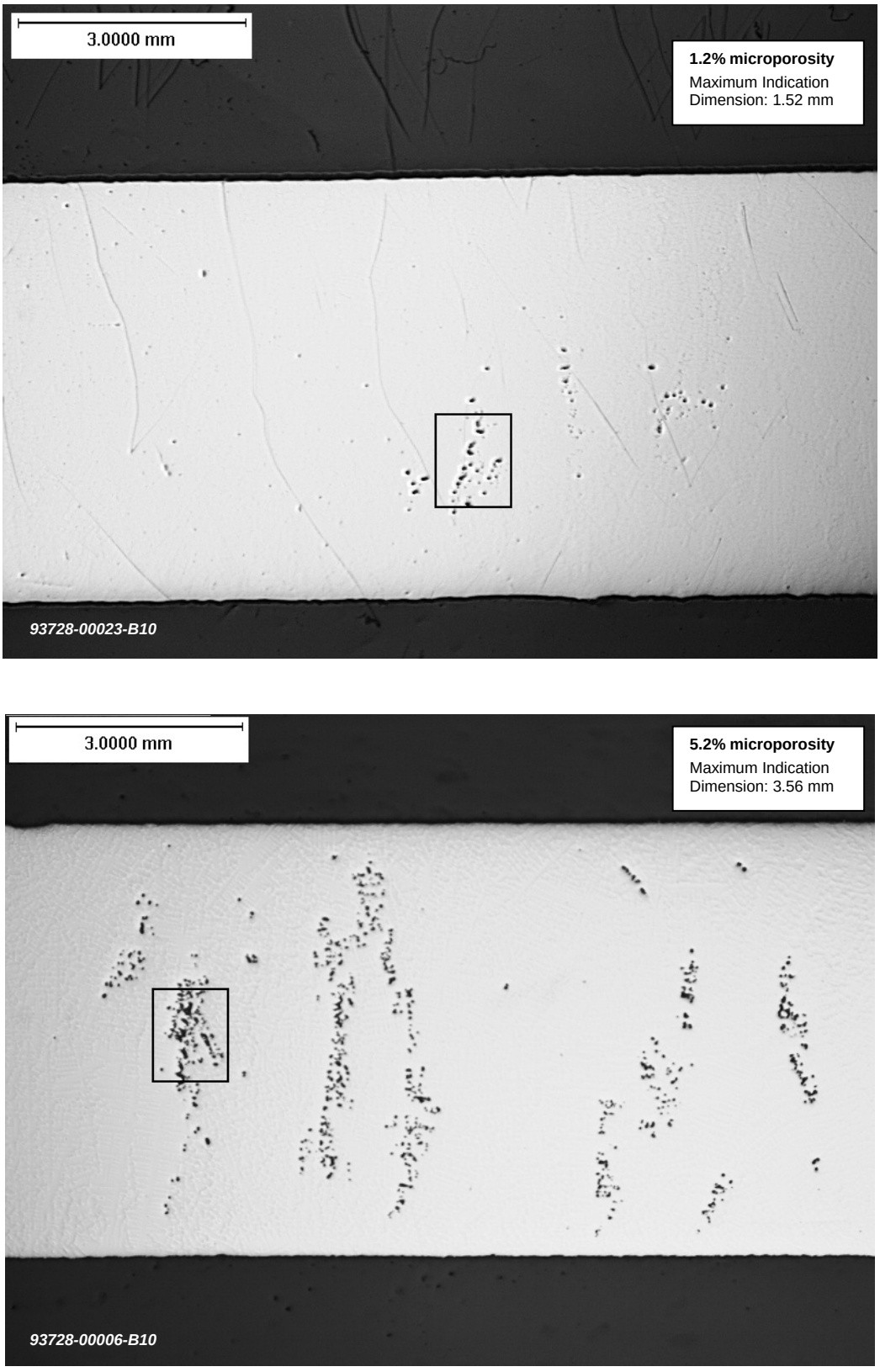


**Figure 46.** Examples of the range in microporosity developed between metal lots in the HTTV castings.

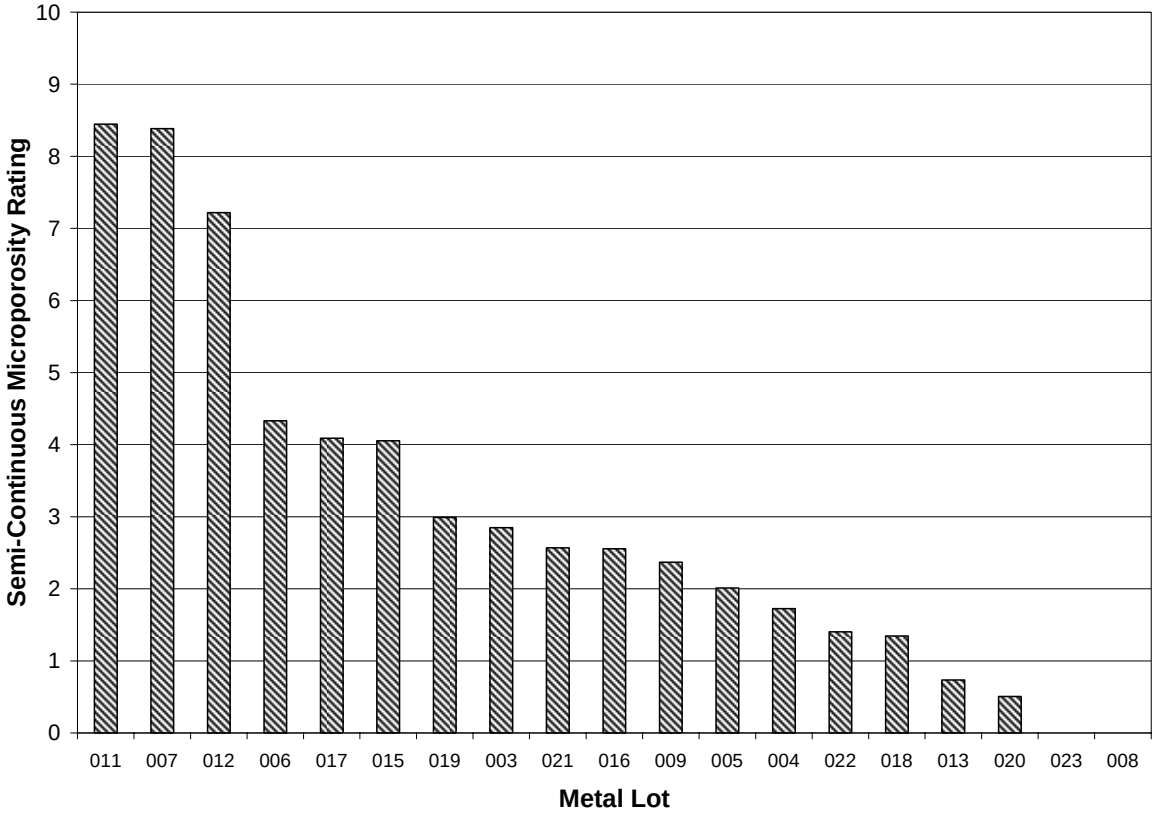


**Figure 47.** SCMPR versus metal lot for all Phase II and Phase III HTTV castings.

## C. Microstructure

*1. Secondary dendrite arm spacing*

The secondary dendrite arm spacing (SDAS) maintained a consistent trend from ML to ML. In each of the four longest bars, the SDAS increased by 40 to 100% between the center portion of the bar and the ends, with the measurements taken at the downsprue fillet radius always being larger than those taken at the feeder fillet radius. On average, the standard deviation across metal lots at any given bar and location was small at 5 to 10 μm; only 8 to 10% of the measured SDAS.

*2. Carbide characterization*

Considerably more variation was found in the distribution and morphology of the carbide structure. Standard deviations for $M_{23}C_6$ grain boundary carbide width varied from 45 to 80% of the average carbide width across all lots. Similarly, the average carbide area fraction in a field of view had a standard deviation of 25 to 50% across all lots for the longest HTTV bar and 45 to 55% for the fourth longest bar. Figures 48 and 49 provide example micrographs of the differences in carbide morphology and distribution described by the quantitative metallography.

The most interesting discovery made during the carbide characterization metallography was the identification of a distinct change in carbide microstructure that occurred near the downsprue and feeder fillet radii. The relative position and length of the transition varied between metal lots. The center of the bars showed what would be considered typical FSX-414 microstructure, dominated with grain boundary and interdendritic $M_{23}C_6$ carbides. Following the transition, $M_7C_3$ became more abundant, the interdendritic $M_{23}C_6$ carbides reduced in number and the $M_7C_3$ coarsened in accordance with the corresponding increase in SDAS. In the most extreme transitions, $M_{23}C_6$ carbides were almost completely replaced with $M_7C_3$. The microstructural transition was more severe closer to the downsprue than the feeder and followed the shape of a chevron which corresponds with the solidification pattern and cooling isotherms depicted in the

solidification simulation results shown in Figure 37. Table 4 provides the details of the carbide transition measurements while Figures 48 and 49 each provide two micrographs taken from the same bar on either side of the transition, illustrating the magnitude of the carbide transition phenomenon. Although establishing a quantitative and definitive explanation for the transition phenomenon was beyond the scope of this investigation, its cause is most likely related to the rejection of differing quantities and compositions of solute ahead of the solidification fronts, as defined by the initial metal lot composition. As the HTTV bars solidify from their centers toward the ends, these differing solute compositions would account for the changes and differences observed in the microstructure created in those areas that are among the last to solidify.

| | Downsprue Fillet | | | Feeder Fillet | | |
|---|---|---|---|---|---|---|
| HTTV Lot Number | Distance from Downsprue | Transition Completion | Width of Transition | Distance from Downsprue | Transition Completion | Width of Transition |
| 93728-00004 | -2.5 | 6.4 | 14.2 | 248.9 | 2.3 | 24.1 |
| 93728-00005 | 2.0 | 3.6 | 12.4 | 247.7 | 17.8 | 17.3 |
| 93728-00006 | -2.3 | 4.6 | 17.5 | 247.7 | 2.5 | 25.1 |
| 93728-00007 | 21.6 | 3.8 | 29.2 | 248.9 | 2.3 | 21.6 |
| 93728-00008 | 4.8 | 1.8 | 4.6 | 246.4 | 3.0 | 4.6 |
| 93728-00009 | -1.3 | 4.3 | 16.5 | 254.0 | 3.8 | 27.7 |
| 93728-00011 | -8.4 | 6.9 | 21.6 | 257.0 | 7.6 | 24.9 |
| 93728-00012 | -7.6 | 6.9 | 24.1 | 251.2 | 3.0 | 15.2 |
| 93728-00013 | 6.4 | 4.6 | 12.7 | 248.9 | 2.5 | 33.0 |
| 93728-00015 | -3.0 | 3.8 | 12.7 | 258.6 | 9.7 | 38.1 |
| 93728-00016 | -3.8 | 7.1 | 24.1 | 251.5 | 5.1 | 20.1 |
| 93728-00017 | -12.7 | 15.2 | 40.6 | 250.2 | 3.0 | 29.5 |
| 93728-00018 | 6.4 | 3.8 | 15.2 | 251.5 | 3.8 | 31.8 |
| 93728-00019 | -6.4 | 7.6 | 30.5 | 251.5 | 3.0 | 34.3 |
| 93728-00020 | -5.1 | 6.4 | 21.6 | 250.2 | 7.6 | 33.0 |
| 93728-00021 | -11.4 | 12.7 | 54.6 | 251.5 | 4.6 | 22.4 |
| 93728-00022 | N/A | N/A | N/A | 247.7 | 3.3 | 20.3 |
| 93728-00023 | -12.2 | 7.6 | 28.2 | 251.5 | 3.8 | 16.0 |

**Table 4.** Carbide transition measurements for each HTTV. All dimensions in millimeters. *Transition Completion* is defined as the point at which the initial microstructural features could no longer be observed.

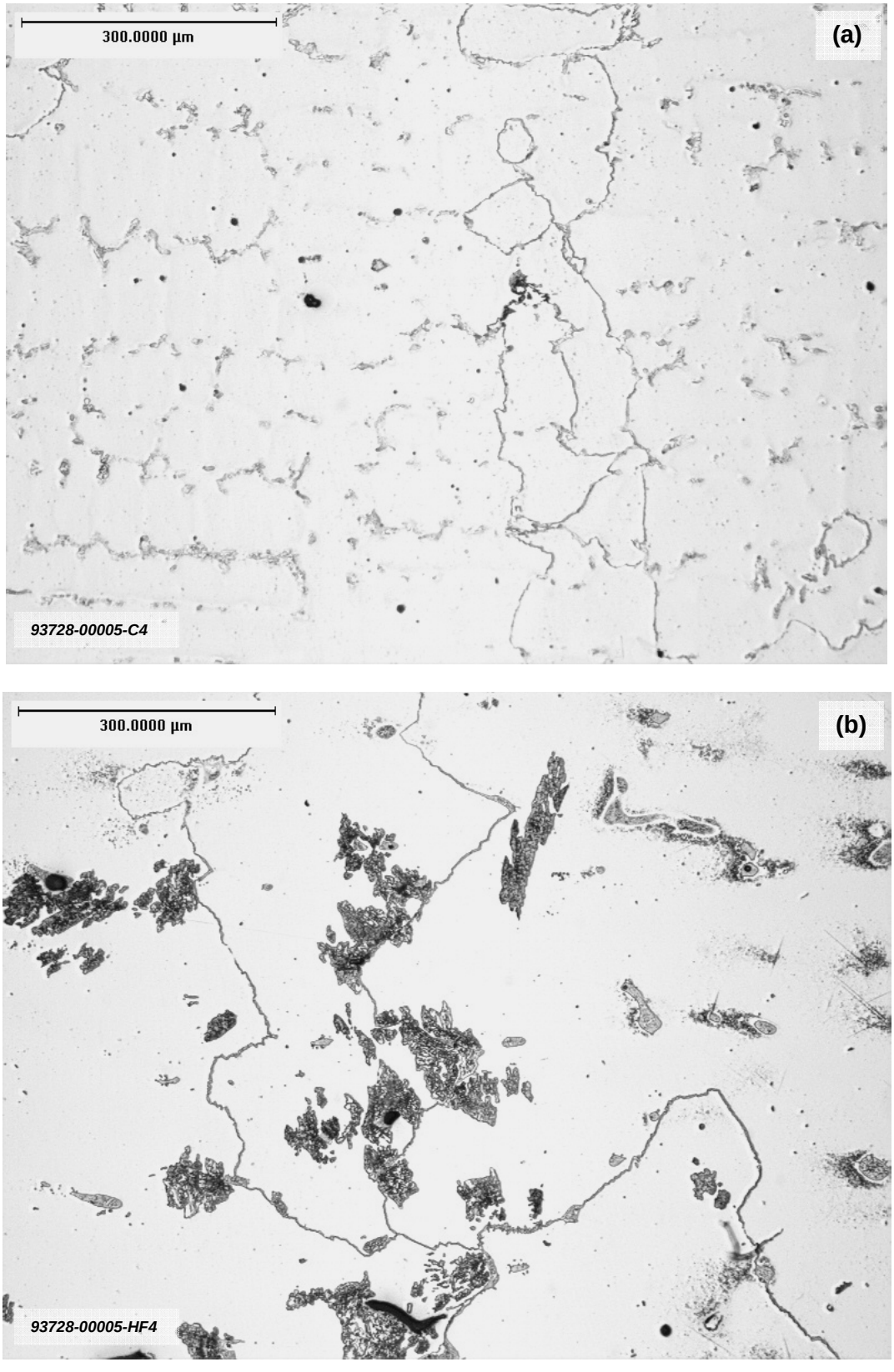


**Figure 48.** Micrographs of the carbide microstructure on either side of a typical carbide transition. (a) Center of longest bar. (b) Same bar, adjacent the downsprue fillet radius. 100x

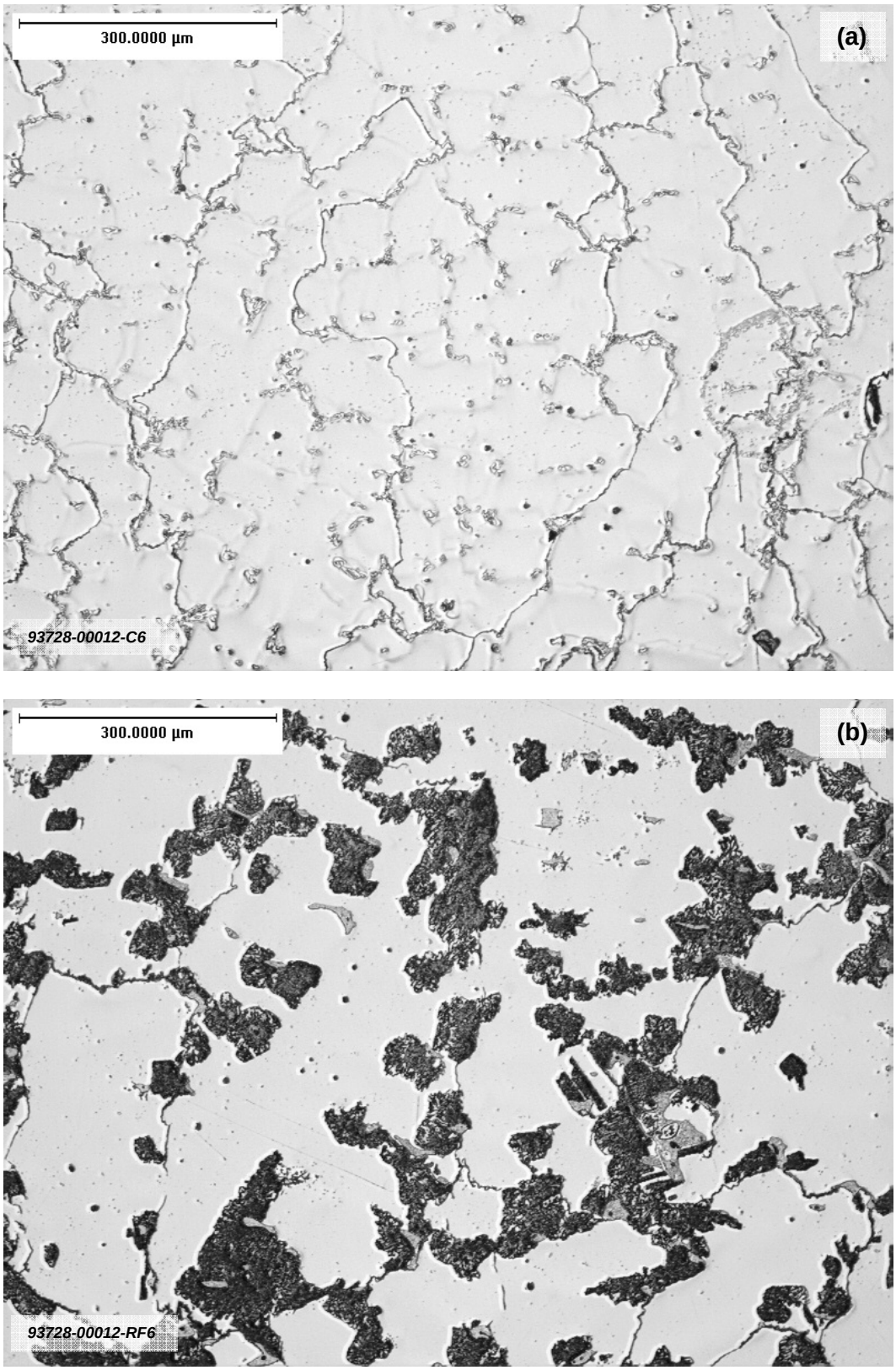


**Figure 49.** Micrographs of the carbide microstructure on either side of a severe carbide transition. (a) Center of third shortest bar. (b) Same bar, adjacent the feeder fillet radius. 100x

*3. Grain size and structure*

In the centers of the HTTV bars, most metal lots showed the typical chill layer of small surface nucleated grains one would expect to occur with a cobalt aluminate inoculated investment face coat, followed by larger grains beneath. Considerable differences in the grain size and structure beneath the chill layer were observed between different HTTV lots. Figure 50 summarizes the average cross-sectional grain size for three positions along the longest HTTV bars from each ML. Although the trend of the bar center having the smallest grain size and the fillet adjacent to the downsprue having the largest grain size is intuitively obvious, the magnitude of the grain size changes from ML to ML was unanticipated. The chart in Figure 51 provides the standard deviation of the average grain size for all HTTV bars by location and ML. This analysis also highlights the substantial difference in cross-sectional grain size developed between metal lots.

Substantial differences in the grain structure were also observed between metal lots in all three areas of the HTTV bars that were evaluated. This was especially evident at the downsprue and feeder fillets where some metal lots produced equiaxed grains in a variety of sizes while others yielded elongated grains that followed the chevron-shaped solidification isotherms pointing toward the center of thermal mass at the bar center and the feeder or downsprue. The micrographs in Figures 52 through 55 provide a comparative pictorial view of the differences in cross-sectional grain size between metal lots.

If the investing process, the casting process and the nucleated surface layer are considered constants, the differences in interior grain structure between metal lots could be influenced by three factors: the effectiveness or amount of heterogeneous nucleation, the width of the MZ and the rate of development of fraction solid versus the normalized width of the mushy zone. Beyond the potential of creating a link to alloy chemistry, developing an in depth understanding of the difference in nucleation kinetics between the metal lots is beyond the scope of this investigation. However when considering Campbell's contention that most of the

solidifying interfaces, such as first-to-form MC carbides, will be well wetted by the liquid, it becomes apparent that some other form of non-wetting particle would either have to form or be entrained and present in order to dramatically influence grain nucleation kinetics. [13] The measured differences in $\frac{df_s}{dT}$ will be discussed in more detail in subsequent discussions.

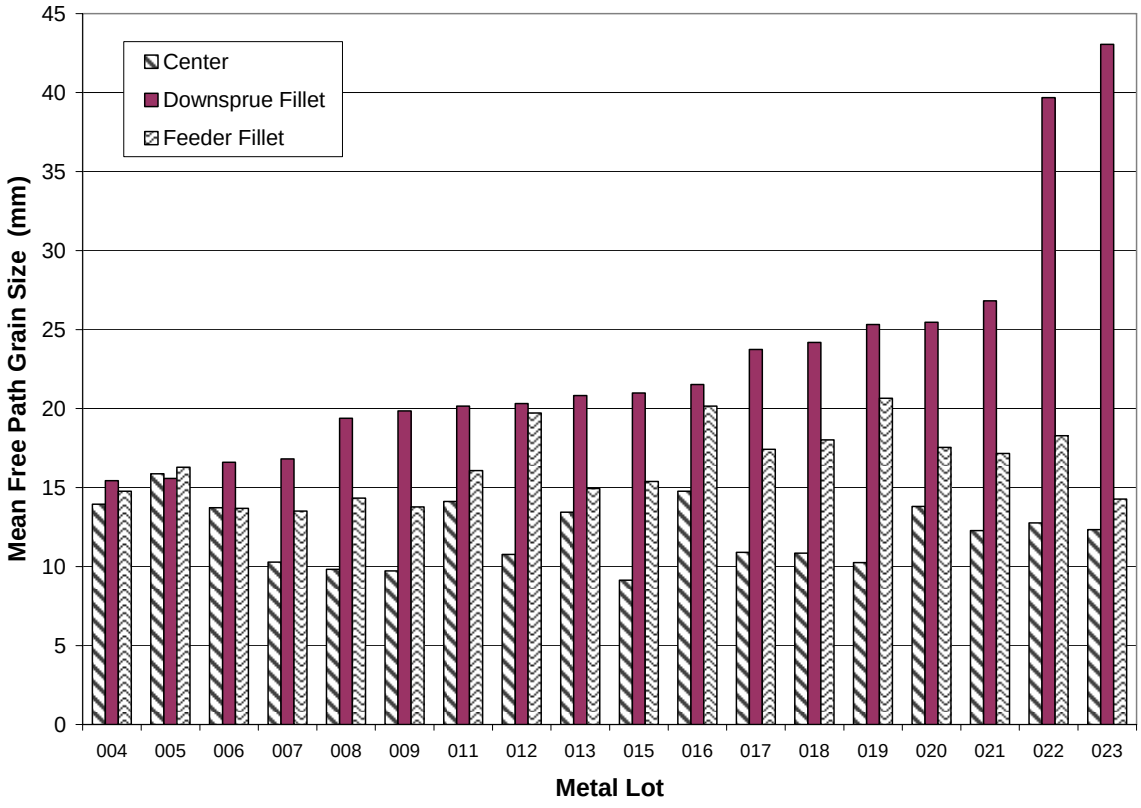


**Figure 50.** Mean free path average grain size for the longest HTTV bar by metal lot.

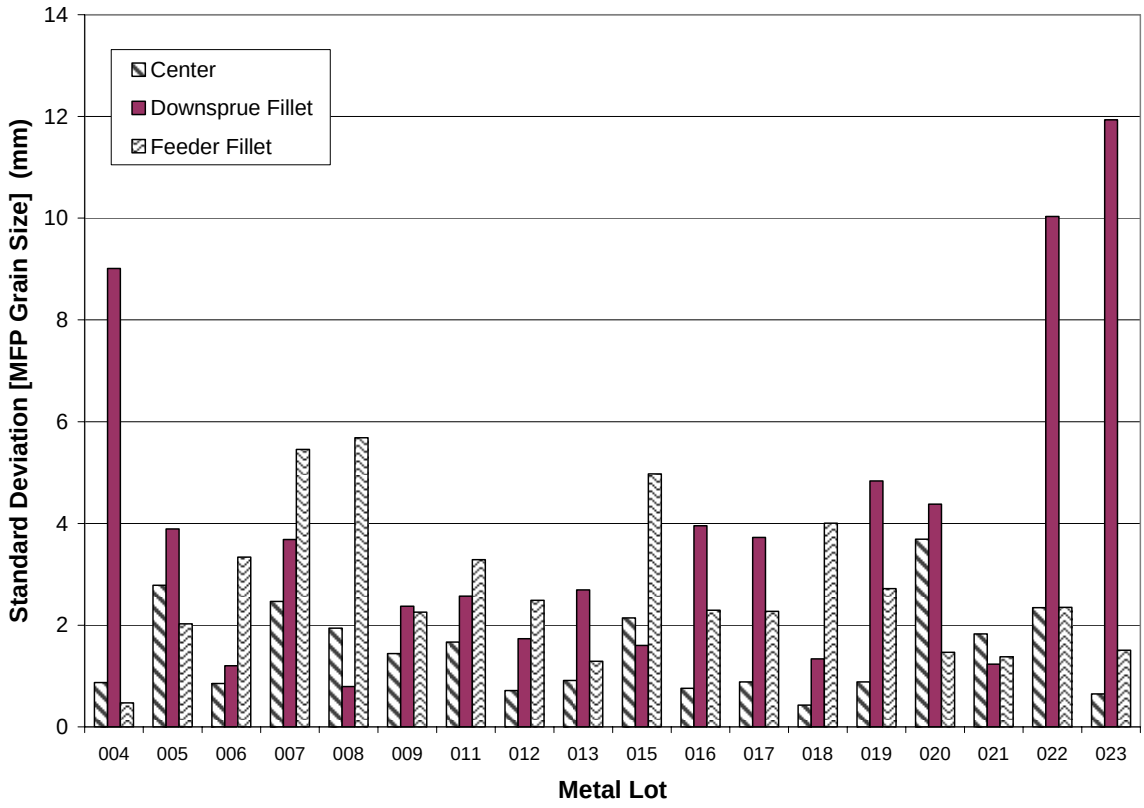


**Figure 51.** Standard deviation of the MFP average grain size across all HTTV bars by metal lot.

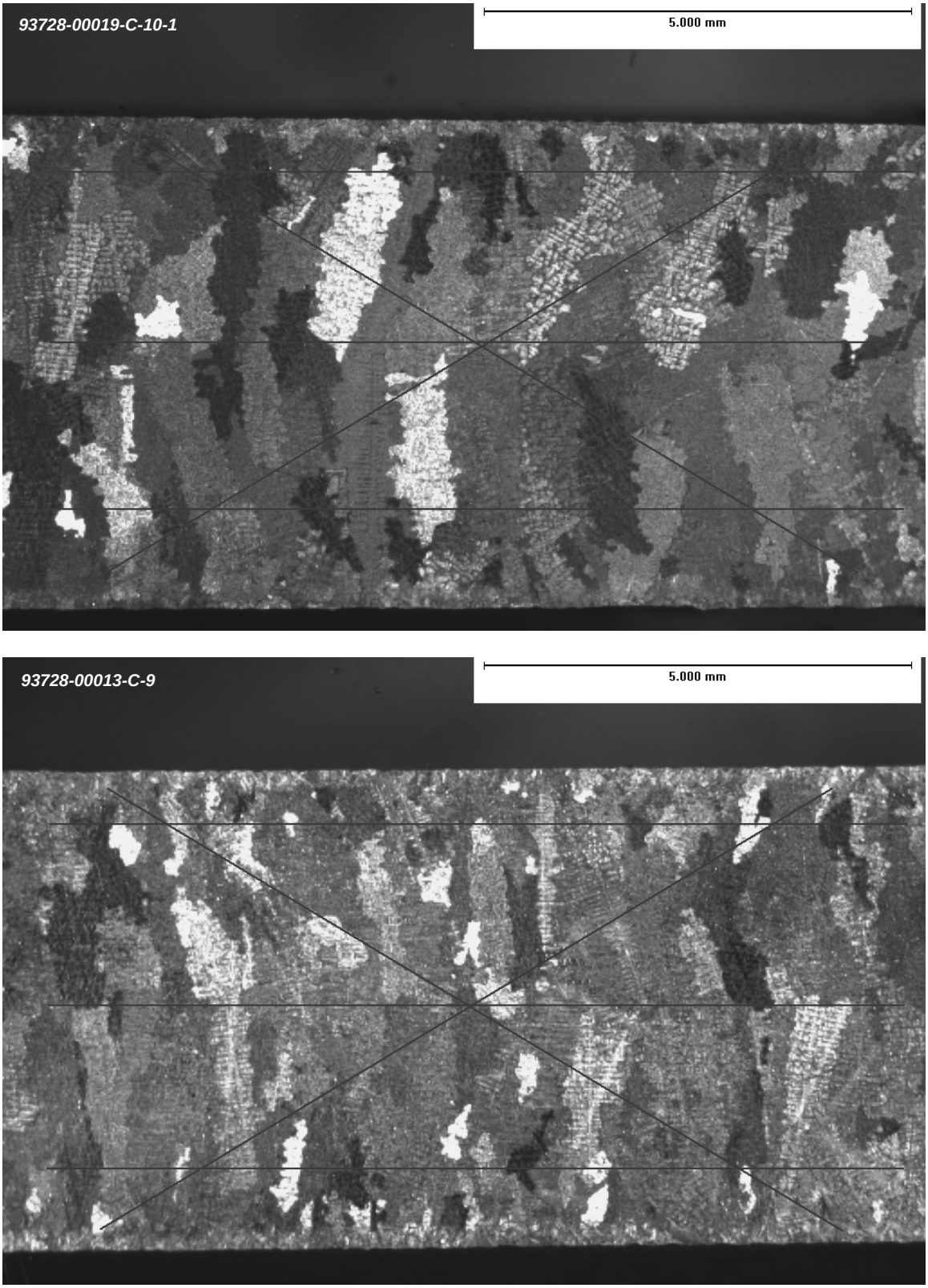


**Figure 52.** Micrographs illustrating the difference in cross-sectional grain size observed between metal lots at the center of the longest two HTTV bars.

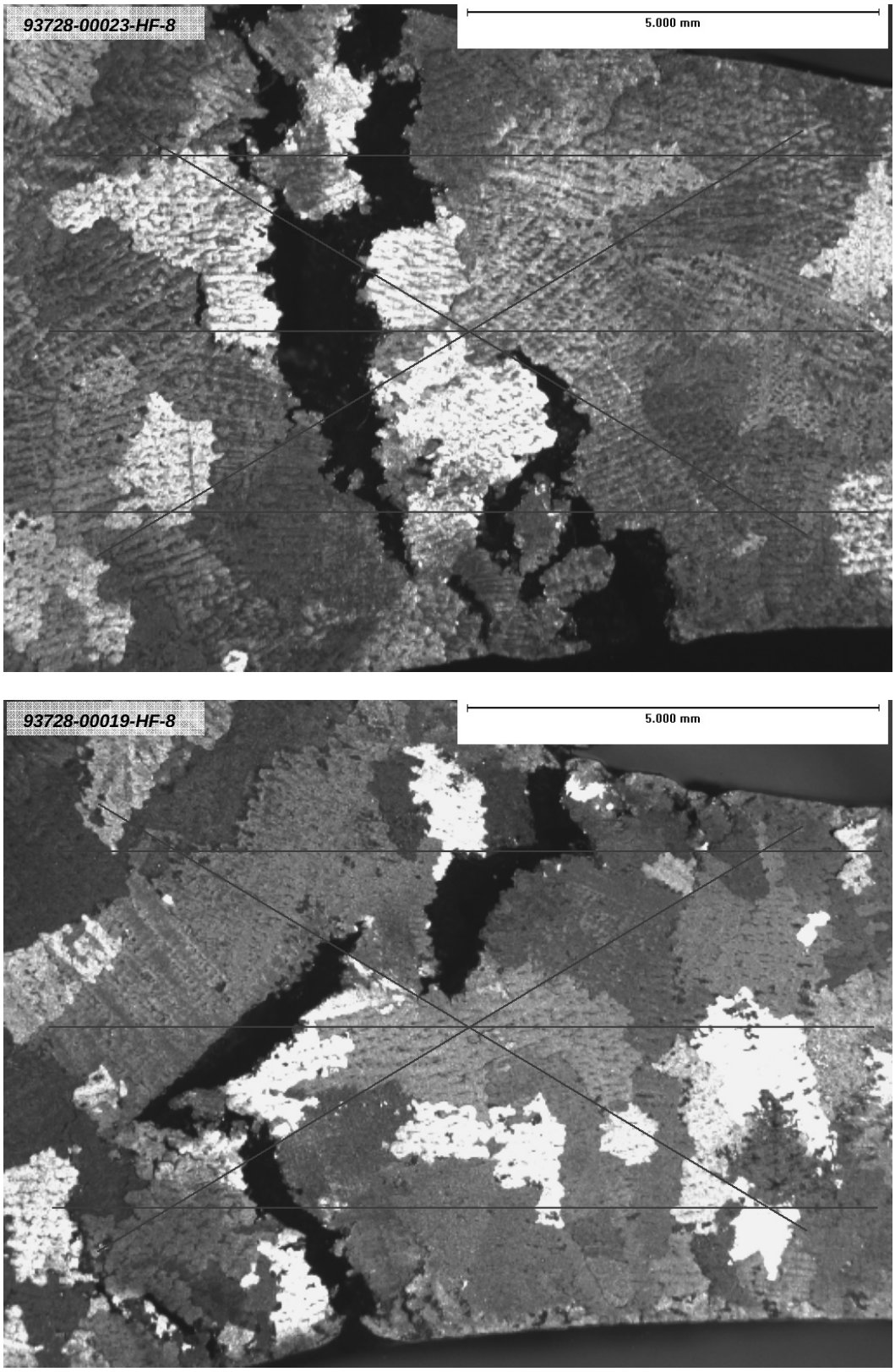


**Figure 53.** Micrographs illustrating hot tears and the cross-sectional grain structure at the downsprue fillet radius in HTTV bars of identical length. Note the irregular structure in the lower example.

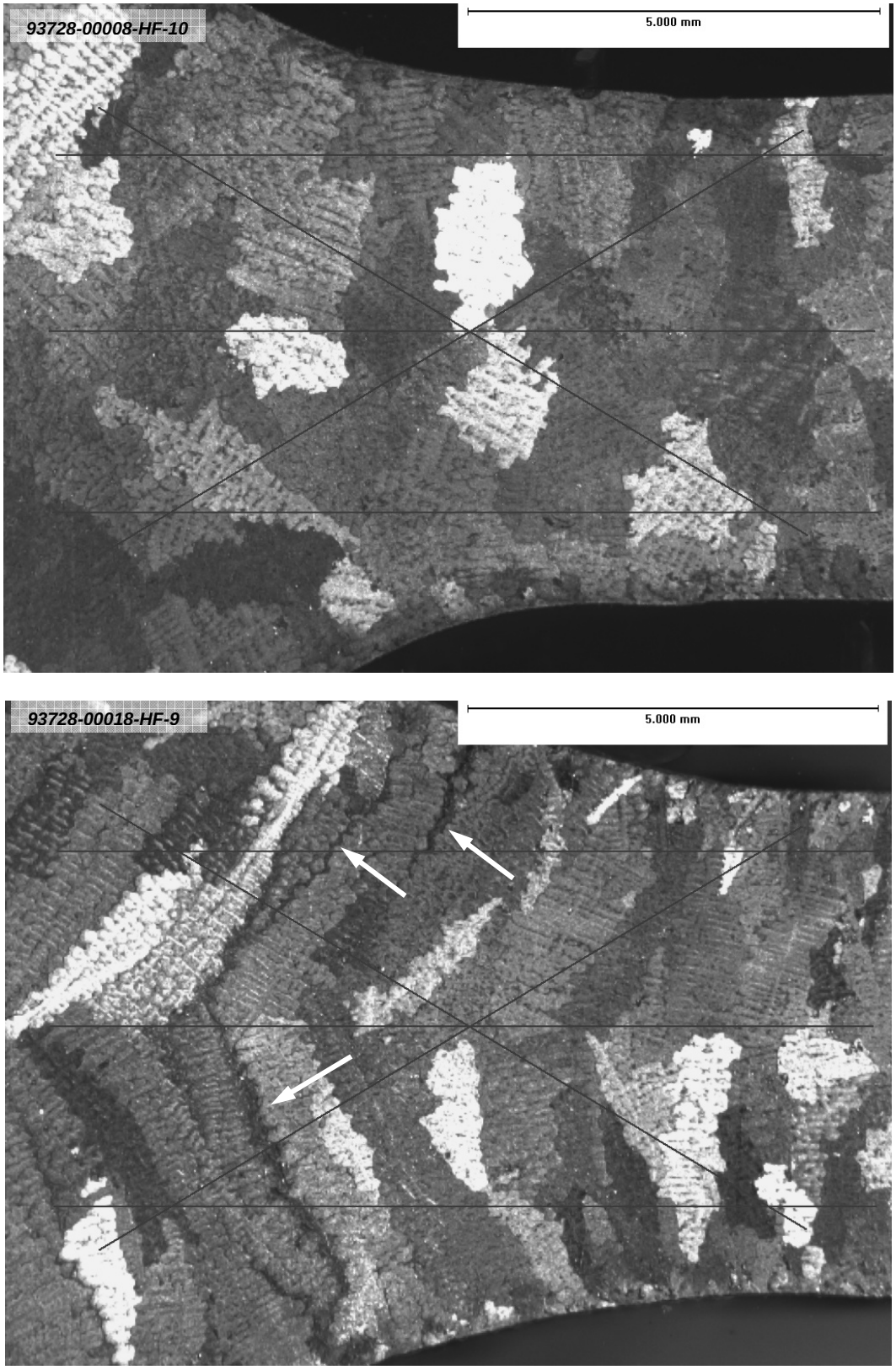


**Figure 54.** Micrographs illustrating the difference in cross-sectional grain size and structure at the downsprue fillet radius in the two longest bars. Arrows indicate where hot tears have formed.

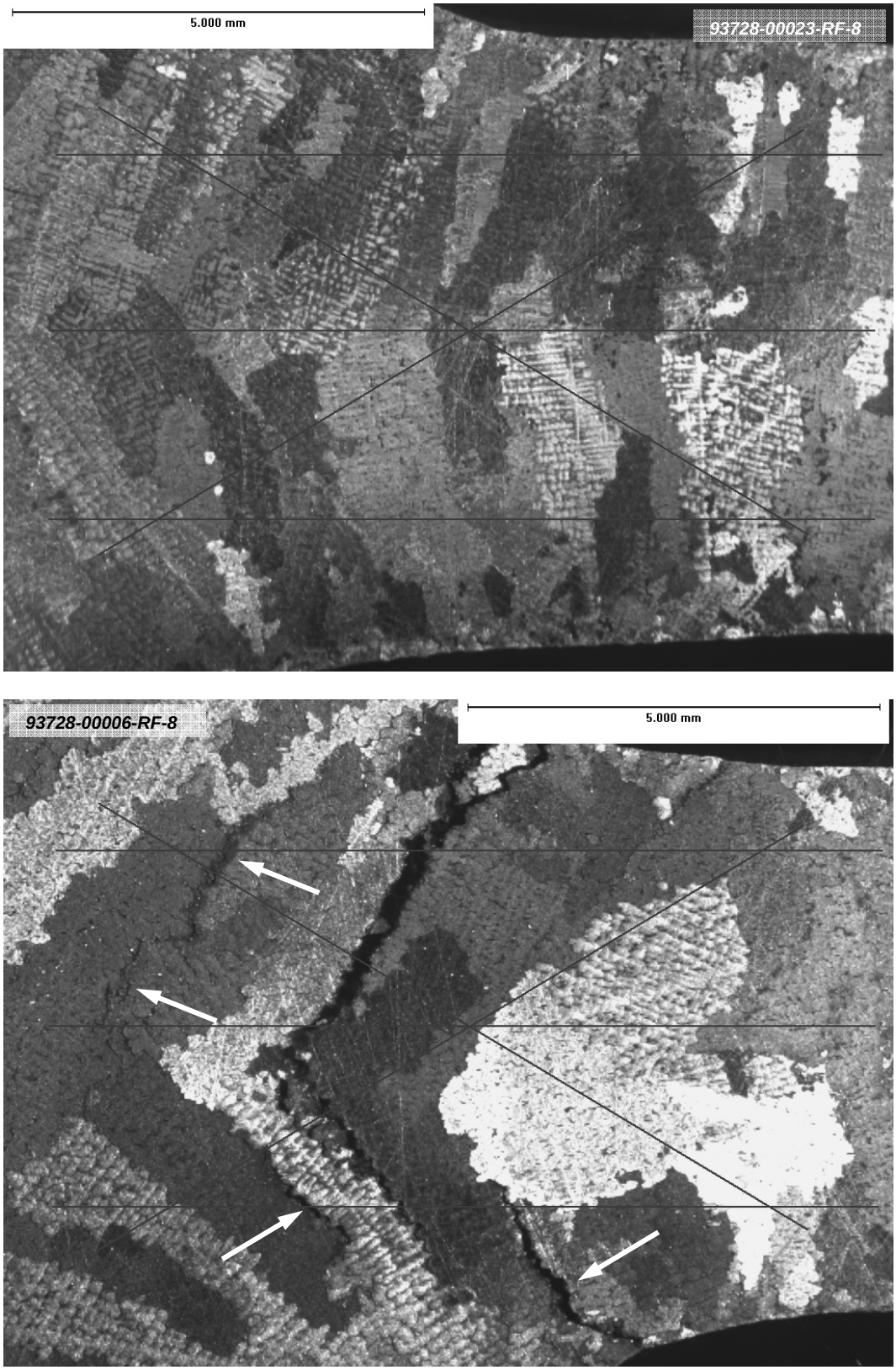


**Figure 55.** Micrographs illustrating the differences in cross-sectional grain size and structure at the feeder fillet radius in bars of identical length. Arrows indicate the smaller hot tears.

## D. Chemical Composition

The preceding results are significant in that marked variation in the solidification behaviour of a single "alloy" (FSX-414) has been documented given relatively small differences in composition from master heat to master heat. Based on the chemical analyses taken directly from the chill samples attached to the HTTV castings, Table 5 quantifies the total variation in FSX-414 chemistry across this investigation. A normalized perspective of the compositional analysis of each HTTV casting is presented within the next two figures. Figure 56 contains composition information for only those elements that are controlled by the GEPS B50A489 specification for FSX-414. By representing the data in this way, it is readily apparent how much of the specification range and what portion of the range is being utilized. Figure 57 lists all other elements that were measured and determined to have significant enough variation between HTTV castings to be included in the statistical analyses.

| Element | Concentration Range (*wt. %*) | Portion of B50A489 Specification Range Consumed | Element | Concentration Range (*wt. %*) |
|---|---|---|---|---|
| **C** | 0.05 | 46.0% | **Mo** | 0.17 |
| **Mn** | 0.25 | 41.7% | **Cu** | 0.07 |
| **Si** | 0.21 | 42.0% | **V** | 0.02 |
| **Cr** | 0.99 | 49.5% | **Nb** | 0.19 |
| **Ni** | 1.08 | 54.0% | **Ta** | 0.08 |
| **Fe** | 1.46 | 73.0% | **Al** | 0.05 |
| **P** | 0.005 | 13.4% | **Ti** | 0.04 |
| **S** | 0.003 | 6.9% | **N** | 0.02 |
| **W** | 0.37 | 37.0% | **O** | 0.03 |
| **B** | 0.004 | 43.3% | | |

**Table 5.** Range of elemental concentration by element across all HTTV metal lots.

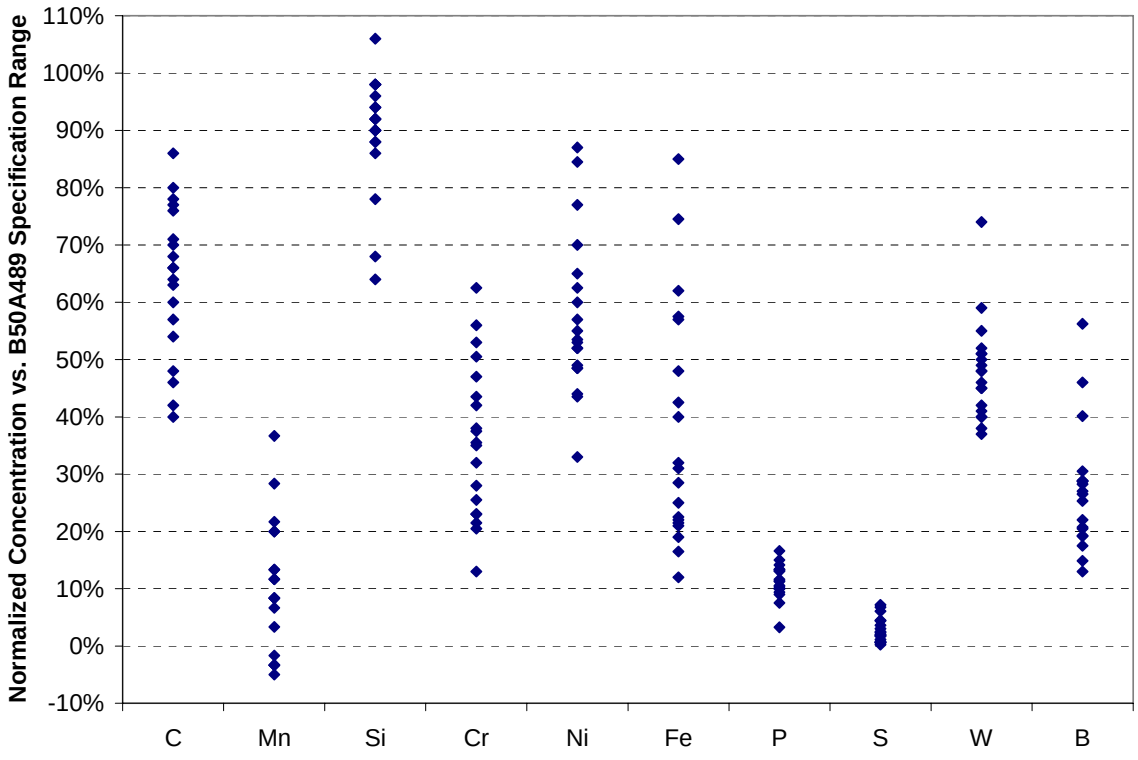


**Figure 56.** Normalized representation of actual HTTV chemistries versus the FSX-414 material specification requirements. As examples of normalization, Cr varies from 13% to 63% of specification which is equivalent to Cr contents ranging from 28.76 wt.% to 29.75 wt.%. B varies from 13% to 56% of specification which is equivalent to 0.006 wt.% to 0.010 wt.%.

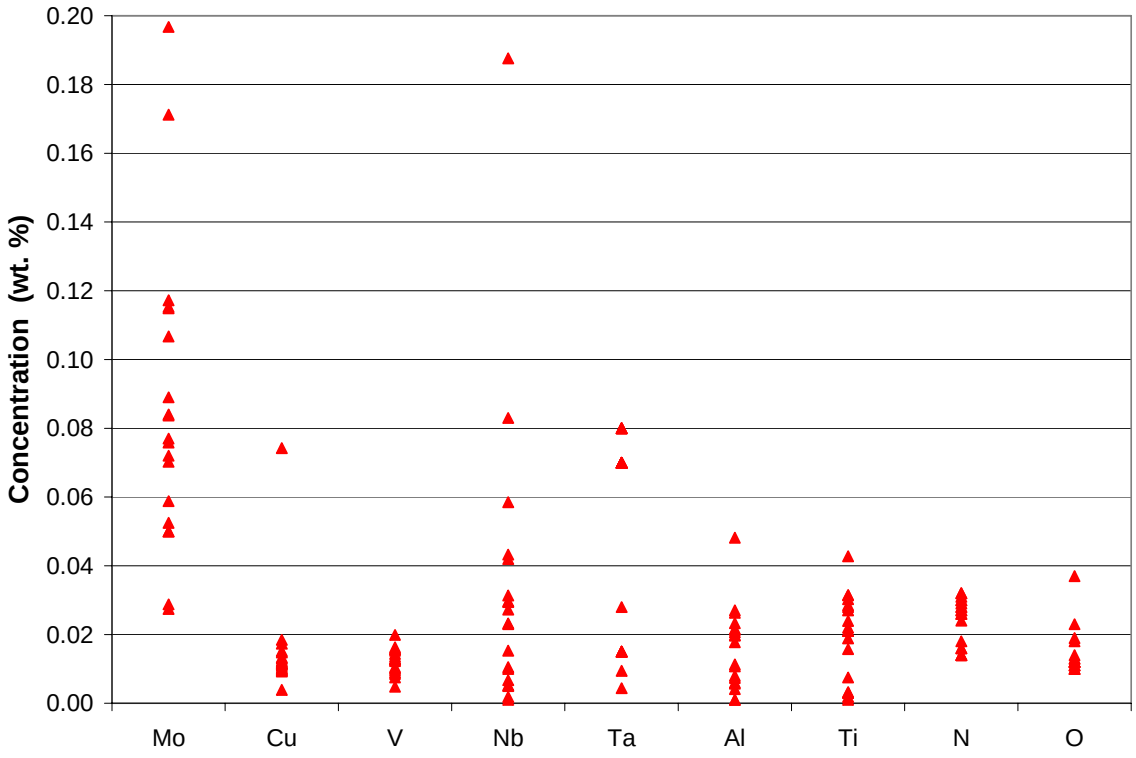


**Figure 57.** Measured concentrations of other elements not controlled by the B50A489 specification, but detected in HTTV castings. Each of these elements were included in the statistical analyses.

## E. Differential Thermal Analyses

The DTA results obtained from samples excised from the HTTV castings confirm the differences in solidification behaviour between master heats that the NDE and metallographic responses indicate. Some of the key DTA data used in the statistical analyses are summarized in Table 6. In addition to the 20°C difference in liquidus temperature between metal lots illustrated in Figure 58, the heating curves also show a significant difference in the enthalpy of the melting reaction between metal lots. Similarly, there are substantial differences in the liquidus temperature and the enthalpy generated by the solidification phase change as shown in the cooling curves in Figure 59. Differences in carbide decomposition and eutectic (carbide) solidification event temperatures are also readily apparent in each set of cooling and heating curves. Lecomte-Beckers [6], Burton [7], D'Souza [54] and many other researchers have thoroughly documented similar findings in the variety of alloys they have tested using DTA. However, this investigation differs from much of the published superalloy DTA experiments based on the substantially smaller variation of composition across the alloys tested and described in Table 5.

| HTTV | First Carbide Decomp'n | Second Carbide Decomp'n | Liquidus | | Total Undercooling | Solidus | | | Actual Mushy Zone |
|---|---|---|---|---|---|---|---|---|---|
| | | | Melting Curve | Cooling Curve | | Cooling Curve (Effective) | Cooling Curve (Actual) | Effective minus Actual | |
| 93728-00004 | 1301.97 | 1325.06 | 1411.86 | 1414.77 | -2.91 | 1378.40 | 1252.00 | 126.40 | 162.77 |
| 93728-00005 | 1263.39 | 1292.62 | 1406.93 | 1410.07 | -3.15 | 1376.14 | 1288.05 | 88.09 | 122.02 |
| 93728-00007 | 1264.36 | 1298.17 | 1408.98 | 1411.00 | -2.02 | 1375.59 | 1285.38 | 90.21 | 125.62 |
| 93728-00008 | 1299.77 | 1329.30 | 1403.65 | 1409.15 | -5.50 | 1376.04 | 1295.08 | 80.97 | 114.07 |
| 93728-00009 | | 1300.10 | 1410.73 | 1376.62 | 34.11 | 1376.52 | 1361.48 | 15.04 | 15.14 |
| 93728-00011 | 1268.99 | 1303.39 | 1416.68 | 1367.52 | 49.16 | 1357.35 | 1328.24 | 29.12 | 39.29 |
| 93728-00012 | 1258.02 | 1303.27 | 1417.67 | 1379.76 | 37.91 | 1360.22 | 1318.14 | 42.07 | 61.62 |
| 93728-00013 | | 1296.95 | 1420.62 | 1402.75 | 17.87 | 1380.86 | 1321.89 | 58.97 | 80.86 |
| 93728-00015 | 1264.91 | 1301.17 | 1418.11 | 1401.30 | 16.81 | 1388.17 | 1307.20 | 80.97 | 94.10 |
| 93728-00016 | 1270.28 | 1301.01 | 1415.33 | 1327.93 | 87.40 | 1320.04 | 1313.07 | 6.97 | 14.86 |
| 93728-00017 | 1271.97 | 1304.18 | 1417.36 | 1406.64 | 10.72 | 1379.74 | 1313.13 | 66.60 | 93.51 |
| 93728-00018 | 1265.17 | 1302.90 | 1416.28 | 1401.59 | 14.69 | 1376.64 | 1334.37 | 42.27 | 67.22 |
| 93728-00019 | 1265.35 | 1299.23 | 1420.49 | 1389.23 | 31.26 | 1379.89 | 1339.71 | 40.18 | 49.53 |
| 93728-00020 | 1265.62 | 1303.56 | 1414.53 | 1381.98 | 32.56 | 1372.03 | 1323.45 | 48.58 | 58.53 |
| 93728-00021 | 1266.58 | 1301.21 | 1419.72 | 1362.64 | 57.08 | 1352.64 | 1324.97 | 27.67 | 37.67 |
| 93728-00022 | | 1301.37 | 1418.51 | 1406.45 | 12.05 | 1387.55 | 1330.90 | 56.65 | 75.55 |
| 93728-00023 | 1266.16 | 1301.07 | 1417.79 | 1396.39 | 21.40 | 1383.94 | 1338.17 | 45.78 | 58.22 |

**Table 6.** Summary of selected event temperatures obtained from the analysis of the DTA analyses conducted on each of the HTTV castings. All temperatures provided in °C.

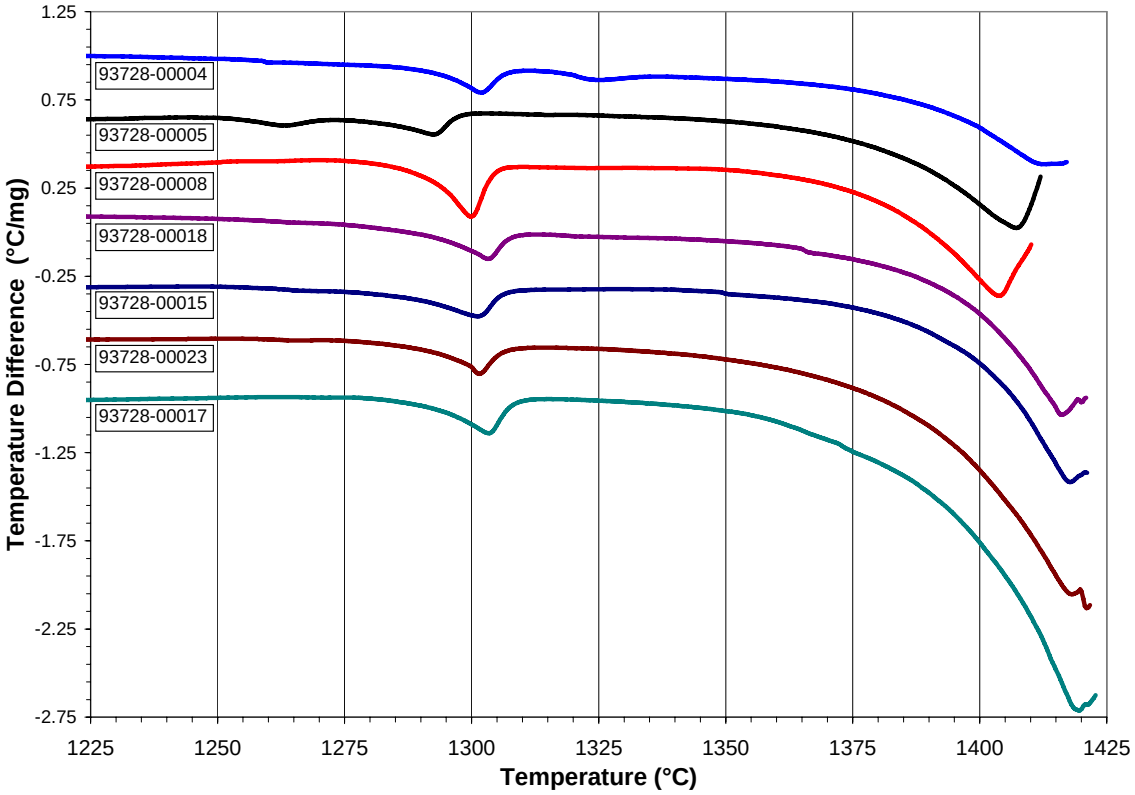


**Figure 58.** Selected DTA heating curves from samples excised from seven different HTTV castings. Curves have been shifted in the y-axis for clarity. Note the differences in temperatures between metal lots for the same events. From Reference [1].

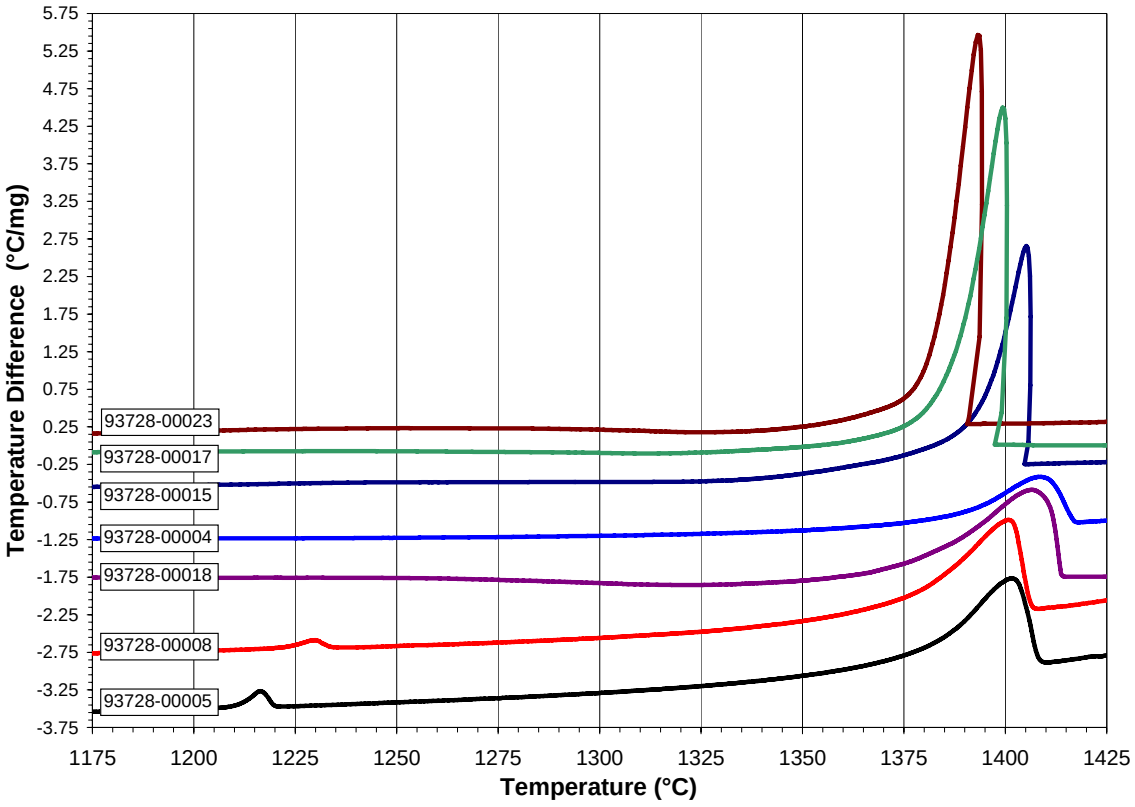


**Figure 59.** Selected DTA cooling curves from samples excised from seven different HTTV castings. Curves have been shifted in the y-axis for clarity. Note the differences in temperatures between metal lots for the same events. From Reference [1].

## F. Thermodynamic Modeling

The thermodynamic modeling (TDM) provided similar results to the DTA testing in so far as to predict a significant difference in the final solidus temperatures of the different HTTV ML chemistries. All of the thermodynamic response variable data was provided in increments of 5°C, so it was not possible to create 1:1 correlations against the DTA results. However, when examining the results of the entire data set, TDM predicts the final solidus temperatures for all HTTV chemistries to span a 25°C range from 1190°C to 1215°C. The DTA results presented in Table 6 have a 109°C range in the final solidus temperatures and a 53°C range if the highest and lowest values from two HTTV castings, 93728-00004 and 93728-00009, are removed. The average DTA solidus temperature is 1316°C, 114°C above the predicted average solidus provided by TDM. As mentioned previously, the TDM makes use of the Gulliver-Scheil relationship which predicts an infinite concentration in a perfectly mixed liquid even at very high fractions solid. In practice however, the Scheil equation's predicted logarithmic decay of the liquid would be superseded by eutectic solidification, resulting in a higher solidus temperature. Despite this, the average solidus temperature difference of more than 100°C appears to be too large to be explained by this difference alone; other possibilities such as poor DTA calibration or the caveats to the TDM previously discussed may also be contributing to the poor correlation.

The TDM predictions above 0.60 $f_s$ for each of the HTTV chemistries are provided in Figure 60. As an initial analysis, the data set was parsed into two groups based on the actual hot tear performance of each metal lot. Several ML have been coded in Figure 60 to illustrate the mixture of results and the insignificance of this approach. It is of interest to note however, that there are two distinct changes in solidification behaviour predicted at ~0.75 $f_s$ and ~0.92 $f_s$. Evidently at these temperatures the TDM has established the composition of the remaining liquid, in effect the homogenous composition of the liquid plus the solute rejected ahead of the solidification front, to have changed so substantially from the baseline alloy chemistry that the model begins to treat the new liquid composition as a different alloy. Based on the

microstructure of FSX-414, the first inflection point could be related to the solidification of either eutectic $M_7C_3$ or secondary $M_{23}C_6$. The final solidification of interdendritic and grain boundary $M_{23}C_6$ could be related to the second change in slope. Unfortunately, the granularity resulting from the TDM data being provided in 5°C increments did not allow for any additional insight to be gained from evaluating $\frac{df_s}{dT}$, i.e. the slope of the curves shown in Figure 60.

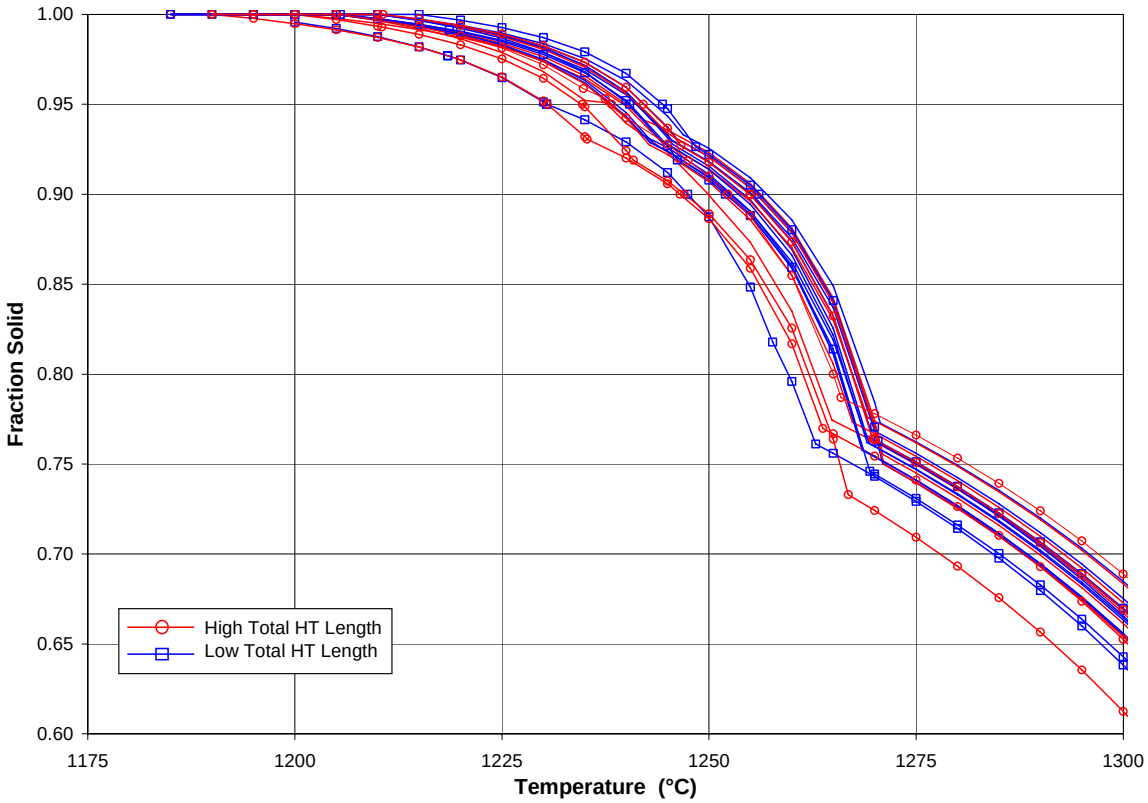


**Figure 60.** Fraction solid versus temperature predictions provided by thermodynamic modeling of each of the HTTV chemistries using JMatPro™ and the Gulliver-Scheil equation. Coding of the data for observed hot tear performance does not yield any visually-apparent trends.

The thermodynamic and material property predictions provided by the TDM were evaluated on an isothermal basis to gain an understanding of the magnitude of the range in these physical properties across the HTTV chemistry range. The inverse relationship between the

development of fraction solid and the calculated ranges in liquid viscosity and surface tension shown in Figure 61 are especially interesting. Intuitively, one might expect that if each of the HTTV alloys solidified similarly, the surface tension and viscosity of the liquid would either maintain little change with temperature, or at least, would follow a similar trend to that of enthalpy. However, the TDM data suggests that if one was to simplify the situation and assume identical liquidus and solidus temperatures for each of the alloys, the inverse relationship of liquid surface tension and viscosity versus $f_s$ would necessarily result in the alloys with greater viscosity and/or surface tension to lose feeding efficiency at a greater rate than the others as the $f_s$ increases, thereby creating a greater propensity of forming microporosity defects.

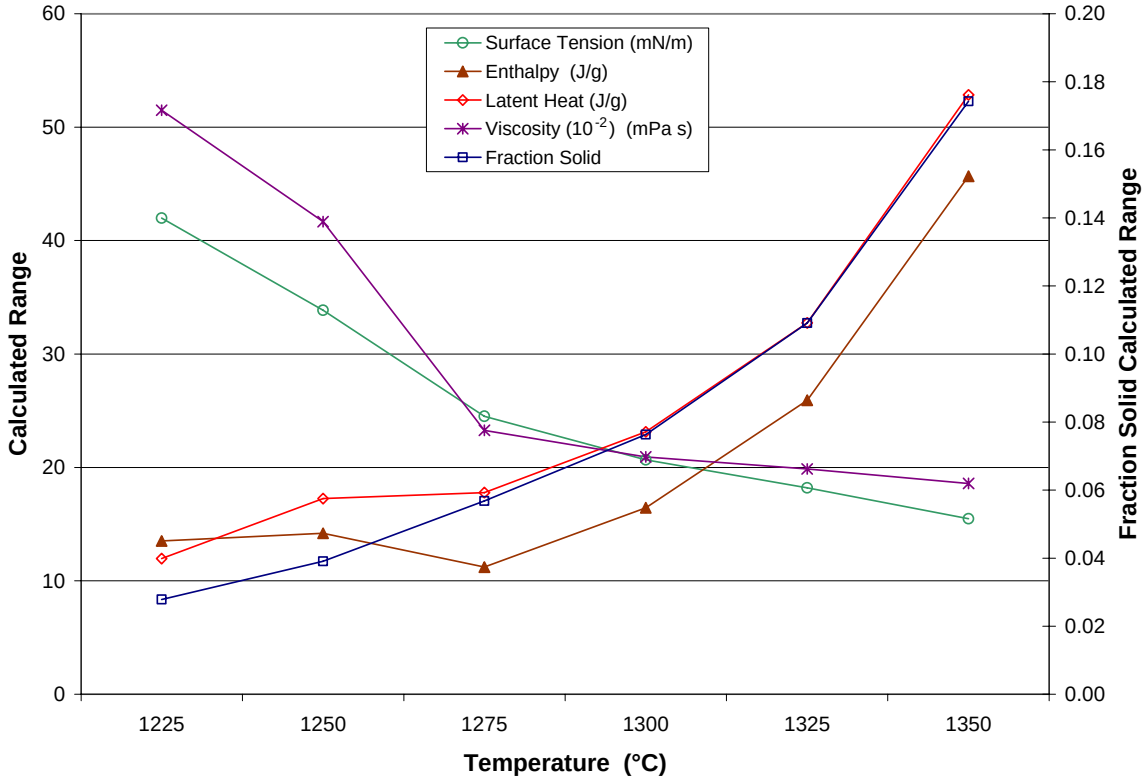


**Figure 61.** Chart of the isothermal range in physical properties predicted by the thermodynamic modeling of each of the HTTV chemistries using JMatPro™.

In order to establish whether the opposing trends in the isothermal comparisons were truly a function of alloy composition or whether shifts in the solidus temperature were driving the opposing relationships seen in Figure 61, surface tension was plotted against fraction solid to normalize the data. As Figure 62 shows, the surface tension of the liquids increase at different rates as solidification progresses; the ML chemistries which produced the greatest microporosity as defined by the SCMPR are highlighted. Although this apparent difference in liquid properties will certainly have an effect on the fluid dynamics and feeding efficiency in a dynamic and constricting mushy zone, the mix of the two categories of data in Figure 62 suggests that surface tension is most certainly not the only factor affecting the development of microporosity.

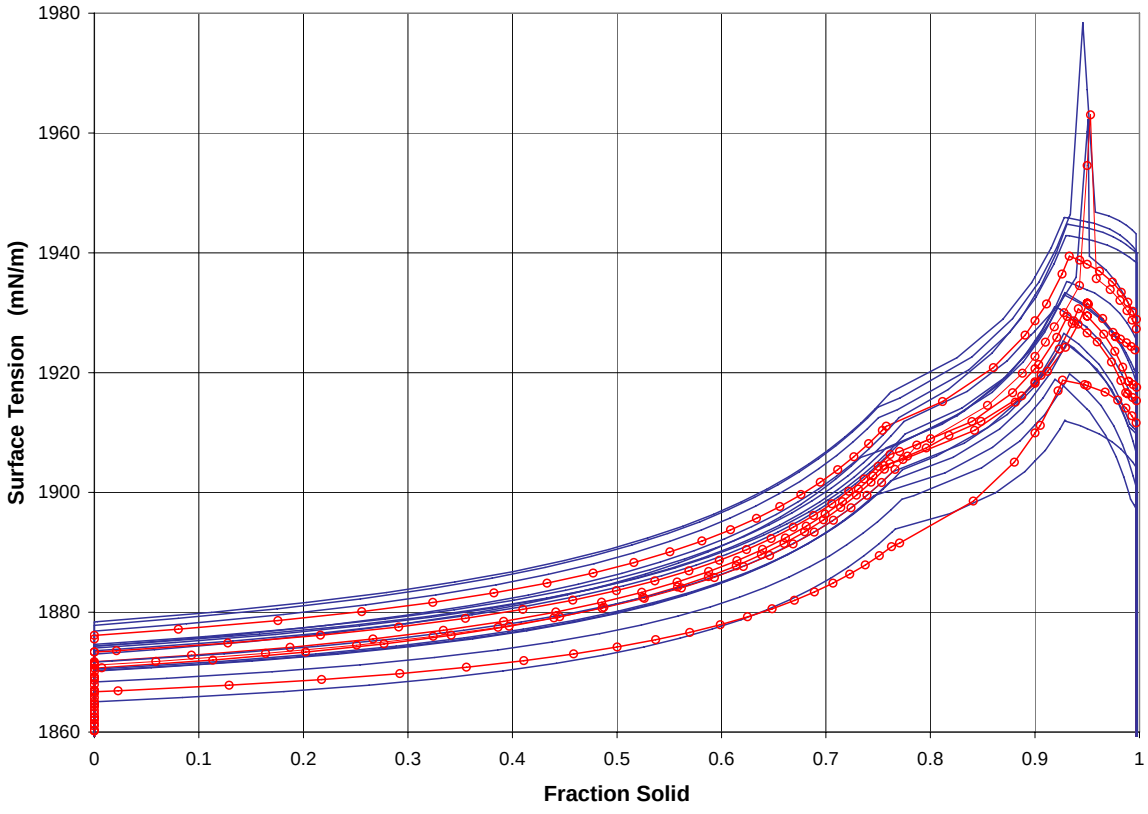


**Figure 62.** Chart of the change in the surface tension of the residual liquid predicted by thermodynamic modeling of each of the HTTV chemistries using JMatPro™. The metal lots with the greatest SCMPR are highlighted with the circled data points.

# VI. STATISTICAL ANALYSES

Prior to this investigation, PCC had used many statistical analysis tools for both continuous and discrete data such as ANOVA, linear and non-linear regression and chi-square to try to discover relationships between FSX-414 chemistry and casting response variables. None of these analyses yielded any statistically significant relationships from multiple sets of either production or experimental data. The remainder of this section will describe the evolution of the statistical analysis methods applied to the data collected from the Phase II and Phase III HTTV casting trials. It is important to note that none of the data from the Phase I screen trial castings was used in any of the statistical analyses in this investigation.

## A. Basic Statistical Analyses

When plotted against each other, the hot tear and SCMPR data for each HTTV casting yield the inverse relationship depicted in Figure 63, again confirming trends observed in PCC production castings. However if the HTTV SCMPR data is separated into two populations, the inverse relationship between hot tears and microporosity is maintained within two more statistically significant fits to the experimental data, as illustrated in Figure 64. Professor Campbell's explanation of interdendritic solidification in long-freezing range alloys previously discussed provides a plausible explanation for the inverse microporosity-hot tear relationship. Specifically, the cyclic process of creating and releasing metallostatic tension which leads to the formation of layer porosity defects could be the mechanism for the release of a portion of the contraction stresses developed during solidification which in turn, minimizes the severity of the hot tear defects that are created.

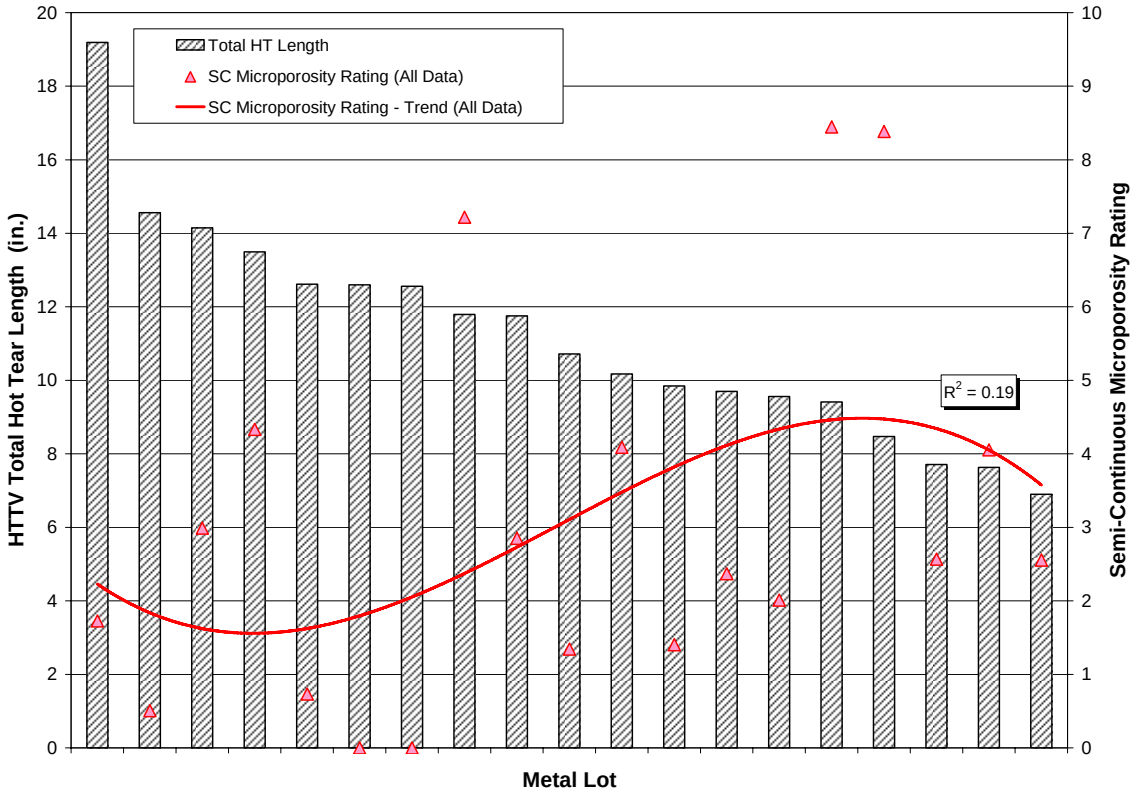


**Figure 63.** Plot of the total length of hot tears versus the SCMPR for all Phase II and Phase III HTTV castings (metal lots). The solid line provides a 3rd order polynomial fit to all of the SCMPR data, yielding a poor fit of only 19%.

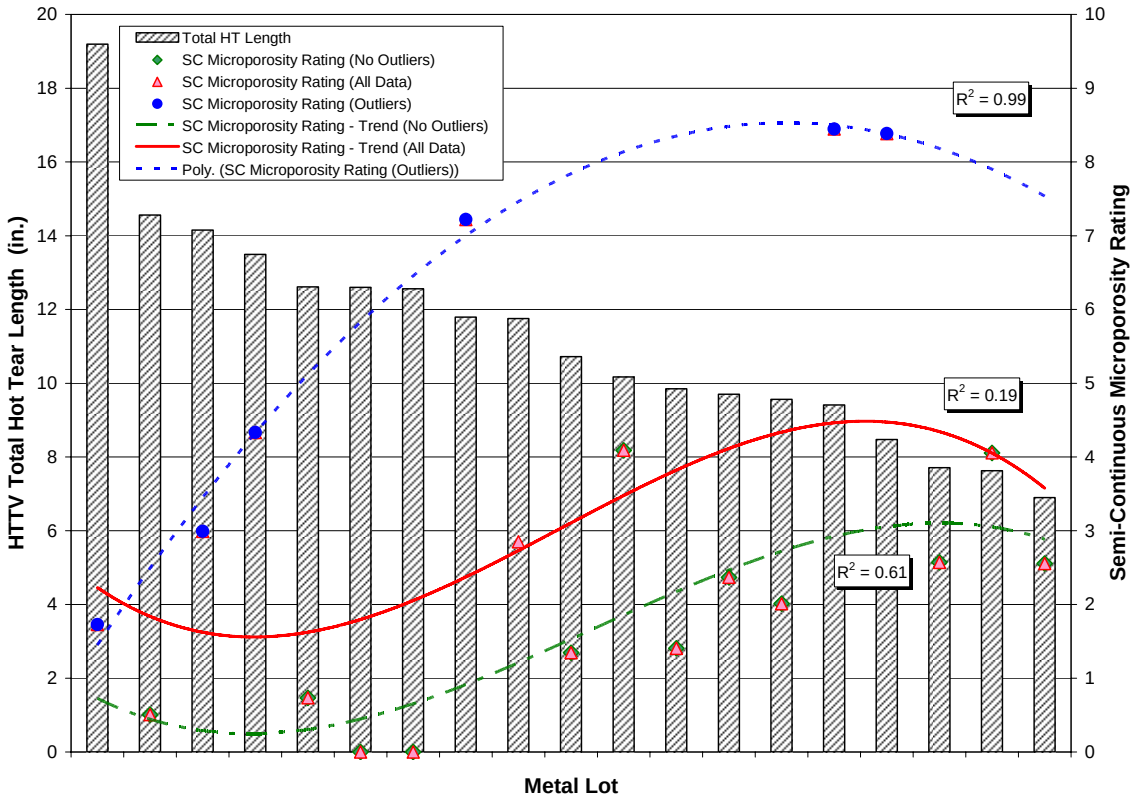


**Figure 64.** Identical data to that presented in Figure 63 with the SCMPR data separated into two populations, which yields more statistically significant relationships. The inverse relationship with total hot tear length is emphasized.

Despite the substantial variation in the hot tear and SCMPR data measured during this investigation, PCC's previous experience with developing statistically significant relationships between variations in single-element concentrations and any of the casting response variables was again confirmed; no statistically-significant relationships could be established. Figure 65 illustrates the most significant regression fit between HTTV hot tears and changes in elemental concentration. Thus, even with the elimination of potential confounding effects of casting geometry and natural long-term fluctuations in investment casting process parameters, the HTTV casting data confirms that the relationships between the predictor or "X" variables and the response or "Y" variables are more complicated than standard statistical analyses can resolve.

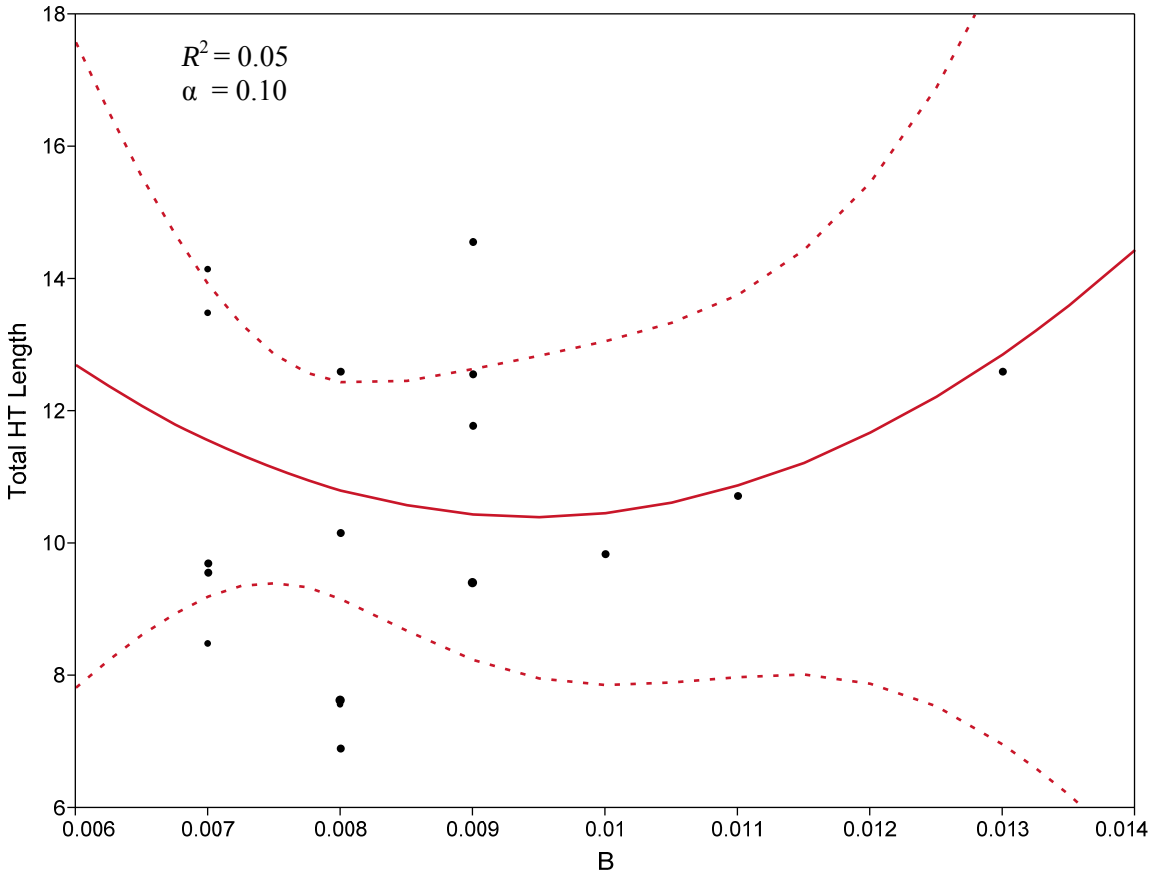


**Figure 65.** Regression analysis of the total length of hot tears for all Phase II and Phase III HTTV castings versus boron concentration. No statistically significant relationship is apparent.

## B. Multiple Linear Regression Analyses - Fit Model

Single-variable regression analyses examine only the variation of a subject (X) variable versus the chosen response (Y) variable. Therefore by definition, any variation in the system that occurs as a function of other variables becomes a component of the error term in the bivariate or single component regression equation. In the unsuccessful bivariate analyses presented above, the noise introduced by the large error terms was more significant than the single-element relationships with the response variables; hence the results were statistically insignificant. In order to account for the multiple relationships and interactions that were evidently influencing the analyses of the HTTV data, the JMP™ Fit Model analysis platform was used in an attempt to create statistically significant simultaneous regression analyses for multiple Y and X variables. In so doing, specific care was taken to ensure that tightly correlated X variables were not used in the same Fit Model as doing so could yield falsely significant statistical relationships. [65,66]

### *1. Microstructure*

Due to the substantial changes in microstructure observed between the center and ends of the HTTV bars, the experimental data was separated into its discrete components by location. This allowed the fit models to resolve and consider as much of the experimental variation as possible, improving the chances of discovering a statistically significant link between the quantitative microstructural measurements and the development of hot tears. Figure 66 provides the results of one of the statistical relationship between hot tears and microstructure which is only marginal, at best. The results become less statistically significant when the results at the feeder and the downsprue are considered together. Analyses of microstructure versus microporosity data and DTA data did not yield relationships that were any more meaningful.

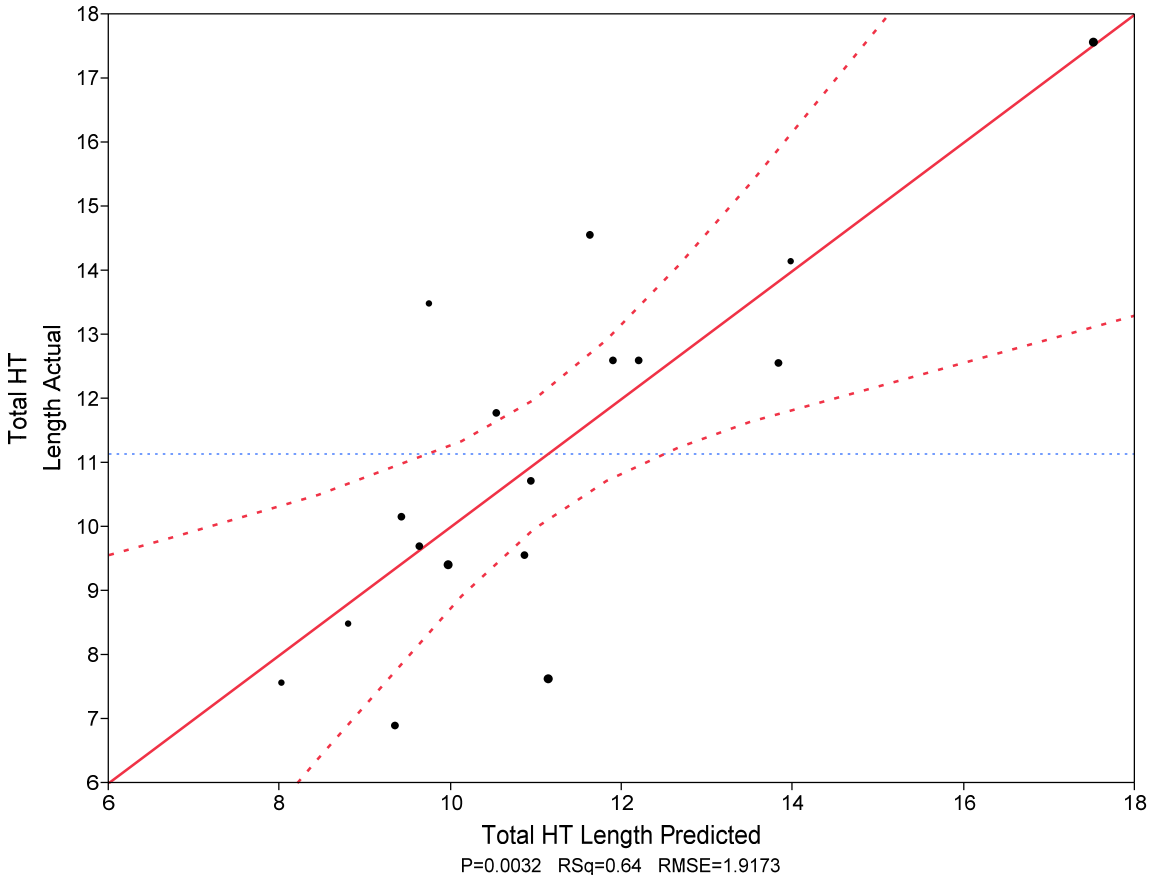


**Parameter Estimates**

| Term | Estimate | Std Error | t Ratio | Prob>\|t\| |
|---|---|---|---|---|
| Intercept | 7.671713 | 1.652703 | 4.64 | 0.0005* |
| MFP Grain Size | 4.819546 | 1.632656 | 2.95 | 0.0112* |
| Sum Area M23C6 FOV (µm2) | 0.0000749 | 2.659e-5 | 2.82 | 0.0146* |
| Carbide Transition Length | -1.915846 | 1.056521 | -1.81 | 0.0929 |

**Summary of Fit**

| | |
|---|---|
| RSquare | 0.640966 |
| RSquare Adj | 0.558112 |
| Root Mean Square Error | 1.917278 |
| Mean of Response | 11.14588 |
| Observations (or Sum Wgts) | 17 |

**Figure 66.** Fit Model analysis, parameter estimates and the summary of statistical fit for total hot tear length versus microstructural response variables; longest HTTV bar at the downsprue. The statistical significance of the relationship is marginal, with $R^2_{adj} = 55\%$. The curved dotted lines represent the 95% confidence interval.

Although the microstructural evaluations of the HTTV bars were thorough, there are several reasons it was not possible to establish statistically valid relationships with hot tear severity, microporosity development or DTA data. First, hot tearing is proportional to the amount of linear contraction which in the case of the HTTV casting, is proportional to bar length. Thus as the cast bars shorten, null hot tear lengths become increasingly prevalent and the HTTV bar length confounds statistical relationships of hot tearing versus available microstructural data. It was apparent during the evaluation of the microstructural samples that a lack of hot tears in the shorter bars did not correspond with highly significant changes in cast microstructure. In other words, the as-cast microstructure does not scale with bar length like linear contraction.

Figure 67 shows a SEM backscatter image of a grain boundary carbide which optically, appears to be $M_{23}C_6$. The wavelength dispersive x-ray (WDX) maps shown in the same figure reveal more dense regions within the carbide which correspond with a lower Cr content and a local concentration of both W and Ta, both of which are known to be strong formers of $M_6C$ carbides in Co-base superalloys. [4,9,13] Correctly discerning $M_{23}C_6$ from $M_6C$ is very difficult, if not impossible, using optical microscopy and was not attempted during this investigation. However, the inability to optically differentiate these two important carbides lends a level of uncertainty to the statistical analysis.

The next difficulty in creating correlating relationships using quantitative microscopy relates to the nature of metallographic evaluations. Although a significant volume of quantitative microstructural data was compiled during this investigation, it is not representative of the macroscopic response variables. Microstructural data was compiled from optical evaluations of multiple fields of view taken at three locations along the bar length as described in Appendix B. However at most, this equates to a 1 mm wide band of quantitative microstructural data from each location. Even when summed, this represents only 0.6% – 1.2% of the total length of the bars exhibiting hot tears. Thus, because it is evaluated over a comparatively large area, the macro grain size evaluation is perhaps the only truly representative microstructural measurement.

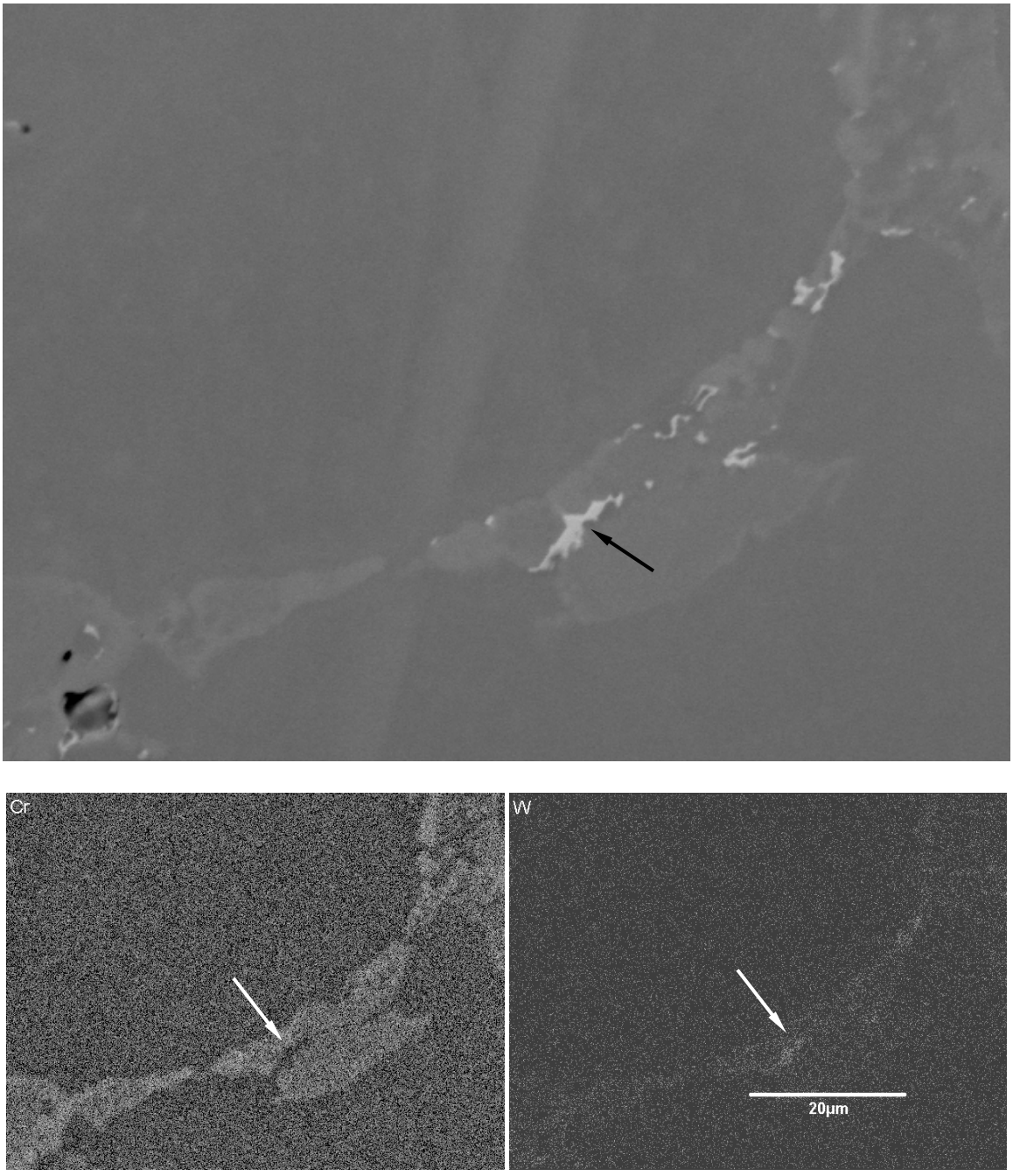


**Figure 67.** SEM backscatter image of the carbide structure at the tip of a hot tear. Lower two images are WDX element maps of Cr and W taken from the same field of view. The maps show the more dense carbide indicated by the arrow in the top view corresponds with what appears to be a Cr-deficient, W-rich $(W,Ta)_6C$ carbide. All of the WDX elemental maps for this field of view are provided in Appendix D.

Finally, all of the quantitative microstructural data are based on evaluations of a single two-dimensional section of each bar. Considering the variable solidification path described in Figure 37, one could justifiably argue that one longitudinal microstructural section does not represent the three-dimensional volumetric entity of a HTTV bar casting.

*2. Hot tears*

Developing a multiple linear regression model of hot tears versus alloy chemistry was not successful. The most statistically significant relationship involved the elements tungsten and silicon and yielded a low adjusted regression coefficient of 37%. In retrospect, this might be expected considering that much of the volumetric solidification process is complete before hot tear defects form, thus it would seem optimistic to expect that a direct relationship could be established. Clearly, hot tears are the end result of an enormously complicated process, resultant defects created by the interactions of chemical, thermodynamic and phase transformation events. Based on this perspective, an attempt was made to progressively link hot tear defects with alloy composition via an intermediate link with quantitative DTA data. The DTA events represent the incremental steps of the solidification process and should therefore provide a relationship to a final outcome, such as a casting defect. Figure 68 shows the statistically significant results of this approach. In evaluating and constructing each of the statistical models, parameters with *p*-values of less than 15% were kept in the model; parameters with less statistical significance were discarded.

The progressive link approach is similar to that of Han [2] who used ThermoCalc™ to predict the solidus and liquidus temperatures of various heats of FSX-414 which had been quantitatively categorized for hot tearing propensity. Han then used the TDM predictions for the solidus temperatures to create a linear relationship describing a threshold chemical composition for hot tear susceptibility.

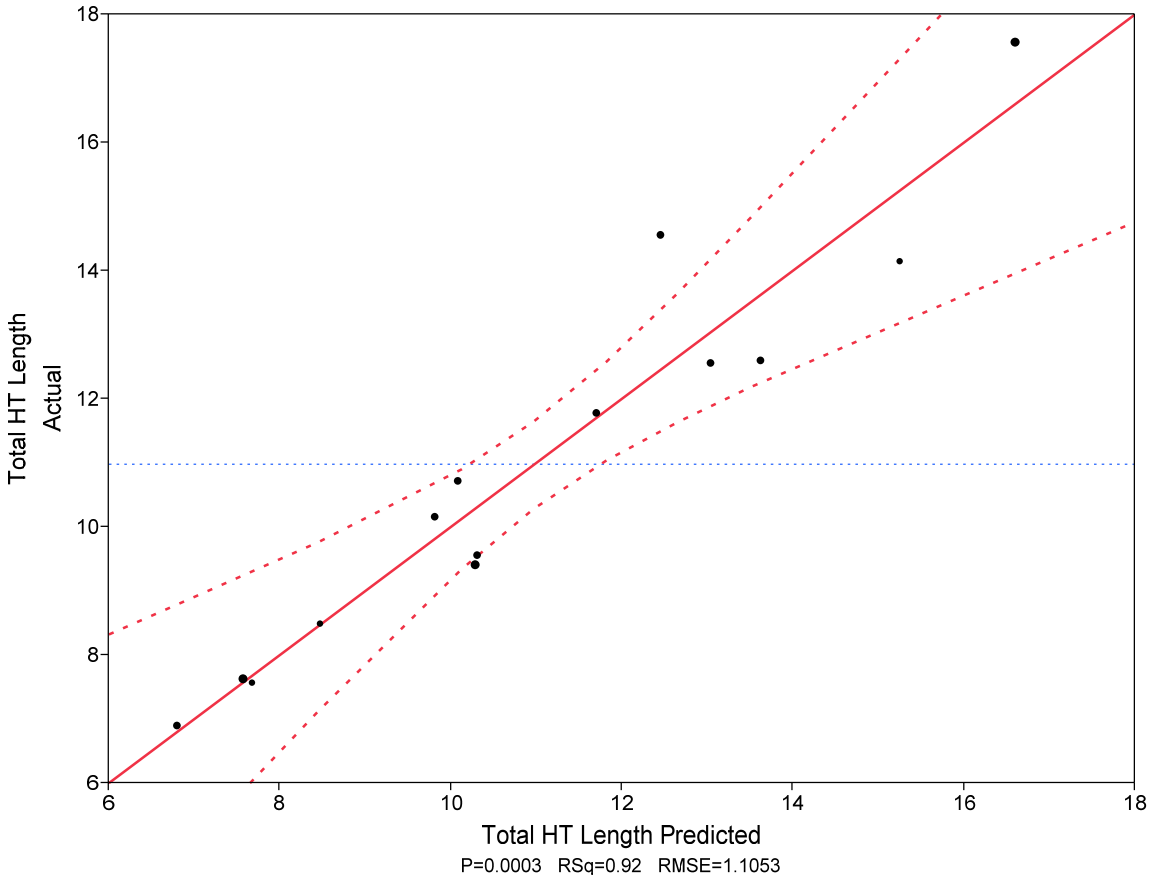


**Parameter Estimates**

| Term | Estimate | Std Error | t Ratio | Prob>\|t\| |
|---|---|---|---|---|
| Intercept | -288.9328 | 47.81505 | -6.04 | 0.0003* |
| Melting Curve - Carbide Decomp 2 Start | 0.2646998 | 0.063006 | 4.20 | 0.0030* |
| Melting Curve - Carbide Decomp 1 | -0.151015 | 0.06414 | -2.35 | 0.0464* |
| Solid'n Curve - Liquidus | -0.191314 | 0.039119 | -4.89 | 0.0012* |
| Solid'n Curve Effective Solidus | 0.3082338 | 0.051471 | 5.99 | 0.0003* |
| Melting Curve - Carbide Decomp 2 Width | -0.08838 | 0.037714 | -2.34 | 0.0472* |

**Summary of Fit**

| | |
|---|---|
| RSquare | 0.920522 |
| RSquare Adj | 0.870848 |
| Root Mean Square Error | 1.105306 |
| Mean of Response | 10.97714 |
| Observations (or Sum Wgts) | 14 |

**Figure 68.** Fit Model analysis, parameter estimates and the summary of statistical fit for total hot tear length versus quantitative DTA data. The model provides an excellent level of statistical significance with $R^2_{adj} = 87\%$. The curved dotted lines represent the 95% confidence interval.

*3. Differential thermal analyses*

Creating a statistically significant link between the quantitative DTA data and the chemical analyses of each of the HTTV castings would complete the progressive statistical link between hot tears and alloy composition. The analyses of the HTTV data provided very strong statistical links between chemistry and DTA events. The average $R^2$ value for the DTA versus chemistry fit models for the events detailed in Table 7 is 90.2%; $R^2_{adj}$ values average 84.4%. Figure 69 shows an example of one of the exceptionally strong fit models. It is also significant to note that no dependencies on a single ML were detected in any of the chemistry versus DTA statistical models. This provides additional support to the relevance and strength of the statistical relationships that were established.

The critical elements affecting the FSX-414 solidus temperature identified in Han's model are identical to as those identified within this investigation. [2] However, the strength of the other relationships and elemental interactions discovered within this investigation strongly suggest that the hot tear susceptibility model proposed by Han lacks the important dimensions of element interaction, an accurate consideration of the effect of phosphorous participation and consideration of alloy solidification behaviour across the entire mushy zone with changes in alloy chemistry.

| | | Carbide Decomposition 1 Start | Carbide Decomposition 1 Peak | Carbide Decomposition 1 Width | Carbide Decomposition 2 Peak | Liquidus - Heating Curve | Liquidus - Cooling Curve | Effective Freezing Range | Actual Freezing Range | Effective Solidus | Actual Solidus |
|---|---|---|---|---|---|---|---|---|---|---|---|
| B50A489 Controlled Elements | C | | | | 1 | 1 | | | | | |
| | Mn | | | | | 1 | | | 1 | | 1 |
| | Si | 1 | 1 | | 1 | | | | | | |
| | Cr | | | | 1 | 1 | 2 | 2 | | 2 | |
| | Ni | | | 1 | | | 2 | 2 | | 1 | |
| | Mo | 1 | | | | | 1 | 1 | 1 | 1 | |
| | Fe | | | 1 | 2 | | 2 | 1 | 1 | 1 | 1 |
| | P | | | | | | | | 1 | | 1 |
| | S | | | | | | | 1 | | | |
| | W | 1 | 2 | | 2 | | | | 1 | 2 | |
| | B | | | | | 1 | | | | | |
| Other Elements | Cu | | | | | 1 | | | | | |
| | V | | | | | 1 | | | | | |
| | Nb | | | 1 | | | | | 1 | | 1 |
| | Al | 2 | 1 | 1 | | 1 | | | | | |
| | Ti | 2 | 2 | | | 1 | | | | | |
| R Sq. (%) | | 92.8 | 96.8 | 83.0 | 89.4 | 90.8 | 90.4 | 88.2 | 95.2 | 90.9 | 84.3 |
| R Sq. Adj. (%) | | 86.6 | 94.9 | 75.5 | 83.1 | 81.6 | 84.6 | 81.1 | 92.4 | 85.5 | 79.1 |

**Table 7.** Summary of chemistry versus DTA fit model analyses. Elements participating in the Fit Models are indicated by shaded squares with numbers representing the highest order interaction with which the element participated in the overall model.

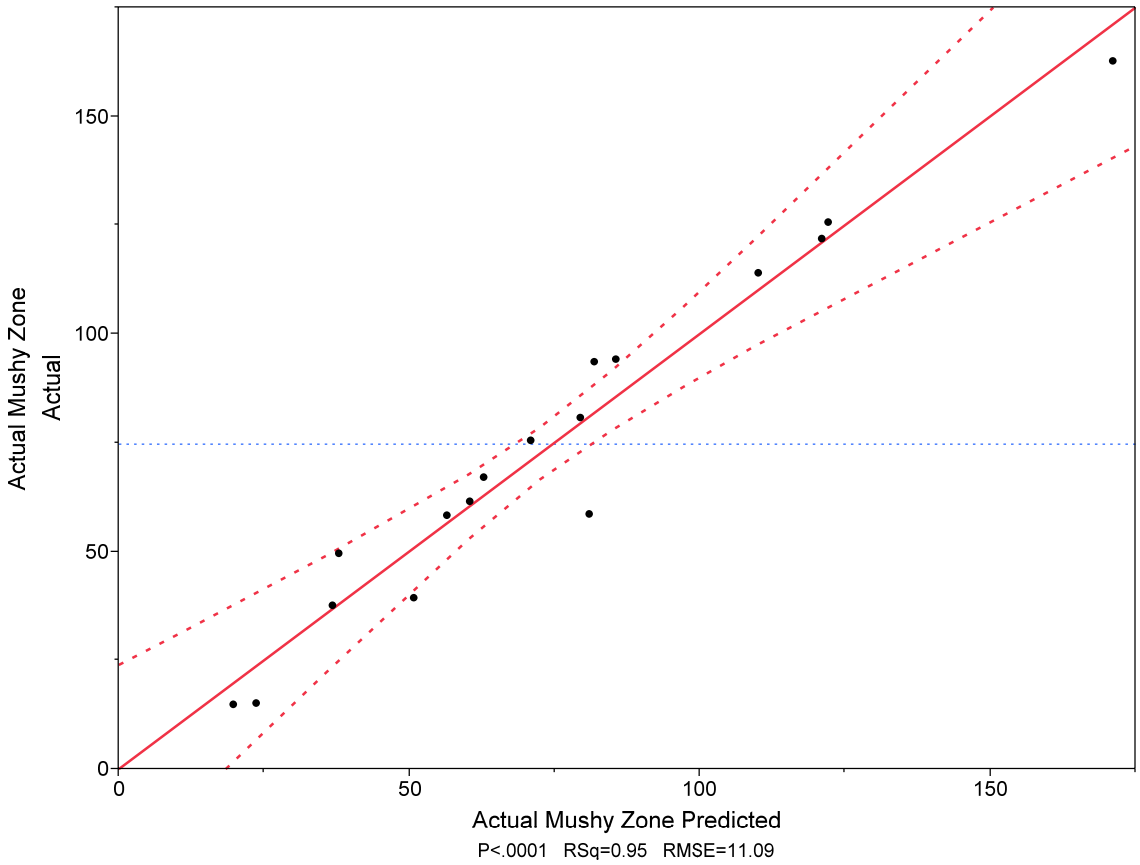


**Summary of Fit**

| | |
|---|---|
| RSquare | 0.952798 |
| RSquare Adj | 0.924477 |
| Root Mean Square Error | 11.08962 |
| Mean of Response | 74.73853 |
| Observations (or Sum Wgts) | 17 |

**Figure 69.** Fit Model analysis and the summary of statistical fit for the width of the mushy zone as determined by quantitative DTA analysis and HTTV actual chemistry. The model provides an outstanding level of statistical significance with $R^2_{adj} = 92\%$. The curved dotted lines represent the 95% confidence interval.

*4. Microporosity*

In contrast to the initial hot tear analyses, statistically significant relationships between the alloy chemistry and all three groups of SCMPR data were identified using the Fit Model analysis. In similar form to the DTA data, the porosity relationships included both first and second order interactions and dependencies upon elements which are not governed by the B50A489 material specification. Because the sample size of the Group 2 data set is so small, all of the factors impacting the data could not be considered within the same model, therefore two fit model analyses were built to ensure that all significant elements were considered. The Group 2 results listed in Table 8 are the average of the two relationships. Although the regression coefficients are exceptionally high for the Group 2 data, the small sample size results in somewhat lower p-values which should not be seen to detract from the significance of the relationship. Figure 70 provides the fit model relationship for all of the microporosity data versus chemistry. Interestingly, no statistically significant relationship could be found for the SCMPR based on any of the quantitative DTA data.

| | | All Lots | Group 1 | Group 2 |
|---|---|---|---|---|
| B50A489 Controlled Elements | C | | | |
| | Mn | 1 | 1 | |
| | Si | | | |
| | Cr | 2 | 1 | 1 |
| | Ni | 1 | 1 | 1 |
| | Mo | | | |
| | Fe | 2 | 2 | 1 |
| | P | 2 | 2 | 1 |
| | S | | | |
| | W | 2 | | 1 |
| | B | | | |
| Other Elements | Cu | 1 | | |
| | V | | | |
| | Nb | | | |
| | Al | | | |
| | Ti | 1 | | |
| R Sq. (%) | | 94.9 | 89.1 | 98.2 |
| R Sq. Adj. (%) | | 87.6 | 76.1 | 91.4 |
| p Value | | 0.0013 | 0.026 | 0.191 |

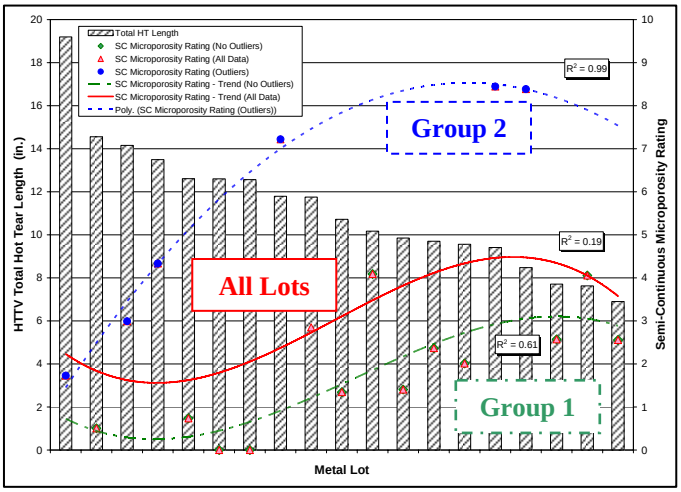


**Table 8.** Summary of chemistry versus SCMPR fit model analyses. Elements participating in the fit models are indicated by shaded squares with numbers representing the highest order interaction with which the element participated in the overall model.

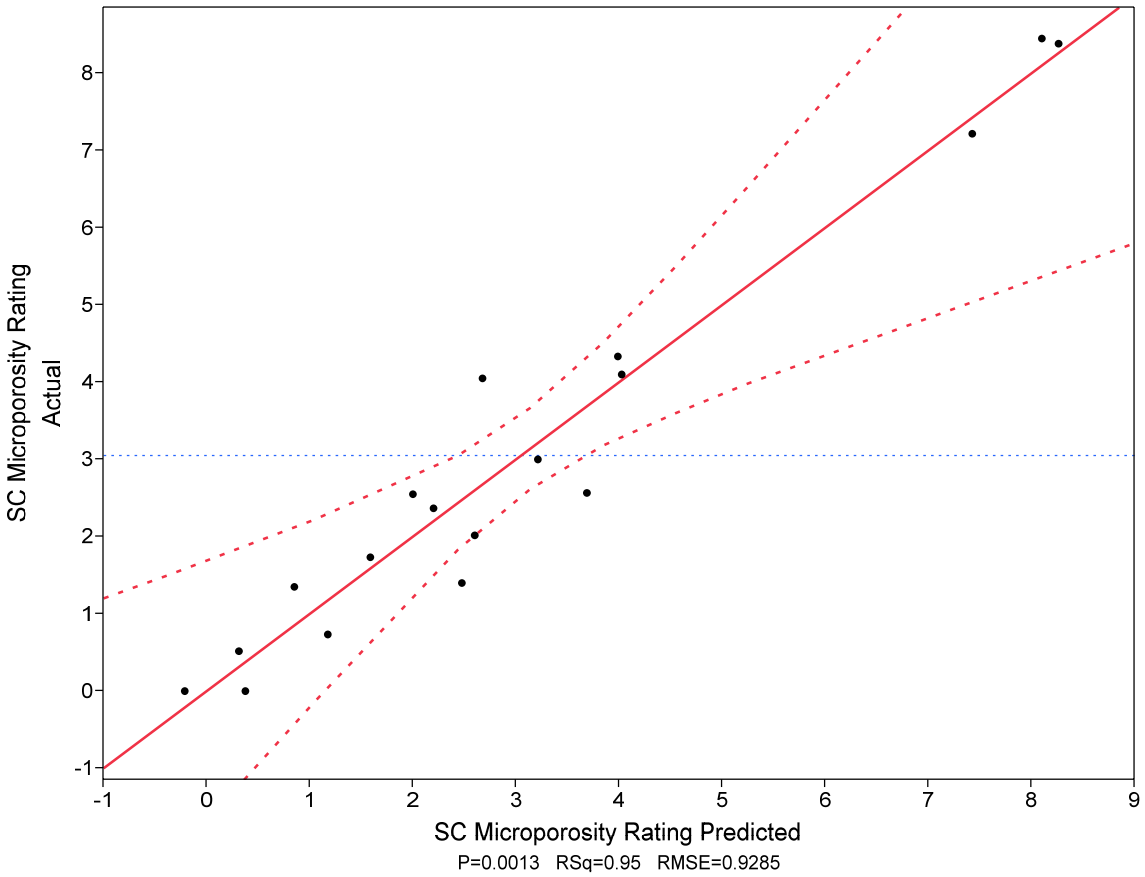


| Summary of Fit | |
|---|---|
| RSquare | 0.949083 |
| RSquare Adj | 0.876345 |
| Root Mean Square Error | 0.928525 |
| Mean of Response | 3.040996 |
| Observations (or Sum Wgts) | 18 |

**Figure 70.** Fit Model analysis and the summary of statistical fit for all SCMPR data and HTTV actual chemistry. The model provides an excellent level of statistical significance with $R^2_{adj}$ = 87%. The curved dotted lines represent the 95% confidence interval.

*5. Summary of statistical models*

Based on the statistical analyses, a picture of the relationship between small changes in alloy chemistry and the macroscopic response variables was constructed and is provided in Figure 71. The method of creating indirect, yet statistically significant relationships between variables and responses and the essential requirement to use multiple linear regression analysis tools containing both first- and second-order relationships explains why the standard, bivariate statistical analysis approach had previously failed to uncover the factors affecting FSX-414 casting quality. In retrospect, this discovery or realization should not be unexpected as the constituents of an alloy are present in order to create particular effects based upon their interaction. It is also reasonable to believe that the interactive effects must begin well above the solidus temperature, thus affecting the outcome of the solidification process. The inflection points observed in the equilibrium thermodynamic model data shown in Figure 60 support this observation.

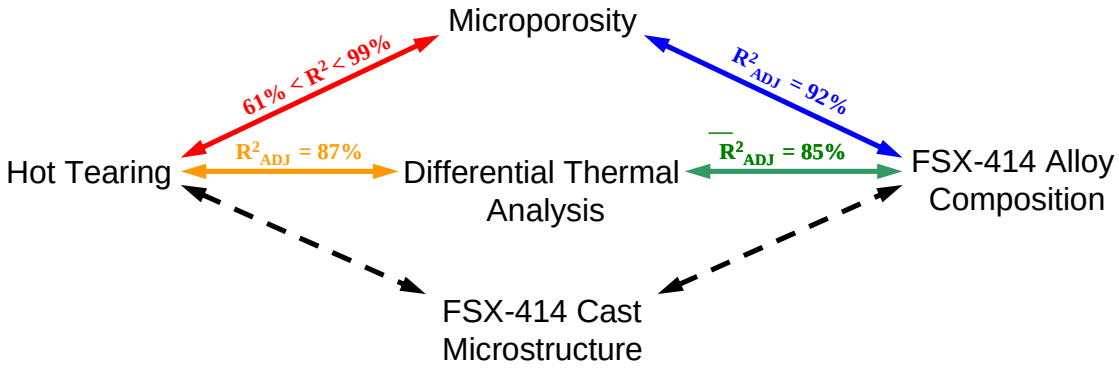


**Figure 71.** Map of the statistical connections discovered between small changes in FSX-414 alloy chemistry and the macro- and microscopic response variables. The links to the as-cast microstructure are dotted as links must exist, but were not able to be statistically validated using the techniques employed during this investigation.

## C. Predictive Modeling

The JMP™ Fit Models created from the analyses of the HTTV castings provide sufficient information to confidently model the behaviour of FSX-414 within the chemistry range and the scale of the microporosity and hot tear defects spanned by the investigation. For those conditions that lie outside of the range of the HTTV experiments, the model results would need to be extrapolated which for first order interactions, provides little risk. First order interactions form a linear relationship that forms a plane in three dimensional space with the response variable. Changes in other components of the Fit Model only modify the location of the plane in three-dimensional, $X_A$-$X_B$-Response space. In contrast, a second order relationship forms the three dimensional saddle-shaped surface as shown in Figure 72. Although any two-dimensional section through such a relationship yields a line, the slope of the line changes along the saddle-shaped surface, as illustrated in Figure 73. Consequently, reliably extrapolating model results from relationships that have second-order dependencies is next to impossible.

After establishing the statistical relationships between all of the predictor and response variables in this investigation, the next step was to design a robust chemistry space within which FSX-414 could be relied upon to produce consistent casting results. Preferably, the optimized chemistry would be balanced such that the new version of the alloy would not be prone to either the creation of hot tear or microporosity defects. Based on current production casting process outputs at PCC, it was determined that a porosity-resistant chemistry was of primary importance; most hot tearing issues had been eliminated via other changes to casting processes. Using the microporosity-chemistry Fit Models created from the HTTV investigation, a target chemistry range was selected to yield SCMPR results between 0 and 4. The selected chemistry was then validated through the series of alloy chemistry-DTA-hot tear severity models to ensure that the selected chemistry range would not exceed a total HTTV hot tear length of 12. The chemistry was iteratively adjusted until a balanced chemistry range for FSX-414 was established. As

illustrated by Figure 74, the second order relationships that exist within the statistical models make it particularly difficult to arrive at and maintain a viable alloy design.

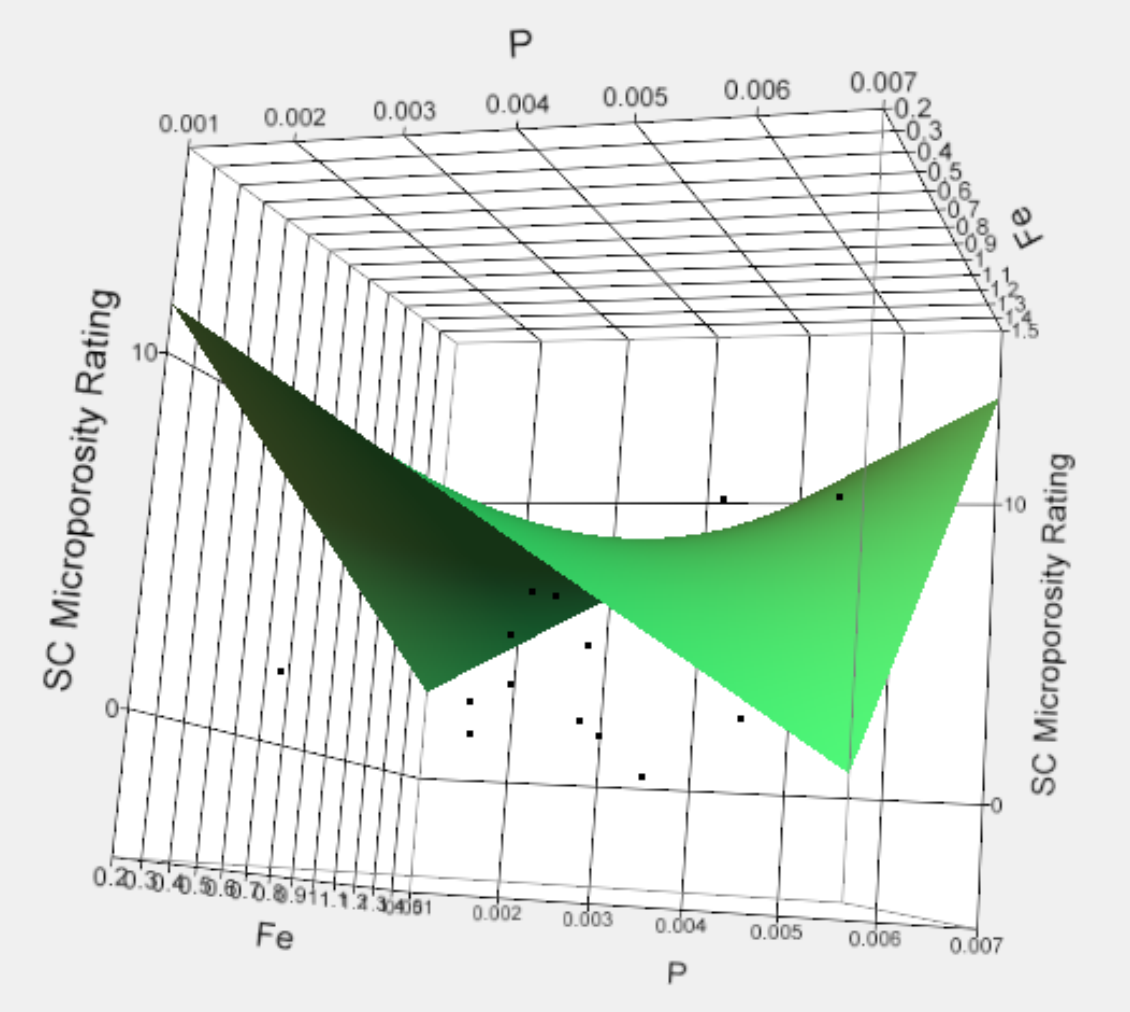


**Figure 72.** View of the saddle-shaped second-order relationship between P and Fe within the Fit Model for microporosity. A change in the concentration of a different element that participates within the same model does not change the shape of the Fe-P relationship, but instead influences the scale of the microporosity response with respect to any single point on the Fe-P surface.

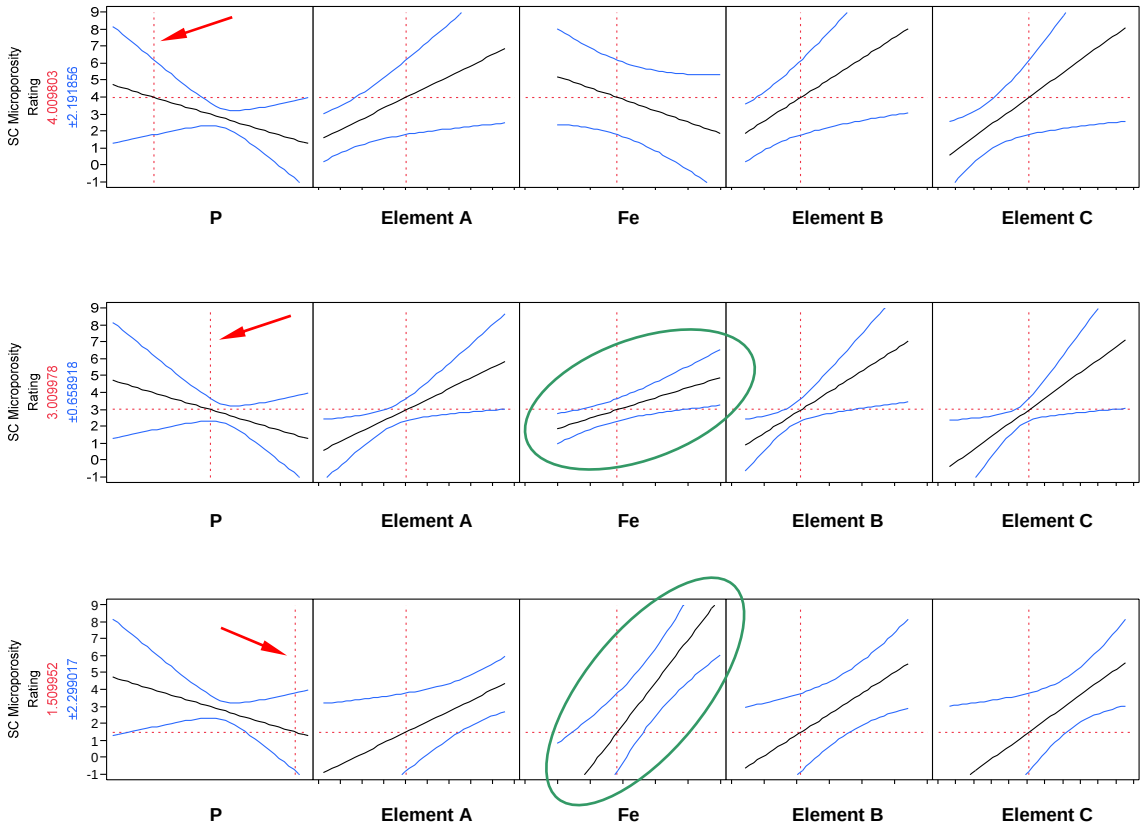


**Figure 73.** Views of a portion of the JMP™ Fit Model Profiler describing the relationship between the SCMPR and chemistry; P and Fe participate in the model with a second order relationship. In changing only the concentration of P between the top and the middle snapshots of the Profiler, the SCMPR is predicted to reduce from 4 to 3. At the same time, the slope of the response for Fe changes from negative to positive. A further increase in the concentration of P as shown in the bottom view decreases the SCMPR prediction to 1.5 and further increases the influence of Fe on the response variable. Also note that aside from changes in their confidence intervals, the other elements remain unaffected by changes in the P concentration.

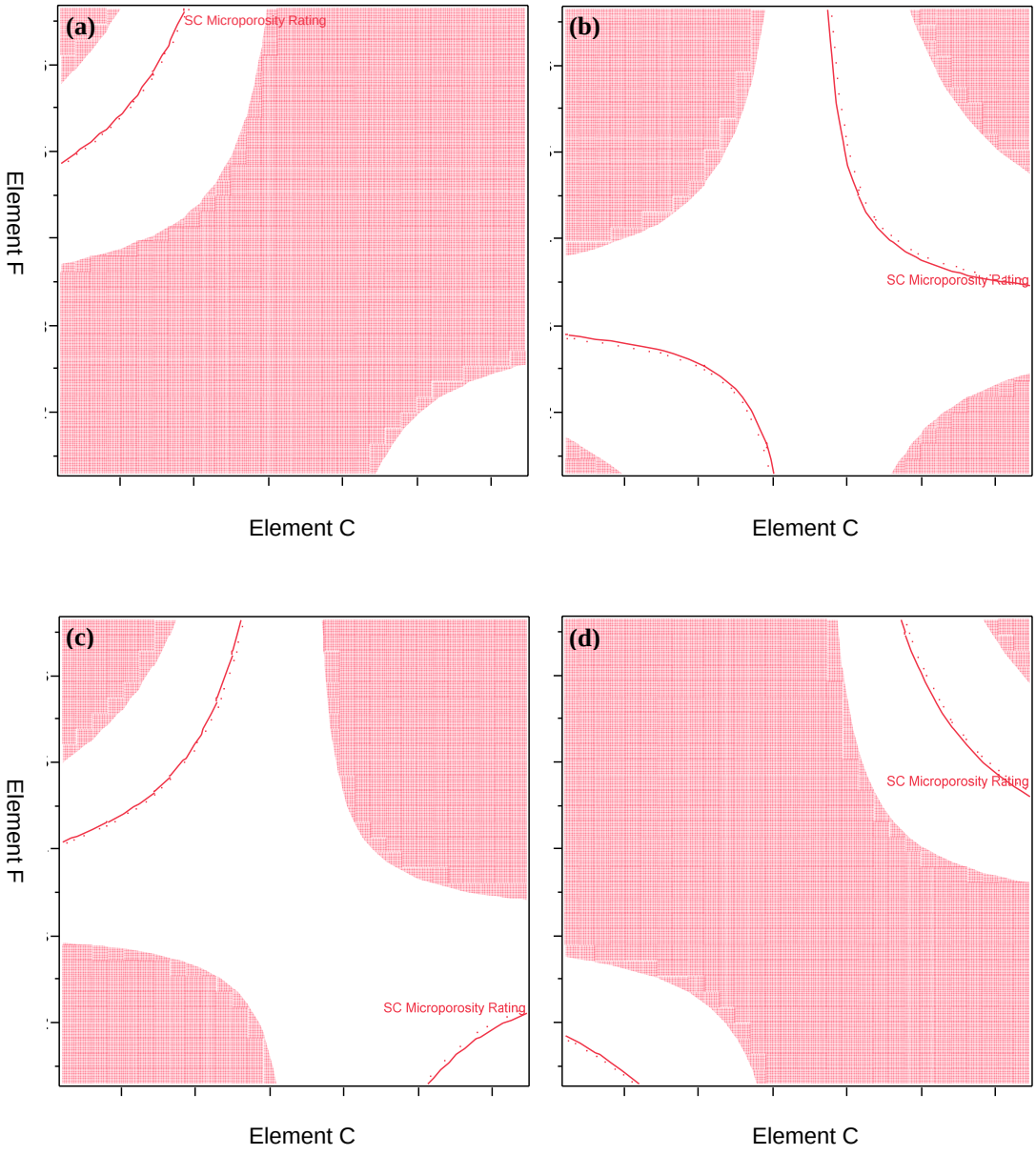


**Figure 74.** Views of the JMP™ Fit Model Contour Profiler for Element C and Element F. Shaded portions of the relationship lie outside of the acceptable SCMPR range of 0 to 4. The solid lines labeled, "SC Microporosity Rating" represent constant contours of SCMPR = 1.5. The scale of the x- and y-axes are identical in all four views. As the concentration of Element D is increased from Frame (a) through Frame (d), the effect of the second-order relationship between Element C and Element F on their target alloy concentration ratios to maintain the desired SCMPR design space can be seen.

# VII. VALIDATION TRIALS

Although the statistical models generated from the HTTV trials were founded upon exceptionally strong regression coefficients, it was necessary to validate their accuracy before using them to optimize the composition of FSX-414 in a predictive way. By employing the HTTV statistical models and the method previously described to determine a target alloy composition based upon a desired outcome of casting quality, "optimized" and "unbalanced" FSX-414 chemistries were created. Three charges were set aside from a single production master heat of AOD refined FSX-414. As the baseline heat had not yet been poured into production castings, no production NDE data was available to classify the heat's tendency to create microporosity or hot tear defects. Table 9 outlines the magnitude of the changes in chemistry for each VTB heat. The relatively small change in the concentration of each element is of particular interest and is consistent with the HTTV casting trial experience.

| | Elements | Baseline (Starting Chemistry) (wt %) | Optimized (Optimized - Baseline) (wt %) | Unbalanced (Unbalanced - Baseline) (wt %) | Range of Balance (Optimized - Unbalanced) (wt %) | Total Range (B'line / Opt'd / Unbal'd) (wt %) |
|---|---|---|---|---|---|---|
| B50A489 Controlled | C | --- | 0.05 | -0.01 | 0.06 | 0.06 |
| | Mn | --- | -0.07 | 0.04 | -0.11 | 0.11 |
| | Si | --- | -0.02 | -0.01 | -0.01 | 0.02 |
| | P | --- | -0.001 | -0.001 | 0.000 | 0.001 |
| | S | --- | 0 | 0 | 0 | 0 |
| | Cr | --- | -0.78 | 0.36 | -1.14 | 1.14 |
| | Ni | --- | 0.47 | -0.73 | 1.20 | 1.20 |
| | W | --- | 0.04 | -0.04 | 0.08 | 0.08 |
| | B | --- | 0.001 | -0.001 | 0.002 | 0.002 |
| | Fe | --- | 0.60 | 0.65 | -0.05 | 0.65 |
| Other Elements | Mo | --- | 0.130 | 0.109 | 0.021 | 0.13 |
| | V | --- | 0.017 | 0.007 | 0.010 | 0.017 |
| | Ti | --- | 0.010 | 0.010 | 0.000 | 0.010 |
| | Al | --- | 0 | 0 | 0 | 0 |
| | Cu | --- | 0 | 0.001 | -0.001 | 0.001 |
| | Zr | --- | 0 | 0 | 0 | 0 |
| | Nb | --- | 0.192 | 0.005 | 0.187 | 0.192 |
| | Co | 50.684 | 50.045 | 50.294 | -0.249 | 0.639 |

**Table 9.** Normalized comparison of the actual chemistries of each of the Validation Test Bar heats.

Alloying additions were calculated and assembled to dope the baseline alloy chemistry to achieve the target compositions for the optimized and unbalanced alloys. All three target compositions are well within the B50A489 material specification and PCC's engineering control limits for FSX-414. Following a trial structure similar to the HTTV experiments, the three VTB molds were poured back-to-back at the PCC Deer Creek facility from the baseline, optimized and unbalanced FSX-414 chemistries using proven production melting techniques and casting parameters. The SCMPR and HTSR for each of the VTB molds as predicted by the HTTV statistical models are charted in Figure 75; calculations for the target chemistries and the actual, measured compositions are provided for the two doped heats.

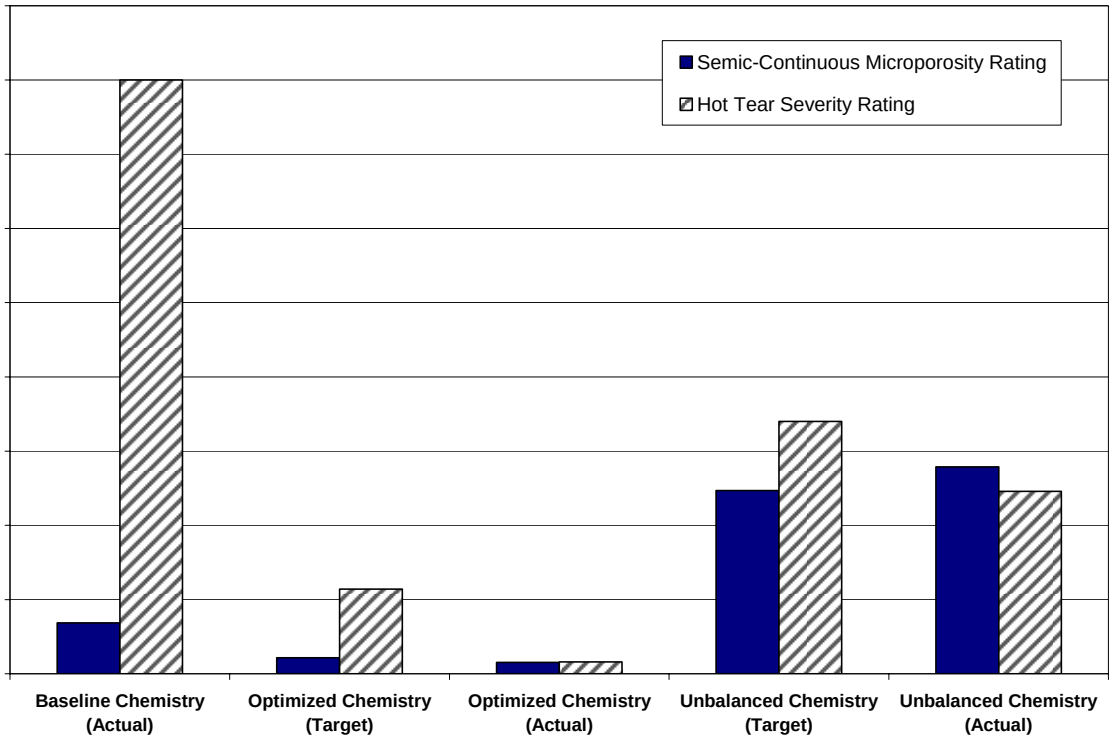


**Figure 75.** Comparison of the predicted SCMPR and HTSR for the target and actual chemistries of each of the Validation Test Bar heats.

## A. Validation Test Bar Microporosity

One bar from each of the VTB molds was sectioned along its longitudinal centerline and prepared for microporosity and microstructural analyses using standard metallographic techniques. It was expected that little difference in microporosity would be observed between the three samples because the validation test bar geometry was specifically created to overpower the tendency of alloys that are prone to microporosity from forming shrinkage defects. Figures 76 and 77 show the worst areas of microporosity detected along the longitudinal centerline for the baseline and optimized alloys, respectively. Although the optimized alloy may arguably show a more homogenous distribution of microporosity, these two alloys performed similarly. The micrograph of the sectioned test bar cast from the unbalanced chemistry shown in Figure 78 illustrates the power of the alloy composition to overwhelm the porosity suppressing effects of the validation test bar geometry.

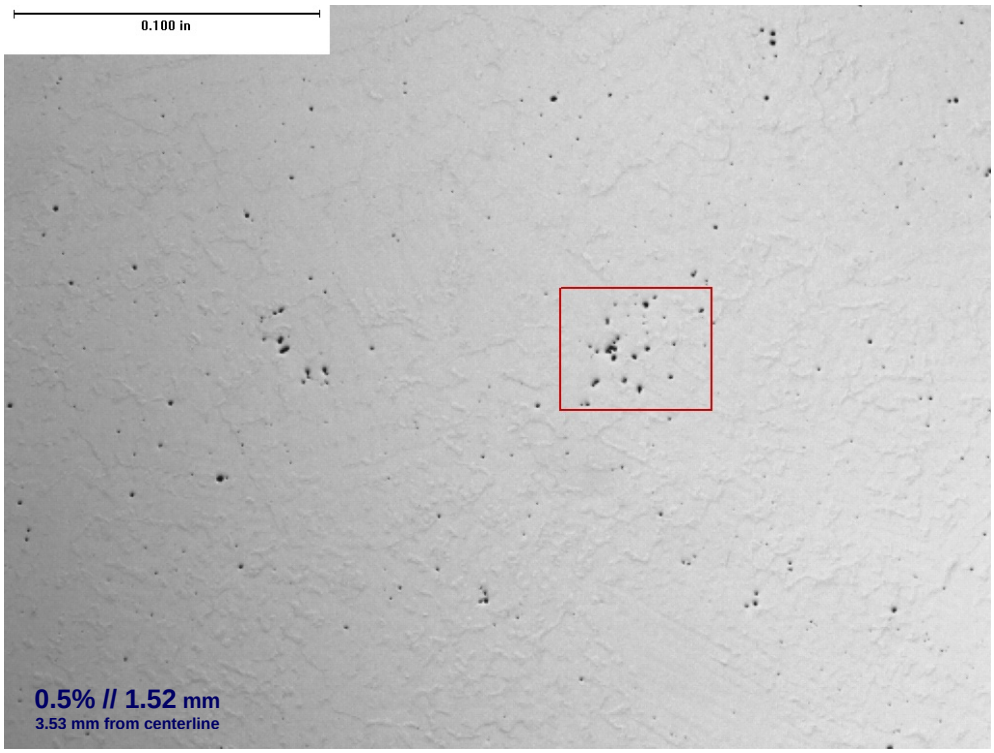


**Figure 76.** Most severe field of microporosity detected along the baseline alloy VTB centerline.

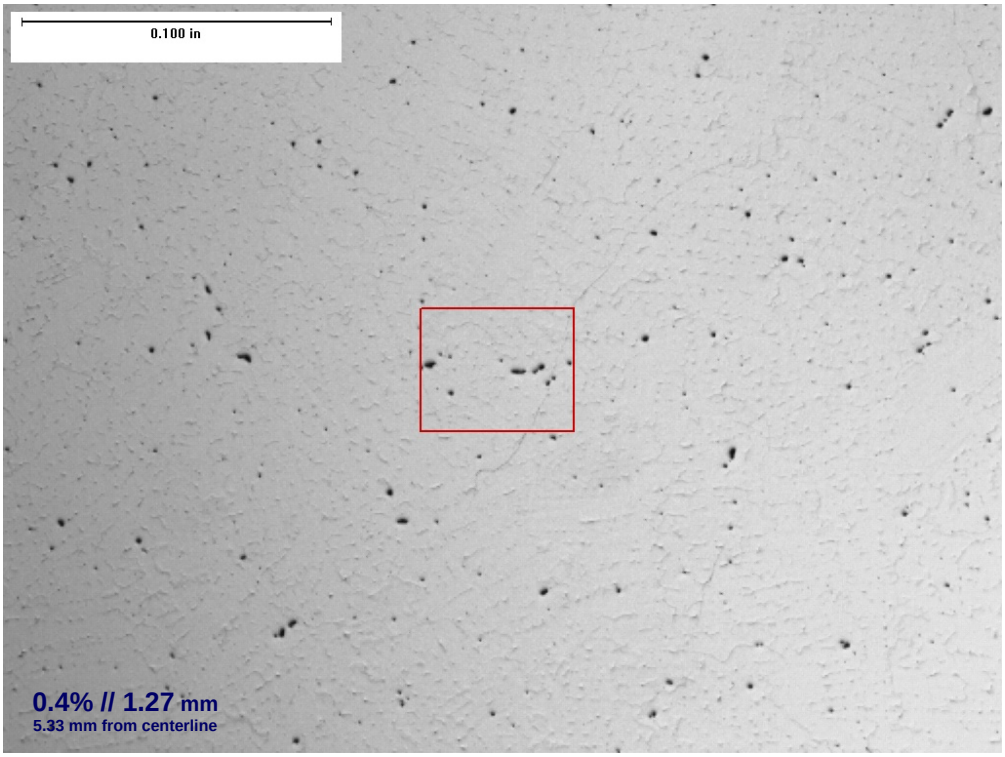


**Figure 77.** Most severe field of microporosity detected along the optimized alloy VTB centerline.

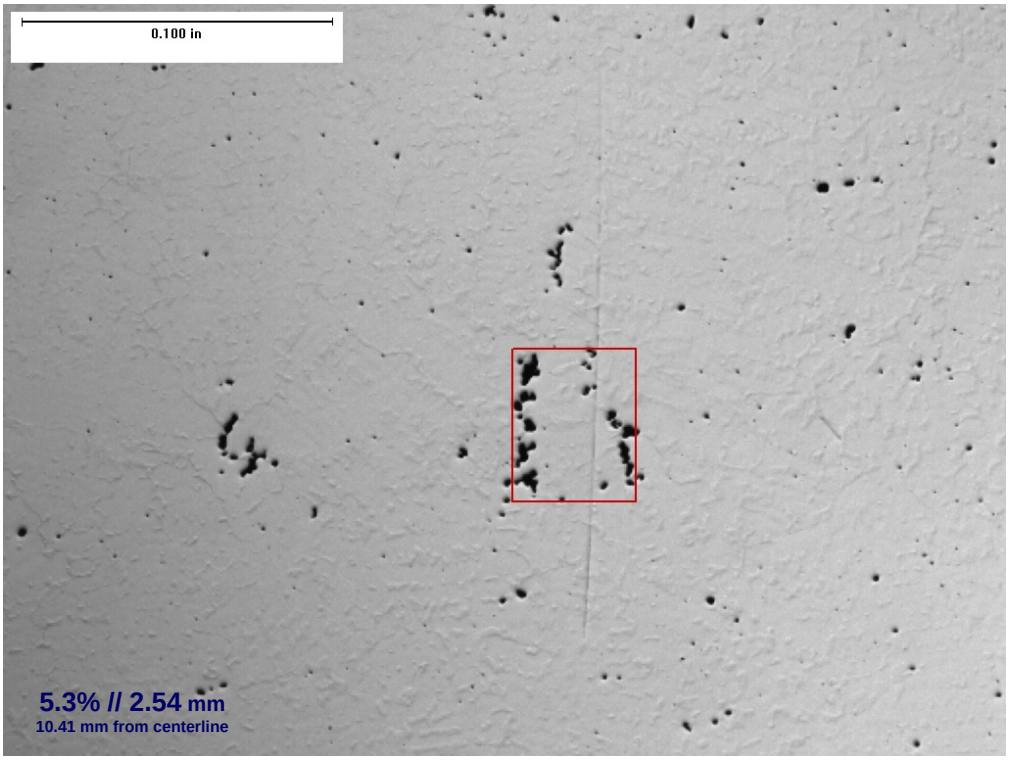


**Figure 78.** Most severe field of microporosity detected along the unbalanced alloy VTB centerline.

## B. Validation Test Bar Microstructure

Following the microporosity analyses, the VTB sections were etched to reveal the carbide microstructure. As shown in Figures 79 through 81, the optimized chemistry shows a greater proportion of $M_{23}C_6$ carbides and markedly less $M_7C_3$ in comparison to the other two alloys. Also, the optimized alloy has a more pronounced interdendritic microstructure that is dominated by primary and secondary $M_{23}C_6$ carbides. Although they differ somewhat, the morphology and scale of the microstructures of the test bars cast from the baseline and unbalanced alloys appear to be more similar to each other than to microstructure of the optimized alloy.

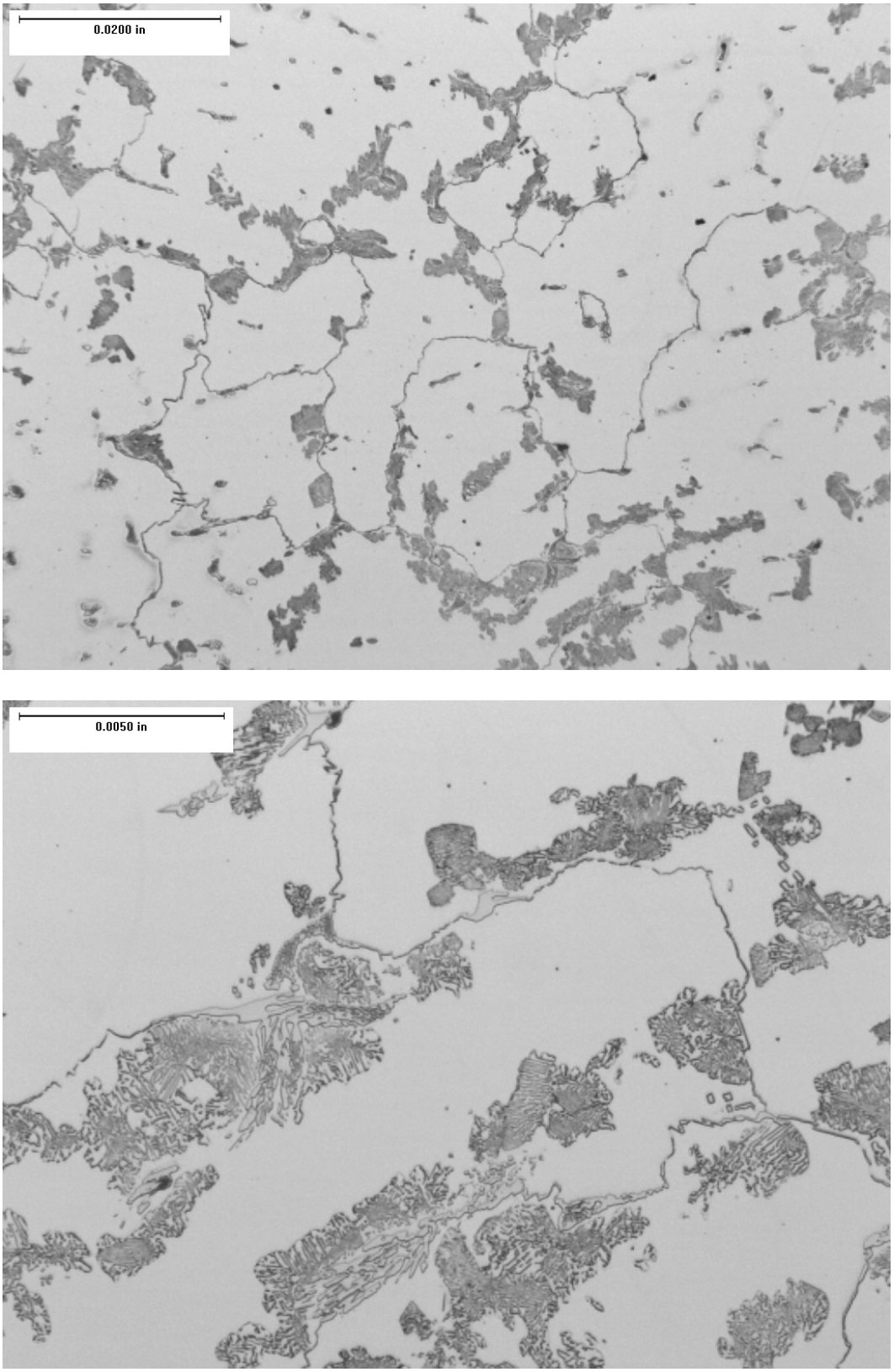


**Figure 79.** Typical carbide microstructure at the centerline of a VTB cast from the baseline alloy chemistry. Micrographs taken at magnifications of 50x (top) and 200x (bottom).

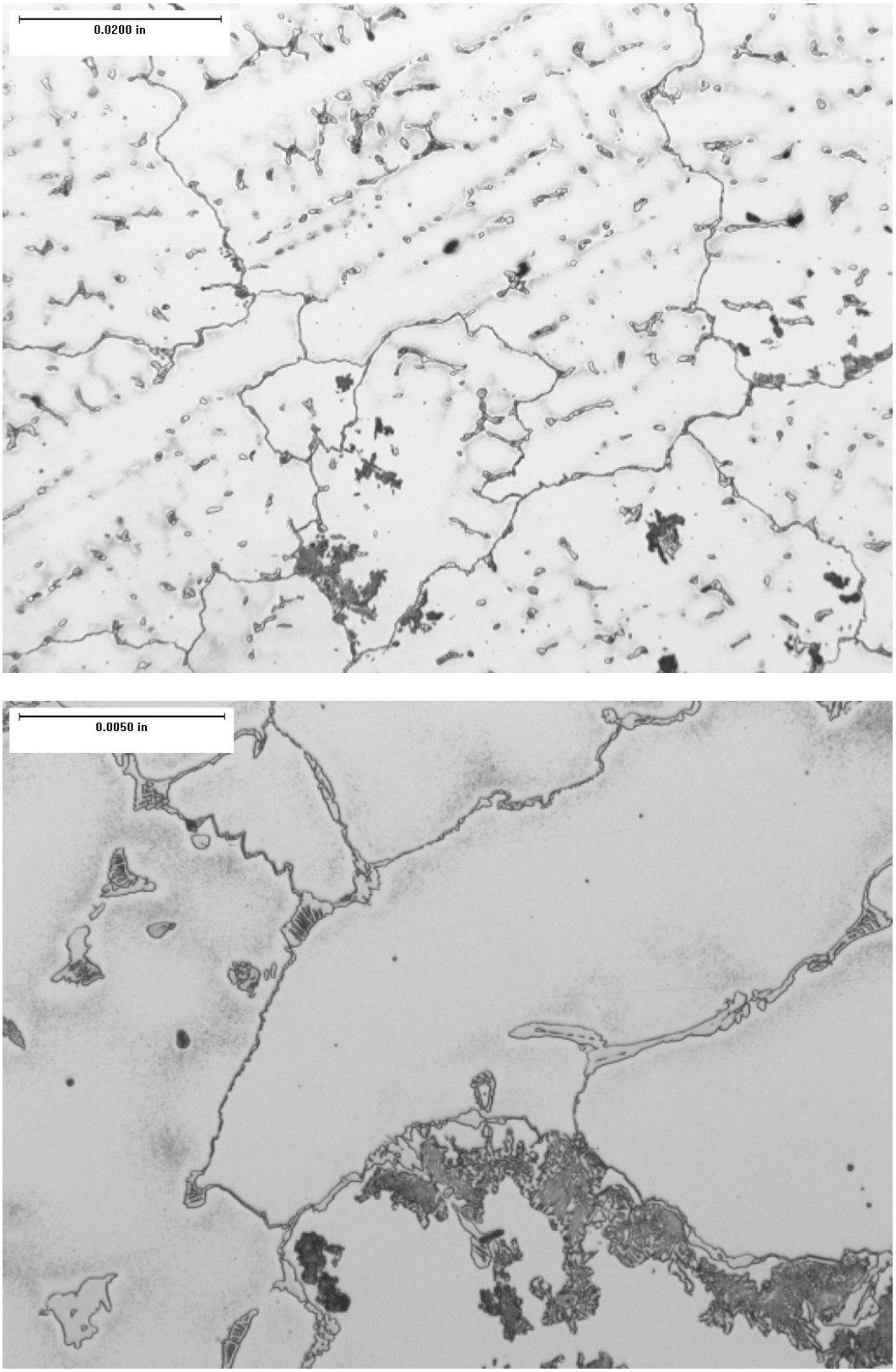


**Figure 80.** Typical carbide microstructure at the centerline of a VTB cast from the optimized alloy chemistry. Micrographs taken at magnifications of 50x (top) and 200x (bottom).

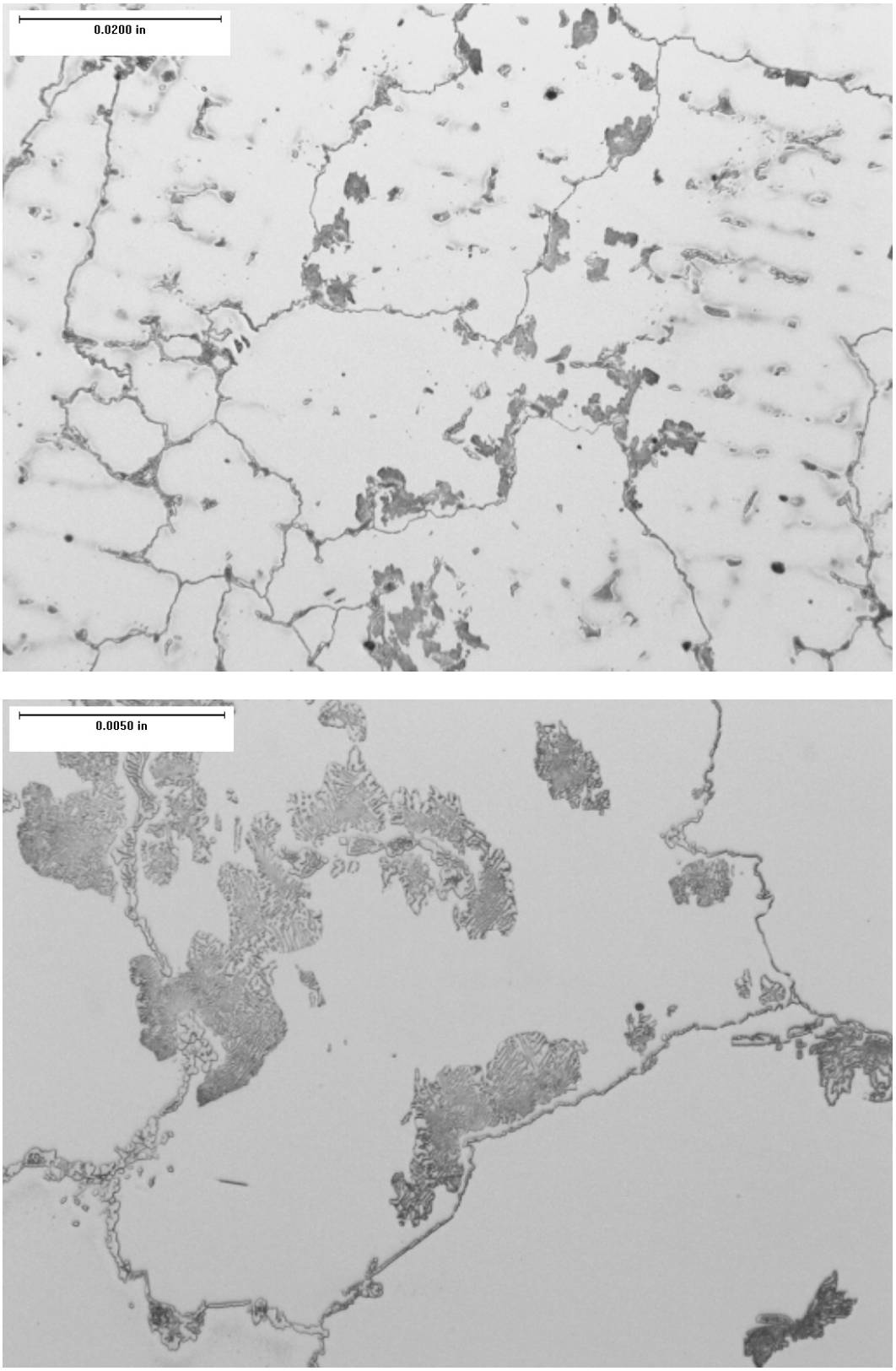


**Figure 81.** Typical carbide microstructure at the centerline of a VTB cast from the unbalanced alloy chemistry. Micrographs taken at magnifications of 50x (top) and 200x (bottom).

## C. Validation Test Bar Grain Structure

Figures 82 through 84 provide photomicrographs of the typical cross-sectional grain structure at the center of the VTB samples; again, differences are visible. The macrostructure of the optimized alloy appears to be more refined and crisp in comparison to the samples from both the baseline and unbalanced alloys.

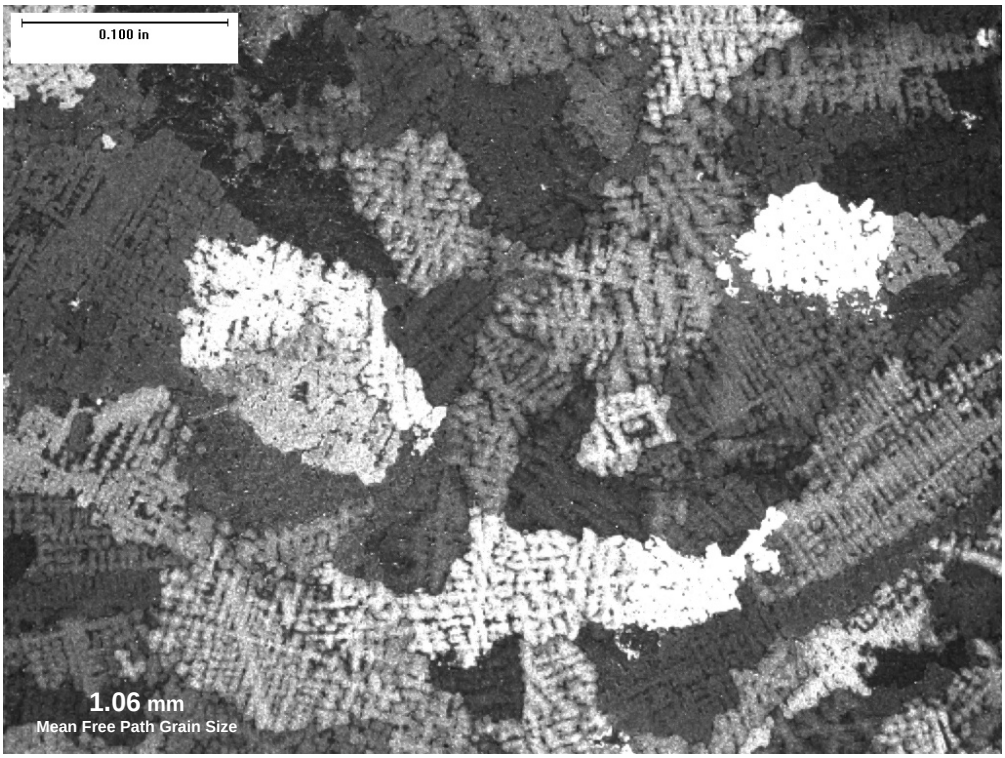


**Figure 82.** Typical grain structure at the center of a VTB cast from the baseline alloy.

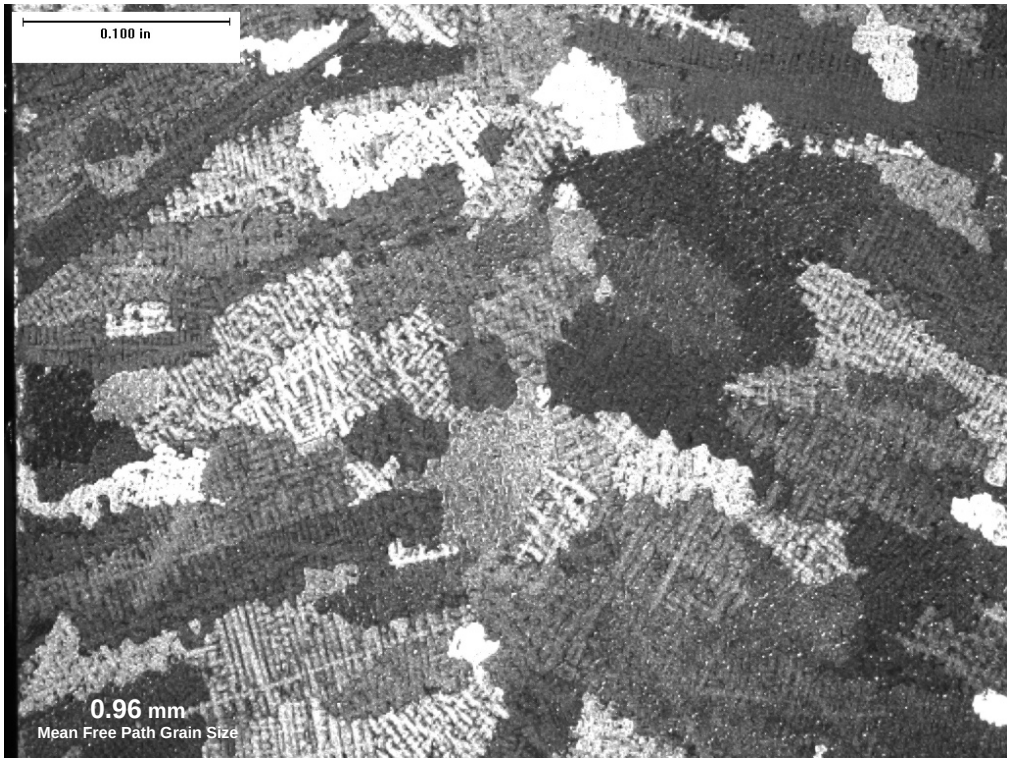


**Figure 83.** Typical grain structure at the center of a VTB cast from the optimized alloy.

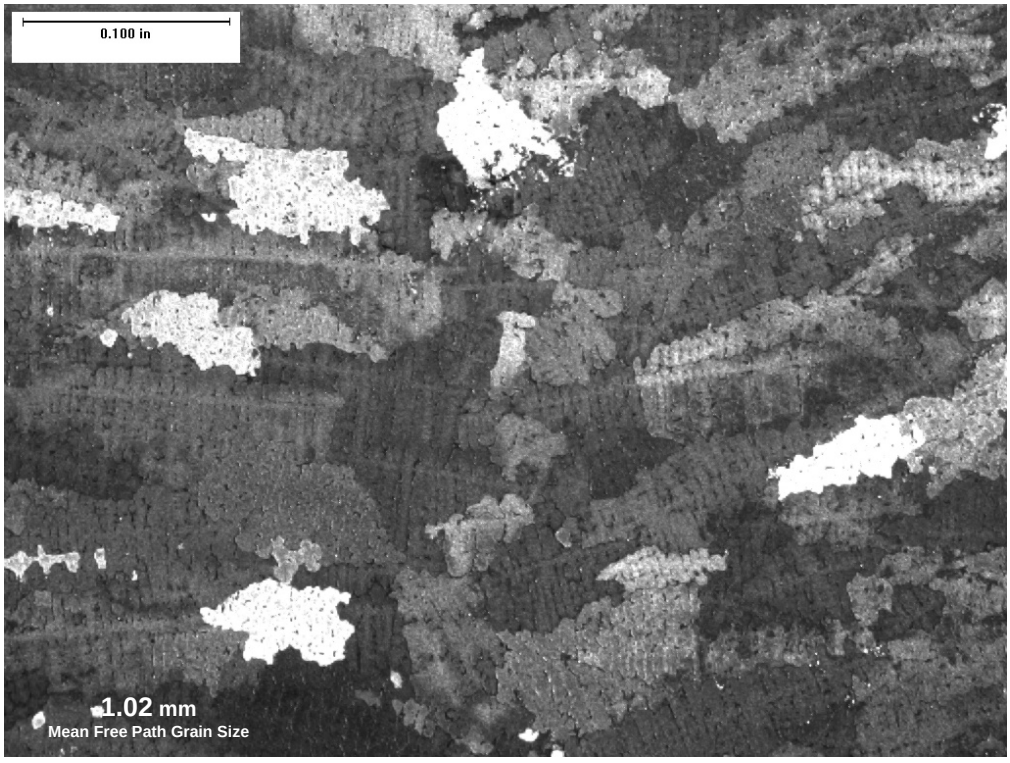


**Figure 84.** Typical grain structure at the center of a VTB cast from the unbalanced alloy.

## D. Stress Rupture Testing

The VTB molds did not provide an adequate number of test bars to complete both the mushy zone tensile tests that had been planned as well as the full compliment of mechanical tests required by the B50A489 FSX-414 alloy specification. Therefore it was decided that stress rupture testing would be the most sensitive tensile test for a high level evaluation of the mechanical properties of the three trial alloys. One test bar from each of the three validation trial molds was selected at random, heat treated and tested for stress-rupture properties per the baseline requirements of the alloy specification. As the data contained in Table 10 describes, each of the three alloys passed the minimum requirements of B50A489. It was noted that the VTB stress rupture results fit within the normal distribution of production FSX-414 master heat qualification test results conducted by PCC Deer Creek.

| Sample | Load Applied *ksi* | Life *hours* | Elongation *4D, %* | Reduction of Area *%* |
|---|---|---|---|---|
| **Baseline** 95320-00001 | 25 | 40 | 31.0 | 30.2 |
| **Optimized** 95320-00002 | 25 | 107 | 30.0 | 45.5 |
| **Unbalanced** 95320-00003 | 25 | 26 | 24.0 | 34.8 |
| **B50A489** Minimum Requirements | **25** | **15** | **10.0** | **20.0** |

**Table 10.** Stress rupture results from the validation test bars which were heat treated and tested in accordance with the requirements of B50A489.

Although there is only a single point of data available for each VTB chemistry, the rupture life of the optimized alloy is so dramatically improved in comparison to the others that it suggests there may be a shift in mechanical property performance based on chemistry. Beltran's [4] observations that atom-equivalent substitutions of Mo for W improve the elevated temperature tensile properties of FSX -414 provide a partial explanation for the VTB stress rupture results. Although a substitution for W was not intentionally made in the VTB alloys, Mo concentrations were managed to particular levels as directed by the HTTV statistical models. In his experiments with a Co-based alloy very similar to FSX-414, Fukui found that the tendency to coarsen carbides could be reduced with additions of Ti, Nb and Zr. By balancing the (Ti, Nb, Zr)/C ratio to ensure $M_{23}C_6$ precipitation was not overly suppressed, such additions were used to enhance creep rupture properties. [67] Because more than one of the elements mentioned above was deliberately managed in the VTB trials, it is presumed that the improvement in the stress rupture properties of the optimized VTB is in fact real due to enhanced solid solution strengthening, smaller grain size and a refined carbide structure; concepts supported by the VTB trial results and the results of both Beltran and Fukui.

## E. Differential Scanning Calorimetry

In comparison to the HTTV DTA data, the DSC data sets collected from the validation trial castings were exceptionally clean, making interpretation of the results relatively straightforward. The liquidus temperatures of the three VTB heats varied across a 7°C range while the solidus temperatures differed by 14°C. Both DSC curves from each of the three heats displayed clear peaks marking the final eutectic solidification event, a feature not always discernable within each of the HTTV DTA data sets. The balanced and unbalanced alloys also displayed evidence of precipitation of another phase, perhaps an MC or $M_6C$ carbide, around 1325°C. This same peak was weakly identifiable in the data from the baseline alloy but was almost small enough to be discounted as signal noise. No clear connection could be established between the change in magnitude of the intermediate peaks and the observed microstructure. Based on these data, it is clear that the magnitude of the intermediate and final carbide precipitation events change appreciably with only small changes in alloy chemistry.

The obvious difference in the magnitude of the knee of the DSC curves between ~1325°C and ~1375°C as seen in Figure 85 led to additional analyses beyond those conducted on the HTTV DTA curves. As previously discussed, the area beneath the DSC curve to the baseline is proportional to the enthalpy of the solidification event. Using stepwise integration between the DSC curve and the calculated baseline, the fraction solid curve was developed for each set of data. Figure 86 provides the calculated $f_s$ versus temperature relationships for the same three DSC curves provided in Figure 85. Because the change in slope of the $f_s$ curves at a specific temperature may not necessarily relate to a difference in solidification behaviour based on the relationship of an alloy's mushy zone with an absolute temperature scale, the rate of change in solid development was normalized against fraction solid as illustrated in Figure 87. Figure 88 expands the latter portion of the curves in Figure 87 to provide more clarity over the critical temperature range. From these data, we see there is a distinct difference in the rate of development of solid between the three FSX-414 variants. These data correlate very strongly

with the results of Zhang and Singer [36] provided in Figure 17 and Figure 18 and discussed previously. Zhang and Singer's data have been incorporated into Figure 87 and Figure 88 to illustrate the very similar trends in the rate of FSX-414 fraction solid development compared to their castability response variables.

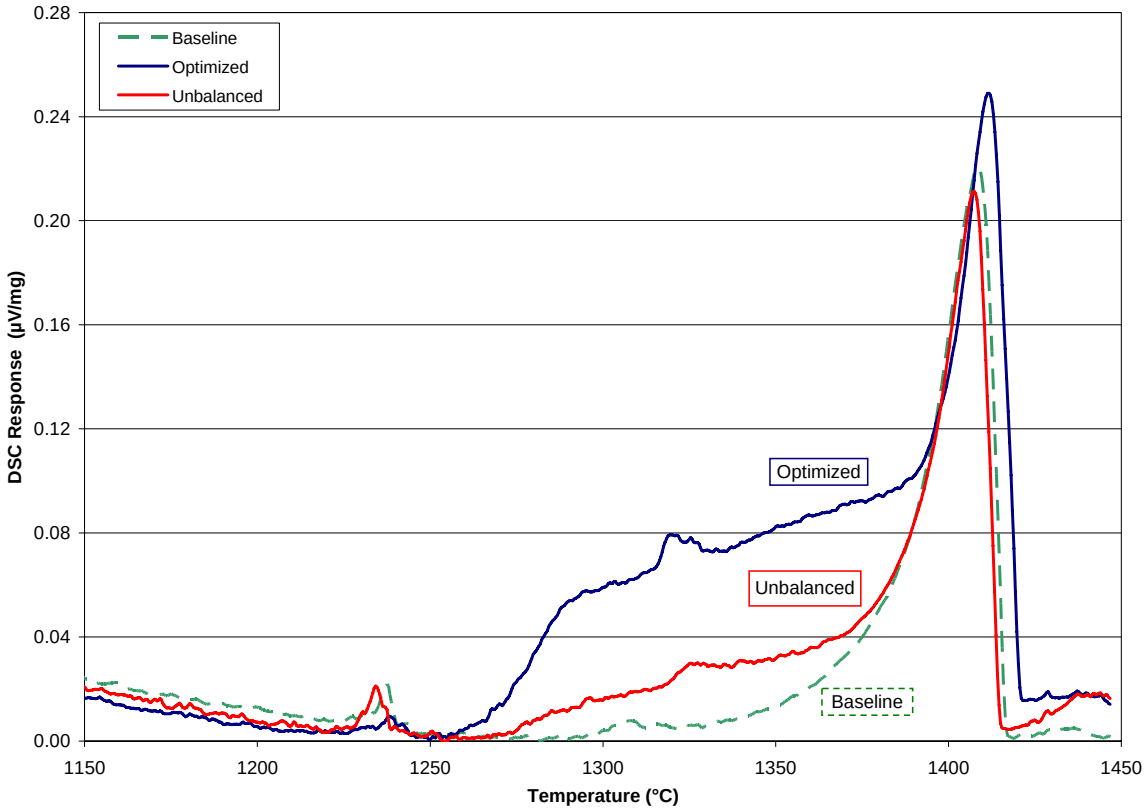


**Figure 85.** Superimposed DSC curves from each of the three VTB trials. Note the marked difference in the shape of the curves between ~1275°C and ~1375°C.

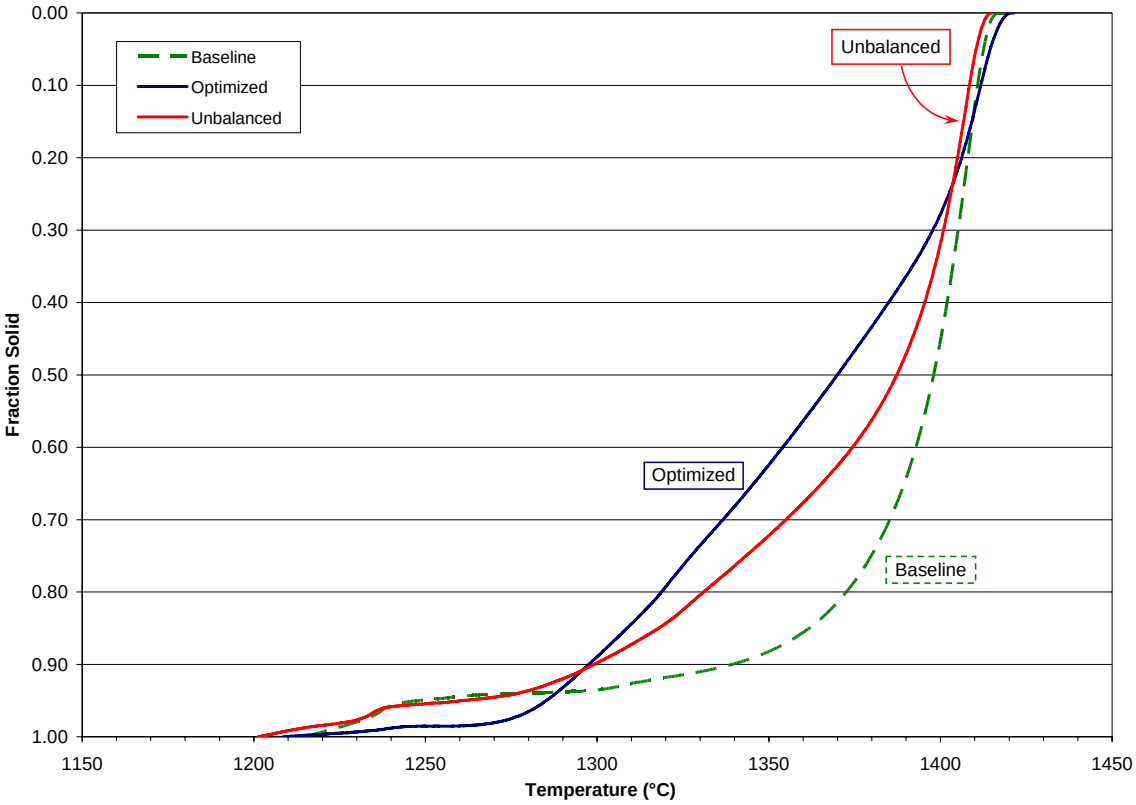


**Figure 86.** Superimposed calculated fraction solid versus temperature curves from each of the three sets of VTB trial DSC data illustrated in Figure 85.

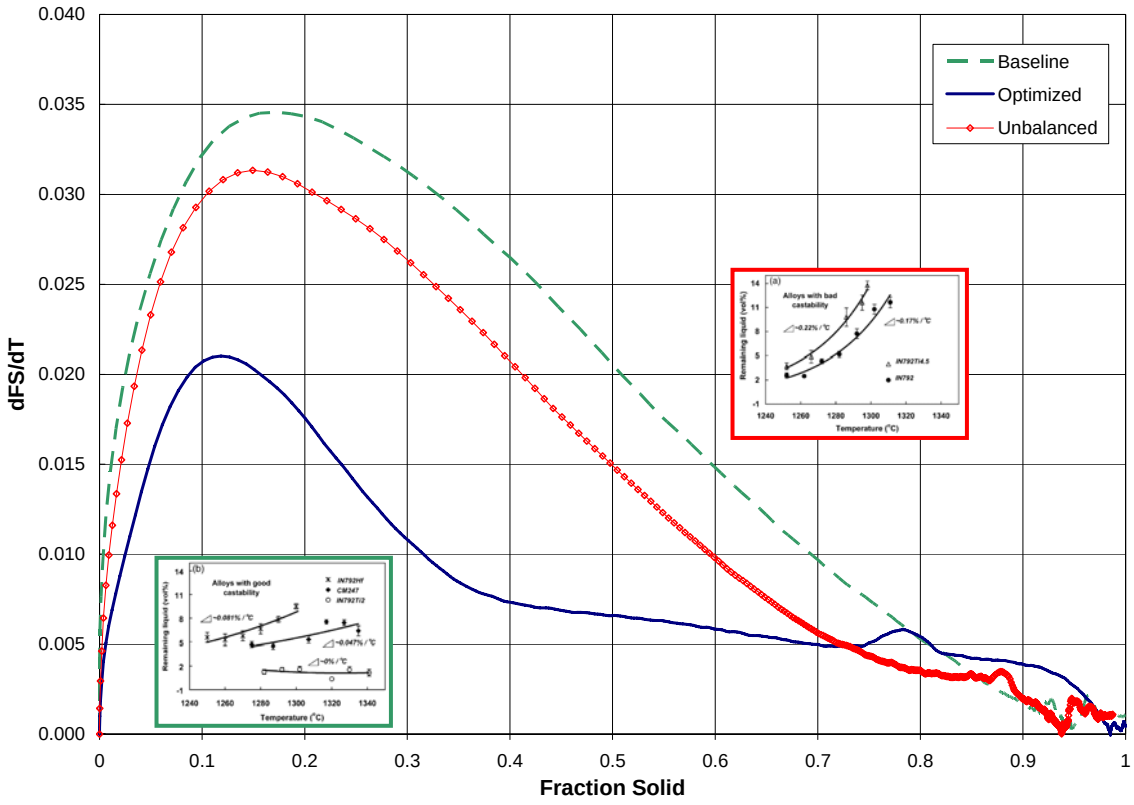


**Figure 87.** Superimposed average rate of change of calculated fraction solid versus temperature curves from each of the three sets of VTB trial DSC data. The results from the duplicate DSC data of each VTB trial were averaged to generate the curves illustrated. Figure 17 (red outline, high propensity for hot tearing) and Figure 18 (green outline, low tendency for hot tearing) have been added to illustrate the similarities between the published literature and the results of the VTB experiment.

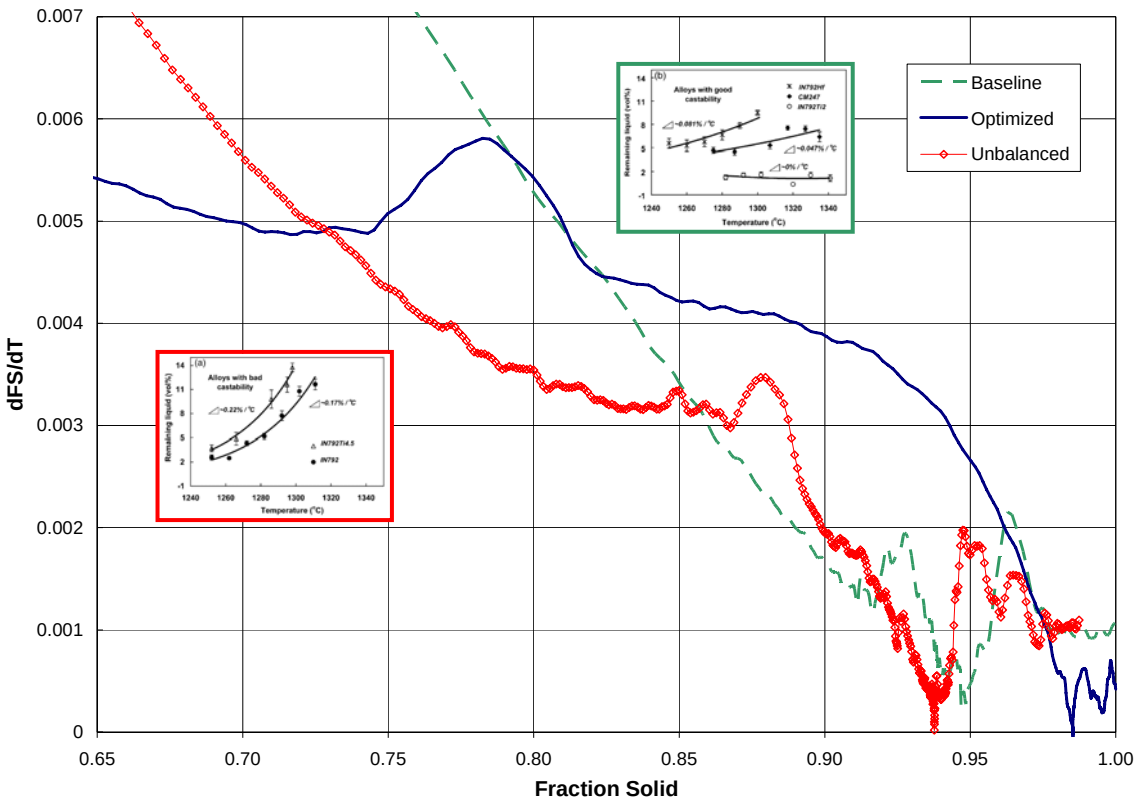


**Figure 88.** Expanded view of the final 35% of solidification from Figure 87; average rate of change of the calculated fraction solid versus temperature for the VTB trial alloys. Figure 17 (red outline, high propensity for hot tearing) and Figure 18 (green outline, low tendency for hot tearing) have been added to illustrate the similarities between the published literature and the results of the VTB experiment.

At the outset of the solidification process, the rate of solid development for all three alloys rapidly increases to its peak rate at a $f_s$ between 0.1 and 0.2, after which there is a constant and generally equivalent decrease in the rate of solidification. Figure 87 shows the optimized alloy develops solid less quickly than either of the other two alloys both initially, and especially after establishing its second, almost constant rate of solidification at 0.4 $f_s$. Figure 88 shows the optimized alloy's slowly decreasing rate of solidification continues beyond 0.9 $f_s$ before the rate of solidification decreases dramatically; a point much further through the mushy zone than either of the other two alloys. The decreasing rate of solidification between 0.94 and

0.98 $f_s$ established by the optimized alloy is identical to the rate established by the other two alloys at higher fractions solid. The final 0.02 solid fraction developed by the optimized alloy is attributed to eutectic carbide solidification. By comparison, the other two alloys appear to generate 3 to 5% of final eutectic carbide.

The peaked increase in the rate of solidification of the optimized alloy at 0.77 $f_s$ is also seen at 0.87 $f_s$ and 0.93 $f_s$ for the unbalanced and baseline alloys respectively. It is interesting to note that these peaks are separated so distinctly across the critical temperature zone between the three similar alloy compositions. In her DTA heating experiments with Udimet 700, Burton discovered that small changes in B and C content changed the shape of the thermogram because the specific composition of the $M_2B_3$ borides had changed. [7] In his review of cobalt-based superalloys, Beltran explains that the morphology and therefore the solidification behaviour of carbides are known to change with alloy composition. [4] Based on these data, it would be reasonable to propose that changes in the specific composition of the $M_{23}C_6$ and $M_7C_3$ carbides would be responsible for the shifts in the FSX-414 VTB thermogram events. The observations of changes to carbide microstructure adjacent to hot tears previously discussed and depicted in Figures 42 through 45 would support this concept as well.

By visually evaluating the volume of the phases in the photomicrographs shown in Figures 79 through 81 and comparing them against the events observed in each of the thermograms in the Figure 88, it appears as though the second to last solidification event represents the freezing of $M_{23}C_6$ carbides in the interdendritic passages. The final thermogram event is therefore most likely related to the formation of the eutectic $M_7C_3$ carbides. Although more specific investigations would need to be conducted to confirm these hypotheses, the assessments are made based on establishing a link between the volume of each phase shown in the photomicrographs and the relative magnitude of the thermogram events.

The inflection points in the thermograms are also reminiscent of those previously described and illustrated in the JMatPro$^{TM}$ thermodynamic model results shown in Figure 60.

The differences in position of the experimental versus theoretical events could be attributed to the incomplete database used for the thermodynamic modeling or to the equilibrium model conditions versus the non-equilibrium DSC sample solidification. Miller, *et al.* caution that thermodynamic predictions should be evaluated with caution as many of the predicted phases does not appear in commercial alloys. Therefore, they counsel that it is essential to baseline the predicted microstructure against the actual microstructure achieved. In some cases, it will be necessary to suppress absent phases from the TDM calculations in order to get satisfactory agreement between atom probe microscopy of actual phases and the thermodynamic model results. [68]

In his team's experiments with steels, Chojecki used TDM to predict the change in length of the MZ based on the composition of the last liquid to freeze. They found that increasing the C content influenced the activity of S to partition to the interdendritic liquid, causing a depression in the interdendritic liquid solidus temperature and therefore increasing the tendency for hot tearing. [44] Although the VTB trials in the present investigation were not constructed to experimentally evaluate the propensity of the FSX-414 alloys to hot tear, one could still reasonably apply Chojecki's experience and propose that once the desired shape of an alloy thermogram is known, alloy and/or casting behaviour could be reasonably predicted. Continuing this train of thought, the postulate provided by Zhang and Singer [36] and Forest and Bercovici [31] that suggests there is opportunity to design castable alloy compositions around an optimal $\frac{df_s}{dT}$ has been supported by this investigation. This type of a laboratory-centered initial approach to alloy development could provide meaningful data to alloy developers more effectively than by running costly and time consuming casting screen trials.

# VIII. SUMMARY AND CONCLUSIONS

The effects of small changes in the chemical composition on the solidification behaviour of FSX-414 have been evaluated. Using a test vehicle casting and charges of material set aside from production heats of VIM master alloy, statistical models were constructed to describe the effects of small changes in alloy composition on the creation of solidification defects. Several elements were found to interact, generating non-planar relationships with the casting response variables. This explains why previous statistically-based studies using less sophisticated analyses could not explain the differences in alloy behaviour from master heat to master heat.

The statistical models were subsequently tested by using them to generate target FSX-414 chemistries for optimized and unbalanced alloy compositions. Validation castings were poured from these chemistries and evaluated, revealing clear differences in microporosity, microstructure and grain size. Detailed analyses of DSC data generated from the recast validation samples showed that the optimized alloy solidified in a distinctly different way. Its lower rate of solidification continued further into the critical temperature range, leaving significantly less eutectic liquid to freeze at the end of the solidification process. The reduced volume of isolated eutectic liquid is responsible for the reduced level of microporosity created by the optimized alloy. The differences observed in the rate of solid development through the mushy zone correlate closely with other published experimental results and suggest that the optimized FSX-414 composition would also be less prone to hot tearing, as intended.

The results of this investigation show that small changes in the balance of the FSX-414 chemistry can result in significant changes to the development of solid through the mushy zone therefore producing differences in the types and severity of solidification-related defects. The interactive effects of elements both within and outside of specification limits and engineering foundry control limits were found to be critical to the success of the FSX-414 alloy characterization and optimization.

When coupled with the appropriate and accurate use of DSC analysis, the novel statistical analysis approach used in this investigation holds significant promise for the optimization of other alloys. Provided that the shape of the DSC curve for both superior and poorly-performing alloy compositions is known, a statistical model could be constructed for any alloy using only DSC and chemistry data to determine the effects and interactions of alloying elements on key metallurgical and/or mechanical property response variables. The statistical model could then be used to create a target alloy composition and to set foundry control limits within customer specification ranges to optimize the response variables of interest. It is both conceivable and possible that much more alloy optimization work, especially early in the development cycle, could be conducted on a laboratory scale, thus dramatically reducing investments in costly and time consuming experimental and production casting trials.

# REFERENCES


1. K. Ronan, "A Statistical Analysis of Variations in Hot Tear Performance and Microporosity Formation Versus Composition in Investment Cast FSX-414", *Superalloys 2008*, (TMS, 2008), 357-366

2. Q. Han, "Influence of Chemical Composition on Hot Tearing Susceptibility in FSX-414 Alloy," Transactions of American Foundry Association, 2004.

3. C.P. Sullivan, J.D. Varin and M.J. Donachie, Jr., "Relationship of Properties to Microstructure in Cobalt Base Superalloys", *Metals Engineering Quarterly*, 9 (2) (1969), 16-28

4. C. Sims, N. Stoloff and W. Hagel, *Superalloys II* (New York, NY: John Wiley & Sons, Inc., 1987), 136-162

5. J.R. Davis, ed., *Alloying: Understanding the Basics*, (Materials Park, OH: ASM International, 2001), 540-548

6. J. Lecomte-Beckers, "Relation Between Chemistry, Solidification Behaviour, Microstructure and Microporosity in Nickel-base Superalloys", *Superalloys 1988*, (TMS, 1988), 713-722

7. C. Burton, "Differential Thermal Analysis and the Mechanisms of Minor Additions in Superalloys", *Superalloys 1976*, ed. D.R. Muzyka et al. (TMS, 1976), 147-158

8. M.F. Rothman, R.D. Zordan, and D.R. Muzyka, "Role of Refractory Elements in Cobalt-Base Alloys", *Refractory Alloying Elements in Superalloys*, ed., J.K. Tien and S. Reichman, (ASM, 1984), 101-115

9. J.R. Davis, ed., *Nickel, Cobalt and Their Alloys* (Materials Park, OH: ASM International, 2000), 367

10. P. Berthod, et al., "Experimental and thermodynamic study of microstructure evolution in cobalt-base superalloys at high temperature", Computer Coupling of Phase Diagrams and Thermochemistry, 27 (2003), 353-359

11. G.F. Vander Voort, ed., *ASM Handbook Volume 9: Metallography and Microstructures*, (Materials Park, OH: ASM International, 2004), 762-774, 834-851

12. J. Campbell, “Feeding Mechanisms in Castings”, *AFS Cast Metals Research Journal*, 5 (1) (1969), 1-8

13. J. Campbell, *Castings* (Jordan Hill, Oxford: Elsevier Ltd., 2003), 205-259

14. A.K Gupta, et al., “Pore formation in cast metals and alloys”, *Journal of Materials Science*, 27 (4) (1992), 853-862

15. T.S. Piwonka and M.C. Flemings, “Pore Formation in Solidification”, Transactions of the Metallurgical Society of the AIME, 236 (1966), 1157-1165

16. J. Lecomte-Beckers, “Study of Microporosity Formation in Nickel-Base Superalloys”, *Metallurgical Transactions A*, 19A (1988), 2341-2348

17. G.K. Sigworth and C. Wang, “Mechanisms of Porosity Formation during Solidification: A Theoretical Analysis”, *Metallurgical Transactions B*, 24B (1993), 349-364

18. G.K. Sigworth and C. Wang, “Evolution of Porosity in Long Freezing Range Alloys”, *Metallurgical Transactions B*, 24B (1993), 365-377

19. R.E. Painter and J.M. Young, “Liquid Metal Treatments to Reduce Microporosity”, *Superalloys 1988*, (TMS, 1988), 417-425

20. Y.W. Lee, E. Chang and C.F. Chieu, “Modeling of Feeding Behavior of Solidifying Al-7Si-0.3Mg Alloy Plate Casting”, *Metallurgical Transactions B*, 21B (1990), 715-722

21. S. Minakawa, I.V. Samarasekera, F. Weinberg, ”Centerline Porosity in Plate Castings”, *Metallurgical Transactions B*, 16B (1985) 823-829

22. M.C. Flemings, *Solidification Processing* (New York, NY: McGraw-Hill, Inc., 1974), 234-239

23. C.M. Hermesmann, “Thermal Simulations for the Prediction of Porosity in Investment Castings for Stellite Grade Superalloys” (M.A.Sc. Thesis, University of British Columbia, 1996), 57-64

24. M.J. Cieslak, et al., “A Melting and Solidification Study of Alloy 625”, *Metallurgical Transactions A*, 19A (1988), 2319-2331

25. Y. Zhu et al., “Effect of P,S,B and Si on the Solidification Segregation of Inconel 718 Alloy”, *Superalloys 718, 625, 706 and Various Derivatives*, ed. E.A. Loria (TMS, 1994), 89-98

26. Y. Zhu et al., “A New Way to Improve the Superalloys”, *Superalloys 1992*, eds. S.D. Antolovich et al., (TMS: 1992), 145-154

27. M. Rappaz, J.-M. Drezet and M. Gremaud, “A New Hot-Tearing Criterion”, *Metallurgical and Materials Transactions A*, 30A (1999), 449-455

28. K.P. Ronan, “The Evolution of Cast Nickel Base Single Crystal Superalloys – A Discussion of Microstructure Mechanical Property Performance, Strengthening Mechanisms and Alloying Additions” (Final Report: MATL 7966, Auburn University, 2008)

29. H.F. Bishop, C.G. Ackerlind and W.S. Pellini, “Metallurgy and Mechanics of Hot Tearing”, *Transactions of the American Foundrymen’s Society*, 60 (1952), 818-833

30. M.S. Lewandowski, R.A. Overfelt, “High Temperature Deformation Behaviour of Solid and Semi-solid Alloy 718”, *Acta Metallurgica*, 47 (18) (1999), pp 4695-4710

31. B. Forest and S. Bercovici, “Experimental study of mechanical properties of aluminum alloys during controlled solidification: application to hot tearing”, *Solidification Technology in the Foundry and Casthouse*, (London: The Metals Society, 1982), 607-612

32. C.S. Lin and J.A. Sekhar, “Solidification morphology and semisolid deformation in the superalloy Rene 108 – Part III Equiaxed solidified microstructures”, *Journal of Materials Science*, 29 (1994), 3637-3642

33. C.S. Smith, “Grains, Phases, and Interfaces: An Interpretation of Microstructure”, AIME Transactions, 175 (1948), 15-51

34. S. Lin, C. Aliravci and M.O. Pekguleryuz, “Hot-Tear Susceptibility of Aluminum Wrought Alloys and the Effect of Grain Refining”, *Metallurgical Transactions A*, 38A (2007), 1056-1068

35. J. Zhang, “Effect of Ti and Ta on hot cracking susceptibility of directionally solidified Ni-based superalloy IN792”, *Scripta Materialia*, 48 (2003), 677-681

36. J. Zhang and R.F. Singer, “Hot tearing of nickel-based superalloys during directional solidification”, *Acta Materialia*, 50 (2002), 1869-1879

37. J. Zhang, “Hot Tearing In Directionally Solidified Ni-Based Superalloys”, *Superalloys 2004*, eds. K.A. Green et al., (TMS: 2004), 727-733

38. Y. Zhou, A. Volek and R.F. Singer, “Influence of Solidification Conditions on the Castability of Nickel-Base Superalloy IN792”, *Metallurgical and Materials Transactions A*, 36A (2005), 651-656

39. N. Wang, et al., “Solidification cracking of superalloy single- and bi-crystals”, *Acta Materialia*, 52 (2004), 3173-3182

40. C. Monroe, C. Beckerman, “Development of a hot tear indicator for steel castings”, *Materials Science and Engineering*, A413-414 (2005), 30-36

41. H.F. Bishop, C.G. Ackerlind and W.S. Pellini, “Investigation of Metallurgical and Mechanical Effects in the Development of Hot Tearing”, *Transactions of the American Foundrymen’s Society*, 65 (1957), 247-258

42. G. Kao and S. Cou, “Hot Tearing of Ternary Mg-Al-Ca Alloy Castings”, *Metallurgical and Materials Transactions A*, 37A (2006), 3647-3663

43. J. Zhang and R.F. Singer, “Effect of Grain-Boundary Characteristics on Castability of Nickel-Base Superalloys”, *Metallurgical and Materials Transactions A*, 35A (2004), 939-946

44. A. Chojecki, I. Telejko, T. Bogacz, “Influence of chemical composition on the hot tearing formation of cast steel”, *Theoretical and Applied Fracture Mechanics*, 27 (1997), 99-105

45. J. Zhang and R.F. Singer, “Effect of Zr and B on Castability of Ni-Based Superalloy IN792”, *Metallurgical and Materials Transactions A*, 35A (2004) 1337-1342

46. R.A. Rosenberg, M.C. Flemings and H.F. Taylor, “Nonferrous Binary Alloys Not Tearing”, Transactions of the American Foundrymen’s Society, 68 (1960), 518-528

47. J.P. Hirth and G.M. Pound, *Condensation and Evaporation, Progress in Materials Science*, Vol. 11, (Oxford, UK: Pergamon Press, 1963), 157-161

48. R.A. Overfelt, M.S. Lewandowski and R.C. Wilcox, “Effects of Mushy Zone Tensile Stresses on Pore Nucleation in Superalloy 718”, Proceedings of the 31st National Heat Transfer Conference, HTD-Vol. 323, V. Prasad et al., eds., ASME, New York, NY, 1996, 49

49. M.H. Yoo and H. Trinkaus, “Crack and Cavity Nucleation at Interfaces During Creep”, *Metallurgical Transactions A*, 14A (1983), 547-561

50. M.S. Lewandowski, “High Temperature Deformation Behavior of Inconel 718 at Temperatures Reaching Into the Mushy Zone” (Ph.D. Dissertation, Auburn University, 2000)

51. R.I. Wu and J.H. Perepezko, “Liquidus Temperature Determination in Multicomponent Alloys by Thermal Analysis”, *Metallurgical Transactions A*, 31A (2000), 497-501

52. J. Lecomte-Beckers, “Study of Solidification Features of Nickel-Base Superalloys in Relation with Composition”, *Metallurgical Transactions A*, 19A (1988), 2333-2340

53. R.M. Kearsey, et al., “Compositional design considerations for microsegregation in single crystal superalloy systems”, *Intermetallics*, 12 (2004), 903-910

54. N. D'Souza, et al., "Solidification path in the Ni-base superalloy, IN713LC – quantitative correlation of last stage of solidification", *Scripta Materialia*, 53 (2005), 729-733

55. G.K. Bouse, "Application of a Modified Phase Diagram to the Production of Cast Alloy 718 Components", *Superalloy 718 – Metallurgy and Applications*, ed. E.A. Loria (TMS, 1989), 69-77

56. M.E. Brown, *Introduction to Thermal Analysis* (Dordrecht, The Netherlands: Kluwer Academic Publishers, 2001), 55-87.

57. W.D. Cao, R.L. Kennedy and M.P. Willis, "The Homogenization Process in Alloy 718". Superalloys 718, 625 and Various Derivatives, ed. E.A. Loria, (TMS 1991), 147-160

58. H.B. Dong, "A Computer Simulation Program for a Two-pan Thermal Analyzers" (Report: Department of Engineering, University of Leicester, 2008)

59. D.R. Poirier, "Permeability for Flow of Interdendritic Liquid in Columnar-Dendritic Alloys", *Metallurgical Transactions B*, 18B (1987), 245-255

60. K.P. Ronan, "FSX-414 Characterization Project Update" (Report Phase I - Update 1, PCC Structurals Inc., 2003)

61. K.P. Ronan, "FSX-414 Characterization Project Update" (Report Phase I - Update 2, PCC Structurals Inc., 2004)

62. K.P. Ronan, "FSX-414 Microstructure Interpretation Guide" (PCC Structurals Inc., 2004)

63. L. Li, "Solidification Modeling of Hot Tear Test Vehicle Structure Iteration 1" (PCC Structurals Inc., May 10, 2004)

64. W. Kurz and D.J. Fisher, *Fundamentals of Solidification*, (Enfield, NH: Trans Tech Publications Inc., 1998), 117-130.

65. Dr. R. Boyles, private conversation with the author, PCC Structurals Inc., 13 July 2004

66. *JMP™ Statistics & Graphics Guide* (Cary, NC: SAS Institute, Inc., 2002)

67. Y. Fukui et al., "Effect of Titanium, Niobium and Zirconium on Creep Rupture Strength and Ductility of Cobalt Base Superalloys", *Metallurgical Transactions A*, 12A (1981), 1033-1039

68. M.K. Miller, S.S. Babu, M.G. Burke, "Comparison of the phase compositions in Alloy 718 measured by atom probe tomography and predicted by thermodynamic calculations", *Materials Science and Engineering*, A327 (2002), 84-88

# APPENDICES

# Appendix A

## Detailed Drawing of Hot Tear Test Vehicle (HTTV) Casting

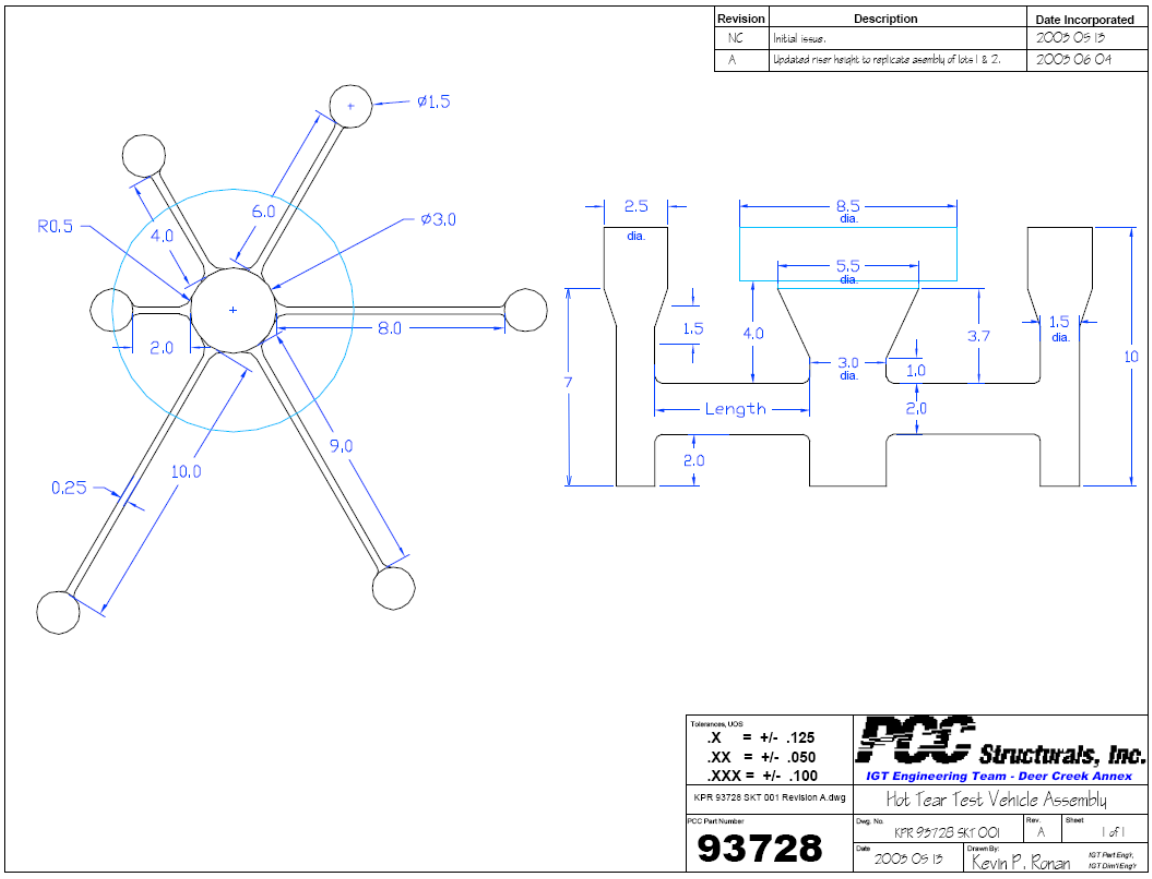

# Appendix B

## HTTV Microstructure Interrogation Plan

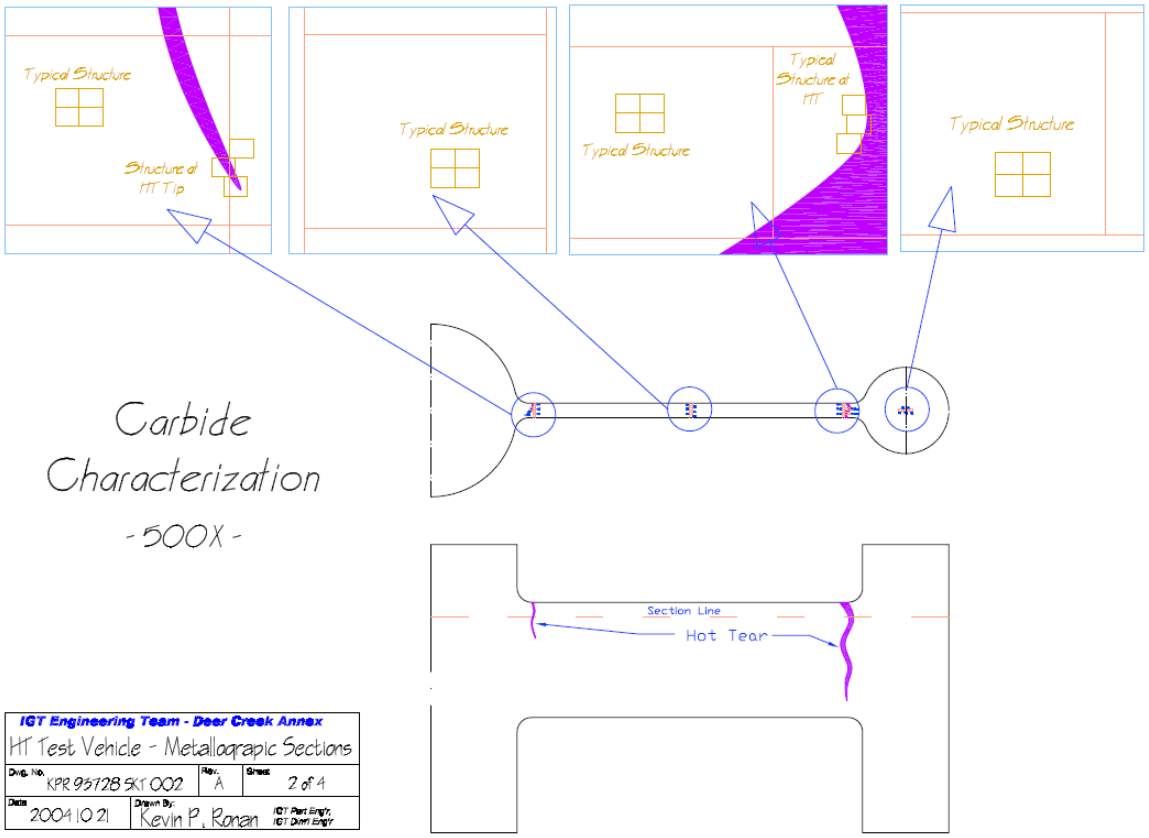

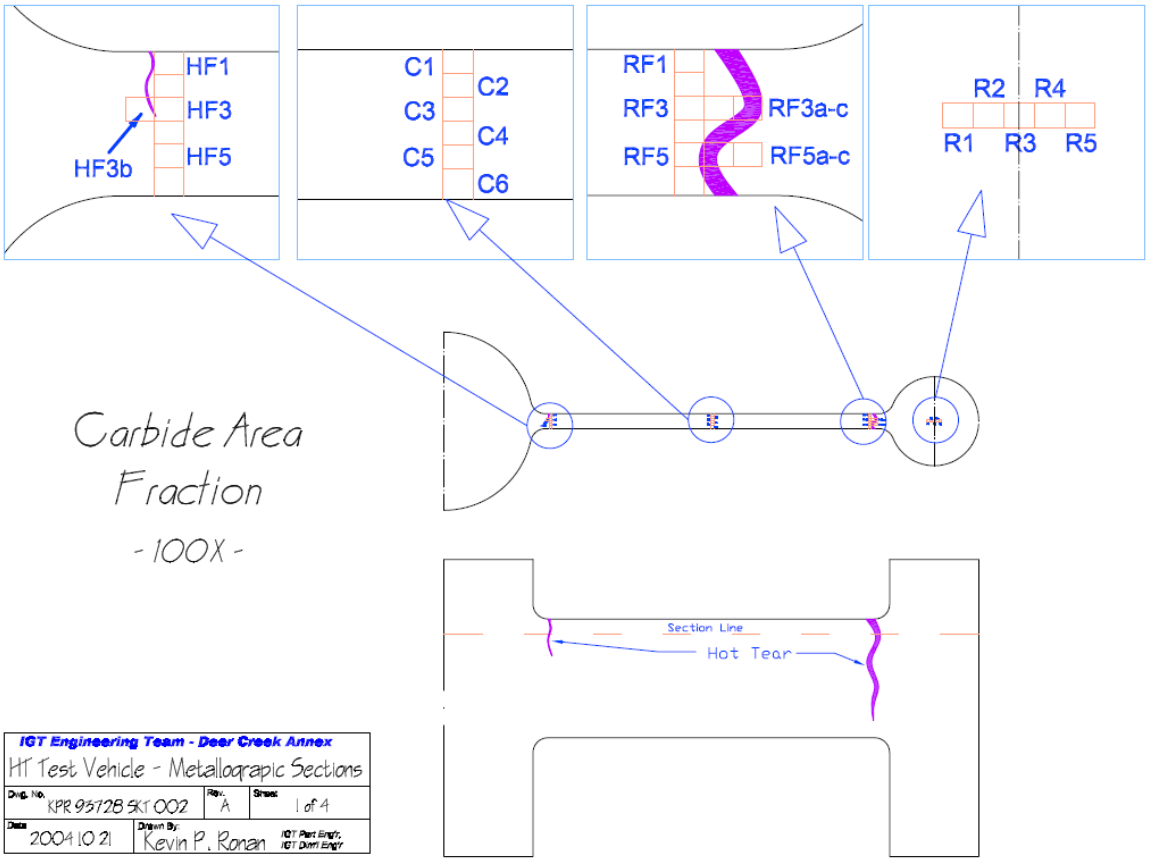
HF1
HF3
HF5
HF3b
C1
C2
C3
C4
C5
C6
RF1
RF3
RF5
RF3a-c
RF5a-c
R2
R4
R1
R3
R5
Carbide Area Fraction
- 100X -
Section Line
Hot Tear
IGT Engineering Team - Deer Creek Annex
HT Test Vehicle - Metallographic Sections
Dwg. No. KPR 95728 SKT 002
Rev. A
Sheet 1 of 4
Date 2004.10.21
Drawn By: Kevin P. Ronan
IGT Plant Engr.
IGT Dsmt Engr

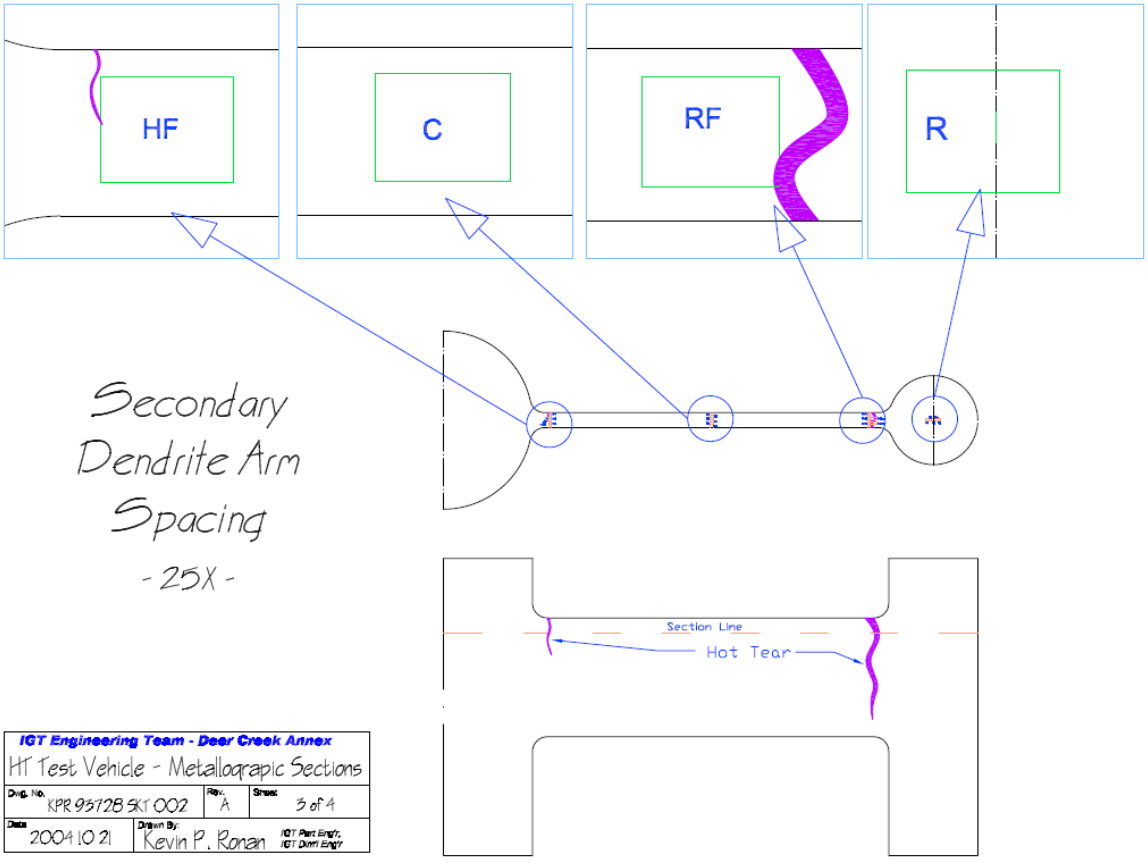


$$SDAS = \frac{\sum_{1}^{k}\left(\frac{L}{(n-1)\bullet M}\right)}{k}$$

$L$ = Length of line drawn normal to secondary dendrite arms

$n$ = Number of dendrite arms intercepted

$M$ = Magnification

$k$ = Number of rows of secondary dendrite arms interrogated

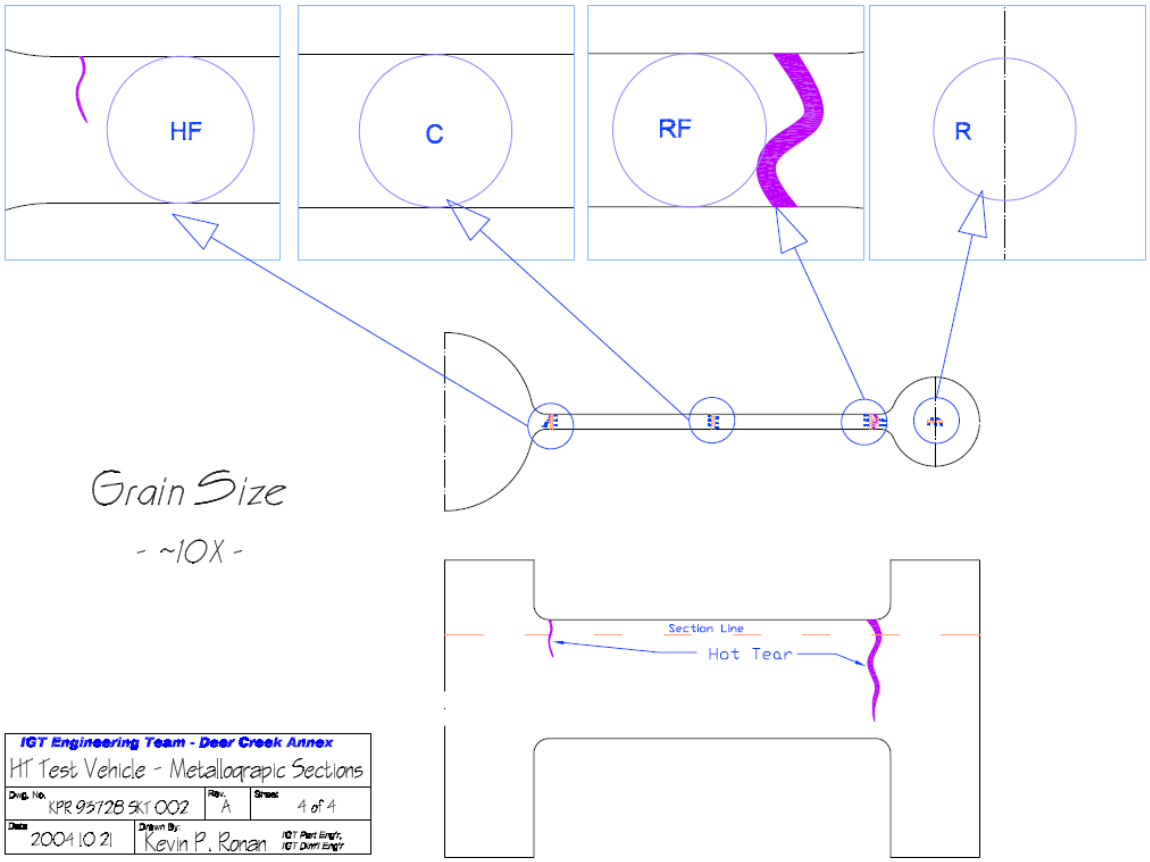


$$GrainSize = \frac{n}{L}$$

$n$ = Number of grain boundaries intercepted

$L$ = Total length of all lines drawn in field of view

**Notes:** Lines intercepting grain triple points are counted as 1 ½ interceptions.

Lines ending exactly on a grain boundary are counted as ½ intercept.

# Appendix C

## FSX-414 Microstructure Interpretation Guide

All samples shown have had their carbide microstructures revealed with a 10% ammonium persulphate electrolytic etch.

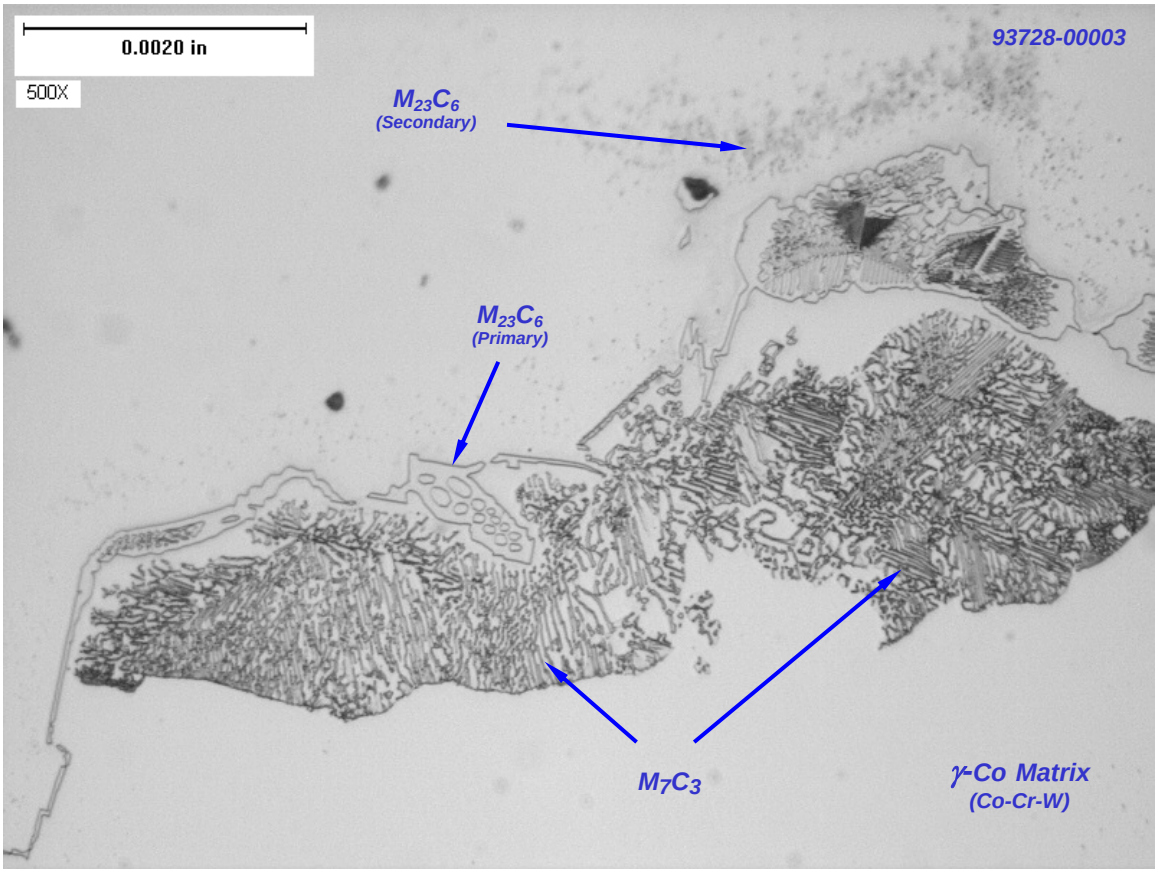

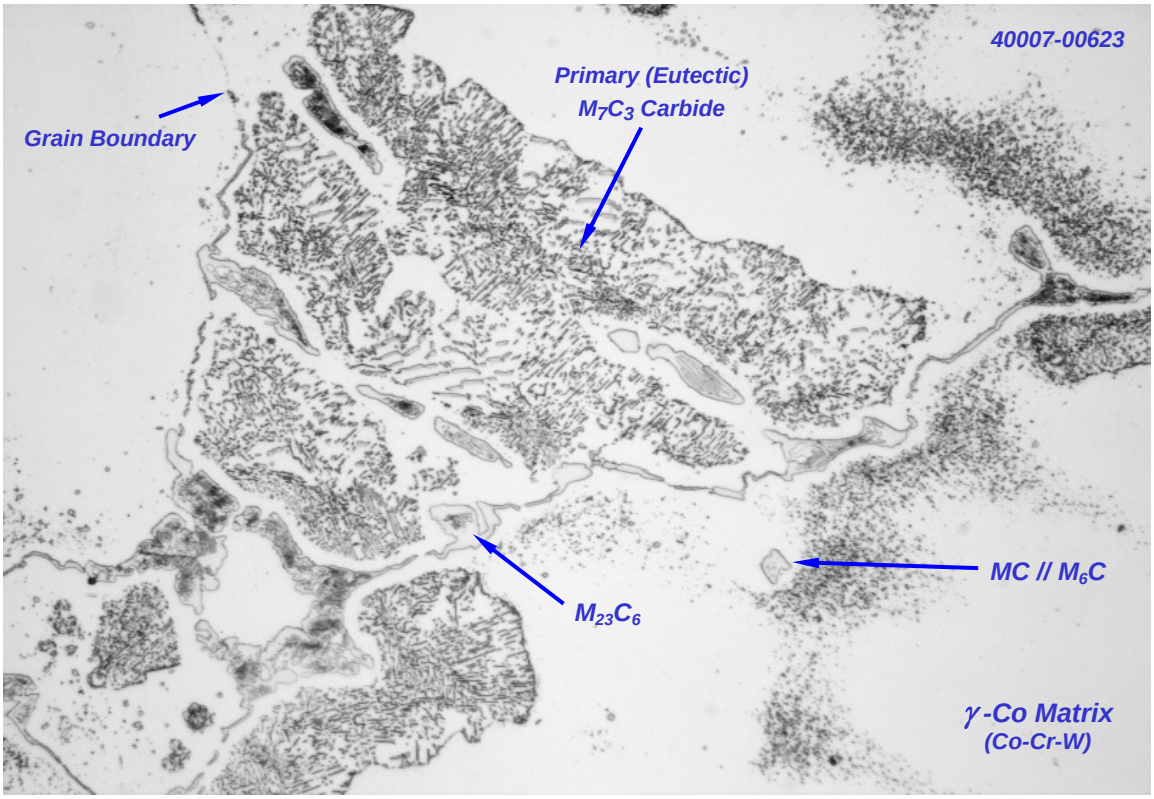
40007-00623
Primary (Eutectic)
$M_7C_3$ Carbide
Grain Boundary
MC // $M_6C$
$M_{23}C_6$
$\gamma$-Co Matrix
(Co-Cr-W)

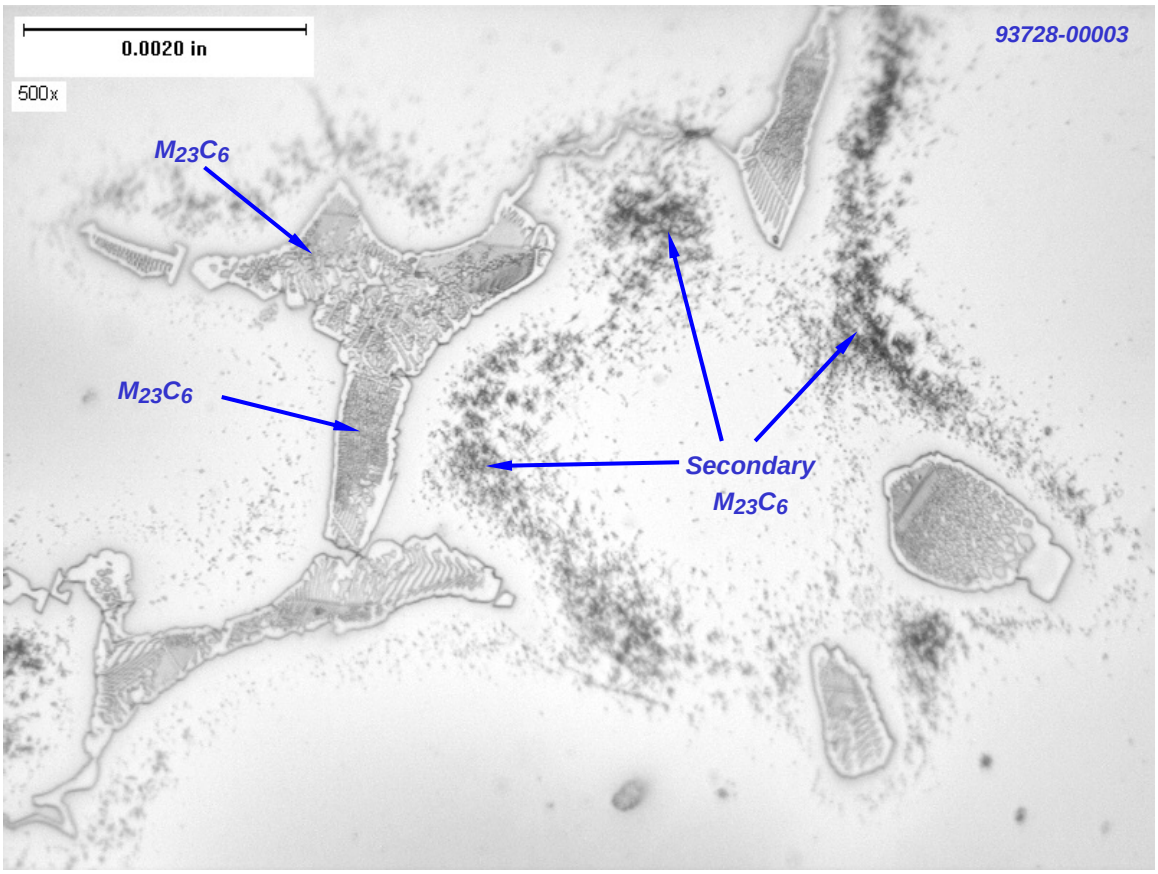
0.0020 in
500x
93728-00003
$M_{23}C_6$
$M_{23}C_6$
Secondary
$M_{23}C_6$

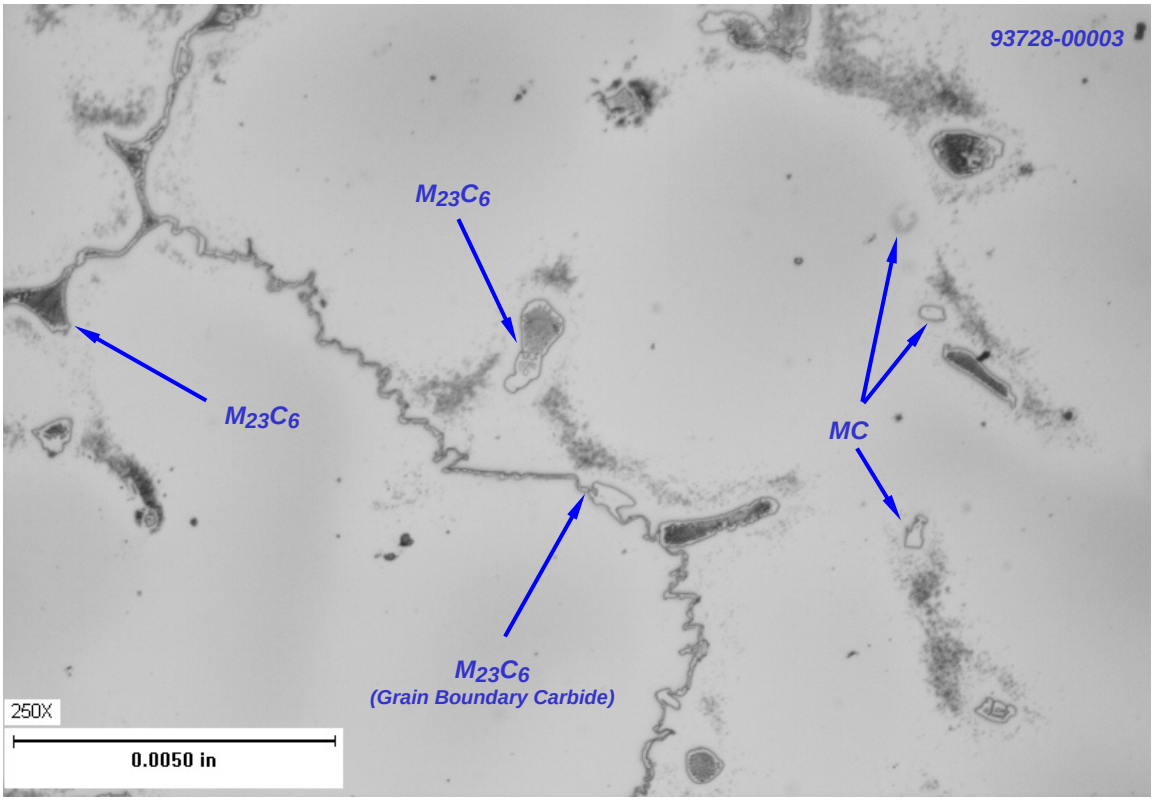
93728-00003
$M_{23}C_6$
$M_{23}C_6$
MC
$M_{23}C_6$
(Grain Boundary Carbide)
250X
0.0050 in

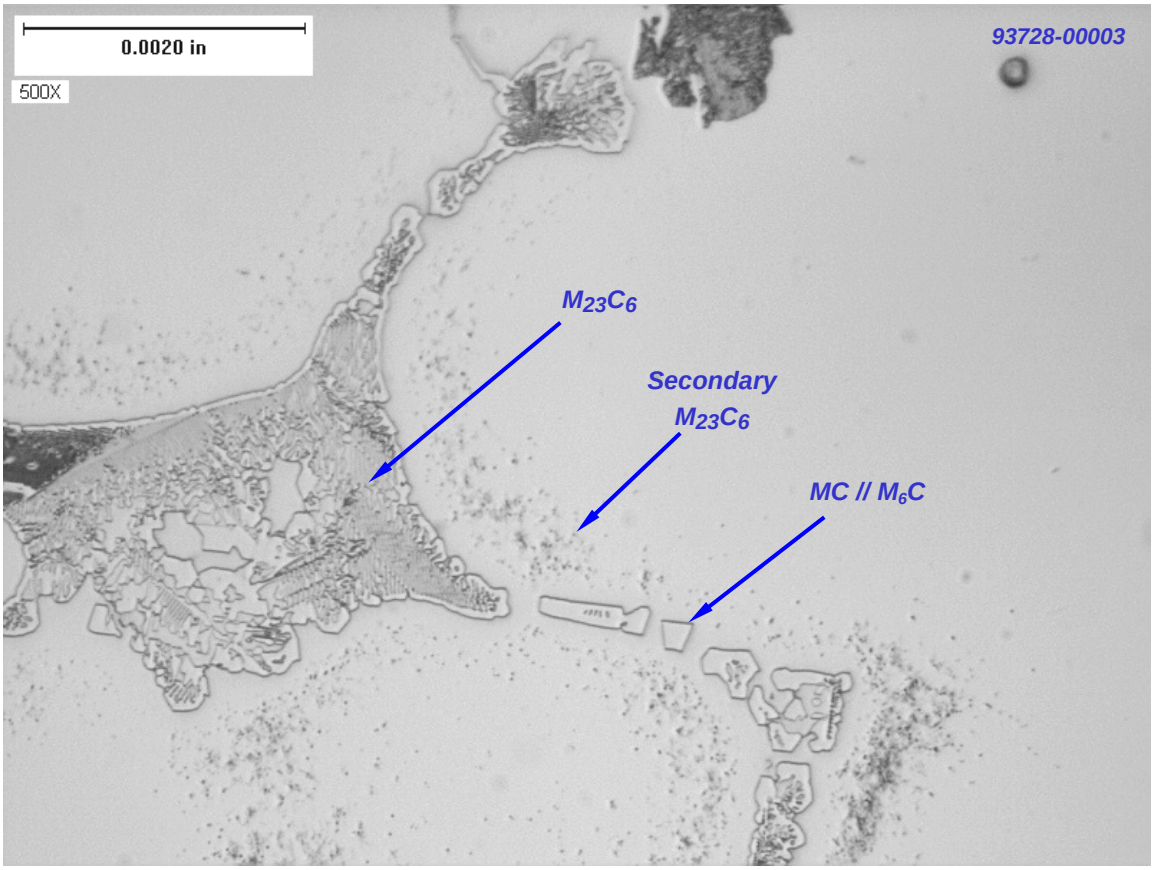
0.0020 in
500X
93728-00003
$M_{23}C_6$
Secondary
$M_{23}C_6$
MC // $M_6C$

# Appendix D

## WDX Maps Characterizing Carbide Chemistry at a Hot Tear Tip

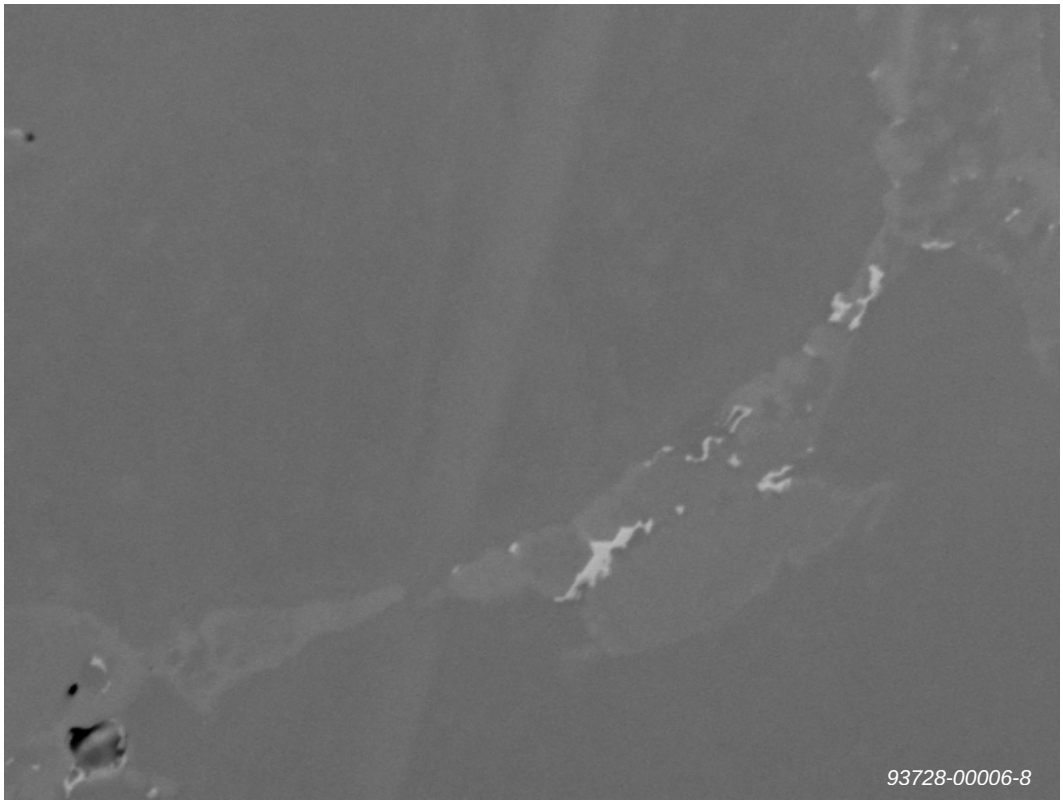


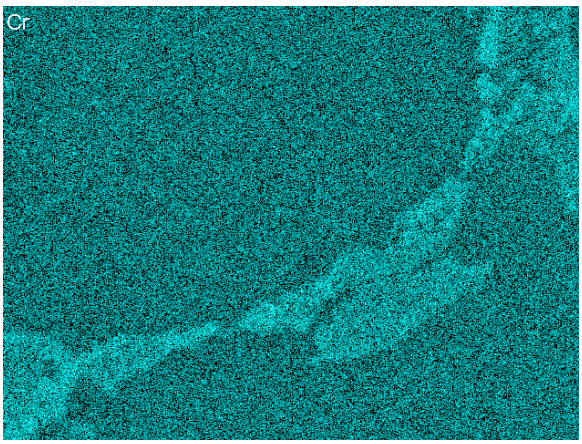


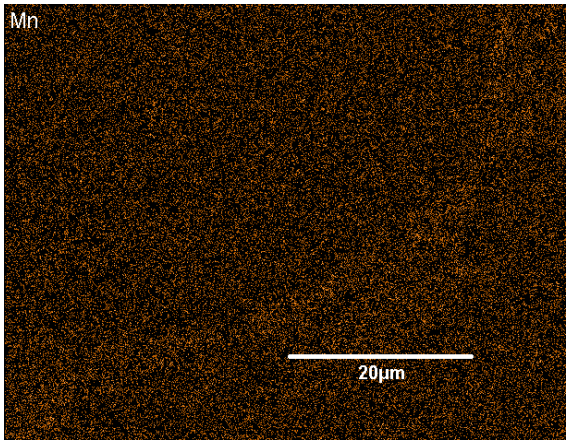

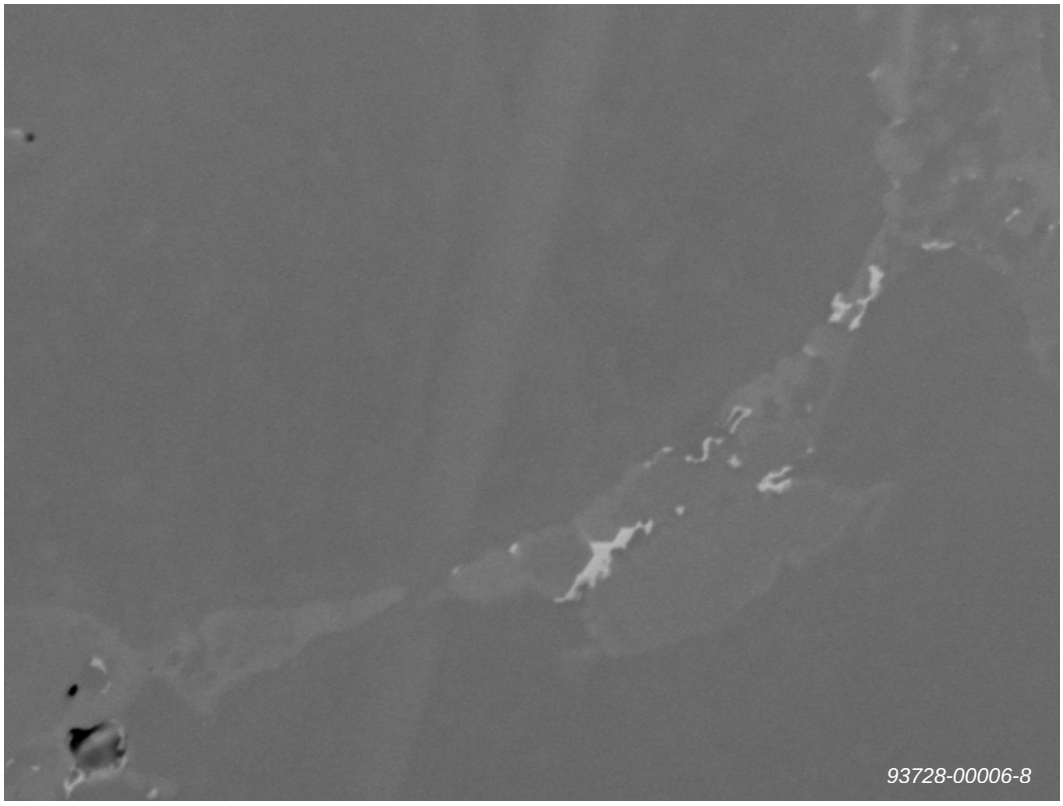
93728-00006-8

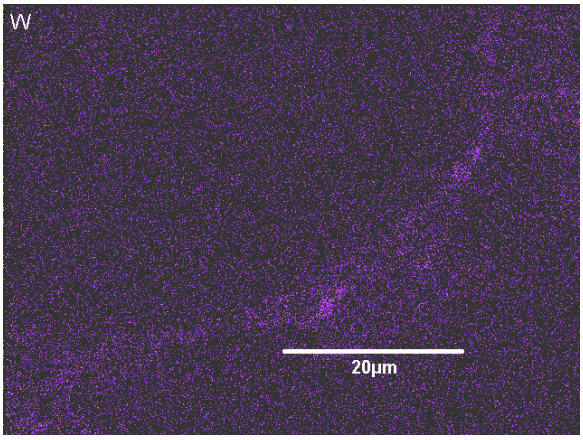
W
20µm

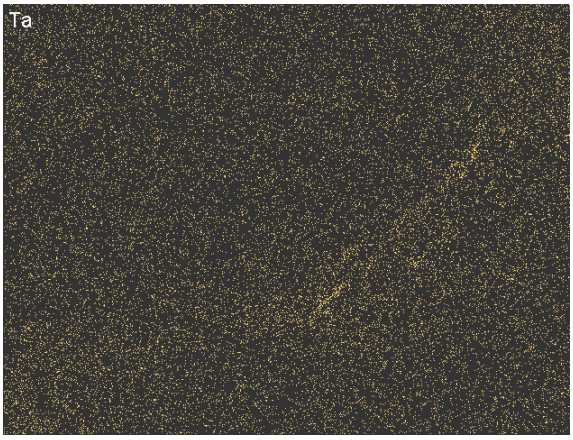
Ta

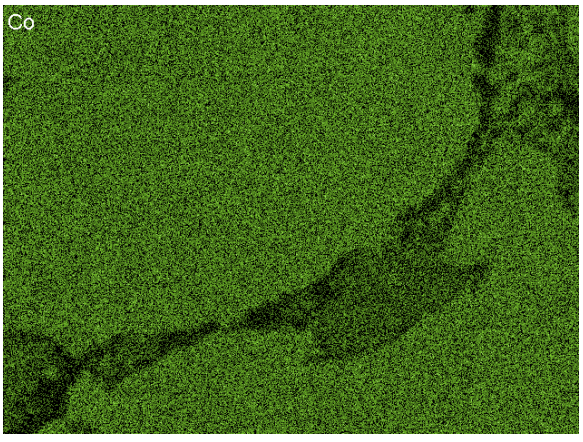
Co

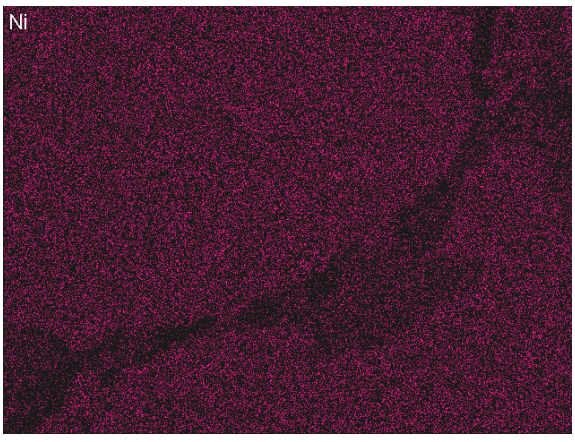
Ni

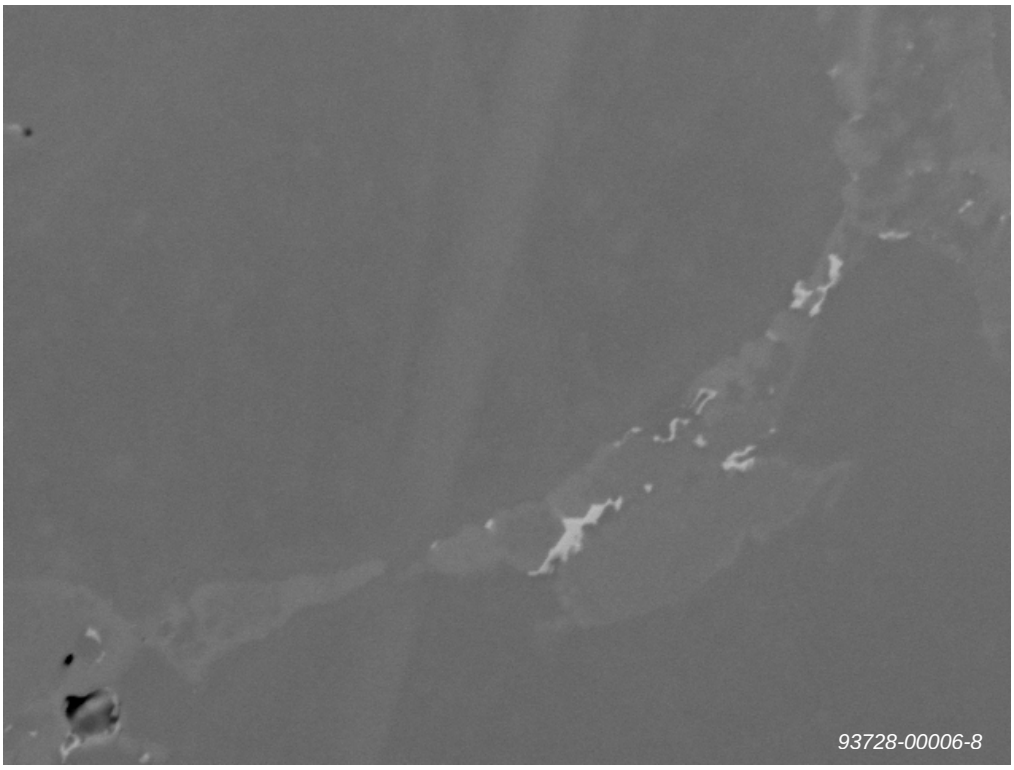
93728-00006-8

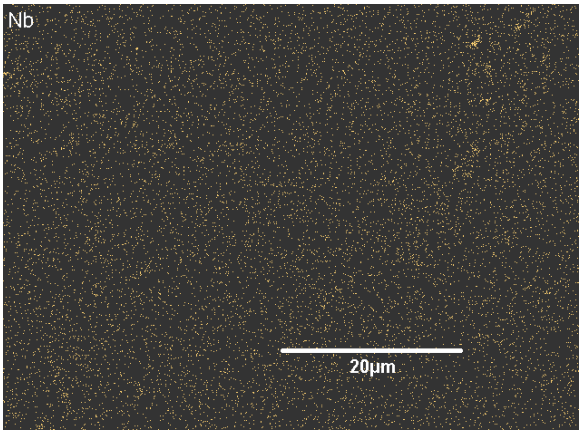
Nb
20µm

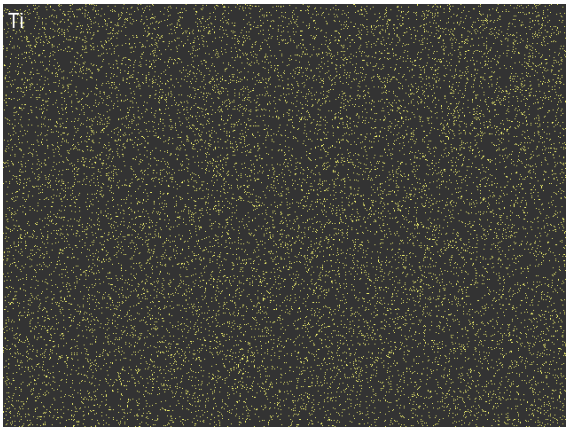
Ti